Mechanics of filaments and spherical particles: role of elasticity and hydrodynamic interaction

A Thesis

submitted to the
Tata Institute of Fundamental Research, Mumbai
for the degree of

Doctor of Philosophy
in Physics

by

S Ganga Prasath

International Centre for Theoretical Sciences
Tata Institute of Fundamental Research
Bengaluru, Karnataka
March 2019
Final version submitted: July 2019

DECLARATION

This thesis is a presentation of my original research work. Wherever contributions of others are involved, every effort is made to indicate this clearly, with due reference to the literature, and acknowledgement of collaborative research and discussions.

The work was done under the guidance of Prof. Rama Govindarajan and Prof. Narayanan Menon, at the International Centre for Theoretical Sciences, Bengaluru.

S Ganga Prasath

In my capacity as supervisor of the candidate's thesis, I certify that the above statements are true to the best of my knowledge.

Prof. Rama Govindarajan

Prof. Narayanan Menon

Date: 28 - March - 2019

To Amma, Appa and Ram.

Acknowledgments

PHILOSOPHY can be a heavily loaded term, primarily due to the history it carries with it. But in a post-modern setting, it carries a more mellow meaning and is acquired piecemeal than through a formal system. My PhD has definitely been post-modern, in the best possible sense of the term. Thanks to two people for making it that way. The fact that I happened to get Rama Govindarajan and Narayanan Menon as my advisors is one of those rare strokes of luck as the engulfing of mitochondria by a bacteria. They both have shown more than they have expressed in words what they stand for and have instilled in me a permanent sense of awe at them. Rama has been the greatest support academically and an unjaundiced friend outside. All the arguments on asymptotics, dominant balance and questioning has taught me how to never be satisfied with a mathematical expression, unless you understand what it represents physically. Once in the ICTS laundry room, I remember her telling me about what kind of research India needs and what stands in the way of India becoming a research super power. Her consciousness about society, India and the need to be multi-cultural are things I will remember. The amount of freedom she has given me to explore, to collaborate with anyone I liked, work on a problem of my interest and the unbridled faith in what I did, has imparted a sense of responsibility. During one of our tea table *addas*, I remember asking her what made her so patient and composed even under a lot of pressure/offensive arguments. To that she narrated the story of his neighbour who though had always the right point never garnered enough attention just because of how irascible he was. That is definitely a lesson I would like to learn, if not now but at least with age. I sincerely thank her for all of this.

I have been incredibly fortunate to have had the opportunity to work with Narayanan. His humility is unparalleled and overshadows his knowledge and understanding of physics. Working with Narayanan is so much fun, watching him write always the right scaling for expressions and learning through those scaling has been immensely insightful. Show him data and he sees the whole story, his method of interpreting data is something I wish I could learn. When it comes to framing a research question, he has taught me what is worth answering and what is not. All my understanding of elasticity is primarily due to him and his approach of how theory serves a purpose only with experiments has impacted my thinking deeply. Also while treading the research path he has showed how to make claims from results, not superfluous and at the same time not underselling has taught me a lot about fairness and ethics in research. I remember asking him once if he believed in any "kind" of philosophy, he in his usual refined self said "*I am a more of live the moment kind of guy*." I still don't understand what he meant but I interpreted as something like philosophy is for people of the past and whats important is to have fun. His yearning to learn new things, from anyone and everyone, his knowledge of anything and everything, the kindness with which he handles difficult situations have taught me the power of composure. He has been more than a mentor, and a friend. At every stage of my PhD he has been encouraging, given me the freedom to collaborate, let me take my own path in research and has always wished (and also put in a lot of effort) for my betterment. I thank him for being what he is.

After moving from Hyderabad to Bangalore, I am so happy to have met Vishal. Vishal is a man

capable of anything, ask him to derive KdV, he will do it when he is half-awake; ask him to go from Navier-Stokes to lubrication theory, he will do that with the drop of a hat; ask him to teach you UTM he will spend a whole afternoon flooding your brain with all his knowledge. Working with him has been the greatest learning experience in Bangalore, of course filled with lot of laughter. If there is one thing I would like to carry from working with him, it is rigour. No equation is threatening, no integral is fearsome, thats his outlook and I wish I could learn that from him. He has always been encouraging and been excited by every problem that I feel excited about. I thank him for all the time he has spent with me, teaching me all that I know about PDEs.

Meeting Joel in Hyderabad was one of the happiest accidents in my PhD. He has been constantly supportive and has patiently been there to listen to all the minor details, hurdles in experiments and calculations when Rama and Narayanan were busy. Beyond a friend, a mentor, Joel is an amazing researcher to look up to. His ability to establish contacts with people in our scientific community has proved extremely useful for me. He has been an amazing host during my visits to Boston and Princeton. Thanks Joel for being such an accommodative person, especially during my visits to US, and France. I am sure we will collaborate even further in times to come and all the best for your career in Aix-Marseille. During one of my visits to Amherst, I was lucky to collaborate with Benny Davidovich. His rigorous attitude towards calculations and feel for asymptotics have surprised me always. I extend my sincere thanks to Benny for spending all his time teaching me his ideas, and detailed notes to explain me the calculation method. I learnt a lot about elasticity during the short visit there. During my Amherst visits, Lee, Deepak and Joey have been very helpful in settling in there and also with my experiments. Thanks also to Jooyoung for his time and helping me out with Zygo. All movie conversations with Deepak and walks to Amherst center with Guangfeng will definitely be remembered.

Through Rama and Narayanan I have gotten to know lot of amazing people. Two of whom I am very happy to have known are Sriram and Shubha. Sriram, I remember when I joined TCIS Hyderabad, came up to me and introduced himself. My parents and I were awestruck at a institute Director being so humble. Just watching him speak is a great sight, he is delighted about everything and knows something or the other about everything. I am happy to have been part of all the super pleasant conversations with him and his family. Shubha, I remember once had an invitation to take someone along to a Hindustani chamber concert in Banjara hills. I was lucky to be the one to go with her to the concert. Starting from then, to the stays I had at their place during my multiple visits to Amherst and even the last visit to their place during Thanksgiving have all been crazy fun. She has been a great person to bounce ideas, discuss science, art, and books. The amount of effort Shubha and Narayanan put in and the help they have been during my stays at Amherst is hard to describe and I am sure very few people would be willing to stretch so much for their students. I thank them from the bottom of my heart. It has also been a lot of fun knowing Achin, Kabir, Achala, and Vidur. Thanks again to their parents for introducing them to me. I have also had a lot of fun knowing Samriddhi, whose witty English styled comments, fascination for Wodehouse, and a hyper enthusiastic working style have inspired me. It has also been great knowing Harish, Smarajit, Prasad, Hari Das and Kirthi, who have all been encouraging.

First two and a half years of my PhD in Hyderabad was nothing but revelry with all amazing people around me. I have managed to be in touch with several of them so far. I am happy to have known Jose, Croor, Bharat, Surbhi, Parvathi, Prathyusha, Ananyo, Suropriya, Rayan, Shubhadeep. The amount of mischief we as a gang indulged in is unparalleled and our rides to have Allam/Lemon chai in Pandey's vehicle to Narsingi are unforgettable. Special thanks to Jose for reading parts of my thesis and giving extremely pertinent and useful comments. He has also been a great source of in-

spiration in terms of the patience he exudes and also the variety of books he reads. Thanks Jose for always being encouraging and for sharing your teenage Mangas with us. It has been great and special knowing Thejas, who since I have known him has remained very close, though by distance has been far for a while now. His good kind of innocence has inspired me and his playfulness has cheered me during lulls. Special thanks to him and Surbhi for keeping in touch and being there. Thejas has been a great and genuine listener and has become more than a friend (I am sure we will be in touch for a long time). Our trip to eastern Europe and tiffin hopping in Malleshwaram will be remembered. Thanks Thejas. Joining violin classes after my first visit to US was one of the right decisions I can confidently say I have taken. Getting to know Vasu sir, Nikhil, Hari, Krishnamurthy, Patanjali has been a great experience. All our Udupi conversations on discussing Ragas, their treatment by different legends were super exciting. I wish I could have more such conversations. Our trip to Coorg with violins on our back was an unforgettable experience. Thanks for being such awesome people.

After moving to Bangalore, I have gotten to know another bunch of amazing and equally fun people. It feels great to have known Priyanka, Jemseena, Saleem, Prita, Sankaran, Mukesh, Rahul, Pushkal, Sumit, Chandan, Jason and Gayatri. Continuing the Hyderabad tradition, all the tea table conversations have been super fun. The badminton gang has been great to burst all the day-to-day stress, for all the road trips and rave parties. Thanks to them for being such jolly good chums. Getting to know Adhip has been special, he has been a partner in crime (Sthayi), and has been very genuine, supportive and provided useful advise whenever I have asked for. I thank him for that and wish him the best for his future. I would like to specially thank Rahul Chajwa and Sumit Birwa for being great lab mates. They have made working in KS Krishnan lab a pleasant experience. All the academic conversations with Chajwa have been very useful, and he has been a great person to bounce ideas. He has also inspired all of us in the lab to work, through his immense hard work. Sumit has been very supportive from the beginning of my PhD and has always been encouraging. All our fun conversations in the lab will definitely be remembered. I thank him for being such a fun sport. Ritabrata, and Pranav have been amazing flat-mates. Living in the same building with them has been extremely peaceful, they gave me enough space and Ritabrata took several of the chores on himself which rightly I should have taken a share. He has also been an amazing listener, be it academic ideas or random discussions, and has acted really mature in several situations, I thank him for that and listening to all the crap I have blabbered. All our jamming sessions, hikes to the western ghats will be remembered.

Being in Bangalore has had the big advantage of proximity to family. Ram and Srinidhi stayed close for more than a year and it was so easy to drop by their place for tea, food and *mokkai puttings*. They have been highly encouraging, supportive and always been there to fall back. All the fights with Ram have been so useful as they have always provided perspective, and I am happy to have had him as a partner in crime. My parents and Ram have been the greatest support throughout my life. They have always been by my side since my school days. I had never imagined that I would end up doing a PhD in physics but when I made that decision, they endorsed it without the slightest of hesitation. In hindsight I think my parents have been very liberal all the way from childhood and my father's vision is really behind this outlook. I also realise now their delightful innocence is really a gift. For a small town boy like myself, a major part of my understanding of world has come from my parents and they have spent an immense amount of effort on us. It would be ludicrous to try to thank them here, all that I can do is try to succeed.

Contents

Publications

1. Ganga Prasath, S., Joel Marthelot, Rama Govindarajan, and Narayanan Menon.
   Relaxation of a highly deformed elastic filament at a fluid interface.
   Physical Review Fluids, 10.1103/PhysRevFluids.1.033903. [arXiv]

2. Ganga Prasath, S., Vishal Vasan, and Rama Govindarajan.
   Accurate solution method for the Maxey-Riley equation, and the effects of Basset history.
   Journal of Fluid Mechanics, 10.1017/jfm.2019.194. [arXiv].
   Selected for Focus on Fluids (article written by Prof. George Haller).

3. Ganga Prasath, S., Joel Marthelot, Narayanan Menon, and Rama Govindarajan.
   Wetting properties of a droplet in contact with a highly-bendable elastic filament. *(to be submitted).*

4. Fabian Brau, Ganga Prasath, S., and Benny Davidovich.
   Morphologies of bendable solids: Insights from a two-dimensional, inextensible model. *(to be submitted).*

5. Vishal Vasan, Ganga Prasath, S., and Rama Govindarajan.
   Boundary-bulk extension of fractional derivatives with application to Maxey-Riley equations.
   (under preparation).

6. Ganga Prasath, S., Joel Marthelot, Rama Govindarajan, and Narayanan Menon.
   Coiling of an elastic filament on the surface of a spherical bubble. *(under preparation).*

"What a useful thing a pocket-map is!" I remarked. "That's another thing we've learned from your Nation," said Mein Herr, "map-making. But we've carried it much further than you. What do you consider the largest map that would be really useful?" "About six inches to the mile." "Only six inches!" exclaimed Mein Herr. "We very soon got to six yards to the mile. Then we tried a hundred yards to the mile. And then came the grandest idea of all ! We actually made a map of the country, on the scale of a mile to the mile!" "Have you used it much?" I enquired. "It has never been spread out, yet," said Mein Herr: "the farmers objected: they said it would cover the whole country, and shut out the sunlight ! So we now use the country itself, as its own map, and I assure you it does nearly as well."

–Lewis Carroll, Sylvie and Bruno Concluded

1 Overview

We look at the mechanics of slender elastic structures, and rigid spherical particles in fluid flows in this thesis. In this chapter we introduce the motivation behind our endeavour by briefly alluding to literature first and detailing the scheme of things that are happening in the field later.

1.1 Large deformation of elastic filaments

Elastic structures with one dimension longer than other two similar dimensions are called filaments. These filaments are all around us, starting from ciliary hairs [75] inside our ears to canopy of trees [37] in farms. External forces and moments applied on the filaments introduce deformations that change the filament's shape. A major understanding of the mechanics of filaments in the previous century came about assuming these deformations to be small. Many text books [130, 53] on mechanics of elastic structures such as beams present the understanding in this limit of small deformation. In the small deformation limit, the forces due to deformation are linear in the displacement field whereas large deformation makes the system of equations non-linear (primarily arising out of geometry rather than large strains). Though the linear theory has provided preliminary insights into the mechanics of filaments, it how-

ever does not capture a wide range of phenomena. It is this non-linearity that has posed a difficulty in several scenarios as handling the non-linearity both numerically and analytically has proven to be difficult.

Another aspect of large deformation is that geometrical constraints such as conservation of length of filament play a very important role. In fact these geometrical constraints are strongly related to the non-linearity itself. Large deformations can be physically introduced in the filaments in two prototypical manners: (a) across entire filament length by externally/internally applied forces and moments, (b) large locally applied external forces and moments. Recent studies [140, 55, 45, 28, 4] in the large-deformation regime have looked at different instabilities in filaments however the specific role of non-linearity has not been clearly addressed. Further, a typical way by which this large deformation is introduced in the filament system is through natural curvature [97, 11] or externally applied body force. It is not clear if these large deformations can be introduced in other manners.

Large deformation localised at a given location on the filament surface has been studied in literature [111, 19] by using the capillary force of a liquid droplet interface. Since surface tension exists only at the droplet interface, placing the elastic structure such that this interface comes in contact with the elastic structure ensures a localised force. In the important experiments of Py et al. [111] (followed by several theoretical studies), a droplet of water is placed on top of a sheet such that the surface tension force at the droplet-sheet contact line can deform the sheet. As the droplet evaporates they saw that the capillary force applied at the contact line deformed the sheet, eventually folding it. This folding mechanism they proposed can be used to fold sheets by design using capillary forces, similar to the paper folding technique of Origami. The sheet equations used by Py et al. [111] are the same as the equations for filaments as they assume invariance in the transverse direction (perpendicular to the length of the sheet) and thus the implications derived by them for sheets are useful for filaments as well. In their experimental regime, though the deformations at the contact line are large, it is however not clear what would happen to the deformations near the contact line when the sheets/filaments were extremely thin. In the thin limit, we expect to have very large localised deformation but the shape of this deformation is not really understood. The general question of how large localised forces on these elastic structures affect global measurable features is very much an open question.

In this thesis we look at three examples where large deformation plays an important role in determining the morphology of filaments: (i) in the first set of experiments we address

the question of role of non-linearity in the dynamics of elastic filaments by performing experiments and deriving implications from the non-linear model developed by Goldstein and Langer [55] for stiff polymers, (*ii*) as a way to introduce large deformation across the length of the filament, we bring in the aspect of geometry of the substrate over which filament lives. By changing the shape of the substrate, we can introduce different kinds of body force as a consequence to the normal reaction from the substrate. In our second set of experiments, we introduce substrate geometry using soap bubbles which hold the elastic filament to it surface. We then ask how does large deformation introduced now through the bubble modify the filament shape, (*iii*) our last set of experiments to understand the effects of very large localised force at a given location on the filament surface uses capillary forces, similar to Py et al. [111], but now in the limit of very thin filaments. We look at the shape the very thin filament takes when large amplitude of capillary force is applied.

Though the focus of the experiments and the supplementing theory are to understand the effects of non-linearity, we also look at other aspects in the experiment which are hitherto unknown. In each of the experiments, we look at different morphologies of the filament through the lens of confinement vs bendability (as detailed later in this chapter). We find the phase space of filament shapes in these settings through theoretical calculations, even though we are limited by experimental capabilities to explore all of them in experiments.

1.2 Particles in fluids

Dynamics of particles in flow is studied by different communities with varied interests such as to understand physics of emulsions [25], dynamics of microorganisms in flows [83], dynamics of dust in atmosphere [13] and so on. Study of particles in fluid flows date back to the time of Stokes [78] in 19th century. The solution to the steady state problem where the force on sedimenting particle is balanced by drag force was solved by Stokes. The time dependent problem was found to be more difficult than the stationary problem and it was solved by Basset [12], in his treatise on hydrodynamics in 1888. The solution was shown to involve a history integral, now named after Basset himself, where the force on a particle depends on the entire velocity along trajectory it has traveled till that time instant. These solutions however do not account for the finite Reynolds number effects, which become important at late times at any value of Reynolds number. This problem of accounting for finite Reynolds number effects was solved in the landmark work of Lovalenti and Brady [90, 91]. The work was ex-

haustive, however the solution obtained was complex and was not extended to many particle systems. Complex systems such as particles in turbulence, which are relevant to understand dynamics of rain formation [57, 46], aggregation of phytoplankton [61, 13] in ocean are limited by the extension of the single particle system to many particle dynamics. Thus there exists a bottleneck to firstly resolve the issue of effects of history integral, if it is important and if so in the kind of scenarios where they are relevant.

Another aspect of the history force, which was only recently understood is its singular nature [47] at the initial time instant. The original solution of Basset resulted in an unphysical integral traversing from $-\infty$ to t, along the entire trajectory of particle. Farazmand et al. [47] showed that the Basset force has a singular contribution if it started at $t = 0$. The numerical methods that exist so far [135, 32] do not include the singular contribution, however they evaluate the integral using a quadrature scheme. These schemes, though provided initial understanding of the dynamics of particles with history effects accounted in turbulence [102], it has failed to create an impact in several scenarios due to the large memory requirements (to store the trajectory of particles). Thus we observe that a numerical technique with low memory cost is an immediate need and also be an effective way to account for the finite Reynolds number effects. In this thesis we address the issues related to storing the history force by a novel technique that maps the non-local history term as a local term by the technique of domain extension. We find exact solution for all time dependent space independent flow velocities. Using this technique, we come up with a spectrally accurate numerical technique that captures the history with only a constant memory cost, independent of time for generic non-linear flow fields.

1.3 Bird's eye view of literature

Modern science can be seen as a continuation of natural philosophy, shed of all the sociological shackles that it was bound by during its time. Understanding phenomena occurring in nature is a theme not new but ancient [129], however the monocle with which we observe and describe the natural phenomena has undergone several changes. These natural processes that occur at observable length scales $\sim \mathcal{O}(\mu\mathrm{m}) - \mathcal{O}(\mathrm{km})$ and time scales $\sim \mathcal{O}(\mathrm{sec}) - \mathcal{O}(\mathrm{hr})$ are generally perceivable by human beings. It is usually portrayed by both the popular media/books and graduate level courses that this human perceivable regime is all understood. However, this is far from the truth as phenomena such as loop formation in leaf vein [71],

locomotion of small aquatic wildlife [82, 81], aggregation of phytoplankton [61, 13], morphology of hair [16, 97], snapping of venus flytrap [51], petal formation in plants [87], insect and bird flight [117], wrinkling of skin [26], sulci/gyri generation in brain [62], villi creation in the gut [125], climbing of creepers around a pole [123], drinking mechanism in birds and animals [2, 120, 116], swimming of large scale organisms such as sharks and whales [52], swarming of birds and insects [99, 126, 132], formation of cloud and rainfall [134, 124, 57, 46] etc. are all topics of recent/current research and a major initiation into their understanding has taken place only in the last two decades. These questions which one would imagine to have prosaic answers, have been shown to have complicated answers mathematically more often than not. An important aspect of all these examples is the role of mechanics, where a specific function or feature in these systems arises out of the interplay between forces.

The motivation behind these researches were often purely fundamental, but have heavily been borrowed for useful work lately. Developments in polymer technology and 3D printers have led to artificial designs in a laboratory to mimic naturally occurring phenomena. These have provided a new methodology to deal with complicated questions for which nature already has an answer, optimal or otherwise. Various robotics technology such as swimmers and amphibian robots of Pliant Energy Systems [48], FestoHQ, soft robots that mimic the hand, fingers and leg [121], or Kirigami inspired snake bots [113] are an outcome of this scheme of thinking. This theme of nature inspired robotics has launched the field of locomotion in esoteric environments for which traditional solutions to migration do not work. Such a design principle is backed by the reasoning that nature has had time by its side to experiment with trial and error to arrive at a solution.

All these human-made robots and evolution-modulated organisms employ instabilities to execute a specific response. By instability we mean that the response executed involves a transition from one equilibrium state to another state by tuning a parameter. Some examples from the aquatic world include various swimming mechanisms: motion by generating traveling waves in jellyfish, flapping flagella in sperms, wagging fins and/or tail in sharks [58, 52]. These instabilities that result in locomotion are generated in these animals via an active process that actuate the muscles or flagella. The active processes that determine the animal's ability to move usually have a feedback response where the amount of force or torque the propelling mechanism generates is a function of its environment. Thus in order to understand the mechanism of propulsion in these animals, it becomes mandatory to primarily understand the instability and also map the feedback network that determines the animal's

response. There still does not exist an example where humans have been able to reproduce exactly the feedback network and the instability mechanics we observe in nature. A step in this direction is the one taken by advance robotics labs such as Boston Dynamics.

Instabilities have also been proposed to harness useful work in manufacturing technologies by using the fact that the pattern formed as a consequence of the instability is precise [31, 100] and most often easily reproducible. Some examples from recent research include patterning a substrate using wrinkles of specified wavelength [73, 64], fabricating thin elastic shells [84], parceling tiny liquid droplets [107, 77], creating lenses using Rayleigh-Taylor instability [93], and manufacturing long filaments made out of glass [21].

1.3.1 Classification of solids and liquids

Every phenomenon described so far involves either of the two class of materials: elastic solids or viscous liquids. Elastic solids based on their geometric aspects can be classified either as bulk solids, sheets, shells, ribbons or filaments [11, 79]. When l, w, t are the length, width and thickness of an elastic structure, it can be boxed into one of the following categories based on the criteria:

$$\begin{aligned} \text{Bulk solids} &: l \sim w \sim t, \\ \text{Sheets} &: l \sim w \gg t, \\ \text{Ribbons} &: l \gg w \gg t, \\ \text{Filaments} &: l \gg w \sim t. \end{aligned}$$

Shells are sheets with intrinsic curvature, whose principal radius of curvature is comparable to that of the largest dimension of the sheet. Each class of these elastic objects has distinct mechanics based on the forces they experience, making this codification worthwhile. Viscous fluids on the other hand manifest themselves as shallow or deep based on the geometric setting in which they are confined. Dynamics in viscous fluids are also classified based on the viscosity of the fluid, where at very high values of viscosity they reduce to the time-reversible Stokes regime and at moderate/low viscosity they are in the inertial regime.

Elastic solids are also fundamentally different from viscous fluids because fluids undergo shear to arbitrary amplitudes when they are applied a constant strain, whereas elastic solids resist strain. At a constant applied stress, fluids shear at a rate dependent on their viscosity

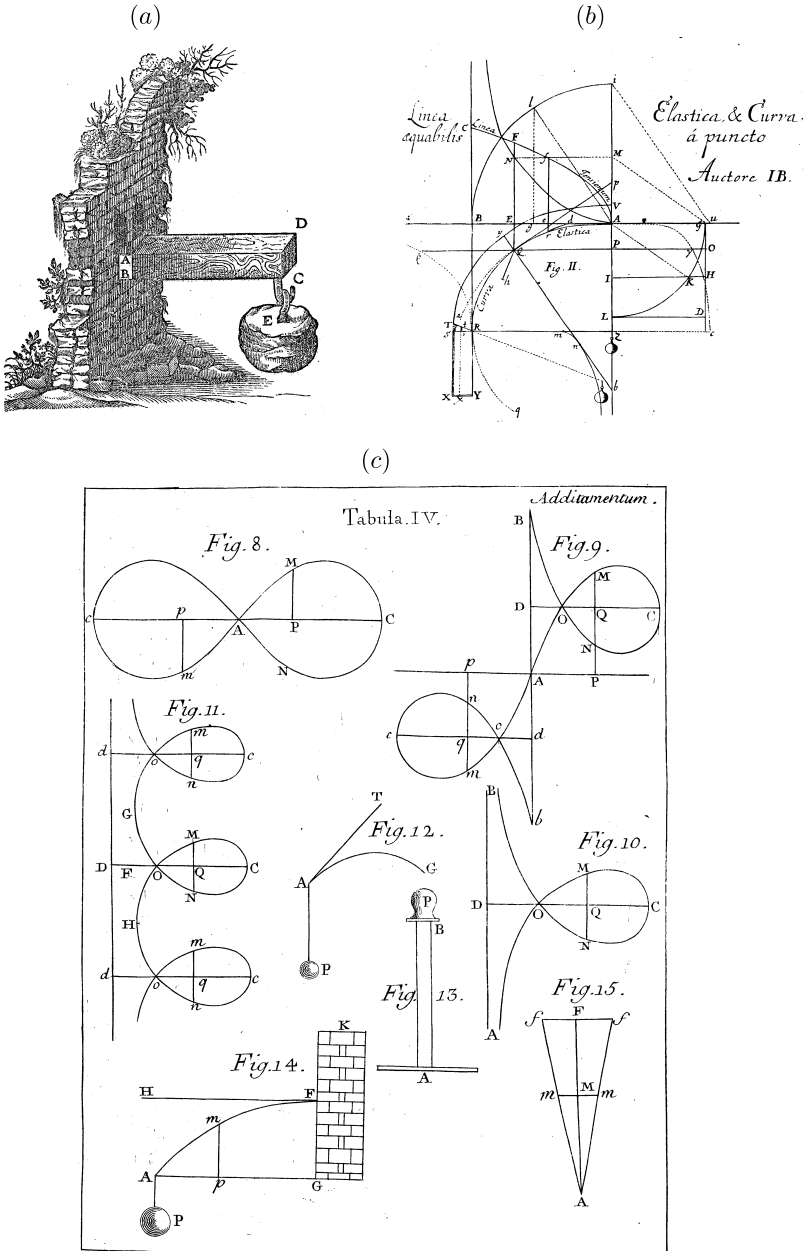

Figure 1.1: (a) Schematic of a load hanging at the end of a beam, a problem considered by Galileo in 1638 in his publication *Discorsi e Dimostrazioni Matematiche Intorno a Due Nuove Scienze.* (b) Problem of the shape of a `spring' with a hanging weight considered by Bernoulli published in *Curvatura Laminae Elasticae* in 1694. (c) Euler's solution in his work *Methodus Inveniendi Lineas Curvas Maximi Minimive Proprietate Gaudentes* in 1744, to the problem proposed by Bernoulli showing different shapes the filament takes, described by elliptic functions.

while elastic solids experience a strain that depends on its stiffness. This fundamental difference between an elastic solid and a fluid manifests itself in important manners. One of the differences being that elastic systems are energy conserving, and are describable using the Hamiltonian framework. Fluid systems on the other hand are intrinsically dissipative, and are driven out of equilibrium in order to form patterns. An isotropic elastic solid, which is of interest in this entire thesis, can be labelled by two constants: E - Young's modulus, ν_p - Poisson's ratio. A viscous fluid on the other hand is described by its viscosity, μ. Young's modulus of an elastic material is the constant of proportionality that relates the applied normal stress and the resulting strain in the material; ν_p on the other hand is the amount of transversal expansion that a material of constant volume undergoes if it is compressed axially; μ of a fluid is the coefficient that relates applied stress and resulting shear in a fluid.

1.4 Inextensible Filaments - the "*elastica*" limit

Slender elastic structures in whom one dimension is much larger than other two similar dimensions are called filaments. If the length of these filaments are preserved under deformation of the structure, they are termed "*elastica*". Euler described the mathematical question of shape of elastica under several prototypical configurations, as a solution to a problem proposed by James Bernoulli in 1691, schematically shown in fig. 1.1. Please refer to Levien et al. [85] for a detail review of the history of the problem. The elastica approximates well the shape of filaments under moderate loading for the following reasons. The argument presented here is a paraphrased version of the scaling discussed in the book of Audoly and Pomeau [11].

Consider a typical force F acting on a filament of length l and thickness t, this generates a stretching given by:

$$\varepsilon \sim \frac{F}{Et^2},$$

where we have just used the relation that stress is proportional to strain with a constant E, the Young's modulus, t^2 here is just the manner in which the area scales, and ε is nothing but the stretching deformation. We can also use the fundamental law of bending that relates bending moment to the force applied, given by:

$$Fl \sim EI\kappa,$$

where $I \sim t^4$ is the area moment for a filament of circular cross-section, κ is the curvature due to the applied force. From this we can write:

$$\frac{\kappa}{1/l} \sim \frac{F}{Et^2} \left(\frac{l}{t}\right)^2.$$

From the above two relations we get:

$$\varepsilon \sim \frac{\kappa}{1/l} \left(\frac{t}{l}\right)^2,$$

from which, given that $l \gg t$ for all filaments, we have $\varepsilon \ll 1$. This simply means that when a filament experiences a force F, the axial strain it experiences is very small as a consequence simply of the aspect ratio of the filament and its mechanics. Now that we see for moderate amplitudes of forces, the filament remains inextensible to leading order. We now look at several scenarios in which the inextensible model has been employed to understand a particular phenomenon.

1.4.1 Statics

Filaments have two modes of bending deformation and one mode of torsional deformation. When the filament is confined to a planar surface, this reduces to only one bending mode. Filaments can undergo instabilities in 2D by undergoing transformation only in this mode. This simple 2D system has been explored in detail in several physical scenarios such as: Euler-buckling where the filament/beam buckles when it experiences an external load [85]; understanding different morphologies of hair where gravity competes in changing an intrinsically curved hair's shape (due to the chemistry involved peptide bond forming process) [11]; snapping of a buckled beam where the beam initially buckled goes unstable when a point-force is applied at a given location in the beam [103]; wrinkle formation in a beam undergoing compression when the filament is bound to a substrate such as a water bath [119].

The 3D problem on the other hand, due to the complexity involved in solving the force and moment balance equations (Kirchhoff equations) is less explored analytically than the 2D counterpart. The numerical techniques required to solve these equations are also complex due to the stiff geometric constraints the elastic system needs to satisfy. This led to special techniques such as Discrete Elastic Rod model, a method initially created by animators to

simulate filaments and later borrowed into physics. Other techniques such as analytical continuation, employing AUTO07p [41] or MANLAB [7] have also been used to understand bifurcation in these systems. Some of the problems such as: shape of elastic filament constrained to a surface i.e., the elastica problem in 3D when the filament is bound to a 2D surface (we will discuss this in detail in chapter 4); Michell's instability [56, 16] where a ring buckles out of plane beyond a critical value of twisting; shapes of knots and Moebius strip as described by the Kirchhoff equations [92]; shapes of DNA, from being straight to one where it gets intertwined (called as plectonemes)[11, 28]; shape of a curly hair which is the equivalent problem of a hair shape in 3D where gravity competes with bending and torsion [97]; packing of an elastic wire in a flexible shell where the filament takes different morphologies as a function of filament to shell's bending rigidity and friction between filament [139]; have been studied using either of these numerical techniques.

Though the theory of elastica has been available since the 19th century, a major probing of this theory has taken place only in the last decade and all recent developments have showed us ways by which slender elastic structures undergo instabilities. These bifurcations that we see in 2D and 3D systems have provided us with completely new ways by which elastic structures behave which was hitherto unknown. These instabilities are all parametric instabilities where the equilibrium filament morphology undergoes a transition from one stable state to another by tuning single parameter in the system. The physical relevance of the parameter and the morphology will be described in detail in the later sections using the framework of '*confinement vs bendability*'.

1.4.2 DYNAMICS

Filament also undergoes temporal instabilities based on the initial configuration and also the parameters involved. Problems such as: motion of stereo cilia in hair-cell inside the ear, asymmetric breaking of a spaghetti [10] when released from a bent state; relaxing rubber band from a stretched state [138]; elastic sewing machine problem [67] where a falling filament forms different patterns on a moving substrate based on the velocity of the substrate; mechanics of lasso [22] where the shape the filament takes as the lasso is rotated by Mexican *vaqueros*; an elastica curling from a flat state to a rolled up state via a self-similar process [24]; lift off and snapping of a falling chain on a pulley [20]; the mechanism behind wagging hair of a runner [72]; dynamics of a ruck in a rug [137] which tries to understand the mechanism

behind the shape of ruck; have been studied using both experiments and theory. In the time-dependent problem, the competition is usually between that of inertial force arising out of the filament's density which is accelerated from a state far from equilibrium and the dynamics happen such that the final state of the filament marches is a minimum energy state. It is worth mentioning here that the inertial forces enable the possibility of elastic waves which travel at the speed of sound in the medium of filament. Temporal instabilities are all around us and understanding them provide important insights into ephemeral processes which we fail to observe in daily life.

1.4.3 Contact with fluids

Instabilities described so far of filaments have body forces applied by means of external moments or twist, or through gravity. Another mechanism by which body forces are usually exerted on filaments is through fluids. When filaments interact with liquid in their bulk, they get affected by the viscosity of the fluid. On the other hand when they are at the interface between liquid and vapour, or between liquid and liquid, they experience capillary force as a consequence of the energy of the interface. Filaments undergo several kinds of instabilities due to both viscosity and capillarity. Some of the phenomena studied from literature include: propulsion of micro-organisms using flapping of flagella [83]; buckling and folding of a floating filament at a liquid interface due to capillary action of the interface [45]; bending papillae of a tongue which help animals drink water [2, 120]; buckling of a filament beyond a critical value of shear [140]; shape of filament when they are at the boundary of minimal surfaces where a soap film is bounded by a thin filament [54]; capillary origami [111] where a drop of liquid placed on a flat sheet assembles into a designed shape as a consequence of capillary force; making an elastic filament rise beyond elastocapillary length scale [63] by soaking the filament made out of Viny Polysiloxane in silicone oil, such that filament swells and raises due to differential growth; instant wrapping of a droplet using flat sheet by dropping liquid droplets on a flat sheet [77, 5]; bundling of hair/brush when dipped in a liquid as a consequence of capillary force exerted by the liquid [17, 18]; buckling of a sedimenting filament [86] due to drag force along the length; spooling of a long filament inside a droplet [43], inspired by spider capture thread; buckling of a helical filament as it is rotated inside a highly viscous fluid [68], used by microorganisms to change directions. These problems show the multitude of instabilities filaments manifest though being a mere 1D entity.

Some of the problems described above involve sheets but are however describable by filament equations or behave as filaments because the third dimension of the sheet does not affect the mechanism of instability, as detailed later in chapter 3. Elastic filaments can experience inhomogeneous forces on its surface due to shear, thus they buckle differently and studying the dynamics of filaments in such a context is easier numerically as the non-linear equations become hard to handle analytically. Tornberg and Shelley [133] came up with a numerical scheme to simulate several filaments in a fluid where the filament is approximated as a simply connected series of Stokeslets with bending and torsional modulus. This model is valid for very low Reynolds number flows i.e., flows where the viscosity of the fluid is high. It is worth mentioning here that these systems are over-damped and filament in this low Reynolds number regime do not exhibit waves. These systems also have the feature of breaking the Scallop theorem (due to time-reversal symmetry of the Stokes equation). Scallop theorem states that if a rigid object executes a periodic motion, it would move forward in one half of the period and return back to the same position where it started after the second half of the period. However addition of elasticity to the system introduces a relaxation time scale inversely proportional to the elastic material's Young's modulus. This aspect will be discussed in detail in chapter 2. This departure from Scallop theorem as a consequence of the elasticity is a common mechanism in several microorganisms that makes propulsion possible at low Reynolds number.

1.5 Confinement vs Bendability

In the previous section we discussed several patterns that filaments form as a consequence of competition between an external body force and bending/twisting force. Though all the instabilities are of interest for the specific purpose and the mechanism by which they occur, there exists a framework one can use to look at them to gain a broad physical understanding. This paradigm is that of confinement vs bendability [36, 73, 122]. Confinement simply quantifies various stressed configurations that coerce a filament to deviate from the stress-free state, of being straight. Large confinement implies large deviation from a straight configuration and small confinement indicates shapes close to a straight line. Let us take the example of Euler buckling to introduce confinement. In the scenario of Euler buckling, an external force is applied at the end of the beam along the axis of the beam. Beyond a critical threshold of applied force the beam buckles and as we keep increasing the magnitude of this force,

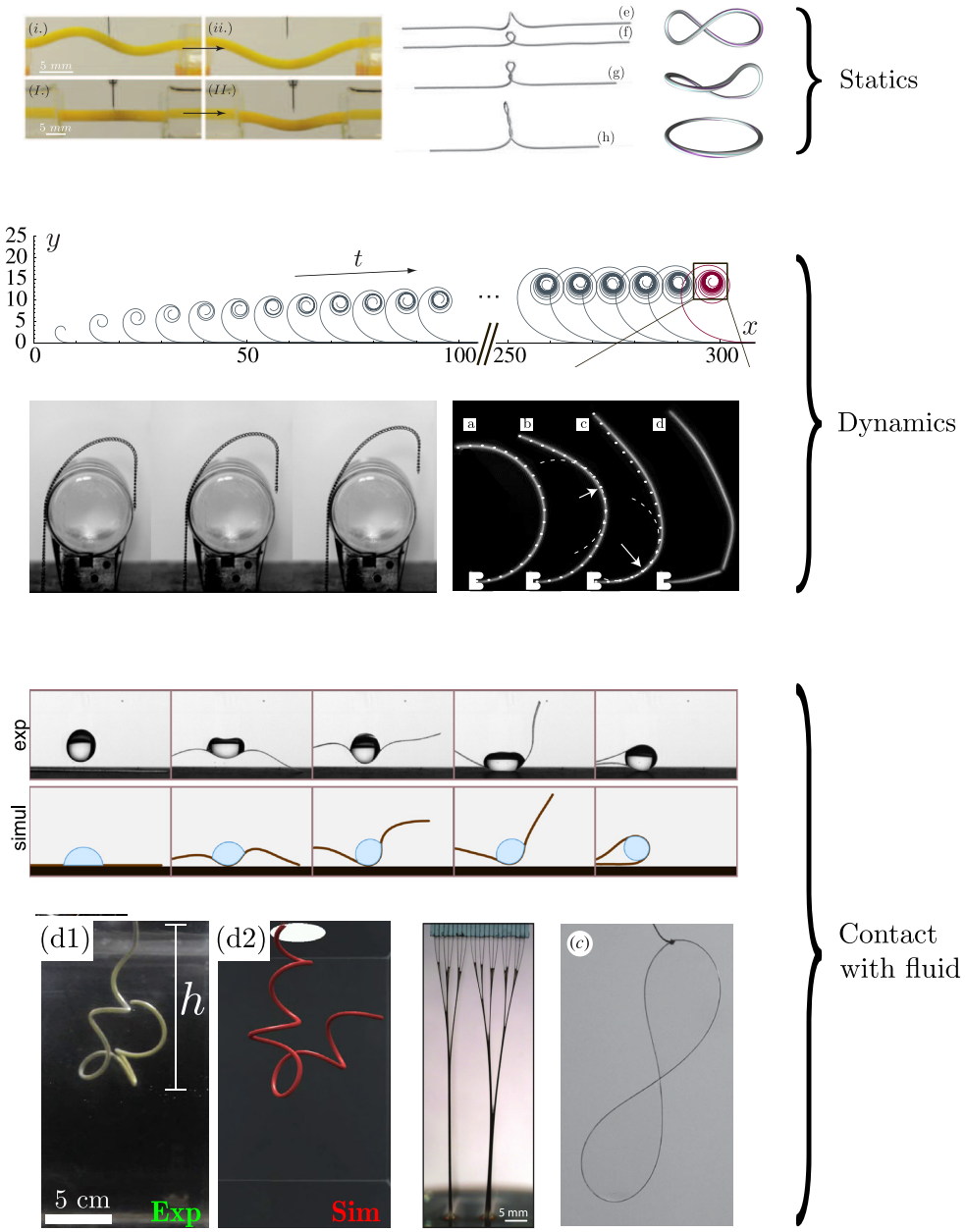

Figure 1.2: Statics: Problems of snapping by applying force on a initially buckled beam [103], plectoneme formation by twisting [11], Michell's instability where [97] the ring goes out of plane with increase in twist. Dynamics (anti-clockwise): Self-similar curling of an naturally coiled elastica [24] released from a flat state, lifting of a falling chain from a pulley [20], asymmetric breaking of a spaghetti [10]. Contact with fluids (anti-clockwise): Instant wrapping of a droplet by dropping it on top of a flat sheet [5], buckling of a helical filament as it is rotated inside a bath of highly viscous fluid [68], bundling instability of a collection of filaments as it is wet by a fluid [17, 18], shape of soap film with a filament at its boundary [54].

larger is the amplitude of buckling. In such a scenario, we can define confinement as the non-dimensional number that quantifies this buckled state. An intuitive choice would be the ratio of end displacement to the length of the beam, whose magnitude increases with increase in buckling amplitude. Thus we can use this ratio to quantify confinement, because larger the magnitude of this ratio, larger is the deviation from the stress-free state of being straight. The bendability on the other hand is a non-dimensional number which captures the competition between applied forces with elastic forces. It is nothing but the ratio of the bending force in filament to the body force that is applied on it. Bendability is dependent only on the material properties such as Young's modulus, filament thickness, and filament length, which are relevant to describe a filament, and also on other properties/constants such as gravitational constant, surface tension, and density of material based on applied body force. Capillary bendability, for example, is the ratio of length scale due to bending force and capillary force. When the surface tension is large or bending stiffness of the filament is small, capillary bendability is large as bendability is proportional to surface tension and inversely proportional to bending stiffness. This implies that the filament is susceptible to bending by the capillary force. Thus bendability informs us whether the elastic structure is easily deformable by the body force.

In order to illustrate the usefulness of this framework we consider an example from literature, which predates the notion of confinement vs bendability. By taking this example we want to highlight the fact that this paradigm extends beyond the examples discussed in this thesis, and we can place retrospectively several other morphological transitions in elastic structures from literature in this framework. The shape of a hair in 3D, as mentioned earlier from the work of Miller et al. [97], involves competition between bending force, torsion and the intrinsic curvature of hair. Let us denote κ_{ic} as the constant natural curvature of the hair which is the resultant of an underlying chemical process. We can define a non-dimensional number $\Phi = \kappa_{\mathrm{ic}} l$, where l is length of the filament. This non-dimensional number is nothing but a geometric quantity that signifies confinement where large Φ implies large deviation from a straight configuration, be it through large values of l or κ_{ic}. The other non-dimensional number is the bendability, which here is due to weight of the filament/hair. We call $\epsilon^{-1} = B\kappa_{\mathrm{ic}}^3/mg$ as the bendability (which we will encounter several times in the thesis) with m being the mass per unit length of hair, B the bending stiffness of hair and g the constant of gravity. Now we can define a phase space of Φ vs ϵ^{-1} where all the shapes of the hair can be represented. As we traverse this phase space we will encounter different instabil-

ities such as ones shown in Miller et al. [97]. Figure 3 in this article is nothing but the phase space we have defined here, however they do not realise the connection with the confinement vs bendability paradigm, which as we already see provides an intuitive notion to the different shapes one sees in their experiments. This framework was initially employed to understand the mechanism of wrinkling in thin elastic sheets but then as we see extends to morphological instabilities in elastic structures in general. We use this paradigm to understand the different phases we observe in our experiments throughout the thesis. We will explore the details of the different phases and the mechanism of transition between them in the ensuing chapters.

As we see, bendability is a quantity composed of material constants and dimensions of the structures at play in the experiments. This provides a very important insight into theories that depend on bendability. It is this fact that in the limit of vanishing material constants (where bendability is either infinity or zero based on definition), the theory must become purely geometric. The reason this must be the case is because elastic structures without these material properties tend to become simple geometric objects i.e., filaments become lines in 3D, sheets and shells become 2D surfaces and so on. On the other hand when bendability values are very small, we go back to the small deformation limit where the forces only deform the elastic structure mildly (which has been the focus of study in the last century). Though most of the mathematics of lines and surfaces have been understood in the 19th century, the connection between these geometric objects and the way by which they couple with material behaviour is very much a modern understanding. The notion of bendability acts as the bridge to traverse between this geometric limit and the small deformation limit. The experiments and theories in this thesis fall in the regime of large enough values of bendability where geometric aspects of the elasticity theory manifest themselves and are far from the small deformation limit.

With this literature overview we now turn towards the outline of the thesis and then describe briefly the contents of each of the chapters in the thesis.

1.6 Thesis outline and motivation

This thesis is divided into two parts. The first part deals with mechanics of elastic filaments and the second part deals with dynamics of particles in flow. Three experiments form the first part of the thesis and these experiments are: (i) releasing a highly deformed elastic filament at the interface of a highly viscous fluid, (ii) placing an oil droplet in the vicinity of a thin elastic

filament such that the droplet contact-line applies a localised force due to surface tension on the filament and (iii) placing a thin elastic filament on top of a spherical bubble such that the filament remains confined on the bubble surface.

In chapter 2 we study the relaxation of a highly deformed filament using experiments and numerical simulation to understand the role of tension in the elastic filament arising due to large deformation. We describe the mechanism by which tension inside the filament affects the relaxation dynamics. We also show how the tension plays a role in relaxing asymmetric initial shapes to symmetric states during relaxation. We state implications of our results to understanding and estimating dissipation, and energy consumption of propulsion in low Reynolds numbers.

In chapter 3 we look at the problem of a droplet in contact a thin elastic filament on the surface of water. The initial part of this chapter deals with the calculations of a cylindrical droplet in contact with an infinitely wide sheet under applied boundary tension. We obtain exact results in the limit of vanishing thickness where the costs to filament/sheet bending are negligible. We find two bifurcations as we change the applied tension where the filament droplet system undergoes shape transitions. These two bifurcations happen as we keep reducing the value of applied tension from a large value, one from a state where the droplet sits with part of its interface exposed to vapour to a state completely wrapped by the sheet. The second bifurcation is when a wrapped state of drop-sheet system with part of sheet exposed to vapour goes unstable and the droplet completely wets the sheet. We then look at shapes the sheet takes in this fully wet state using direct numerical minimisation. This problem in higher dimensions is known by the name "*Willmore problem*." In the latter half of the chapter we use thin filaments to understand the validity of predictions made by the theory. Our experiments involve using the interface of air-water as the substrate to do mechanics. We confine filament to this interface and place a droplet in the vicinity of the filament. One end of the filament is attached to a soft beam (used as a sensor to measure tension in the filament) and the other end is attached to a translational stage (to apply tension). Our experimental observations of contact angles as a function of applied boundary tension, are captured accurately by the theory which assumes vanishing thickness of filament. We also use our 2D experimental setup to study wrapping of droplet using filament.

Following the droplet-on-filament problem we probe the question of morphology of filaments confined to a 2D surface with finite positive gaussian curvature. To this end we took the simplest possible such surface, i.e. a sphere and our experiment were performed on a

spherical soap bubble. A thin filament is inserted on the surface of bubble from its north pole, with gravity pointing towards south. We find that gravity starts affecting the filament shape beyond a certain length of filament and size of bubble. The confinement vs bendability approach again provides a window through the different shapes we observe in both experiments and theory. Confinement, which we call specific to this problem as the coiling parameter, is nothing but the ratio of length of filament to bubble radius. Bendability here is nothing but the ratio of bending force to force due to gravity. Using a simple geometric theory we describe the critical point at which gravity affects the shape of the filament. As we further increase the length of the filament on the sphere or reduce the bubble size for a fixed filament length, we see that the filament starts coiling on the surface of bubble.

The second part of the thesis deals with dynamics of particles in a low Reynolds number flow. As we have seen in the previous section, the history integral in the MR equations has long been neglected. In chapter 5 we discuss in detail the technique we have developed to solve this equation and further show that exact solutions exist for several simple scenarios. We firstly show that the MR equations can be reformulated as a boundary condition to 1D heat equation. Using Unified Transform Method (UTM), which is a spectral technique to solve partial differential equation in bounded domains, we solve the system of equations for all time dependent space independent flows. Our results provide a new path to solve different kinds of integro-differential equations. The numerical method we develop for complex flows achieves spectral accuracy, by leveraging the properties of Discrete Chebyshev Transform. In the last part of this chapter we solve the problem of particle dynamics in n-vortices where both the particle and flow evolves in time.

In the closing section of the thesis, we provide future directions from insights obtained out of this work. We also propose a few open questions that might be immediately solved using the techniques developed in this thesis.

"Jeeves," I said. "A rummy communication has arrived. From Mr. Glossop." "Indeed, sir?" "I will read it to you. Handed in at Upper Bleaching. Message runs as follows: When you come tomorrow, bring my football boots. Also, if humanly possible, Irish water-spaniel. Urgent. Regards. Tuppy." "What do you make of that, Jeeves?" "As I interpret the document, sir, Mr. Glossop wishes you, when you come tomorrow, to bring his football boots. Also, if humanly possible, an Irish water-spaniel. He hints that the matter is urgent, and sends his regards." "Yes, that is how I read it. But why football boots?" "Perhaps Mr. Glossop wishes to play football, sir."

–P.G. Wodehouse, Very Good, Jeeves!

2 Relaxing elastic filament

This chapter is a verbatim reproduction of our article in Physical Review Fluids titled "*Relaxation of a highly deformed elastic filament at a fluid interface*".

2.1 Introduction

Highly deformed slender elastic filaments are to be found across several decades of length scales starting from crops and tree canopies in wind [37], aquatic plant stems in flowing streams [96], propelling flagellae of organisms [110, 88, 66, 141], stereocilia inside ears [30, 75], to suspensions of fibres (see ref. [89] for a recent review). The most heavily studied of these examples is the driven dynamics of flagella [140, 142], where the balance is between forces due to bending, which tend to straighten the filament, and viscous drag, which acts to damp the motion.

Unless they are held in that state by external or internal forces, filaments will relax from a highly bent state to their equilibrium, stress-free state. For a filament with bending modulus B and length L_o, the bending energy per unit length is $B\kappa^2/2$, quadratic in the local curvature κ. This leads to bending moments and forces $\sim BL_o^{-3}$ that are linear in the displacement from the unstressed conformation of the filament [79]. Balanced against the drag $8\pi\mu L_o/\tau$ from a fluid of viscosity μ, we obtain a characteristic time scale for dynamics over the length of

the filament: $\tau = 8\pi\mu L_o^4/B$. However, when the deformations are large, another source of stress becomes significant: in order to satisfy the constraint of constant length, a gradient of tension appears along the filament. This tension is a nonlinear function of the geometry [55]. Previous work has concentrated on bending alone, and the role of this nonlinearity is largely unexplored. The goal of this work is to understand the relaxation of a highly-deformed filament from its high elastic-energy state, with full consideration of the nonlinear effects of the geometry.

We perform experiments to study the relaxation to a straight configuration of an initially highly deformed elastic filament. The dynamics are restricted to a two-dimensional plane by placing the filament at the interface of a viscous fluid. The filament is initially deformed by holding its ends in place with two fine needles at the interface. When these are removed, it relaxes towards a straight, unbent shape. Fig. 2.1(a) shows the initial deformed state and several intermediate steps in this relaxation process. We vary the parameters of this system – the length, diameter and material of the filament – to understand the time-dependence of this process. In order to probe internal variables such as the tension, we solve a numerical model [55] to compute elastic forces in the filament. This model includes a fully nonlinear treatment of the elasticity of the filament, but a simplified description of the hydrodynamic drag. We also perform Particle Image Velocimetry to visualise the flow-field around the filament and validate the results of the theoretical model.

2.2 Experimental methods

The filaments we use are made of a elastomer, vinyl polysiloxane (VPS), which was prepared with two different Young's moduli, E (of $240\mathrm{kPa}$ and $800\mathrm{kPa}$). The precursor material is injected into a capillary tube which defines the diameter d of the filament. Once the polymer cures, the filament is extracted from the tube and cut to the desired length L_o. All deformations of the elastomer are fully reversible.

This filament is placed on the surface of a cylindrical dish of glycerol. The ends of the filament are held, then released by needles attached to a tweezer mechanism mounted on a translational stage. The air-glycerol surface tension is $64\mathrm{mN/m}$, so that the filament stays on the interface and the dynamics are fully 2-dimensional. No twist occurs in the experiments and also there is no rolling. The high viscosity ($\mu \sim 1.412\mathrm{Pa.s}$ at 100% concentration) keeps the dynamics in the stokesian regime; the Reynolds number $Re \approx 10^{-2} - 10^{-3}$ immediately

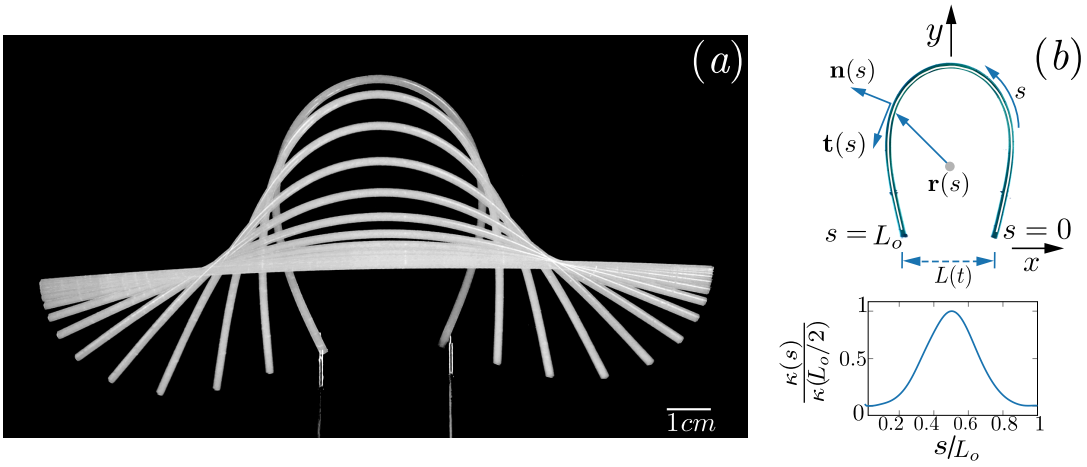

Figure 2.1: (a) Superimposed images of the filament taken at intervals of 1 sec. The two needles at the bottom of the image are used to release the filament from its initial configuration. (b) The thick white line over the filament (seen as the cyan outline) is the Bezier fit. We plot below this the corresponding curvature computed with this fit. Here the position vector is $\boldsymbol{r}(s)$ and the unit vectors $\mathbf{n}(s)$ and $\mathbf{t}(s)$ in the normal and tangential directions.

after release, when the filament is moving at its fastest. As shown in fig. 2.1(a), at no time in the relaxation process does any part of the filament come close to self-contact (or to the walls of the dish), so capillary forces can be neglected.

We track the filament shape as a function of time using a Nikon D5000 camera at a resolution of $4288\text{px} \times 2848\text{px}$ and a frame rate of 1fps. As shown in fig. 2.1(b), from the images we extract $\boldsymbol{r}(s,t)$, the position vector of the filament centerline along the arc length s, using the following procedure. We first separate the filament from the background, and then reduce these pixels to a set of equally spaced points.

In order to accurately take higher order derivatives with respect to material coordinates, we make a Bezier fit to these points. This is a unique polynomial fit of $\mathcal{O}(l^n)$ to a given set of n points in $\boldsymbol{r}(s) = \mathcal{B}\{x(l), y(l)\}$, l being the parameterisation of the Bezier curve. As l goes from 0 to 1, s goes from 0 to L_o, but note that the two are not linearly related. The analytical form of the fit allows us to calculate $\kappa(s)$ (fig. 2.1(c)) as a continuous function. The curvature is given by

$$\kappa(s) = \frac{x'y'' - y'x''}{(x'^2 + y'^2)^{3/2}},$$

where the primes denote differentiation with respect to l. We also compute the elastic energy

$\mathcal{E}_{el}(t)$ $[= (1/2)\int_0^{L_o} B\kappa^2(s)ds]$ from the curvature profiles extracted from the images. In appendix. 7.1.1 the details of the image extraction algorithm is provided in detail. The code for the tracking and extraction procedure is also available in GitHub.

2.3 Experimental results

Since the elasticity of the filament is determined by its bending modulus $B = E\pi d^4/64$, we vary d and E to study the dependence of the relaxation time on these filament parameters. We also vary L_o; since the distance between the needles holding the filament in its initial configuration is fixed the initial average curvature, and the relative initial separation between the ends, both vary. From the sequence of images that characterize the shapes of the relaxing filament, we extract two relevant physical quantities. One observable is the non-dimensional end-to-end distance, $L(t)/L_o$ (see fig. 2.1), as a function of time. We also report the elastic energy $\bar{\mathcal{E}}_{el}(t)$, normalized by that of a filament of length L_o rolled into a circle: $2B\pi^2/L_o$. These quantities are plotted in the insets of fig. 2.2(a, b), for two different values of Young's modulus, and for several values of the length L_o. It is apparent that the relaxation time increases monotonically and strongly with L_o and decreases with increasing E.

As shown in the main fig. 2.2(a, b), all the data for length and elastic energy collapse on a single scaled curve. The time has been scaled in each case by $\tau = 8\pi\mu B^{-1}L_o^4$. Even though we are in a very nonlinear regime, these curves collapse when plotted in terms of t/τ. We remark that the time scale τ has been obtained merely by balancing viscous and bending forces in the linear regime. In all the data in fig. 2.2 we have chosen the origin of time $t = 0$ as the instant where non-dimensional elastic energy, $\bar{\mathcal{E}}_{el} = 0.4$ but the data collapse even at negative times thus defined. Moreover, upon choosing just $\bar{\mathcal{E}}_{el}(t = 0)$ as 0.4, the respective end-to-end distances automatically collapse at the initial time. The value of 0.4 is arbitrary and the scaling works well for any other origin of time. We note that most of the relaxation is accomplished when the nondimensional time is very small, that is, $t/\tau \sim 2 \times 10^{-2}$ rather than $t/\tau \sim \mathcal{O}(1)$.

We also vary the bending modulus through its strong dependence on d, the diameter of the filament. We choose two different diameters, $d = 1.04mm$ and $0.57mm$ with Young's modulus fixed at $E = 240kPa$, at several different lengths (L_o varied from 4.1cm to 7.3cm for $240kPa$ and from 4.6cm to 7.8cm for 800kPa). The data in the insets of fig. 2.2(c, d) track the measured relaxation dynamics and show that the smaller diameter relaxes slower. Once

again, the relaxation dynamics collapses when data obtained by varying L_o and d are plotted against the scaled time, t/τ as shown in fig. 2.2(c, d). The slowest and the fastest dynamics span a factor of 27 variation in time scale τ.

There are two major findings in our experiments. First, the time scale τ used to collapse the data is taken from the balance of forces in the linear regime, even though most of the dynamics we probe are in the deeply nonlinear regime, where curvature $\sim L_o^{-1}$. Second, the time-scale of relaxation is about two orders of magnitude smaller than τ. A deeper understanding of this puzzle requires us to quantify the dynamics in the nonlinear regime. The nonlinear regime is governed by the internal tension, which is not accessible in our experiments. We thus turn to a numerical simulation of the fully nonlinear equations discussed below.

2.4 Nonlinear dynamical equations

2.4.1 Elastic force

The energy in an elastic filament arises from its bending modes (see [55, 133] for more details). The mechanical energy of bending as well as a constraint term to enforce length conservation yields an elastic energy of:

$$\mathcal{E}_{el} = \frac{B}{2}\int_0^{L_o} \kappa^2(s)ds + \int_0^{L_o} \frac{T(s)}{2}\{|\mathbf{t}(s)|^2 - 1\}ds, \tag{2.1}$$

$T(s)$ here is the lagrange multiplier enforcing length constraint. This lagrange multiplier is the tension inside the filament, which is the tangential component of the force inside the filament. The curvature $|\kappa(s)| = |\boldsymbol{r}_{ss}(s)|$ and assuming perturbation in $\boldsymbol{r}(s)$, the position of the filament, the variation in elastic energy takes the form:

$$\delta\mathcal{E}_{el} = B\int_0^{L_o} (\boldsymbol{r}_{ss}\cdot\delta\boldsymbol{r}_{ss})ds + \int_0^{L_o} \frac{T(s)}{2}\{\boldsymbol{r}_s\cdot\delta\boldsymbol{r}_s\}ds \tag{2.2}$$

The first term can then be expanded by the method of integration by parts as:

$$B\boldsymbol{r}_{ss}\cdot\delta\boldsymbol{r}_s|_0^{L_o} - B\boldsymbol{r}_{sss}\cdot\delta\boldsymbol{r}|_0^{L_o} + B\int_0^{L_o}(\boldsymbol{r}_{ssss}\cdot\delta\boldsymbol{r})ds \tag{2.3}$$

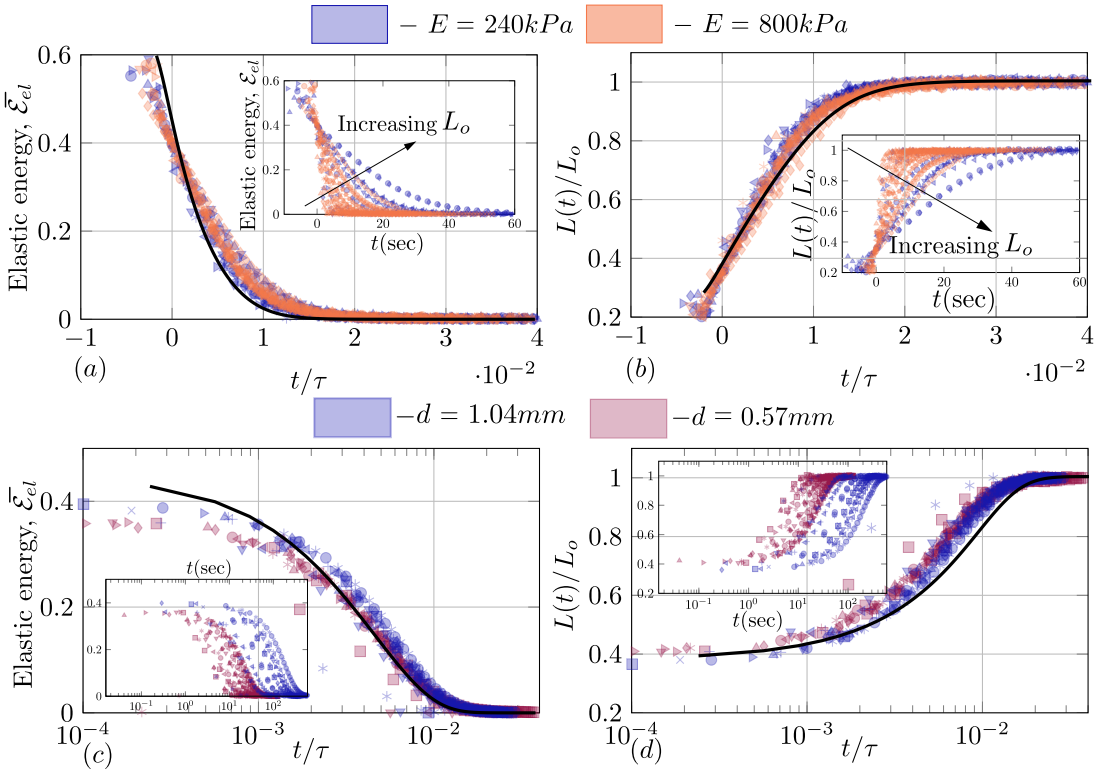

Figure 2.2: (a) Normalised elastic energy, $\bar{\mathcal{E}}_{el}$ and (b) non-dimensional end-to-end distance, $L(t)/L_o$ for two different values of Young's modulus, E (240kPa and 800kPa) and different lengths (L_o varied from 4.1cm to 7.3cm for 240kPa and from 4.6cm to 7.8cm for 800kPa). The insets show the data as functions of dimensional time, whereas the main figures are plotted in terms of scaled time t/τ. $(c), (d)$ Similar plots to that of $(a), (b)$ for two different diameters, $d - 0.57\text{mm}, 1.04\text{mm}$ ($E = 240\text{kPa}$) and L_o varied between $4.6\text{cm} - 7.2\text{cm}$ for the former and $3.3\text{cm} - 6.3\text{cm}$ for the latter. The solid lines in all the subfigures indicate results obtained by solving eqs. 2.8, 2.9 numerically, and scaled by a factor of 4.2 in time, as discussed later in the text.

A similar manipulation for the second term leads us to:

$$T(s)\boldsymbol{r}_s \cdot \delta\boldsymbol{r}_s|_0^{L_o} - \int_0^{L_o} [\partial_s(T(s)\boldsymbol{r}_s) \cdot \delta\boldsymbol{r}]ds \tag{2.4}$$

Now the force due to elastic energy can be written as:

$$\boldsymbol{f}_{el} = -\frac{\delta\mathcal{E}_{el}}{\delta\boldsymbol{r}}$$

This results in:

$$\boldsymbol{f}_{el} = -B\boldsymbol{r}_{ssss} + \partial_s[T(s)\boldsymbol{r}_s] \tag{2.5}$$

2.4.2 Viscous force

The viscous force per unit length is simply approximated as a drag-coefficient times the velocity of the rod itself. The coefficient turns out to be $8\pi\mu$ and the expression for force is given by:

$$\boldsymbol{f}_{vis} = 8\pi\mu\partial_t\boldsymbol{r}(s)$$

In an over-damped situation, the viscous force balances the elastic force and can thus be written as:

$$8\pi\mu\partial_t\boldsymbol{r} = -B\boldsymbol{r}_{ssss} + \partial_s[T(s)\boldsymbol{r}_s]. \tag{2.6}$$

Though the drag due to anisotropy of filament is different along its axial and transverse direction, we use here an isotropic form as the effects of anisotropy are small described in detail in app. 7.1.6.

2.4.3 Constraints from geometry

In the previous subsection we saw that the length constrain is induced as a lagrange multiplier and is the source for tension itself. Now the constraints from geometry helps us obtain an expression for tension.
The tangent is a unit vector and we would like it to remain so throughout the curve. This results in:

$$\partial(\boldsymbol{r}_s \cdot \boldsymbol{r}_s) = \partial(|\hat{\mathbf{t}}|^2) = 0$$

$$\boldsymbol{r}_{ss} \cdot \boldsymbol{r}_s = 0$$

Again using the same trick, we get:

$$\boldsymbol{r}_{sss} \cdot \boldsymbol{r}_s = -|\boldsymbol{r}_{ss}|^2$$

$$\boldsymbol{r}_{ssss} \cdot \boldsymbol{r}_s = -3\boldsymbol{r}_{ss} \cdot \boldsymbol{r}_{sss}$$

$$\boldsymbol{r}_{sssss} \cdot \boldsymbol{r}_s = -3|\boldsymbol{r}_{sss}|^2 - 4\boldsymbol{r}_{ss} \cdot \boldsymbol{r}_{ssss}$$

Now differentiating eq.2.6 with respect to s and taking scalar product with $\boldsymbol{r}_s$, we have terms $\boldsymbol{r}_{sssss} \cdot \boldsymbol{r}_s$, $\boldsymbol{r}_{ss} \cdot \boldsymbol{r}_s$. Using the above relations, the final equation for tension in dimensional form is:

$$(\partial_{ss} - |\boldsymbol{r}_{ss}|^2)T(s) = -B[3|\boldsymbol{r}_{sss}|^2 + 4(\boldsymbol{r}_{ss} \cdot \boldsymbol{r}_{ssss})] \tag{2.7}$$

After a brief non-dimensionalisation: $\boldsymbol{r} \to L\boldsymbol{r}$, $t \to \tau t$, the equation of motion for the rod is:

$$\bar{\mu}\partial_t \boldsymbol{r} = -\underbrace{\boldsymbol{r}_{ssss}}_{\mathcal{F}1} + \underbrace{\partial_s[T(s)\boldsymbol{r}_s]}_{\mathcal{F}2}, \tag{2.8}$$

$$(\partial_{ss} - |\boldsymbol{r}_{ss}|^2)T(s) = -(3|\boldsymbol{r}_{sss}|^2 + 4(\boldsymbol{r}_{ss} \cdot \boldsymbol{r}_{ssss})). \tag{2.9}$$

The boundary conditions are: $\boldsymbol{r}_{ss}(0) = \boldsymbol{r}_{ss}(L_o) = 0$ corresponding to zero moment and $\boldsymbol{r}_{sss}(0) = \boldsymbol{r}_{sss}(L_o) = 0$, $T(0) = T(L_o) = 0$, corresponding to zero force at the free ends. The non-dimensional viscosity, $\bar{\mu}$ is given by:

$$\bar{\mu} = \frac{8\pi\mu L^4}{EI\tau}.$$

Note that when we set $\tau_1 = \tau$, we get $\bar{\mu} = 1$, and the above equation becomes parameter-free. Equations 2.8 and 2.9 constitute the basic equations for the mechanics of the filament. There are two approximations in these equations for the dynamics of the filament centreline. First, the hydrodynamic interaction between points on the filament is neglected. Second, the drag force due to the motion of the filament is assumed to be isotropic. Furthermore, in our experiments, we do not have an independent measure of the drag at the interface (which will depend on wetting properties among other things), and so in the theoretical computations of drag, we use the value of the bulk viscosity of the liquid. An effective viscosity at the interface contains an unknown factor to be determined experimentally.

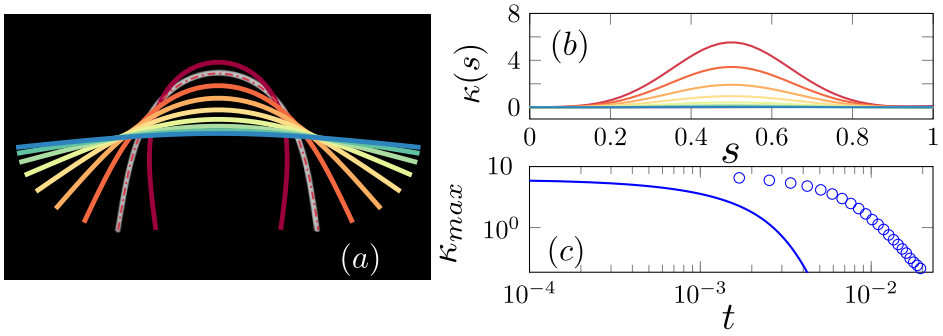

Figure 2.3: (a) Shape of the filament for various time instants in the simulation super-imposed on each other, with an experimental image, seen in white, in the background. (b) Evolution of curvature, $\kappa(s)$ vs s for different times. $\kappa(s)$ is always positive and decays monotonically with time. (c) The decay of the maximum value of curvature compared with that of experiments ($\circ$) without any fitting parameter in the numerics. All quantities are non-dimensionalised using L_o and τ as scales.

2.4.4 Numerical method and validation

As in Tornberg and Shelley [133] we solve the tension equation as well as the equation of motion by discretizing the filament into inter-connected rods of length ds while conserving the total length using penalisation. We use a TDMA scheme to calculate $T(s_i)$ using the value of $\boldsymbol{r}(s_i)$ at discrete arc-lengths, s_i. A skew-finite difference is used for implementing the boundary conditions in higher-order derivatives. Here we give the details of the tricky 4-th derivative arising in the bending term in eq. 2.8. We have:

$$D_4\boldsymbol{r} = \begin{cases} (-2\boldsymbol{r}_{j+5} + 11\boldsymbol{r}_{j+4} - 24\boldsymbol{r}_{j+3} + 26\boldsymbol{r}_{j+2} - 14\boldsymbol{r}_{j+1} + 3\boldsymbol{r}_j)/ds^4, & j = 0, \\ (-\boldsymbol{r}_{j+4} + 6\boldsymbol{r}_{j+3} - 14\boldsymbol{r}_{j+2} + 16\boldsymbol{r}_{j+1} - 9\boldsymbol{r}_j + 2\boldsymbol{r}_{j-1})/ds^4, & j = 1, \\ (\boldsymbol{r}_{j+2} - 4\boldsymbol{r}_{j+1} + 6\boldsymbol{r}_j - 4\boldsymbol{r}_{j-1} + \boldsymbol{r}_{j-2})/ds^4, & 2 \le j \le N-2, \\ (2\boldsymbol{r}_{j+1} - 9\boldsymbol{r}_j + 16\boldsymbol{r}_{j-1} - 14\boldsymbol{r}_{j-2} + 6\boldsymbol{r}_{j-3} - \boldsymbol{r}_{j-4})/ds^4, & j = N-1, \\ (3\boldsymbol{r}_j - 14\boldsymbol{r}_{j-1} + 26\boldsymbol{r}_{j-2} - 24\boldsymbol{r}_{j-3} + 11\boldsymbol{r}_{j-4} - 2\boldsymbol{r}_{j-5})/ds^4, & j = N. \end{cases}$$

Here $\boldsymbol{r}_j = \boldsymbol{r}(s_j)$, D_4 is the fourth-derivative matrix, N is the number of rods and we choose $N = 62, L_o = 8$ and discretisation in time $dt = 10^{-4}$ in our simulations. We use a semi-implicit scheme for spatial derivatives and a second order central difference scheme in time.

Fig. 2.3(a) shows the evolution of the computed filament shape, compared to an image from the experiment. More quantitatively, we go back to fig. 2.2(a, b), where we show $\bar{\mathcal{E}}_{el}(t)$

vs t/τ and $\bar{L}(t)$ vs t/τ computed by setting $\bar{\mu} = 1$. The time-evolution of the shape agrees well with the experimental data, a sample of which is shown in fig. 2.3(a). The evolution of $\bar{L}(t)$ (see eq. 7.4 in the appendix) depends only on the gradient of $T(s)$ at the boundary. The fast evolution of $\bar{L}(t)$ at early times is a consequence of $T(s)$ having a gradient of large magnitude at the boundary. However, the simulation result is offset from the experimental data by a factor of 4.2. This discrepancy between experiment and simulation could be due to (i) absence of hydrodynamic interaction and anisotropic drag in the simulation, (ii) neglect of wetting properties of the filament, and potentially most importantly (iii) our use of the bulk viscosity of the liquid in the model even though the drag occurs at an interface. In the experiment the filament at the interface is partially exposed to air and is only partially submerged in the viscous liquid. Thus the effective viscosity at the interface is expected to be less than that of the bulk liquid, explaining at least in part the factor of 4.2. We emphasize that the idealizations in the numerical model are in the treatment of drag, and not in the elasticity of the filament.

Indeed, fig. 2.3(b) shows that the computed curvature is always positive along the filament. The maximum of the curvature as a function of time is shown in fig. 2.3(c), where it is compared to the experimental data. As discussed earlier, the time evolution of experiment and numerical computation have the same functional form, but the time scale observed in the numerics is faster.

2.4.5 Tension

Having validated our model, we now move to computed quantities that are not accessible in the experiments. As is clear in figure 2.3, the curvature is not uniform, and therefore the filament should not be expected to open uniformly. In fig. 2.4(a) we show the tension, $T(s)$ computed using eq. 2.9. The relationship between curvature and tension is not linear and depends on higher derivatives of curvature. Consequently, unlike the curvature, which is always positive, the tension changes sign from compressive in the central region to tensile near the free ends. Force balance along the tangential direction thus requires that the viscous drag force be a function of arc-length.

In order to test whether the tension distribution observed in the simulation results are supported by experimental observations of the viscous drag on the filament, we use Particle Image Velocimetry (PIV) to measure the velocity field at the interface. We make a suspension

of hollow glass spheres of 10μm average diameter in the fluid and illuminate the interface with laser sheets (Wicked Lasers < 500mW and wavelength ≈ 532nm). The motion of the particles from the recorded images is tracked using open-source package, PIVLab [128]. The resultant velocity field for the relaxation is plotted in fig. 2.4(c). As the filament begins to relax, two symmetric pairs of vortices are formed. Tension in the system has contributions only from the tangential projection of the stress tensor. Now using eq. 2.8 we can write:

$$\boldsymbol{r}_s \cdot \hat{\mathbf{t}}\, \partial_s T(s) = \bar{\mu} \partial_t \boldsymbol{r} \cdot \hat{\mathbf{t}} + \boldsymbol{r}_{ssss} \cdot \hat{\mathbf{t}}$$
$$T(s) = \int_0^s (\boldsymbol{r}_{ssss} \cdot \hat{\mathbf{t}} + \bar{\mu} \boldsymbol{r}_t \cdot \hat{\mathbf{t}}) ds$$

This quantity goes to zero at the position where net bending force is balanced by viscous dissipation. Comparing the PIV field and fig. 2.4(b) we observe that this location is close to the point where vorticity changes sign. This location moves towards the ends of the filament as it relaxes, consistent with the simulation results.

To separate the contributions of the linear bending force, $\mathcal{F}1$, and the nonlinear tension arising from length conservation $\mathcal{F}2$, we plot in fig. 2.4(b) these individual terms on the right side of eq. 2.6. Surprisingly, the linear ($\mathcal{F}1$) and nonlinear ($\mathcal{F}2$) terms are comparable in magnitude, though opposed in sign, even for the highly deformed regime. The algebraic sum of these forces is balanced by a viscous term that is much smaller in magnitude than each of these terms.

Viewed in the light of these results, it is evident that ignoring the tension term in the large deformation limit not only leads to non-conservation of length but leads to a significant over-estimation of the dissipation due to viscosity. Second, as we see from the energy functional, $T \sim B/L_o^2$, the nonlinear tension term ($\mathcal{F}2$) has the same scaling as the bending term ($\mathcal{F}1$). In other words, τ emerges as a single time scale in the problem, even in the nonlinear regime. We recall that the filament relaxes much faster experimentally than the time scale τ, i.e., the balance between the two terms leads to a small numerical prefactor.

2.5 Asymmetric initial conditions

All the results we describe above are for initial shapes that are symmetric about the midpoint of the filament ($\kappa(L_o/2 - s) = \kappa(s)$). If the filament is released from an asymmetric, highly deformed shape, we find experimentally that it first deforms into a symmetric shape, then

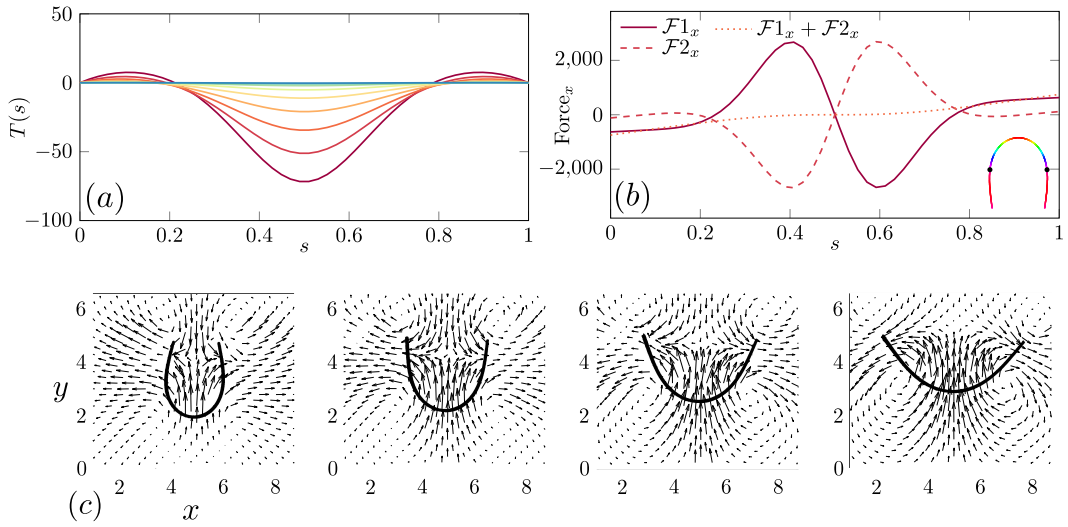

Figure 2.4: (a) Tension, $T(s)$ vs s at various time instants. The profile of tension changes shape as it decays, which is evident from the fact that the position where it crosses zero travels towards the ends in time. (b) x-component of force due to bending ($\mathcal{F}1$), tension ($\mathcal{F}2$) and the resultant viscous force (their sum) from eq. 2.6 for the filament configuration shown at the bottom right. The contribution from bending force and that of tension are very similar in magnitude but opposite in sign, so a small viscous force (as seen) is sufficient to balance them. The filament in the inset is colored based on $T(s)$ and the dots show the position where $T(s)$ goes to zero. (c) Velocity field obtained by PIV where a pair of vortices is formed on each side of the filament. The tension in the filament vanishes near the location where the sign of vorticity changes. Scales in units of cm.

relaxes along the sequences of symmetric shapes we have previously shown. This is shown in fig. 2.5(a, b) via the evolution of $\bar{\mathcal{E}}_{el}(t)$ and $\bar{L}(t)$. The images of filaments shown label the initial condition in each of three data sets displayed. We have chosen $t = 0$ to be the point where there is no experimentally discernible asymmetry. For $t > 0$ the relaxation follows the same path in all cases.

In the linear regime, the relaxation time of a Fourier component varies only with wavelength, and any initial asymmetry would be preserved. Thus we emphasize here that the collapse into a symmetric shape is a consequence of being in a deeply nonlinear regime. The linear regime of our problem is similar to another curvature-driven problem – that of the relaxation of a perturbed liquid-air interface [14, 15] – in that they flow to attracting set of shapes at long times. We show this explicitly by simulating five different asymmetric initial-conditions each with a straight portion attached to a semi-circular portion as in fig. 2.5(e). The total length of the filament for all the initial conditions is held fixed while the diameter, b of the semi-circular section is varied. We quantify the asymmetry in terms of the difference in curvature on either side of the midpoint: $\phi = \int_0^{L_o/2} |\kappa(L_o/2 - s) - \kappa(s)| ds$. ϕ takes a value of o for a completely symmetric shape and positive values for different levels of asymmetry. We plot $\phi(t)$ in fig. 2.5. In all cases, the filament first rapidly becomes symmetric and then relaxes more slowly to a straight line. The straight section first curves in order to attain overall symmetry, thus showing that tension must play a role, as there is no bending force on the straight section. The time-scale to reach the symmetric shape increases monotonically with b. (see fig. 7.4 of appendix to see the movement of $T(s)$ along the filament to regions of zero bending force.)

We make an energy argument to show that the energy of the symmetric state is a minimum with respect to asymmetric perturbations. Let us assume a smooth symmetric profile for curvature, $\hat{\kappa}(s) = \hat{\kappa}(-s)$. We perturb the curvature, $\hat{\kappa}(s)$, while maintaining the boundary conditions, with a function $-\epsilon(s)$ in $s \in [-L_o/2, 0]$ and with $\epsilon(-s)$ in $s \in [0, L_o/2]$. The

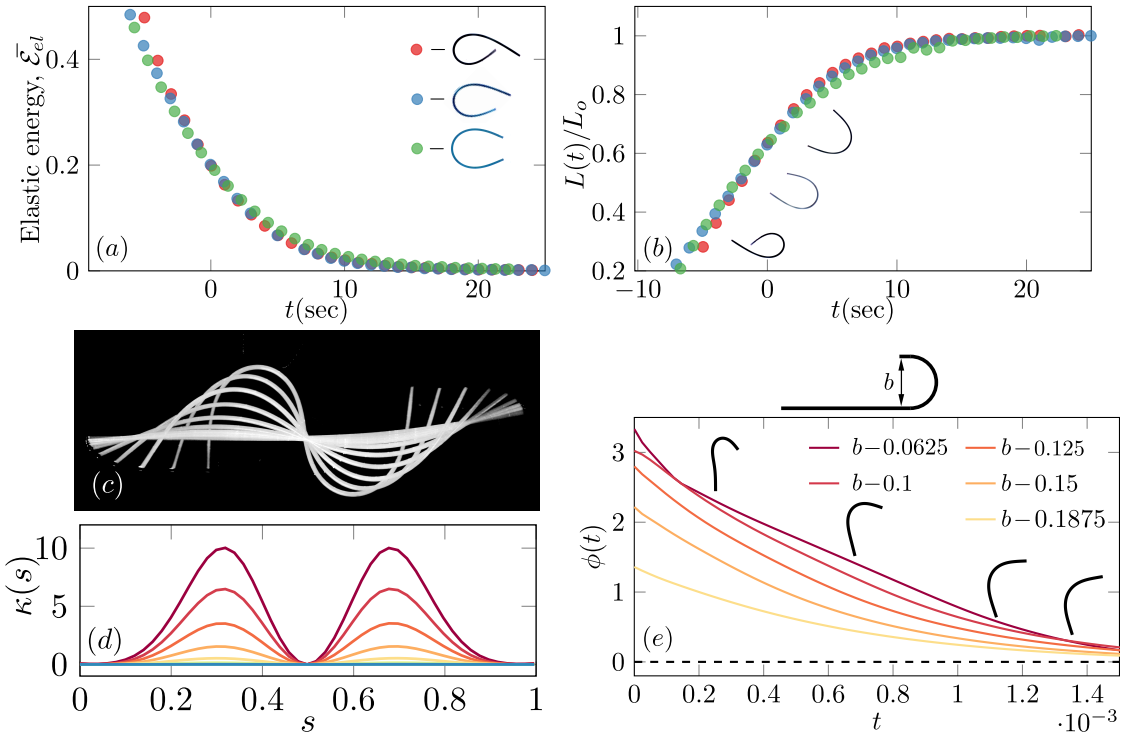

Figure 2.5: (a) Evolution of elastic energy and (b) $L(t)/L_o$ for the two asymmetric initial conditions shown in the legend from experiments, compared with the symmetric case ($L_o = 6.5\text{cm}, E = 240\text{kPa}, d = 1.1\text{mm}$). We see that the curves merge quickly and the decay beyond that time becomes identical. (c, d) Evolution of a rod with symmetric $\kappa(s)$ about $s = 0.5$ which relaxes to a straight configuration along a symmetric path. (c) consists of superimposed images from experiment while (d) is from numerics for the same initial condition. (e) Non-dimensional parameter $\phi(t)$ which quantifies the asymmetry in a given configuration. This is plotted for different initial conditions with different values of b, where b is the diameter of the semi-circular section shown above the plot. b here is varied between 0.0625 and 0.1875. We see that a configuration with smaller b symmetrises faster.

total elastic energy becomes:

$$\begin{aligned}\mathcal{E}_{el} &= \frac{B}{2}\left[\int_{-L_o/2}^{0}(\hat{\kappa}(s)-\epsilon(s))^2 ds + \int_{0}^{L_o/2}(\hat{\kappa}(s)+\epsilon(-s))^2 ds\right] \\ &= \frac{B}{2}\left[\int_{-L_o/2}^{L_o/2}\hat{\kappa}^2(s) ds + \int_{0}^{L_o/2}(\epsilon^2(-s)+\epsilon^2(s)) ds\right] \\ &\geq \frac{B}{2}\int_{-L_o/2}^{L_o/2}\hat{\kappa}^2(s) ds\end{aligned}$$

It is thus evident that for a given curvature, a symmetric shape has minimum energy. This shows that asymmetric perturbations about an arbitrarily large-deformation state will be relaxed to a symmetric state. To emphasize the fact that it is a symmetric stress or curvature, rather than a symmetric shape, that is attained, we show an example in fig. 2.5(c,d) where $\boldsymbol{r}(s)$ is not symmetric but $\kappa(s)$ is. These initial conditions also relax along a stress-symmetric sequence of shapes. The fast relaxation of the asymmetric stress state to a symmetric one is to be expected because the effective length of the portion of the filament under tension is shorter at early times, and changes with time as the tension gets distributed everywhere in the filament.

2.6 Conclusion

We find that the entire relaxation process of a highly deformed elastic filament is described by a single time scale arising out of balancing viscous drag and bending force. Force balance is achieved by a near-cancellation of two large elastic contributions, one of them purely nonlinear, with the difference balancing the external viscous drag. The time-scale of relaxation in both our experimental and numerical data is much faster than the characteristic time scale from the linear dynamics. We do not have a simple qualitative explanation for this, but observe that the relaxation as measured by the end-to-end distance, for instance, is governed by large tension gradients (see eq. 7.4). This experimental setting may possibly be used to measure interfacial viscosity by watching the relaxation of a filament with known elastic properties and geometry. Alternatively, once the drag at an interface is calibrated for a known elastic rod, this setting can be used to infer the bending modulus of a filament. The preference for symmetric shape of the filament over asymmetric shapes would make the experiment robust to small variations in initial conditions.

Story:...But what is the point of your listening to a story? You can't pass it on. Man: I'll listen to you! S: You will? M: Yes. S: There is a condition, however. You can't just listen to the story and leave it at that. You must tell it again to someone else. M: That I certainly shall, if I live. But first I must be alive to... That reminds me. I have a condition too. S: Yes? M: I must not doze off during the tale. If I do, I die. All your telling will be wasted. S: As a self-respecting story, that is the least I can promise.

–Girish Karnad, Naga-mandala

3

2-D mechanics of sheet/filament in contact with a droplet

In this chapter, we explore the effects of large deformation by considering the scenario of a liquid droplet in contact with a thin elastic filament. The motivation for this problem comes from the question of morphology of a thin elastic sheet with a liquid droplet sitting on top of it (ref. Huang et al. [64], Schroll et al. [122]). The 2D version of this problem is discussed in this chapter, where we perform calculations for a cylindrical droplet sitting on top of an infinitely wide sheet. The calculation of the shape of an infinitely wide sheet and that of a filament are the same due to the translational invariance of all the relevant variables in the infinite transverse direction. In the second part of this chapter, we perform experiments using thin elastic filaments and compare the results from experiments with the calculation for infinitely wide sheets. We find that several aspects that were earlier explored in the 3D problem by Schroll et al. [122] translate to the 2D scenario of a droplet in contact with a filament.

3.1 Introduction

The pressure inside a liquid droplet surrounded by vapour is given by Young-Laplace law: $p = \gamma(1/R_1 + 1/R_2)$, where R_1 and R_2 are the principal radii of curvature of the liquid interface, and γ the liquid vapour surface tension. When this droplet is in contact with a solid surface, the solid-vapour surface tension as well as liquid-solid surface tension modify the shape of droplet and as a consequence $p \sim \gamma R_{dr}^{-1} \sin^{2/3}(\vartheta_Y/2)$ [122] where R_{dr} is the droplet radius, while ϑ_Y is Youngs' contact angle. When this solid substrate is made of a soft-elastic material, γ can create stretching at very small length scales $\sim \mathcal{O}(\mu\text{m})$ [69] and the pressure depends on the magnitude of deformation at the contact-line. However, when the substrate is a thin floating elastic sheet (shown schematically in fig. 3.1(a)), the sitting droplet applies a Laplace-pressure on the sheet. This pressure creates bending deformations of $\mathcal{O}(l_{\text{ec}})$, where l_{ec} is the elastocapillary length. Different regimes of bending vs capillary force arise by comparing l_{ec} with the size of the droplet, R_{dr}. The bending of an elastic sheet due to the presence of a droplet has been explored in detail in the "capillary-origami limit" [111, 101, 118, 19] where $l_{\text{ec}} \sim R_{dr}$. In the other limit of $l_{\text{ec}} \ll R_{dr}$, mechanics of the droplet sheet system is very different and has been explored in earlier works [65, 73, 122, 108]. The sheet forms wrinkles when the droplet is placed on top of it due to the droplet's surface tension at the drop-sheet contact line. This surface tension induces in-plane stress at the contact-line, which gets transmitted as hoop stress buckles to result in wrinkles. Though the displacement of sheet in the 3D problem has been solved earlier [65, 36, 73, 122, 108], the relation between pressure and these deformations as a function of boundary tension is largely unexplored. Second, in the 3D problem, the theory predicts that the contact angle is a function of the applied tension at the boundary of the sheet, which was difficult to measure in experiments due to complications arising out of wrinkles.

In this chapter we move to a 2-dimensional version of the problem of droplet on top an elastic sheet but without the complications of wrinkles, folds and crumples. Our system consists of a cylindrical droplet sitting on top of an infinitely wide sheet with applied tension at its edges. We are able to eliminate the complications that arise in 3D since the 2D version of a droplet on sheet cannot exhibit wrinkles, due to the absence of gaussian curvature in a 2D sheet. In a 2D scenario, all deformations of the sheet are isometric to a plane and thus there is no stretching involved in the displacement of sheet.

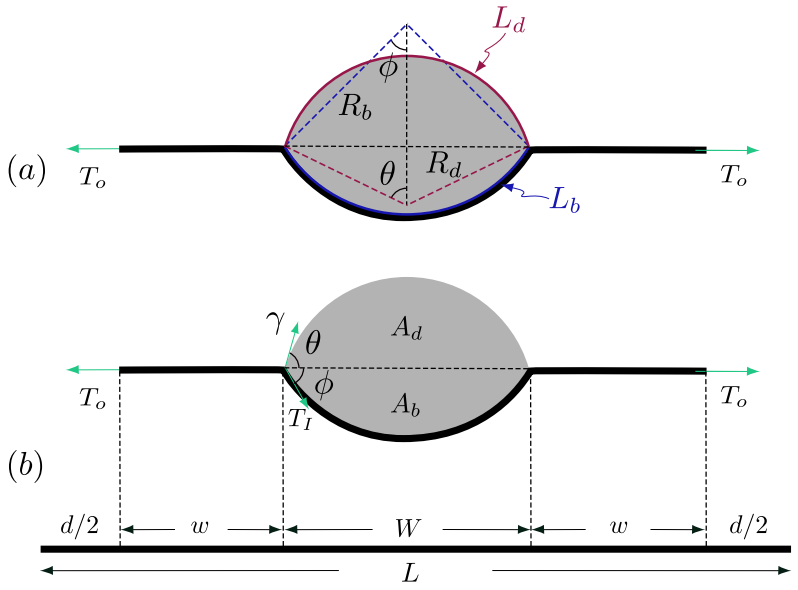

Figure 3.1: Phase diagrams for two classes of contact angles, ϑ_Y showing three different types of sheet morphologies: open-state, closed-state, wrapped-state in the non-dimensional tension, $\tilde{T}$ vs bendability ϵ^{-1} space. (a) $\vartheta_Y < \pi/2$, (b) $\pi/2 < \vartheta_Y < \pi$. On top is the schematic of the setup, where T_o is the applied tension and w the droplet radius.

3.2 Relevant parameters and limits of present work

The drop-on-sheet problem has several length-scales though, as we shall see, only a few length scales play an important role in the sheet morphology:

- thickness of sheet, t,
- elasto-capillary length scale (arising out of balancing bending force and surface tension), $l_{\text{ec}} = (Et^3/\gamma)^{1/2}$ where E is the Youngs' modulus of sheet, and droplet-vapour surface tension γ,
- balancing surface tension and stretching, $l_m = \gamma/E$ which is relevant close to the contact line
- length of the sheet, L,
- the radius of droplet, R_{dr}.

In this intrinsically multi-scale problem, we are interested in a regime where the sheet is inextensible, $l_m \ll t$, when there is a clear scale separation between the size of droplet and

elasto-capillary length, $R_{dr} \gg l_{\text{ec}}$ and for sheets larger than the size of droplet $L \gg R_{dr}$. We can use a non-dimensional number to indicate the scale separation between elasto-capillary length and droplet size, which is called the bendability, $\epsilon^{-1} = (R_{dr}/l_{\text{ec}})^2 = \gamma R_{dr}^2/Et^3$. Another non-dimensional number constructed out of geometry of sheet and droplet is the ratio between length of sheet and droplet size, $\Phi = L/R_{dr}$. Scale separation now implies $\epsilon^{-1} \gg 1$ and $\Phi \gg 1$. The reason we are interested in such a regime is because the dependence of contact angle of droplet on the mechanics of the sheet is found to be a high-bendability phenomenon in the 3D scenario and we would like to firstly see if that is true in the 2D version. Our setting is shown schematically in fig. 3.1(a) where we have the droplet in gray on top of a floating sheet in black.

Beyond bendability and sheet length to droplet size, we also have the externally applied boundary tension T_o, which can be non-dimensionalised using γ to give $\tilde{T} = T_o/\gamma$. The dimension of the tension here is $\mathrm{N/m}$ as the applied force along the sheet is spread across its entire width. Thus we need the following four non-dimensional quantities to describe the droplet-sheet configuration:

$$\tilde{T} = T_o/\gamma, \quad \epsilon^{-1} = \gamma R_{dr}^2/Et^3, \quad \Phi = (L/R_{dr}), \quad \vartheta_Y.$$

3.3 Manifesto

In the regime of $\epsilon^{-1} \to \infty, \Phi \gg 2\pi$, the sheet remains straight for large enough tension and the contact angle seen here is ϑ_Y. This changes as we reduce tension, the sheet now bends but remains in a "partial-wetting state", where the length of exposed liquid-vapour interface is $\mathcal{O}(R_{dr})$ (schematically shown in fig. 3.1(a)), and we evaluate the pressure as a function of $\tilde{T}$. In the partial wetting configuration, we also calculate the contact angle of the droplet on top of this sheet and show that it depends on the applied boundary tension, $\tilde{T}$. Since the calculation is assuming vanishing thickness of the sheet, the angles do not depend on any of the material properties. This important prediction is measured using a quasi-2D experimental setup in the second part of this chapter. The stresses in the sheet we find depend only on the contact angles. For very large values of bendability, i.e., $\epsilon^{-1} \to +\infty$ and $\tilde{T} < \cos^2(\vartheta_Y/2)$, the partial wetting state goes unstable and makes a transition to "partial-wrapping state" characterised by the sheet covering the drop completely, however with part of the sheet still exposed to the vapour. The shapes are shown schematically in fig.3.2(a). We calculate the bifurcation

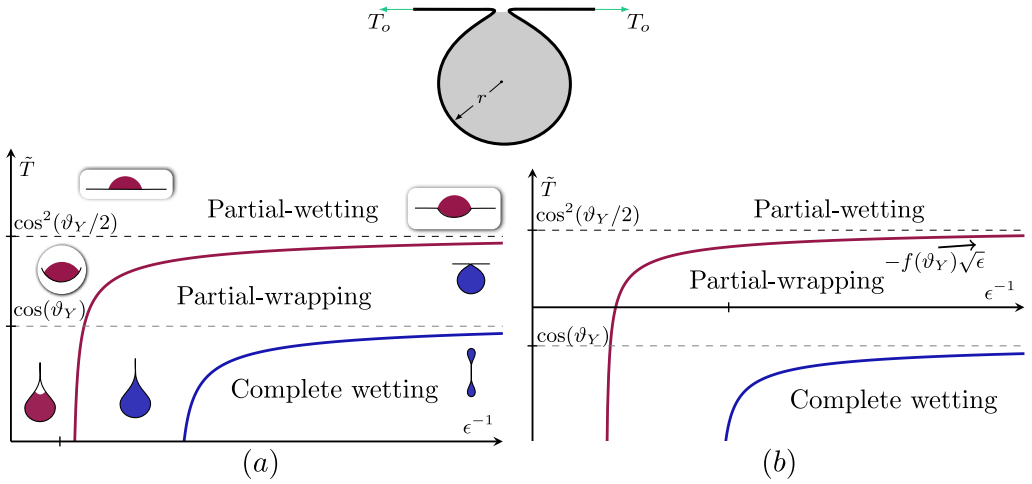

Figure 3.2: Phase diagrams for two classes of contact angles, ϑ_Y showing three different types of sheet morphologies: open-state, closed-state, wrapped-state in the non-dimensional tension, $\tilde{T}$ vs bendability ϵ^{-1} space. (a) $\vartheta_Y < \pi/2$, (b) $\pi/2 < \vartheta_Y < \pi$. On top is the schematic of the setup, where T_o is the applied tension and w the droplet radius.

curve when $\epsilon^{-1} \to +\infty$ and show that the transition from partial-wetting state to partial-wrapping state is super-critical.

Apart from evaluating the pressure close to the bifurcation curve, we demonstrate that near the partial-wrapping state the sheet exhibits a universal self-similar shape close to the contact-line, independent of ϵ^{-1}. As the non-dimensional tension is decreased even further, we show that a lower limit exists, i.e., $\tilde{T} = \cos\vartheta_Y$ below which the sheet undergoes a secondary instability into a "complete wetting state", where the drop wets the entire sheet. In the complete wetting state, the ends of sheet come in contact and moment balance ensures that the ends are indistinguishable from other points on the sheet surface. The shape of the sheet is given by the solution to the Willmore problem [8] in two dimensions, which is the shape that minimises bending energy for a fixed volume of droplet. We compute the wrapped shape using direct numerical minimisation of total energy of the drop-sheet system where the pressure appears as a lagrange-multiplier that preserves drop area. By using simple scaling arguments we explain the mechanism of mode-selection in any wrapped configuration.

3.4 Mechanics at large ($\epsilon^{-1} \gg 1$) and infinite bendability ($\epsilon^{-1} \to \infty$)

3.4.1 Physics in the capillary-origami limit

Let us consider the case of small bendability, $\epsilon^{-1} \sim \mathcal{O}(1)$ with $\Phi \gg 2\pi$, where the surface tension can bend the sheet only gently. In the absence of applied tangential tension, the in-plane force balance would give: $T_I \approx -\gamma \cos\vartheta_Y$, where T_I is the tension in the buckled zone. Note that T_I is compressive for $\vartheta_Y < \pi/2$ and tensile for $\pi/2 < \vartheta_Y < \pi$. The sheet buckling due to the droplet's Laplace pressure is very similar to the Euler buckling scenario where the sheet buckles beyond a critical T_I^c. The critical sheet tension is calculated by energy balance between work done by T_I and the stored bending energy, which gives $T_I^c \sim \epsilon\gamma$. We see that when the bendability of the sheet is very small, i.e., $\epsilon \ll 1$, T_I^c will be larger than $(-\cos\vartheta_Y)$, which means that the surface tension is not strong enough to buckle the sheet. However as we reduce the value of ϵ or increase ϵ, we would reach a state where the $T_I^c < (-\cos\vartheta_Y)$, which is when the sheet would buckle. This example provides a naive mechanism for the sheet buckling due to the presence of a droplet, we will however see in detail the contributions of different energies to sheet buckling in the presence of an applied boundary tension in the ensuing subsections.

3.4.2 Drop-sheet morphologies as different phases

Note: The infinite bendability calculation presented in the first part of this chapter was derived by Benny Davidovitch and Fabian Brau. I have however rederived these expressions since these results are important for the experiments detailed in the second half of the chapter. In the first part, I had contributed to the work by solving the sheet shape in inner and outer regions and also reproducing the results of Neukirch et al. [101], which is not shown here.

The total energy of the drop-sheet system in the absence of applied tension at sheet ends can be written as the sum of contributions from surface energies and bending: $\mathcal{U}_s = \mathcal{U}_{\text{surf}} + \mathcal{U}_{\text{bend}}$. In the limit of vanishing thickness, $t \to 0$ or $\epsilon^{-1} \to +\infty$, the contributions from $\mathcal{U}_{\text{bend}} \to 0$, as the cost of bending is vanishingly small. Thus the state of the drop-sheet system is dominated by contributions from different interfaces: liquid-vapour, liquid-sheet,

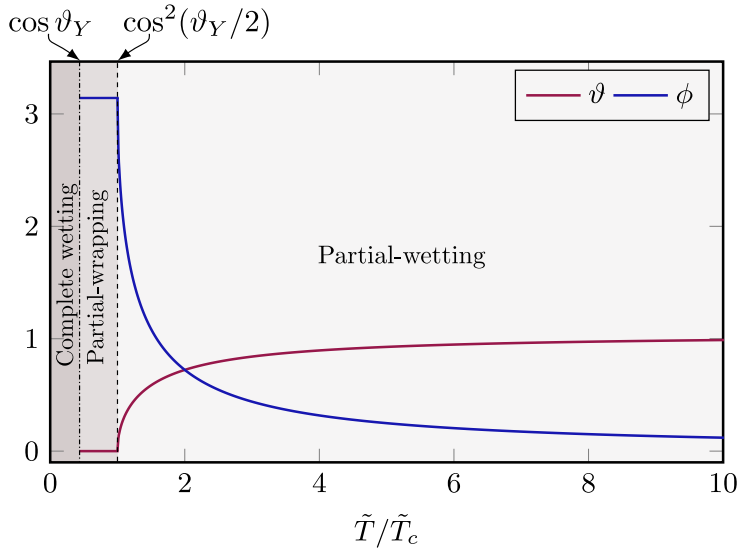

Figure 3.3: Contact angles ϑ, ϕ of the droplet sitting top of the elastic sheet which undergo bifurcation for different values of boundary tension, $\tilde{T}$ when $\vartheta_Y = \pi/3$. Here $\tilde{T}_c = \cos^2(\vartheta_Y/2)$ is the critical non-dimensional tension for transition from partially-wetting phase to partially wrapped phase. We see $\vartheta = \phi$ happens when $\tilde{T} = 2\tilde{T}_c$. $\tilde{T} = \cos\vartheta_Y$ is the transition criteria on tension for transition from partially-wrapped phase to complete wetting.

sheet-vapour. We can write the energy contributions from different interfaces as (see fig. 3.1):

$$\mathcal{U}_s = 2\gamma_{sv}(L - L_b) + (\gamma_{sv} + \gamma_{sl})L_b + \gamma L_d, \tag{3.1}$$

where L_b is the length of the wet region, $L_d = (L - L_b)$ the length of dry region, γ_{sv} is the surface tension of solid-vapour interface, γ_{sl} is the surface tension of solid-liquid interface. We know from Young-Laplace-Dupré (YLD) relation that equilibrium contact angle is related to the surface energies by the relation: $\cos\vartheta_Y = \Delta\gamma/\gamma = (\gamma_{sv} - \gamma_{sl})/\gamma$. We can use the YLD relation to write the energy as:

$$\mathcal{U}_s = \mathcal{U}_{\text{surf}} = 2\gamma_{sv}L - \gamma\cos\vartheta_Y L_b + \gamma L_d. \tag{3.2}$$

Apart from the energy of the interface, we also know that the droplet volume is conserved. In the 2D limit this translates to the area being conserved. We can write the expression for

the area of the droplet in terms of θ, ϕ, R_b, R_d shown in fig. 3.1(b) as:

$$A = \pi R_{dr}^2 = R_d^2\left(\theta - \frac{1}{2}\sin 2\theta\right) + R_b^2\left(\phi - \frac{1}{2}\sin 2\phi\right), \tag{3.3}$$

which is the sum of contributions from the top and bottom part in fig. 3.1(b). Here R_d, R_b are the radius of curvatures of the drop and the buckled region of sheet, R_{dr} is the radius of droplet. This area expression is arrived by summing sections of a circle as the droplet is not deformed by gravity or other such body forces. We can normalise area to get the non-dimensional form:

$$\frac{A}{R_b^2} = \frac{\left[\sin^2\phi\left(\theta - \frac{1}{2}\sin 2\theta\right) + \sin^2\theta\left(\phi - \frac{1}{2}\sin 2\phi\right)\right]}{\sin^2\phi} = \frac{G^2(\phi,\theta)}{\sin^2\phi}. \tag{3.4}$$

Using geometry we also have the relations: $L_b = 2\phi R_b$, $L_b = 2\theta R_b$, $R_b \sin\theta = R_d \sin\phi = W/2$. These relations can be immediately derived from the schematic shown in fig. 3.1(a). As described earlier, we have applied tension T_o at the ends of the sheet and so the total energy of the system is a contribution of the surface energies and the work done by the tension. Now the tension displaces the sheet ends by a distance $d/2$ as shown in fig. 3.1(b), so the work done $\mathcal{U}_t = -dT_o$, due to tension at both ends. The displacement can be written in terms of L, w, W as $d = L - 2w - W = L_b(1 - \sin\phi/\phi)$. Here we use the geometric relation that $2w = (L - L_b)$, as can be seen in fig. 3.1(b) and also the relation between W and L_b from earlier. Finally the expression for the total energy, which is the equivalent of enthalpy for this open system, is the difference between surface energy and work done due to tension. This can be written in non-dimensional terms after expressing all the variables in terms of just $\theta, \phi, \tilde{T}$ as:

$$\mathcal{U}_f = \mathcal{U}_s - \mathcal{U}_t = \ 2\gamma_{sv}L + 2\gamma\left[\theta\sin\phi - \phi\sin\theta\cos\vartheta_Y + \tilde{T}\sin\theta(\phi - \sin\phi)\right], \tag{3.5}$$

$$\bar{\mathcal{U}}_f(\phi,\theta) = \left(\frac{\mathcal{U}_f - 2\gamma_{sv}L}{2\gamma\sqrt{\pi}R_{dr}}\right) = \frac{[\theta\sin\phi - \phi\sin\theta\cos\vartheta_Y + \tilde{T}\sin\theta(\phi - \sin\phi)]}{G(\phi,\theta)}. \tag{3.6}$$

The final expression for energy $\bar{\mathcal{U}}_f$ is dependent only on two variables θ, ϕ for a given value of $\tilde{T}$ and equilibrium configuration of the droplet-sheet system is obtained by extremising this energy expression. We obtain the solution by solving the equations: $\partial_\phi\mathcal{U} = \partial_\theta\mathcal{U} = 0$.

We get two expressions for $\tilde{T}$, which must be the same:

$$\tilde{T} = \frac{2\phi(\cos\vartheta_Y \sin\phi + \sin\theta) + \cos(\theta + 2\phi) - \cos\theta}{2\sin\phi(\phi - \sin\phi)} \tag{3.7}$$

$$= \frac{2\theta(\cos\vartheta_Y \sin\phi + \sin\theta) + \cos\vartheta_Y \cos(2\theta + \phi) - \cos\vartheta_Y \cos\phi}{2\sin\phi(\theta - \sin\theta\cos\theta) + 2(1 - \cos\phi)\sin^2\theta}. \tag{3.8}$$

We can obtain an expression for $\cos\vartheta_Y, \tilde{T}$ in terms of θ, ϕ by solving the above two expressions in MATHEMATICA as

$$\cos\vartheta_Y = \frac{\sin(\theta + \phi)}{\sin\phi} - \frac{\sin\theta}{\sin\phi} \tag{3.9}$$

$$\tilde{T} = \frac{\sin(\theta + \phi)}{\sin\phi}. \tag{3.10}$$

We see in eq. 3.9 that the first term on the right hand side is nothing but $\tilde{T}$, from eq. 3.10. Now in order to interpret the second term in eq. 3.9, we use the fact that the Laplace pressure in the droplet is given by $p = \gamma/R_d = T_I/R_b$ (see fig. 3.1(a)). This implies that

$$\tilde{T}_I = \frac{T_I}{\gamma} = \frac{R_b}{R_d} = \frac{\sin\theta}{\sin\phi}.$$

This immediately leads to interpreting the eq. 3.9 as

$$\tilde{T} - \tilde{T}_I = \cos\vartheta_Y, \tag{3.11}$$

which remarkably resembles the Young-Laplace-Dupré relation, except that the surface energies are now replaced by the stress in the sheet. We call this the *elastic Young-Laplace-Dupré relation*. The second aspect of this finding is that we can immediately expand eq. 3.10 as:

$$\tilde{T} = \tilde{T}_I \cos\phi + \cos\theta, \tag{3.12}$$

which is nothing but the local force balance at the contact line. A important difference however is that this arises out of global energy minimisation. Equation 3.11, 3.12 thus provide the stresses inside the sheet and show that there exists a jump in the stress at the contact line dependent on the equilibrium Young's contact angle.

Transition from open state to closed state

We started out by solving for the contact angles and how they relate to the stresses in the sheet. We have calculated the stresses in the previous section and we now evaluate the angles from the minimised solution. Using the equations obtained by minimising energy in eq. 3.7, 3.8, we obtain an expression for $\cos\theta, \cos\phi$:

$$\cos\theta = \frac{\tilde{T}^2 - \tilde{T}_I^2 + 1}{2\tilde{T}}, \tag{3.13}$$

$$\cos\phi = \frac{\tilde{T}^2 + \tilde{T}_I^2 - 1}{2\tilde{T}\tilde{T}_I}. \tag{3.14}$$

Few important implications arise just by looking at the expression for $\cos\theta, \cos\phi$. Firstly we want the vales of θ and ϕ to be real and this implies $\cos\theta, \cos\phi$ lie in the interval $[-1, 1]$. This immediately implies from eqs. 3.13, 3.14 that $\tilde{T} + \tilde{T}_I \geq 1$ and $|\tilde{T} - \tilde{T}_I| \leq 1$. Using eq. 3.11 these expressions simply mean:

$$|\cos\vartheta_Y| \leq 1, \tag{3.15}$$

$$\tilde{T} \geq \tilde{T}_c = \cos^2(\vartheta_Y/2). \tag{3.16}$$

The first inequality simply defines the criteria for partial wetting whereas the second inequality is more interesting as it sets a lower bound on the value of tension for which partial wetting phase exists.

When $\tilde{T} \to \tilde{T}_c$ the tension in the buckled zone approaches $\tilde{T}_I \to \sin^2(\vartheta_Y/2)$. For values of tension lower than $\tilde{T}_c$ we see that the sheet configuration in partial wetting phase goes unstable and enters a partial wrapping phase. We describe the characteristics of this transition in the next subsection by expanding the energy of the system around this "fixed point".

Partial wetting-wrapping transition

We see from the previous subsection that the lower bound on tension for stable partial-wetting phase implies that the configuration goes unstable below a critical tension value, denoted by $\tilde{T}_c$. For $\tilde{T} < \tilde{T}_c$, the energy of the system $\bar{\mathcal{U}}_f$ is minimised when $\phi = \pi, \theta = 0$. This simply means that there is no liquid-vapour interface, $L_d \to 0$ whereas $L_b \to 2\pi R_{dr}$. The reason why this phase is called "partially-wrapped" phase is because there is a fract of the sheet which

is still exposed to vapour, i.e., the length of the dry region is not zero. The total energy of the partially-wrapped phase is given by:

$$\bar{\mathcal{U}}_{\text{wrap}} = \bar{\mathcal{U}}_f(\phi = \pi, \theta = 0) \to \sqrt{\pi}(\tilde{T} - \cos\vartheta_Y).$$

Now to probe the transition from partial wetting to partial wrapping, we expand around the equilibrium configuration $\phi = \pi, \theta = 0$. We introduce new variables (which we will see is more useful) in terms of ϕ, θ. These are: $\delta\phi = \pi - \phi, \delta\tilde{T}_I = \tilde{T}_I - \sin^2(\vartheta_Y/2) = \sin\theta/\sin\phi - \sin^2(\vartheta_Y/2)$. The control parameters $\tilde{T}, \vartheta_Y$ can then be written as: $\delta\tilde{T}_o = (\tilde{T} - \tilde{T}_c), \vartheta_Y = \arccos(\Delta\gamma/\gamma)$. Equation 3.14 can be written using these new variables as:

$$\delta\phi^0 = \arccos\left[\frac{1 - 8\delta\tilde{T}_o(1 + \delta\tilde{T}_o) - \cos 2\vartheta_Y}{1 + 8\delta\tilde{T}_o(1 + \delta\tilde{T}_o) - \cos 2\vartheta_Y}\right] \tag{3.17}$$

$$\delta\tilde{T}_I^0 = \delta\tilde{T}_o. \tag{3.18}$$

Here the superscript of 0 is introduced to indicate the solution of the energy minimised configuration. When $\delta\tilde{T}_o \to 0$ we get back the solution at the transition such that $\delta\phi \to 0, \delta\tilde{T}_I \to 0$. To see how they approach the energy minimised state, we expand the solution expression around $\delta\tilde{T}_o \to 0$ state to get:

$$\delta\phi^0 = \frac{4}{\sin\vartheta_Y}\sqrt{\delta\tilde{T}_o} + \mathcal{O}(\delta\tilde{T}_o^{3/2}), \tag{3.19}$$

$$\theta^0 = \delta\phi^0 \sin^2\left(\frac{\vartheta_Y}{2}\right). \tag{3.20}$$

We can substitute this into the energy expression in eq. 3.6 to get:

$$\bar{\mathcal{U}}_f^0 = \sqrt{\pi}\sin^2\left(\frac{\vartheta_Y}{2}\right) + \sqrt{\pi}\delta\tilde{T}_o - \frac{16}{3\sqrt{\pi}\sin\vartheta_Y}\delta\tilde{T}_o^{3/2} + \mathcal{O}(\delta\tilde{T}_o^{5/2}). \tag{3.21}$$

We note that as $\delta\tilde{T}_o \to 0$, the variables $\delta\phi^0, \delta\tilde{T}_I^0$ and the energy $\bar{\mathcal{U}}_f^0$ as well as their derivatives approach the equilibrium value continuously to the partially wrapped state. This simply implies that the partial-wetting to partial-wrapping transition in the limit of vanishing bending effects is a second order transition or a super-critical bifurcation.

Equipartition of angles under large tension

In the work of Schroll et al. [122] it was observed that for large boundary tension the angles $\phi, (\vartheta_Y - \theta)$ are equal. It would be interesting to see if the low-dimensional analog of the same problem also carries this feature. In order to do that, we expand the expressions 3.13, 3.14 in the limit $\tilde{T} \gg 1$ and we get:

$$(\vartheta_Y - \theta) = \frac{\sin\vartheta_Y}{\tilde{T}} + \mathcal{O}(1/\tilde{T}^2), \tag{3.22}$$

$$\phi = \frac{2\sin\vartheta_Y}{\tilde{T}} + \mathcal{O}(1/\tilde{T}^2), \tag{3.23}$$

which leads to the conclusion that $(\vartheta_Y - \theta)/\phi \to 1/2$. Thus we see that in the 2D version of the droplet-on-sheet problem, the contact angles get equipartitioned.

Partial-wrapping to Complete wetting transition

The energy of the sheet in the partially wrapped phase can be written in dimensional form as:

$$\mathcal{U}_{\text{wrap}} = 2\gamma_{sv}L + (T_o - \Delta\gamma)L_b,$$

where $L_b = 2\pi R_{dr}$ for circular wrapping, however other non-circular shapes are possible for reduced values of tension $\tilde{T} < \tilde{T}_c$, where $2\pi R_{dr} < L_b \leq L$. Moreover we see that for $T_o/\gamma < \cos\vartheta_Y$, the energy contribution of the second term is negative for $0 < \cos\vartheta_Y < 1$, i.e., $0 < \vartheta_Y < \pi/2$ and thus the total energy is minimised when $L_b = L$, as more the negative contribution from the second term, the lower the total energy gets. Thus entire dry portion of the sheet is encapsulated by the droplet for $\tilde{T} = T_o/\gamma < \cos\vartheta_Y$. This phase we call the complete wetting phase and we see a transition from partial-wrapping to completely wet phase in the limit of vanishing sheet thickness for $\tilde{T} < \cos\vartheta_Y$. The partial wrapping to complete wetting transition happens for $-1 < \cos\vartheta_Y < 0$ or $\pi/2 < \vartheta_Y < \pi$ when the tension $T_o < \gamma\cos\vartheta_Y$ which means that the tension must be compressive,. Thus we see for this range of contact angles, the drop-sheet morphology remains in partially-wrapped phase for all values of extensile boundary tension.

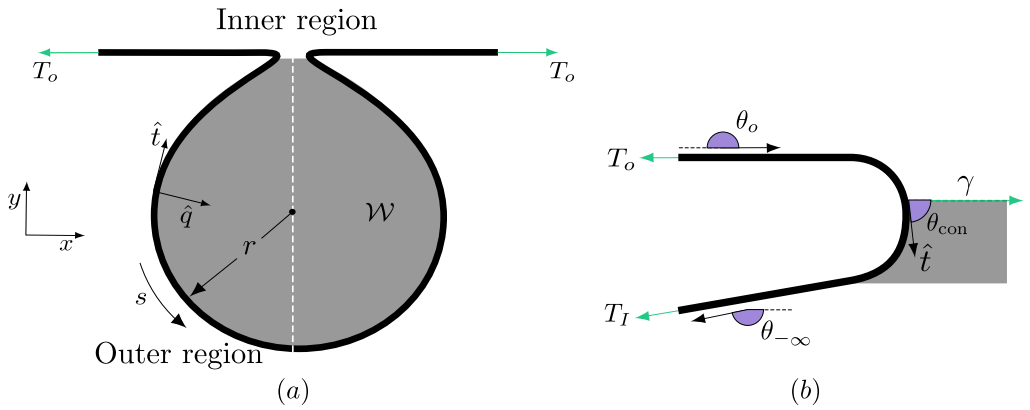

Figure 3.4: Schematic of the inner-zone, close to the contact line. $\theta_{\rm con}$ - contact angle of droplet, determined from force balance; θ_o - far-field angle at the applied tension end; x_{in} - half-length of liquid-vapour interface; z_w - leading order height of bending from liquid interface.

3.5 Bendability effect on partial-wetting to partial-wrapping transition

In the previous section we looked at the sheet morphology and their transitions under different values of tensions, in the limit of $\epsilon^{-1} \to +\infty$. In all the experiments, which we discuss in detail in the later sections of the chapter, we also want to understand the effects of non-zero values of ϵ. We account for finite bending rigidity by considering the energy due to bending in the total energy. The bending energy of the sheet is nothing but:

$$\mathcal{U}_{\rm bend} = \frac{B}{2}\int_{-L/2}^{L/2} \kappa^2(s)\,\mathrm{d}s, \tag{3.24}$$

where $B = Et^3$ is the bending stiffness, $\kappa(s)$ is the curvature along the sheet arc-length s. We will see in the next section that there is a universal solution to the shape of the sheet, obtained by accounting the bending energy close to the partial wetting to partial wrapping transition. We show that we can split the sheet into two regions, the inner region or commonly referred in fluid mechanics nomenclature as the boundary layer, close to the droplet contact line and the outer region, far from the contact line (shown schematically in fig. 3.4). In the ensuing subsections we present the shape of the sheet in both these regions.

Inner region and outer region

The equilibrium equations obtained by minimising the bending energy of the sheet are known as the Föppl-von Karman (FvK) equations for large deformation or the Kirchhoff equations. Kirchhoff equations are derived for filaments, however since the transverse axis of the sheet in our case does not play a role in the sheet morphology, the equations reduce to that of filament. We show here that there exists an ϵ^{-1} independent asymptotic self-similar solution to Kirchhoff equations close to the contact line, i.e., the inner region has a bendability independent self-similar solution. We divide the sheet into two parts: dry and wet regions, where sheet is in contact with vapour and droplet respectively. Now the force balance in the normal and tangential directions of the sheet can be written as [11, 79]:

$$\begin{aligned} B\left[\ddot{\kappa}(s) + \frac{\kappa^3(s)}{2}\right] - T_j\kappa(s) &= -\gamma\sin(\theta_{\text{con}})\delta_d(s) - p_j \\ T_o - T_I &= -\gamma\cos\theta_{\text{con}} \end{aligned} \tag{3.25}$$

where θ_{con} is the angle between the tangent vector at contact-line and meniscus (shown in fig. 3.4), $j =$ dry/wet with T_j, p_j being the corresponding tension in the sheet and Laplace pressure. $T_j = T_o, p_j = 0$ in the dry region, $T_j = T_I, p_j = p$ in the wet region.

The outer zone in the wet region is defined by the region far from the contact line. Since high-bendability implies scale separation between elastocapillary and droplet size, the relevant length scale far from contact line is nothing but droplet size, $r \sim R_{dr}$ (refer fig. 3.4) as bending is important only close to the contact line. This simply implies $\kappa \sim r^{-1}$ everywhere and thus the force balance in the outer wet region gives

$$\frac{B}{2}r^{-3} - T_I r^{-1} \approx p.$$

Dominant balance between any two terms gives us three possible scenarios:

$$\frac{pr}{\gamma} \approx -\frac{1}{2}\epsilon; \quad \frac{|T_I|}{\gamma} \ll \epsilon, \tag{3.26}$$

$$\frac{|p|r}{\gamma} \ll \epsilon; \quad \frac{T_I}{\gamma} \approx \frac{1}{2}, \epsilon \tag{3.27}$$

$$\frac{pr}{\gamma} = \frac{T_I}{\gamma} \gg \epsilon. \tag{3.28}$$

The first two are rather peculiar as their realisations are physical only when $\theta_{\text{con}} \approx \pi/2$ where tension vanishes with ϵ, while the third scenario is more general. Using this, we can generalise the pressure for $\epsilon^{-1} \gg 1$, $T_I \kappa_o = p$ and $\kappa_o \to r^{-1}$ forms the outer solution to leading order. This we see is also consistent with the solution obtained in the earlier section where the sheet takes the shape of a circle of radius r where $r \to R_{dr}$ when $\epsilon^{-1} \to +\infty$.

Now moving close to the contact-line which is the inner zone, eq. 3.25 has two elasto-tensile length scales, l_o, l_i: one each in dry region (where the tension is T_o) and wet region (where the tension is T_I). The point of $s = 0$ is used to denote the location of contact line on the sheet. We can solve the Kirchhoff equations parameter-free to leading order in both dry and wet regions when scaled using appropriate length-scale.

$$l_o = \epsilon^{1/2} \tilde{T}^{-1/2} R_{dr}, \; l_i = \mathrm{x}^{-1/2} \epsilon^{1/2} \tilde{T}^{-1/2} R_{dr}, \tag{3.29}$$

where we have introduced a new non-dimensional number $\mathrm{x} = T_I/T_o$. This unique combination accounts for effect of tension in dry/wet region as well as bendability. The leading order non-dimensional pressure inside the droplet from eq. 3.25 becomes: $\tilde{p} = \epsilon^{1/2} \tilde{T}^{-1/2} \mathrm{x}^{-1/2}$, which is evidently $\mathcal{O}(\sqrt{\epsilon})$ and will not play a role in determining sheet's shape at $\mathcal{O}(1)$. This we show in detail here.

Dry region

The dry region exists in the region defined by $s \in [L/2, s_d^*)$ where s_d^* is the coordinate that needs to be found by matching with that of the wet region solution. The non-linear curvature equation for a sheet with infinite lateral width can be written from eq. 3.25:

$$B\left[\ddot{\kappa}(s) + \frac{\kappa^3(s)}{2}\right] - T_o \kappa(s) = 0 \tag{3.30}$$

This if we scale by bendability dependent l_o, we are left with a parameter free non-dimensional equation:

$$\left[\hat{\kappa}_d''(\hat{s}) + \frac{\hat{\kappa}_d^3(\hat{s})}{2}\right] - \hat{\kappa}_d(\hat{s}) = 0 \tag{3.31}$$

We see that this equation can be integrated by multiplying with $\hat{\kappa}_d'$ and we get:

$$(\hat{\kappa}_d')^2 = -\frac{1}{4}\hat{\kappa}_d^4 + \hat{\kappa}_d^2$$

This gives us the functional form for curvature that decays to zero at far-field as:

$$\hat{\kappa}_d(\hat{s}) = \frac{-4\mathrm{e}^{\hat{s}}}{\mathrm{e}^{2\hat{s}}+1} = -2\,\mathrm{sech}(\hat{s}).$$

The analytical form of the curvature is integrated to obtain the angle $\psi(\hat{s})$ which the tangent vector makes with x-axis. This angle can further be used to calculate the coordinate of the sheet. It is worth highlighting that the solution in the dry region is complete and not perturbative as the pressure in the dry region is zero everywhere. It is the pressure in the wet region that, we will show, that is accounted at higher orders in ϵ.

Wet region

In the wet region, defined along $s \in [s_w^*, 2\pi R_{dr})$, where s_w^* is again a value arising out of matching with the dry solution, the equation governing the behaviour of the sheet is, as seen in eq. 3.25:

$$B\left[\ddot{\kappa}(s) + \frac{\kappa^3(s)}{2}\right] - T_I\kappa(s) = p \tag{3.32}$$

where T_I is the tension inside sheet in wet zone and p the Laplace pressure of droplet. When we are in a scale separated regime of $R_{dr} \gg l_{\mathrm{ec}}$, where l_{ec} is the elasto-capillary length scale, we can see from eq. 3.28 that the terms due tension and Laplace pressure are to leading order of magnitude $\mathcal{O}(R_{dr})$. To put it differently, the pressure effect on the shape of the sheet in the inner region occurs only at higher orders in ϵ. Thus in the wet region close to the contact line, the filament is governed mainly by the non-linear bending and tension. The equation when scaled using $l_i = \mathrm{x}^{-1/2}\epsilon^{1/2}\tilde{T}^{-1/2}R_{dr}$, the leading order equation is:

$$\left[\hat{\kappa}_w''(\hat{s}) + \frac{\hat{\kappa}_w^3(\hat{s})}{2}\right] - \hat{\kappa}_w(\hat{s}) = 0. \tag{3.33}$$

We know that in the infinite bendability limit, $p = T_I/R_{dr}$ and thus the non-dimensional pressure becomes $\tilde{p} = \epsilon^{1/2}\tilde{T}^{-1/2}\mathrm{x}^{-1/2}$, which is $\mathcal{O}(\sqrt{\epsilon})$. This shows that the solution maintains a similar functional form as dry-region to leading order given by:

$$\hat{\kappa}_w(\hat{s}) = \frac{-4\mathrm{e}^{\hat{s}}}{\mathrm{e}^{2\hat{s}}+1} = -2\,\mathrm{sech}(\hat{s})$$

We note here that the curvature of the sheet, $\hat{\kappa}_d(\hat{s}_d), \hat{\kappa}_w(\hat{s}_w) \to 0$ in the limit $\hat{s}_d \to$

$-\infty, \hat{s}_w \to \infty$. This is because $\hat{s}_d \to -\infty$ corresponds to $s = -L/2$ in the limit $\epsilon \to 0$ and $\hat{s}_w \to \infty$ corresponds to $s = \pi R_{dr}$

Matching conditions

At the contact line, the solution from the dry and wet region needs to be matched with self-consistent set of matching conditions. These conditions arise out of continuity of curvature for torque balance, jump in gradient of curvature due to normal-force balance, and in-plane force balance. Continuity of curvature at the contact line can be written in non-dimensional terms as:

$$\hat{\kappa}_d(\hat{s}_d^*) = \sqrt{\mathrm{x}}\, \hat{\kappa}_w(\hat{s}_w^*), \tag{3.34}$$

where we see the appearance of $\sqrt{\mathrm{x}}$ because of T_I appearing in the length scale of wet region. The normal force balance can be obtaining be integrating eq. 3.25 at the contact line and the contributions are only from the linear bending term and surface tension which has a delta force at the contact line. This reads as:

$$\tilde{T}(\hat{\kappa}_d'(\hat{s}_d^*) - \mathrm{x}\, \hat{\kappa}_w'(\hat{s}_w^*)) = -\sin\theta_{\mathrm{con}}. \tag{3.35}$$

Finally, the in-plane force balance on the other hand is simply:

$$\tilde{T}(1 - \mathrm{x}) = -\cos\theta_{\mathrm{con}}. \tag{3.36}$$

However we now know from the outer solution that to leading order in ϵ, the stresses satisfy the elastic Young-Laplace-Duprét relation, derived in eq. 3.11. This simply means that the contact angle in the inner region from eq. 3.36, $\theta_{\mathrm{con}} = \vartheta_Y$. We can also rewrite eq. 3.36 in terms of $\delta\tilde{T}_I, \delta\tilde{T}_o$ as simply:

$$\cos\theta_{\mathrm{con}} = \cos\vartheta_Y + (\delta\tilde{T}_o - \delta\tilde{T}_I), \tag{3.37}$$

using the relation $\delta\tilde{T}_I = \tilde{T}_I - \sin^2(\vartheta_Y/2), \delta\tilde{T}_o = \tilde{T}_o - \cos^2(\vartheta_Y/2)$. Moreover we know that $\delta\tilde{T}_I = \delta\tilde{T}_o$ in the limit $\epsilon \to 0$.

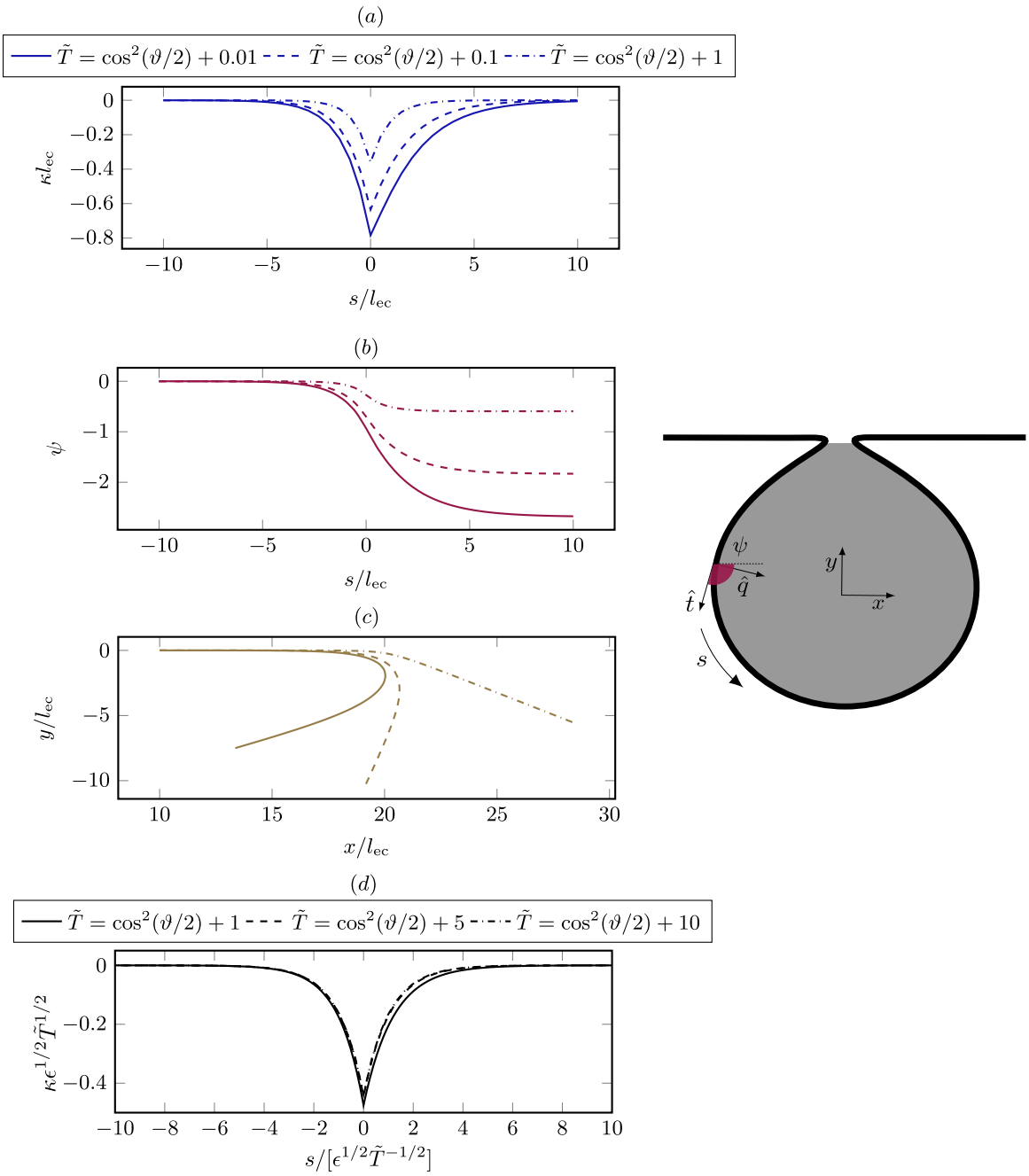

Figure 3.5: $(a) - (c)$ The curvature of the sheet $\kappa(s)$, angle the tangent makes with the contact line, $\psi(s)$ and shape of sheet close to the contact line for different values of tension in the partial-wrapping phase. (d) Scaled curvature of the sheet for large values of tension collapses onto a single curve, showing the self-similar nature in the large tension limit. All plots are for $\vartheta_Y = \pi/3$.

If $\theta_{\text{con}} = \vartheta_Y$, we can write the continuity of curvature and normal force balance as:

$$\sqrt{(\tilde{T} - \cos\vartheta_Y)}\,\text{sech}(\hat{s}_w^*) = \sqrt{\tilde{T}}\text{sech}(\hat{s}_d^*), \tag{3.38}$$

$$\tilde{T}\text{sech}(\hat{s}_d^*)\tanh(\hat{s}_d^*) - \left[\tilde{T} - \cos\vartheta_Y\right]\text{sech}(\hat{s}_w^*)\tanh(\hat{s}_w^*) = -\frac{\sin\vartheta_Y}{2}. \tag{3.39}$$

The above two equations can be solved exactly for $\hat{s}_d^*, \hat{s}_w^*$ in MATHEMATICA. The solution reads:

$$\hat{s}_d^* = -\,\text{acosh}(a\tilde{T}^{1/2}) \tag{3.40}$$

$$\hat{s}_w^* = \text{acosh}[a(\tilde{T} - \cos\vartheta_Y)^{1/2}], \tag{3.41}$$

$$a = \frac{2}{\sin\vartheta_Y}[b + \sqrt{b^2 - 1}]^{1/2}, \quad b = 2\tilde{T} - \cos\vartheta_Y.$$

The angle the tangent along the sheet makes with x-axis is obtained by integrating the solution for curvature and is given by:

$$s < 0 : \psi(\hat{s}_d) = \pi + 2\text{atan}\left[\tanh\left(\frac{\hat{s}_d + \hat{s}_d^*}{2}\right)\right], \tag{3.42}$$

$$s > 0 : \psi(\hat{s}_w) = \pi - \phi - 4\text{atan}\left[\tanh\left(\frac{\hat{s}_w + \hat{s}_w^*}{2}\right)\right]. \tag{3.43}$$

We plot in fig. 3.5(c) the shape of the sheet close to the contact line, using these expressions. We observed in the experiments, as we detail later in this chapter, that the curvature close to contact line decreases with increase in tension. Thus for large values of tension, $\tilde{T} \gg 1$ we find that rescaling κ by multiplying it with $\epsilon^{1/2}\tilde{T}^{1/2}$ and s by $\epsilon^{1/2}\tilde{T}^{-1/2}$ collapses different curvature shapes on to a single curve as shown in fig. 3.5(d).

3.6 Complete wetting phase as Willmore problem

The completely wet state as we have seen in section 3.4.2 is characterised by the entire sheet engulfing the droplet where the wetting length of the sheet, $L_b = L$. The shape of sheet when its length is $2\pi R_{dr}$ is a perfect circle of radius R_{dr} as it possesses minimum bending energy. But for any $L > 2\pi R_{dr}$, the droplet has to increase its perimeter while preserving its area to adapt to increase in sheet length.

The contribution to bending energy of sheet arises from Laplace pressure of droplet and moreover since there is no liquid-vapour interface, surface energy contribution from liquid-solid contact and solid-vapour contact is a constant. Leaving aside this constant surface energy, the total energy can be written as:

$$\mathcal{U}_{\text{bend}} = \frac{B}{2}\int_0^L \kappa^2 \mathrm{d}s - \int_0^L T(|\mathbf{t}|^2 - 1)\mathrm{d}s - p\left[\int_{\mathrm{d}\Omega} \mathrm{d}A - \pi w^2\right] \tag{3.44}$$

where T is the tension in the sheet which enforces length constraint, Laplace pressure p is the lagrange multiplier that preserves area, $\mathrm{d}\Omega$ is the boundary of the droplet. The problem of minimising the squared difference of principal curvature for a surface with a given enclosed volume has been studied in 3D, and is called as Willmore energy [8]. This Willmore energy in the 2D setting becomes the complete wetting problem we have here. We see that when the energy is scaled by B, the solution is independent of bendability and the problem is purely geometric whose state is determined uniquely by the value of $\Phi = L/R_{dr}$.

Near circular wraps, $\Phi \sim 2\pi$

The solution to shape of sheet for $\Phi = (2\pi + \eta)$, where $\eta \ll 1$ can be approximated by a shape with two halves of a circle of radius $(R_{dr} - \mathrm{d}R_{dr})$ connected by a rectangle of width, λ. The bending energy of such a configuration is $\mathcal{U} = B\pi/(R_{dr} - \mathrm{d}R_{dr})$ and constraints of length, area combine to give:

$$\frac{(L-2\lambda)^2}{4\pi} + \lambda\left(\frac{L-2\lambda}{\pi}\right) = \frac{\pi L^2}{(2\pi+\eta)^2}.$$

This geometric problem under $\eta \ll 1$ can be expanded and we find:

$$\begin{aligned}\lambda &\approx \frac{L\sqrt{\eta}}{2\sqrt{\pi}}\left(1 - \frac{3\eta}{8\pi}\right)\\ \frac{\mathrm{d}R_{dr}}{R_{dr}} &\approx \sqrt{\frac{\eta}{\pi}}\left[1 - \frac{1}{2}\sqrt{\frac{\eta}{\pi}} + \frac{\eta}{2\pi}\right]\end{aligned}$$

which shows both the increase in length as well as change in radius, $\lambda, \mathrm{d}R_{dr} \sim \sqrt{\eta}$ away from a circle.

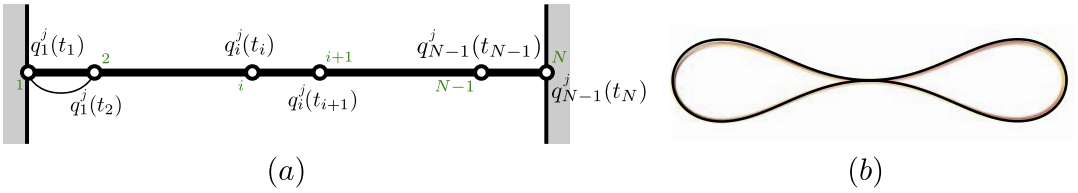

Figure 3.6: Schematic representation of the sheet represented using $q_i^j(t), j = x, y$. Both $q_i^x(t)$ and $q_i^y(t)$ are series of rods connected to its neighbour under consistency condition of continuous slope and curvature at end points.

Numerical minimisation of Willmore energy

We compute the sheet morphology for differen values of Φ by direct numerical minimisation of total energy of drop-sheet system in eq. 3.44. This is performed by expanding the sheet position vector $(x(s), y(s))$ in a cubic-hermite polynomial basis and expressing bending energy in terms of coefficients of these polynomials explained in detail in the ensuing subsections. In order to minimise the energy function in a wrapped state for different values of $\Phi > 2\pi$, we write the energy of system in terms of $(x(t^d), y(t^d))$ with t^d being an arbitrary parameter that goes from 0 to 2π. The connectivity of sheet's ends is ensured by: $x(0) = x(2\pi), y(0) = y(2\pi)$.

$$\mathcal{U}_{\text{bend}} = \frac{B}{2}\int_0^{2\pi} \kappa^2(t^d)\,\mathrm{d}t^d - T\left(\int_0^{2\pi} (x'^2(t^d) + y'^2(t^d))^{1/2}\,\mathrm{d}t^d - L\right),$$

where the curvature in this new parameterisation is nothing but:

$$\kappa(t^d) = \frac{x'(t^d)y''(t^d) - y'(t^d)x''(t^d)}{(x'^2(t^d) + y'^2(t^d))^{3/2}}. \tag{3.45}$$

We now divide the sheet into $(N-1)$ rods each of constant length (see fig. 3.6(a)), $l = L/(N-1)$. The discrete points $(x(t_i^d), y(t_i^d)) = (x_i, y_i)$ are then used to construct a spline

using Hermite polynomials:

$$q_i^x(t^d) = x_i + s_i^x(t^d - t_i^d) + \frac{x_i' - s_i^x}{l}(t^d - t_i^d)^2 + \frac{(s_i^x + s_{i+1}^x - 2x_i')}{l}(t^d - t_i^d)^2(t^d - t_{i+1}^d), \tag{3.46}$$

$$q_i^y(t^d) = y_i + s_i^y(t^d - t_i^d) + \frac{y_i' - s_i^y}{l}(t^d - t_i^d)^2 + \frac{(s_i^y + s_{i+1}^y - 2y_i')}{l}(t^d - t_i^d)^2(t^d - t_{i+1}^d). \tag{3.47}$$

Variables s_i^x, s_i^y are the slope of spline at the beginning of i^{th} rod and

$$x_i' = \frac{x_{i+1} - x_i}{l}, y_i' = \frac{y_{i+1} - y_i}{l}.$$

The bending energy term can be expanded using the curvature expression from above and integrated using a Gauss-quadrature scheme given by:

$$\mathcal{U}_{\text{bend}} = \frac{B}{2}\int_0^{2\pi} \kappa^2(t^d)\mathrm{d}t^d, \tag{3.48}$$

$$= \frac{B}{2}\sum_{i=1}^{N-1}\sum_{j=1}^{M} \frac{(t_{i+1}^d - t_i^d)}{2} w(j)\kappa_i^2(m_j), \tag{3.49}$$

$$m_j = \frac{(t_{i+1}^d - t_i^d)}{2}\cos\left(\frac{j\pi}{(M-1)}\right). \tag{3.50}$$

The function $w(j)$ is the weight function for the quadrature scheme on Lobotto points. The curvature between nodes $(i, i+1)$ can be explicitly written using the $q_i^x(t^d), q_i^y(t^d)$ as:

$$\kappa_i(t^d) = \frac{q_i^{x'}(t^d)q_i^{y''}(t^d) - q_i^{y\prime}(t^d)q_i^{x''}(t^d)}{(|q_i^{x'}|^2(t^d) + |q_i^{y'}|^2(t^d))^{3/2}}. \tag{3.51}$$

What remains to be done is to match the slope, second derivative and end points of the sheet. This can be written as:

$$s_1^j = s_N^j, \tag{3.52}$$

$$q_1^{j''}(t_1^d) = q_{(N-1)}^{j''}(t_N^d), \tag{3.53}$$

$$2s_1^j + s_2^j + 2s_N^j + s_{N-1}^j = 3(j_1' + j_{N-1}'), \text{ for } j = (x, y). \tag{3.54}$$

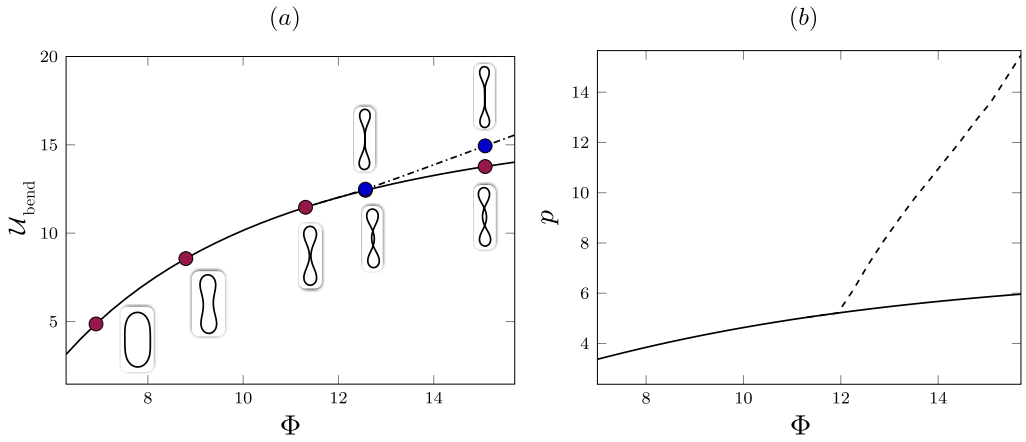

Figure 3.7: Energy of the sheet in a wrapped state as a function of $\Phi = (L/R_{dr})$ with and without self-intersection. $\Phi = 2\pi$ represents a circle and all higher values are non-circular configurations and numerically we find the critical value where self-intersection begins to be $\Phi_c \approx 12.5$.

Apart from these boundary conditions, we also have the consistency condition that ties two rods together. This is used to find slopes at nodes t_i^d:

$$s_i^j + 4s_{i+1}^j + s_{i+2}^j = 3(j_i' + j_{i+1}').$$

From eq. 3.49 we see that the discrete form of bending energy is only a function of the coefficients of the hermite polynomial and we minimise this energy with $(N+1)$ rigid constraints. N of them come from length conservation of each of the rod while the last one to keep the area fixed for a given R_{dr}. These integral constraints are again written in quadrature form and supplied into the minimisation toolbox of MATLAB.

Non-intersecting boundary condition

We see from fig. 3.7 that as we decrease the size of droplet for a fixed sheet length which increases the value Φ, there exists a critical value of Φ which we call Φ_c beyond which the sheet starts to self-intersect, while still preserving area (trajectories of solid line in fig. 3.7(a)). The numerical minimisation with area constraint however works because the sign of area in the intersected region is opposite to other region. In order to look for physically relevant solution, we must prevent sheet from passing through itself. We do that by the following technique:

- Compute two points $(x_m, y_m), (x_k, y_k)$ that are closest along the sheet for $\Phi \lesssim \Phi_c$ and

might touch for a higher value of Φ.

- Locate a series of n_c points that are neighbouring (x_k, y_k), on either of its sides.
- To ensure non-crossing, with respect to vector $\tilde{\mathbf{x}}_{m+1}$ these $2n_c+1$ must points remain on the same side as we increase Φ beyond Φ_c where $\tilde{\mathbf{x}}_j = (x_j - x_m, y_j - y_m)$.
- Using the sign of cross-product we can write:

$$\mathrm{sgn}(\tilde{\mathbf{x}}_{m+1} \times \tilde{\mathbf{x}}_k) < 0.$$

This we supply as inequality constraints for $2n_c+1$ points into the minimisation toolbox. The advantage of this technique compared to other techniques such as adding same signed charges at nodes is that the form of the energy of the sheet remains unchanged, except now for a few additional constraints.

3.6.1 Sheet morphology when $\Phi \gg 2\pi$

Using the numerical technique describe in the previous subsection, we go beyond small variations about a circle, i.e., we explore the regime of $\Phi \gg 2\pi$. We see from fig. 3.7(a) the shape of the sheet for $\Phi > 2\pi$ and we also see a dipole mode with two lobes as the minimum energy morphology of the sheet. A simple way to see this mode selection is to calculate the energy for a mode with n-lobes. Like in section 3.6, we can approximate n-lobes of the sheet as circles of radius α connected to each other by straight segments of length λ. The bending energy of such a state is given by $\mathcal{U}_{\mathrm{bend}} = nB\pi/\alpha$. Moreover from area constraint we have $\alpha = R_{dr}/\sqrt{n}$. Thus we see that $\mathcal{U}_{\mathrm{bend}} \sim n^{3/2}$. Since in the scenario we are interested in $n \geq 2$, we see dipole being the least energy mode. In order to ensure that the dipole mode is not a meta-stable solution, we initialise the numerical minimisation with shapes that have higher modes and find that the minimised solution eventually reach a dipole (see fig. 3.8(a)). Moving ahead, by simply minimising the energy in eq. 3.44 the solution starts self-intersecting after a critical $\Phi_c \approx 12.5$ and since these self-intersection solutions are unphysical, we ensure that any two points on the sheet do not cross each other by the technique described earlier. In fig. 3.7 we plot the energy with and without non-intersecting constraint and Φ_c is the point at which the energy deviates from that of self-intersecting solutions.

In this complete wetting phase we see that the energy diverges with increase in Φ, however not indefinitely. This divergence is cut-off by the smallest length-scale in our working limit,

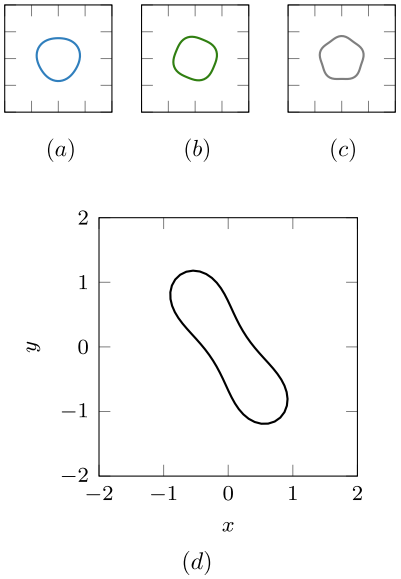

Figure 3.8: Three different initial conditions corresponding to (a) tripole (b) quadrupole, (c) pentapole modes that result in the same dipole solution, (d) $\Phi = 1.08$ for these numerical optimisations.

which is l_{ec}. When the lobes in the wrapped state are smaller than $\mathcal{O}(l_{\mathrm{ec}})$, surface tension can no more hold the sheet wrapped and the parcel becomes unstable. We can see that in the limit $\epsilon^{-1} \gg 1$, the region of stable wrapping is set by the absolute value of ϵ^{-1} but the shape interestingly is independent of this value.

3.7 Findings

So far we have derived the solution for the morphologies of thin elastic sheets in contact with a liquid droplet, with applied boundary tension. We have obtained exact results in the singular limit of $\epsilon^{-1} \to 0$, and in this limit there are two bifurcations resulting in three distinct phases which we call the partial-wetting phase, partial-wrapping phase and complete wetting phase. We also find that the stresses in the sheet obey an elastic Young-Laplace-Dupré relation, very similar to the classical Young-Laplace-Dupré relation, arising here out of global energy minimisation. In the regime close to the transition of partial-wetting to partial wrapping, we look at the shape of sheet close to the contact line and far from it. The problem of shape near contact line has an inner region dominated by competition between bending and tension and an outer region dominated by Laplace pressure of droplet. The morphology of

the sheet in the inner region follows a universal self-similar shape, independent of ϵ and the sheet is circular in shape in the outer region.

In the complete wetting phase, we characterise the sheet shape by showing that the energy in this phase is nothing but 2D Willmore energy, and use a Hermite polynomial based spline technique to describe the sheet shape. The numerically minimised sheet shape is described by a single parameter $\Phi = L/R_{dr}$. When the length of the sheet is $L = 2\pi R_{dr}$, i.e., $\Phi = 2\pi$ the sheet becomes a circle while for very large values, $\Phi > 12.5$ the sheet starts self-intersecting. We come up with a simple technique to robustly capture the physically relevant shapes, without modifying the form of the Willmore energy.

3.8 Background to experiments

The wetting properties of a drop on a rigid substrate determines the angle of contact with the solid, known as the Young angle of contact. However if the substrate is a soft solid [69, 127, 70, 104] or an unstretchable but thin film [64, 122, 131], it can deform under the capillary action of the drop. In the former case, the liquid-vapour surface tension induces large localised stretching close to the contact line while in the latter, the film bends without stretching, resulting in large bending close to the contact-line. In both these scenarios the perceived contact angle at scales of the droplet-size deviates from the Young's contact angle, ϑ_Y [3]. The magnitude of this contact angle is obtained from a global energy minimisation rather than a simple local force balance [122]. This anomalous contact angle behaviour has several applications ranging from bio-locomotion to creating hydrophobic fabric [17, 27, 42, 23].

We study a two-dimensional version of the wetting experiment at an air-water interface, where the thin sheet is replaced by a slender elastic filament and is wet by a nearly flat oil drop floating on the water interface. The three-dimensional problem of a droplet of liquid on top of a floating thin sheet [64] was initially studied because the capillary forces at the contact-line generate a radial wrinkling pattern [64, 122]. However, from the viewpoint of studying the contact angle, the wrinkles are a hindrance, as they impede the measurement of the contact angle and the deformation of the sheet close to the contact line where there is large localised bending. On the other hand, the 2D system does not have the complication of wrinkles which arise in 3D. When the droplet size approaches the size of the sheet, if the sheet is highly bendable then it can wrap around the droplet and enclose it entirely. Wrapping in 2D can occur with smooth, isometric bending, unlike in 3D, thus the 2D filament-droplet

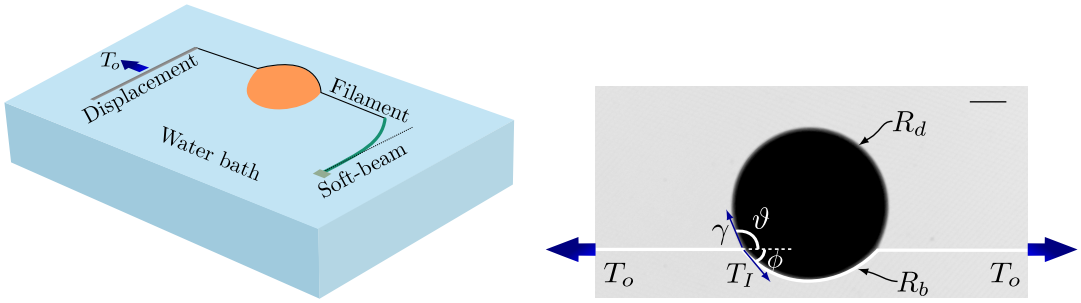

(a) (b)

Figure 3.9: (a) Schematic of the experimental setup where a droplet of Mineral oil (orange) is placed in the vicinity of a floating thin elastic filament at the air-water interface of a water bath. One end of the filament is connected to a soft beam (green) whose end displacement is used to measure the applied tension T_o. Tension in our experiments is controlled by inducing in-plane displacement of the free end of the filament. (b) Variables of interest are shown on top of an image from experiments : ϑ, ϕ - angle made by the droplet with the buckled filament; T_o - applied boundary tension and T_I - tension in the droplet-wet region, γ - effective surface tension of the 2-D droplet along `contact-line' as detailed in the article; R_d, R_b - radius of curvature of the free interface of droplet and the radius of curvature of the filament wet by droplet. The scale bar in the image is $5\mathrm{mm}$. Further details of the setup are provided in fig. 7.7.

system allows us to study phenomenon of wrapping of the droplet by the filament more easily than in the 3D system.

The entire range of phenomena, from the Young contact geometry, to large deviations from apparent Young contact, to wrapping, can be obtained by tuning the competition between the liquid-vapour surface tension, and the bending rigidity of the sheet over the scale of the drop. This competition is captured in a dimensionless parameter called the bendability, which is the ratio of the droplet-size, w to the capillary-bending length, l_{ec} which is the length scale at which sheet bending and capillary forces are similar in magnitude. Most studies [111, 4, 118, 109, 43, 101] are in the regime where the bendability is $\mathcal{O}(1)$ while our experiments are in the high-bendability limit. We achieve this limit by using thin filaments and large droplet sizes. This guarantees a separation in scales between droplet size and capillary-bending length, and the behaviour in this limit is dramatically different from that in low bendability limit [122, 106, 76]. Another method to smoothly modify the rigidity of the filament to the capillary force applied by the droplet is to place the filament under tension. When the filament is under large tension, it does not deform and the Young scenario is recovered; when it is slack, then large deformation and wrapping can occur.

As shown in fig. 3.9(b), we measure the contact angles ϑ, ϕ of a partially wetted filament

as a function of applied tension. We show in this paper that the contact angles exhibit a universal behaviour in the thin-filament limit which were not measured in earlier work on the equivalent 3D systems[131, 64, 122]. In the limit of infinite bendability, our results match well with theory derived early in the chapter, with the effective surface tension of the 2-D droplet being the only fitting parameter. Under large magnitudes of applied tension, the theory predicts that though ϕ and $(\vartheta_Y - \vartheta) \to 0$, the ratio $(\vartheta_Y - \vartheta)/\phi$ asymptotes to a constant of 1/2. We measure this ratio in our experiments and observe the trend predicted by the theory to hold true. We also find that the applied tension and the tension in the buckled zone obey a force balance relation remarkably similar to the Young-Laplace relation. In the theory of vanishing bending stiffness, the region close to the contact-line is of infinite curvature. However, in the experiments the filament has a finite magnitude of curvature denoted by $1/R_{\text{eb}}$, an elasto-bending scale; we study the variation of R_{eb} with T_o, the applied boundary tension. The effects of finite bendability here produce deviations from the high bendability theory. In the wrapped regime when the filament length is less than the perimeter of droplet, we find that the filament forms part of a circle around the drop, unlike in the sheet wrapping experiment[106] where the shape resembles a parachute. The circular shape ensures there is no jump in curvature at the interface between filament end and droplet interface; this leads to seamless wrapping as observed in the case of ultra-thin sheets [76]. Whereas for low-bendability filaments, the radius of curvature of the droplet-interface diverges as the ends of the filament approach each other.

3.9 Relevant variables for droplet-on-filament

Four length scales govern the overall mechanics of the filament-drop system. These are the diameter d of the filament, the droplet radius R_{dr}, the length of the filament L, the capillary-bending length scale $l_{\text{ec}} = (B/\gamma)^{1/3}$ with B being the bending stiffness, given for a filament of circular cross-section as: $B = E\pi d^4/64$, (E - Youngs' modulus of filament material). A fifth length scale arising out of stretching, $l_m = \gamma/E$ (γ - droplet-vapour surface tension) is irrelevant in our experiments because $l_m = 0.03\mu\text{m} \ll d \approx \mathcal{O}(10\mu\text{m})$. Moreover we are interested in a high-bendability regime where the size of droplet is much larger than the capillary-bending length scale, $R_{dr} \gg l_{\text{ec}}$. The non-dimensional quantity that indicates this scale separation is the bendability: $\epsilon^{-1} = (R_{dr}/l_{\text{ec}})^2$.

By varying these length-scales and the applied tension we can explore the phases of the

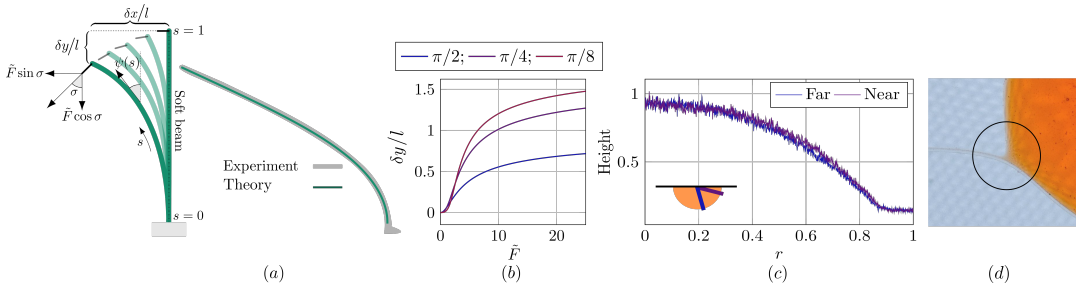

Figure 3.10: (a) Schematic of the soft beam attached to one end of the filament to measure tension in the filament with the relevant variables: $\psi(s)$ - angle between tangent and vertical; $\tilde{F}$ - non-dimensional force applied at beam's end; σ - angle at which the force is applied; s - non-dimensional arc-length; $\delta x/l, \delta y/l$ - non-dimensional displacement along x, y-direction. Alongside is the image of the beam from the experiment superimposed on the numerically-solved shape from eqn. 3.56. (b) Numerically computed displacement $\delta y/l$ vs non-dimensional force, $\tilde{F}$ for three different σ values: $\pi/2, \pi/4, \pi/8$. (c) Fluorescence intensity along two radial lines, one close to the contact-line of PDMS filament and one far from it (shown schematically in the inset). This indicates that the presence of the filament does not distort the 3D height profile of the drop, except perhaps very close to the 4-phase contact line as shown in (d) where we see 3-D effects appear as the droplet becomes thin near the contact line. The droplet we use here is of Mineral oil and is dyed using Sudan Red dye.

filament-drop phase diagram. The axes of the diagram are three non-dimensional quantities constructed from these variables:

$$\tilde{T} = T_o/(\gamma d), \quad \epsilon^{-1} = (R_{dr}/l_{\rm ec})^2, \quad \Phi = (L/R_{dr}). \tag{3.55}$$

Here T_o is the applied tension at the sheet boundary, as seen in fig. 3.9(b); $\tilde{T}$ is the non-dimensional applied tension; Φ the ratio of filament length L to droplet radius R_{dr}. In the partially wet regime we maintain the limit: $\epsilon^{-1} \gg 1, \Phi \gg 2\pi$. In the second part of the article we explore the other regime of $\epsilon^{-1} \gg 1, \Phi \leq 2\pi$ to understand the wrapping mechanism.

3.10 Experimental set-up

Our experiment consists of a thin elastic filament floating at air-water interface, placed in contact with a floating oil droplet as shown in fig. 3.9(a). One end of the filament is attached to a translation stage and the other end to a beam made out of a soft elastic material (Vinyl polysiloxane). We control the tension in the filament by moving the beam. As described in detail later, though the floating droplet is three-dimensional in shape, it is flattened by gravity and so behaves approximately like a two-dimensional object. We define the contact

angles ϑ and ϕ in the plane of the air-water interface (see fig. 3.9(b)). The effective surface tension of this 2-D droplet is the line tension of the droplet at the air-water interface. In the partially-wrapped state we vary the size of the droplet, diameter of the filament and the applied boundary tension, while in the wrapping experiments, we vary the droplet size for various filament diameters. These three parameters help us explore different high-bendability morphologies of the filament. We image the filament shape and measure the curvature of the filament close to contact-line of the droplet. The procedure used for filament shape extraction from images is the same as described for relaxing filaments in chapter 2, whose details are in appendix. 7.1.1. Near full wrapping, we use fluorescence imaging to accurately capture the shape of the filament. This allows us to calculate the radius of curvature of the filament and that of the droplet as a function of its bendability.

Making filaments

The thin filaments used in our experiments are made out of Polydimethylsiloxane (PDMS) whose Young's modulus is $E = 1\text{MPa}$. We use a mixture of PDMS base (Sylgard 184, Dow Corning), accelerator and cross-linker in the ratio (10:2:1) at room temperature, and as the mixture begins to set, we take a droplet of this mixture and pull it using tweezers to create thin long threads which then set. We make filaments whose diameter d varies between $80\mu\text{m} - 200\mu\text{m}$ and with length, $L = 1000d$. In appendix 7.2 we provide details to make the filament and images of these filaments under microscope.

Measuring tension

The capillary forces originate from surface tensions that are $\sim 10\text{mN/m}$ (source: Data Sheet), and they act on filaments $\sim 100\mu\text{m}$ in diameter, resulting in forces of $\mathcal{O}(\mu N)$ in magnitude; this demands a sensitive force sensor. We clamp a long, soft beam at one end to a translation stage and attach the filament at its other end. This is shown schematically in fig. 3.9(a). The soft beam is made of Vinyl polysiloxane (VPS) and has a diameter of 0.5mm, length of $l = 6\text{cm}$ and Young's modulus of $E_s = 200\text{kPa}$. When the translational stage is displaced the beam bends and we track the tip of the soft beam at the end attached to the filament. The standard small deflection approximation gives the dependence of force on displacement as: $F \approx 3B_s\delta x/l^3$ where B_s is the bending stiffness of soft beam, given by $B_s = E_s\pi t_b^4/4$, t_b - beam diameter, δx - horizontal displacement, l - length of soft-beam as shown in fig. 3.10(a).

However, for the range of tension we are interested in (which we shall see later, traverses more than a decade in non-dimensional tension scale), we require the solution to the full non-linear beam equation. Here, unlike in the small displacement limit, the displacement in the vertical direction of the beam, δy cannot be neglected and for large tensions the displacement in this direction is sensitive to applied tension as shown in fig. 3.10(b). Furthermore, the angle between the end of the filament and the initial configuration changes as a function of tension creating an angle σ (up to a maximum of 30 degrees in experiments). We measure σ, δx, δy for each tension value in the experiments. We then find solutions to the non-linear problem given by:

$$\psi''(s) + \tilde{F}\cos\sigma\sin\psi(s) + \tilde{F}\sin\sigma\cos\psi(s) = 0, \tag{3.56}$$

where ψ is the angle between the tangent to the beam and vertical (see fig.3.10(a)), s the non-dimensional arc-length along beam (non-dimensionalised using l) with $s = 0$ indicating the fixed end and $s = 1$ is the end connected to the elastic filament. $\tilde{F} = Fl^2/B_s$ is the non-dimensional applied force. We solve this system numerically using a shooting method [9] under boundary conditions: $\psi(0) = 0, \psi'(1) = 0$. From the solution for different values of $\tilde{F}$ for a given σ we look for the $\tilde{F}$ that corresponds to the measured $\delta x/l$ and $\delta y/l$, which is the required quantity to compute T_o. This procedure is executed for all displacements and we show in fig. 3.10(a) that the computed shape (green line) matches well with the experimentally observed shape (gray line).

Droplet and scale separation

We use mineral oil of density 0.86 g/mL for the droplets. The oil is dyed with Sudan red G, a hydrophobic, water-insoluble dye. This captures the shape of the droplet precisely as we image it under uniform light. The oil droplet is a three-dimensional object with three length-scales relevant at different regions of the droplet. These are R_{dr} - radius of droplet, d - diameter of filament, l_c - capillary length. The droplet size R_{dr} is the largest of these length-scales, d is relevant close to the region where the droplet is in contact with filament and l_c in the curved region approaching air-water interface. For large droplets, gravity ensures a uniform thickness $\sim l_c$ and if we work with small-d filaments, then we are in a scale separated regime given by: $d \ll l_c \ll R_{dr}$. Furthermore the quantities of interest in our experiments ϑ and ϕ, are all $\mathcal{O}(R_{dr})$ features. We ensure this separation by choosing R_{dr} in the range

$0.5\text{cm} - 2\text{cm}$ with the capillary length of Mineral oil $l_c = 1.8\text{mm}$ and $d = 80\mu\text{m} - 200\mu\text{m}$. In fig. 3.10$(c)$ we plot the droplet surface profile close to filament contact line, and far from it, to show that the shape of the droplet is not strongly perturbed in the thin direction by the presence of the filament and thus the 2-D approximation is valid.* We measure these profiles in our experiments by measuring the fluorescence intensity of a droplet with Nile Red under a uniform light source. These intensities act as proxy for the height of the droplet and we have plotted the scaled value of the intensity (scaled by the maximum value, at the center of the droplet) in fig. 3.10(c).

Visualising filament

In order to visualise the filaments in our wrapping experiments we wet the filament in a solution of Nile Red (HIMEDIA RM9734) in ethanol and allow the ethanol to evaporate. We leave the droplet uncoloured and shine a laser beam (Wicked Laser, 500mW at 500nm) on the filament. The filament fluoresces in the red, and a filter is used to eliminate the green illumination line. Though Nile Red is a hydrophobic dye and diffuses into mineral oil at long timescale, our experiments were performed before the dye diffuses into the droplet.

Highlights of theory

We make comparisons to a theory of a 2-D drop-on-sheet problem, $i.e.$, a drop modelled as a cylinder sitting on top of an inextensible rectangular sheet, in the infinite-bendability limit. This involves minimising the total surface energy of the system, with contributions from liquid-vapour, liquid-solid, and solid-vapour interfaces. The analysis reduces to a purely geometric question with contact angle, ϑ_Y and applied tension, $\tilde{T}$ being the relevant parameters. Given these parameters, the complete shape of the droplet and sheet is predicted, for a fixed

*We do not explore here in detail the question of why the filament chooses to sit at the three phase contact line instead of passing undeviated over or under the drop. Possibly the bending energy lost in curving around the drop is more than compensated by the oil-air and water-air interface protected by the filament.

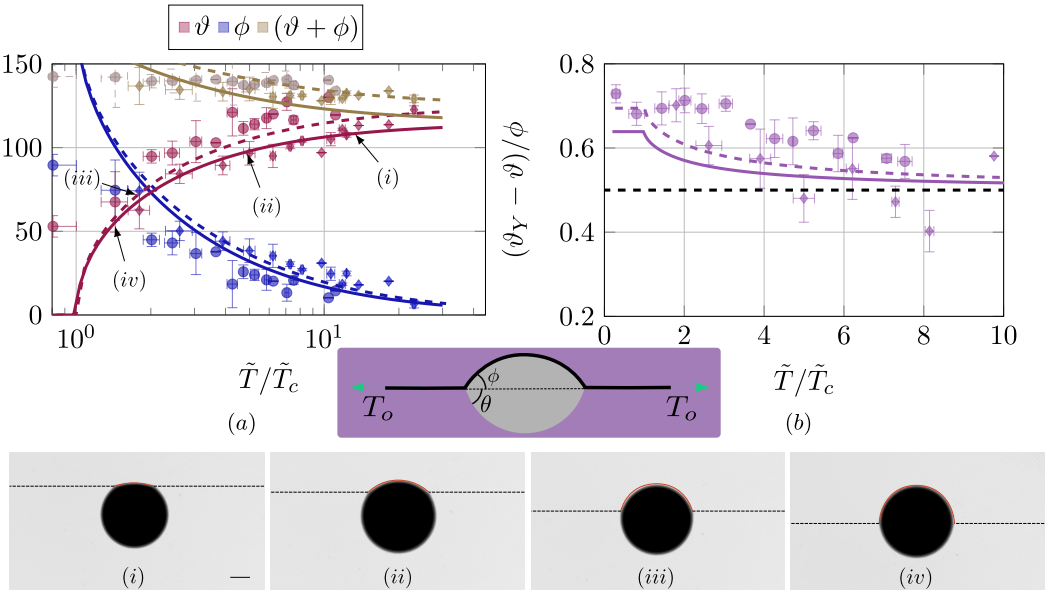

Figure 3.11: (a) Measured values of ϑ and ϕ from experiments for different bendability values of the drop-filament system. For the filament diameter $205\mu\mathrm{m}$, we choose four different droplet sizes: $12.7\mathrm{mm}, 13.8\mathrm{mm}, 18.0\mathrm{mm}, 20.2\mathrm{mm}$ shown using ○. Similar angles ϑ and ϕ measured for a filament of diameter 77μm and three different droplet sizes : $10.6\mathrm{mm}, 14.2\mathrm{mm}, 16.6\mathrm{mm}$ plotted as ◇. We see a clear collapse of all the data indicating a universal behaviour of perceived contact angle in the high-bendability limit, with solid line being eqns. 3.57, 3.58 for $\vartheta_Y = 115°$ and dashed line for $\vartheta_Y = 125°$. The point where ϑ, ϕ intersect is where $\tilde{T} = 2\tilde{T}_c$, which in our experiments give $T_c/d = 2.2\mathrm{mN/m}$, from $\gamma = 7.6\mathrm{mN/m}, \vartheta_Y = 115°$. (b) Computed values of $(\vartheta_Y - \vartheta)/\phi$ in experiments (symbols) compared to the theoretical predictions from eqs. 3.57, 3.58 which approach a value of $1/2$ at large tensions. ○ corresponds to the thicker and ◇ to the thinner of the filaments. $(i) - (iv)$ show the shape of filament-drop system as the tension in the filament is decreased. Scale bar in (i) is $5\mathrm{mm}$.

area of droplet. The expressions for the angles ϑ, ϕ are given by eq. 3.13, 3.14:

$$\cos\vartheta = \frac{(1 + 2\tilde{T}\cos\vartheta_Y - \cos^2\vartheta_Y)}{2\tilde{T}}, \tag{3.57}$$

$$\cos\phi = \frac{(1 - \cos\vartheta_Y/\tilde{T} + (\cos^2\vartheta_Y - 1)/2\tilde{T}^2)}{1 - \cos\vartheta_Y/\tilde{T}}. \tag{3.58}$$

From the expressions above, we see that the angles remain at $\vartheta = 0, \phi = \pi$ for values of tension $\tilde{T}$ smaller than a critical tension, $\tilde{T}_c = \cos^2(\vartheta_Y/2)$. This is precisely the transition from a partially wet state where only a part of the drop boundary is covered by the sheet, to a wrapped state where the droplet boundary is completely encapsulated. Interestingly the tension at which $\vartheta = \phi$ occurs at $\tilde{T} = 2\tilde{T}_c$. We will use the critical tension, $\tilde{T}_c$ to measure the unknown line tension γ in our experiments.

3.11 Results

Contact angle and critical wrapping tension

In fig. 3.11(a) we plot ϑ, ϕ as functions of $\tilde{T}$, scaled by the critical tension for wrapping, $\tilde{T}_c$. We show data for filaments of two different diameters, 77μm and 205μm. The data were taken by varying the tension while holding the drop size fixed. The drop size was then varied in the range $10.6\text{mm} - 20.2\text{mm}$. These two filament diameters and the different droplet sizes helped us span bendability values between $\epsilon^{-1} = 80 - 1920$. The procedure used for extracting the contact angles from the experimental images is explained in detail in appendix. 7.2.4. In order to compute the bendability $\epsilon^{-1} = (R_{dr}/l_{\text{ec}})^2$ of the droplet-filament system, we need the line-tension of the oil droplet. To obtain γ, we note in fig. 3.11(a) that as the magnitude of tension increases there is a crossover in magnitude between ϕ and ϑ. From the infinite bendability theory we expect this cross-over to happen at $\tilde{T}/\tilde{T}_c = 2$ (see eqns. 3.57 & 3.58). In order to match this cross-over point in experiments, γ is the only fitting parameter. The γ-value here is difficult to measure since this is not the usual surface tension of a liquid-vapour interface but is the line-tension of the droplet contact line with the water bath. Traditional measuring techniques such as pendant droplet technique, tensiometers do not provide a measure of this line-tension. We find that all the data collapse with the analytical expression in fig. 3.11(a) for $\gamma = 7.6\text{mN/m}$. To extract ϑ_Y we measure the contact angle for $\tilde{T} \gg \tilde{T}_c$. For this surface tension γ, we find $T_c = 2.2\text{mN/m}$ when $\vartheta_Y = 115^\circ$ for the thicker filament and $T_c =$

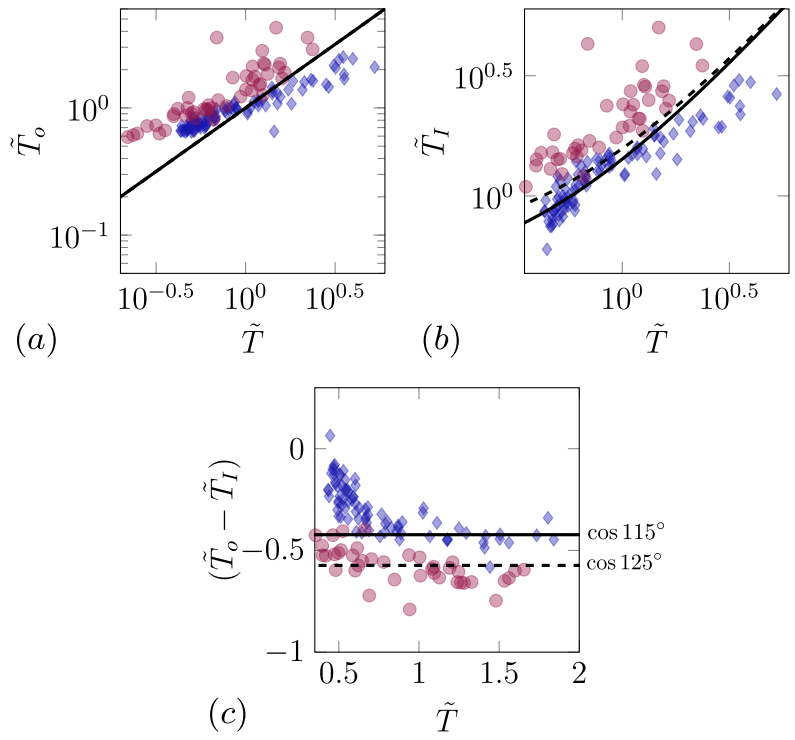

Figure 3.12: (a) Non-dimensional applied tension $\tilde{T}_o$, (b) tension in the portion of the filament wet by the droplet $\tilde{T}_I$, and (c) the difference between these tension values, $(\tilde{T}_o - \tilde{T}_I)$ evaluated by using angles ϑ, ϕ measured from experiments (using eqn. 3.59) as functions of the applied tension, $\tilde{T}$ measured using soft-beam displacement. ○ correspond to filament diameter 205μm and ◇ to diameter 77μm for different droplet sizes. The solid and dashed lines respectively indicate theoretical predictions from eqn. 3.60.

$1.6\mathrm{mN/m}$ when $\vartheta_Y = 125°$ for the thinner one in our experiments.

Now for $\tilde{T} \gg \cos^2(\vartheta_Y/2)$ we can expand the eqs. 3.57, 3.58 to get

$$\phi \approx \frac{2\sin\vartheta_Y}{\tilde{T}},\ \vartheta_Y - \vartheta \approx \frac{\sin\vartheta_Y}{\tilde{T}}. \tag{3.59}$$

From this it is easy to see that for applied tension, $\tilde{T} \gg 1$, the asymptotic value of the function $(\vartheta_Y - \vartheta)/\phi \to 1/2$. Using the measured values of ϑ, ϕ and ϑ_Y in our experiments, we compute $(\vartheta_Y - \vartheta)/\phi$ as shown in fig. 3.11(b). The trend predicted by the analytical expression is captured, though the data are noisier at large tensions due to finite precision in the measurement of ϕ whose magnitude approaches zero.

In the infinite bendability limit, the normalized internal stresses are related to geometric

variables ϑ and ϕ alone through the expressions

$$\tilde{T}_I = \frac{\sin\vartheta}{\sin\phi},\ \tilde{T}_o = \frac{\sin(\vartheta+\phi)}{\sin\phi}. \tag{3.60}$$

These expressions are derived by using the relation that the tension in the buckled zone is given by $T_I/(dR_b) = \gamma/R_d$ where R_b, R_d are the radius of buckled zone of sheet and the radius of the droplet interface. Now the ratio $\tilde{T}_I = T_I/(d\gamma) = R_b/R_d$ can be written in terms of ϑ, ϕ. The expression for $\tilde{T}_o$ on the other hand is derived by minimising the total energy of the system as detailed in the previous section. In fig. 3.12(a) we compare the boundary tension $\tilde{T}_o$ computed from ϑ, ϕ and eqn. 3.60 and the direct measurement of tension using the deflection of the soft beam-$\tilde{T}$. We next compare in fig. 3.12(b) experimental data for $\tilde{T}_I$, the stress in the buckled zone obtained from the measured contact angles, to the analytical expression for $\tilde{T}_I$ for two different $\vartheta_Y = 115°, 125°$ corresponding to the thick and thin filament. The jump in the magnitude of tension at the contact line is proportional to the equilibrium contact-angle ϑ_Y and is given by: $(\tilde{T}_o - \tilde{T}_I) = \cos\vartheta_Y$, which is the equivalent for thin-filaments of the Young-Laplace-Dupré relation. In fig. 3.12(c) we compare the difference $(\tilde{T}_o - \tilde{T}_I)$ as a function of applied tension $\tilde{T}$ and see that it remains constant, close to the value $\cos\vartheta_Y$, predicted by theory. There is a reasonable match between experiments and the above expression 3.60 with the biggest deviations at small tensions.

Close to the contact-line

The angles and tensions measured in the previous section were compared with an infinite-bendability theoretical model. In this section, we explore quantities that reflect more obviously the finite bendability of the filaments. In the infinite-bendability prediction, the filament is buckled into a circle of radius R_b where it is in contact with the droplet, and straight elsewhere with a sharp cusp connecting the straight region and the wetted region. However, finite bendability introduces finite curvature, $1/R_{\text{eb}}$, in this transition zone close to the contact line.

We measure $1/R_{\text{eb}}$ as a function of applied tension, $\tilde{T}$ for three different droplet sizes ($w = 6.2\text{mm}, 7.6\text{mm}, 9.4\text{mm}$) as shown in fig. 3.13$(c)$. To image the filament shape near the droplet, we dye the filament (and not the droplet as in the previous section) with Sudan Red G and illuminate with a uniform white light source. After extracting the filament shape, we do a B-Spline curve fit to the filament shape and calculate the signed curvature as a function of

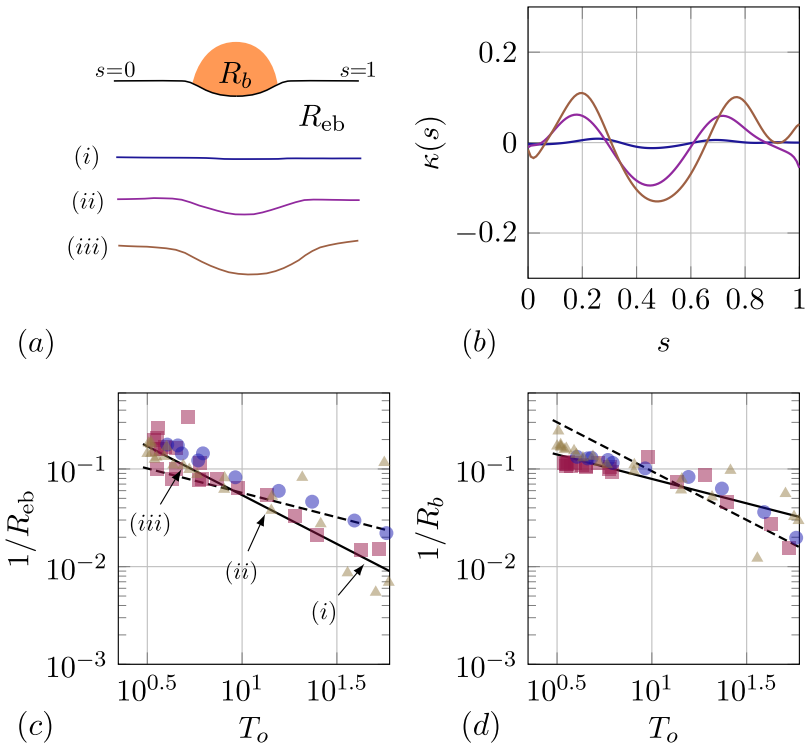

Figure 3.13: (a) Three different filament shapes extracted from experiments as the applied tension T_o is decreased for a fixed droplet size of $R_{dr} = 6.2\text{mm}$ and filament diameter $d = 120\mu$m. (b) Corresponding signed curvature, $\kappa(s)$ of shapes in (a) computed as a function of non-dimensional arc length s (scaled using filament length) after fitting Bezier spline to the extracted shapes. $1/R_{\rm eb}, 1/R_b$ correspond to maximum and minimum of $\kappa(s)$. (c) The curvature of transition-zone close to the contact-line between filament and droplet, $1/R_{\rm eb}$ and (d) the curvature of the droplet wet part of filament, $1/R_b$ as a function of applied boundary tension T_o (in μN) for a filament of fixed diameter $d = 120\mu$m but for three different droplet sizes $R_{dr} = 6.2\text{mm}(\triangle), 7.6\text{mm}(\bigcirc), 9.4\text{mm}(\square)$ and several values of T_o. The corresponding bendability values calculated using these different droplet sizes are $\epsilon^{-1} = 74, 110, 190$. The solid lines in (c, d) correspond to $T_o^{-1}, T_o^{-1/2}$ and the dashed ones are $T_o^{-1/2}, T_o^{-1}$.

filament arc length as shown in fig. 3.13(b). The three shapes in fig. 3.13(a) correspond to three different tensions in decreasing magnitude for a fixed droplet size of $w = 6.2\text{mm}$. We identify the maximum value of curvature $\max(\kappa(s))$ with $1/R_{\rm eb}$ and the minimum value, $\min(\kappa(s))$ with $1/R_b$. We find that both curvatures decrease with increasing outer tension T_o as shown in fig. 3.13(c, d).

The curvature $1/R_b$ of the buckled part of the filament may be estimated in terms of the 2D Laplace pressure of the free surface of the droplet. This naive estimate predicts $1/R_b \sim 1/T_I$,

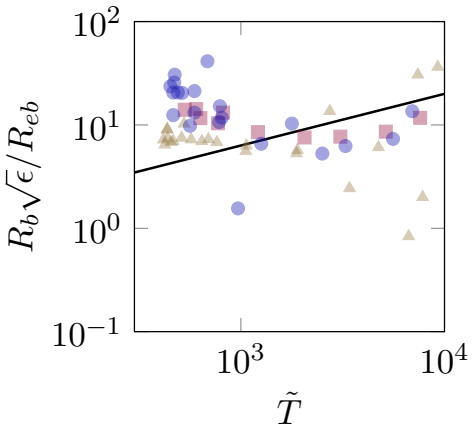

Figure 3.14: $R_b\sqrt{\epsilon}/R_{\text{eb}}$ computed using the data shown in fig. 3.13(c, d), as a function of applied tension with solid line indicating $\tilde{T}^{1/2}$.

however, the data are more consistent with $1/R_b \sim 1/\sqrt{T_I}$ (note that T_I and T_o are proportional to each other). The length-scale R_{eb} close to the contact line can be estimated from balancing bending forces and tension in the filament. In an idealized 2D situation, the tension jumps across the contact line resulting in a change in curvature from $\epsilon^{-1/2}\tilde{T}_I^{-1/2}$ in the region wet by the droplet to $\epsilon^{-1/2}\tilde{T}_o^{-1/2}$ outside. However, the experimental measurement of $1/R_{\text{eb}}$ show curvature decreasing as T_o^{-1}. There are three major differences between the experiment and the model: one is that the filament bendability ranges from 74-190, whereas the model assumes infinite bendability. A second respect in which the experiment is non-ideal is that the meniscus near the contact line is fully 3-dimensional, as shown in fig. 3.10(d). This 3-dimensionality comes about because the droplet close to the contact line sees the effects of the thickness of the filament and the shape of the droplet at this scale depends now on the filament thickness. Moreover our assumptions of scale separation where the observables were of the $\mathcal{O}(R_{dr})$ fails at this scale. Lastly the theoretical estimates also assume fixed area of the droplet while in the experiments a fixed volume of droplet is maintained as the tension is varied. In this process the projected area varies, with only 5% change over the range of tensions in the experiment. We guess that these contribute to the large spread in $R_b\sqrt{\epsilon}/R_{\text{eb}}$ vs T_o/γ shown in fig. 3.14(b), which scales as $\tilde{T}^{1/2}$ as seen in fig. 3.5(d).

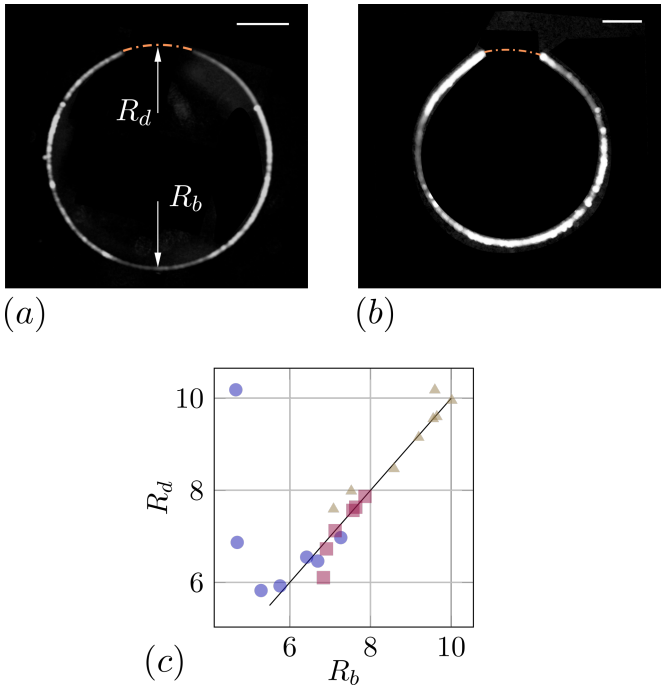

Figure 3.15: (a, b) Fluorescence images showing shape of filament encapsulating the droplet for a filament of diameter $d = 90\mu$m, 170μm and a droplet of size $R_{dr} = 7.5$mm, 2.3mm with droplet-interface shown as dashed-line. The scale bar is 3.7mm. (c) Radius of curvature of the buckled zone in the filament, R_b vs the radius of curvature of free interface of the droplet, R_d in mm. Solid line indicates $R_b = R_d$. We consider three different filament diameters $d = 80\mu$m$(\triangle), 90\mu$m$(\square), 170\mu$m$(\bigcirc)$.

3.II.I Wrapping process

In order to emulate the process of complete wrapping of the droplet, we adopt the following procedure. A freely floating filament is brought into contact with a floating droplet such that $\Phi < 2\pi$ and the droplet size is reduced until the ends of the filament come close to touching. This we do by sucking the oil droplet from the water bath using a syringe and imaging it after each such volume reduction. We extract the shape of the filament from fluorescence images such as in fig. 3.15(a). The experimental details of the fluorescence setup is provided in appendix. 7.2.3. This procedure is followed for three different filament diameters, $d = 80\mu$m, 90μm, 170μm. The parameters R_d and R_b, the radius of curvature of the droplet-water interface and radius of curvature of the buckled zone describe the geometry of the droplet-filament system. In the high-bendability limit, as we shall see, these are enough to describe the system's entire shape.

First, we observe that the thinnest filament has a constant curvature along the length as shown in fig. 3.15(a). This radius of curvature matches that of the droplet interface radius of curvature, R_d plotted in fig. 3.15(c) corresponding to $\triangle$, where the solid line indicates $R_d = R_b$. As the droplet size decreases the buckling radius decreases as does the droplet interface radius. However the thickest filament corresponding to $\bigcirc$ shows a deviation from the straight line hinting that the interface becomes flatter before the ends come in contact. This divergence is a low-bendability effect which does not exist for the thinnest filament as seen in fig. 3.15(b).

Second, in the high bendability limit the shape of the filament is part of a circle which is in contrast with the behaviour of an axisymmetric sheet seen in Paulsen et al. [106] where the solution is not part of a sphere but resembles that of parachute. This difference comes about from geometric constraints of area being preserved in inextensible sheets where it is the length that is preserved in filaments. From the force-balance equation we have:

$$B\left[\ddot{\kappa}(s) + \frac{\kappa^3(s)}{2}\right] - T_o\kappa(s) = -\frac{\gamma}{R_{dr}} \tag{3.61}$$

where $\kappa(s)$ is the curvature along the filament. Now in the high-bendability limit the dominant balance comes from tension in filament and droplet surface tension, γ. However since $T_o \approx \gamma$ this implies $\kappa \approx R_{dr}^{-1}$. The partially wrapped circular droplet now obeys Young-Laplace relation over free interface of the droplet and the elastic Young-Laplace relation over the filament. We see that R_{dr} determines the entire shape of the filament-droplet system, independent of any physical parameters in the system, just as in the unwrapping scenario. The seamless behaviour seen in Kumar et al. [76] must be a consequence of the continuity of curvature at the sheet-droplet boundary, as we observe in the case of filaments. This is in stark contrast with the capillary origami [111], where the wrapped state of the origami presents large openings with pointed ends because $\epsilon^{-1} \sim \mathcal{O}(1)$. The post-contact shapes of the filament where it takes the famous tennis racquet shape is shown in appendix. 7.2.3.

3.12 Conclusion

The two dimensional experimental system developed here to study capillary bending and wrapping illuminates some features of its three dimensional counterpart. The inextensible, infinite-bendability 2D model gives a good description of the geometry of the contact an-

gles in partial wetting. The tension inside the wetted region and the applied tension obey the predicted elastic version of the Young-Laplace-Dupré relation. However, some features of the experimental system, such as the 3D geometry of the drop near the contact line, not high enough values of bendability in some of the experiments affect the comparison with the purely 2D model, infinite bendability. Furthermore, fundamental questions such as the mechanism behind effective surface tension of a floating droplet in contact with a filament need further probing. The 2-D system also provides a venue to further explore different phases in the wetting phase-diagram shown in fig. 3.2, such as the partial wrapping phase and the complete wetting phase.

"The only people who see the whole picture,' he murmured, 'are the ones who step out of the frame"

–Salman Rushdie, The Ground Beneath Her Feet

4

Shapes of a filament confined to a bubble surface

4.1 Introduction

Geometry enters elasticity theory through the deformation that an elastic structure undergoes from a reference configuration in space. In the case of elastic filaments, this is manifested in the form of the curvature vector and its orientation in a given coordinate system, which are required to describe the filament. Another aspect by which geometry comes into play in slender elastic structures is through intrinsic curvature. The filament has a natural curvature to which it relaxes in the absence of an external body force. This natural curvature couples with bending and torsional moments to compete with applied body forces in determining the filament morphology. These two ways by which geometry manifests through intrinsic filament characteristics have already been explored in literature. However a third way by which geometry can affect filament morphology is through the filament's confinement. When the filament is confined to a 2D surface the geometry of the surface modifies the filament's configuration. This forms the motivation of this chapter where we look at the shapes an elastic filament takes when it is confined to a 2D surface.

The surface we choose to explore the filament shapes is that of a sphere as this is the sim-

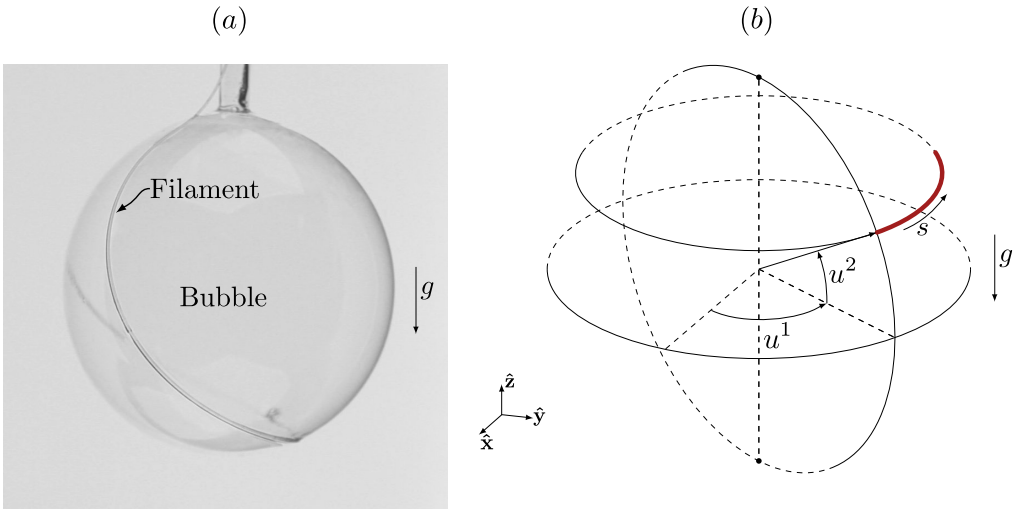

Figure 4.1: (a) Experimental setup with a bubble hanging from the end of a capillary tube of diameter 1mm and filament sitting on the bubble surface with one end hinged to the capillary tube. (b) Coordinate system used in the calculation where $u^{(1)}$ is the azimuthal angle, $u^{(2)}$ is the polar angle and s being the arc-length of the filament.

plest 2D closed surface with positive Gaussian curvature everywhere. This we realise in experiments using a spherical soap bubble as our substrate and a thin elastic filament made out of Silicone polymer. Our experimental system is shown in fig. 4.1(a) where the dark line is the elastic filament sitting on the surface of the bubble. We hold one end of the filament hinged to the north pole of the bubble where tge north-south vector is defined as being parallel to the direction of gravity. Under such a setting we probe the different shapes the filament takes on this spherical surface and the role of the spherical metric in determining the filament's shapes. Before we delve into the details of the length-scales that are important in this experimental system, we describe our experimental setup in detail now.

4.2 Experimental setup

Our experimental setup consists of a pendent soap bubble, hanging at the end of a capillary tube as shown in fig. 4.1(a). The bubble is made out of DAWN soap solution with high concentration of Glycerol (1:4 by volume) to reduce the effects of draining as Glycerol is highly viscous with viscosity of 1000 Cst. This helps the bubble survive longer before bursting. We place a thin elastic filament made out of Silicone on top of the bubble. We wet the filament

by dipping it in the soap solution before placing it on the surface of the bubble as we do not want the effects of filament surface energy to affect the filament behaviour on the surface. One end of the filament is gripped near the end of capillary tube (see fig. 4.1(a)) and the other end is free. We use a micropump to control the volume of air inside the bubble. Micropump supplies a specified flow rate of fluid by pushing the end of a syringe connected to the pump at a constant rate. The photo of the experimental setup, the details of the bubble making procedure and the filament making procedure are provided in appendix. 7.3.1. We explore different shapes the filament takes by reducing slowly the volume of air inside the bubble. We find that our system does not have any hysteresis until the filament is separated and does not come into self-contact. Thus increase in volume of air in bubble also works. We repeat this experiment for different filament lengths and thicknesses (we use thickness and diameter interchangeably in order to refer to the filament diameter). As we shall see, this helps us explore the phase-space of filament morphologies on this spherical bubble. All our experiments are in the quasi-static regime and the dynamics of fluid are slow such that they do not affect the shape of the filament.

Our filaments are made by first melting a bar of Silicone at $300°C$ using a Silicone gun and then lifting a small droplet of the melt using tweezers. This droplet is then pulled quickly such that they form a long filament that sets within few seconds. We check these filaments by observing them under a microscope to check for uniformity in thickness as well as to measure their thickness (see appendix 7.2). After this fabrication procedure, these transparent filaments are coated with Sudan Red G dye (SIGMA 17373), using a procedure already described in chapter 3. Sudan Red dye makes the filament visible in uniform white light as shown in fig. 4.1(a).

4.3 Relevant length-scales

A free standing elastic filament whose intrinsic curvature is infinity chooses a configuration that minimises the bending energy arising out of the available two bending modes in a 3-dimensional space. We neglect the torsional mode here because the twist due to the filament confined to the sphere is small. Though the torsional stiffness of a filament is proportional to d^4 (d - filament thickness), just like bending stiffness, but the angle of twist due to confinement is small and thus we neglect this effect. If the filament is confined to a flat surface, such as a horizontal soap film, with both ends of the filament free, the filament remains straight as

this configuration has a total energy of zero. Now when the filament is confined to a spherical surface, the configuration that minimises bending energy in the given spherical metric can no more be zero as the sphere has positive Gaussian curvature everywhere on its surface and thus the filament needs to have non-zero bending everywhere.

For a spherical bubble, which is the substrate on which the filament lives, made of a fluid of surface tension γ, radius R_b and a filament of length L, Youngs' modulus E, density ϱ, and thickness t, there are six length-scales that are at play in the experiments. These are L, R_b, t, capillary length $l_c \sim \sqrt{\gamma/\varrho g}$, elasto-capillary length $l_{\mathrm{ec}} \sim (B/\gamma)^{1/3}$ and lastly the elasto-gravitational length scale $l_{\mathrm{eg}} \sim (\varrho g \pi t^2/(2EI))^{1/3}$. In this multi-scale problem we want to ensure that the bubble remains spherical $i.e.$, we want the capillary length to be the largest length scale in the system and we want the surface energy of the bubble to not affect filament bending $i.e.$, we want the elasto-capillary length to be very small. This is ensured by operating in a scale-separated regime: $t \ll l_{\mathrm{ec}} \ll (L, R_b, l_{\mathrm{eg}}) \ll l_c$. When the relevant length-scales are $(L, R_b, l_{\mathrm{eg}})$, the filament morphology is governed by geometry, bending force and weight of filament. This scale separation in our experiments is ensured by choosing a thin ($d \sim \mathcal{O}(100\mu\mathrm{m})$), soft filament ($E \sim 1MPa$) with a bubble size much larger than filament diameter ($l, w \sim \mathcal{O}(\mathrm{cm})$) leading to an elasto-capillary length-scale $l_{\mathrm{ec}} \sim \mathcal{O}(\mathrm{mm})$. A non-dimensional number that quantifies the relative importance of gravity and bending $i.e.$, the "*elasto-gravity*" bendability is defined as $\Omega_g = (l_{\mathrm{eg}}/R_b)^3 = \varrho g R_b^3 \pi t^2/(2EI)$. Large Ω_g implies strong effects of gravity and small Ω_g implies strong effects of bending. The ratio of capillary force and bending force can be quantified using capillary inverse bendability, $\Omega = (l_{\mathrm{ec}}/R_b)^3$. The scale separation mentioned above can also be written as $\Omega^{-1} \gg \Omega_g^{-1} \gtrsim 1$. Furthermore the filament remains inextensible and we are in the "*elastica*" limit (described in detail in chapter 1). This, as we have seen in earlier chapters, is ensured by choosing $l_m = \gamma/E \sim \mathcal{O}(\mathrm{nm}) \ll t$.

The radius of the bubble R_b is the only length-scale associated with the 2D spherical surface and the non-dimensional number pertinent to a filament of length l on this surface is $\varphi = (l/R_b)$. We call this non-dimensional number the "*coiling parameter*", as we will see later this number helps describe the state of coiling. The two non-dimensional numbers of interest thus are the coiling parameter φ and the elasto-gravity bendability Ω_g^{-1}. Different morphologies of the elastic filament on the spherical bubble are described in the phase space defined by φ vs Ω_g^{-1}. Changing filament length l and bubble radius w and filament thickness d helps explore different regions of the phase-diagram in experiments. We will see the

numerical values of these variables used in our experiments in the results section.

4.3.1 Energy of the system

In our experiments one end of the filament is hinged to the polar north with respect to the direction of gravity. We first illustrate the coiling instability theoretically when both the filament ends are free on the bubble and will later extend our analysis to the fixed-end scenario by accounting for the work done against gravity to hold the filament in place, as we study in our experiments. This simple calculation provides important insights into the coiling instability which will help us understand further the fixed end scenario.

The total energy of the filament confined to a spherical surface is given by:

$$\mathscr{E} = \frac{EI}{2}\int_0^L \varkappa^2(s)\,\mathrm{d}s + \varrho g\frac{\pi d^2}{4}\int_0^L (\boldsymbol{\mathcal{S}}(s) - \boldsymbol{\mathcal{S}}_o)\cdot\hat{\boldsymbol{z}}\,\mathrm{d}s, \tag{4.1}$$

where $\boldsymbol{\mathcal{S}}(s) \equiv \boldsymbol{\mathcal{S}}(u^{(2)}(s), u^{(1)}(s))$ is the location of the filament on the surface of the sphere with $\boldsymbol{\mathcal{S}}_o$ being a reference location, $\varkappa(s)$ the magnitude of curvature along arc-length s and $\hat{\boldsymbol{z}}$ the direction against gravity (see fig. 4.1(b)). For the specific case of a sphere we can explicitly write the parameterisation as:

$$\boldsymbol{\mathcal{S}}(u^{(2)}, u^{(1)}) = w(\cos u^{(2)}\cos u^{(1)}, \cos u^{(2)}\sin u^{(1)}, \sin u^{(2)}).$$

The curvature vector $\boldsymbol{\varkappa}$ can be decomposed in the orthogonal Darboux frame as:

$$\boldsymbol{\varkappa} = \varkappa_n\hat{\boldsymbol{N}} + \varkappa_g(\hat{\boldsymbol{N}}\times\hat{\boldsymbol{d}}_3), \tag{4.2}$$

$\varkappa_n$ being the normal curvature along the surface normal given by

$$\hat{\boldsymbol{N}} = \frac{\boldsymbol{\mathcal{S}}_{u^{(1)}}\times\boldsymbol{\mathcal{S}}_{u^{(2)}}}{||\boldsymbol{\mathcal{S}}_{u^{(1)}}\times\boldsymbol{\mathcal{S}}_{u^{(2)}}||}.$$

where $\boldsymbol{\mathcal{S}}_{u^{(j)}}$ denotes derivative with respect to u^j and $\varkappa_g$ is the geodesic curvature along the binormal direction $(\hat{\boldsymbol{N}}\times\hat{\boldsymbol{d}}_3)$, with $\hat{\boldsymbol{d}}_3$ being the tangent vector along the curve $\boldsymbol{\mathcal{S}}(s)$. The arc-length, curvature and total energy can be written in non-dimensional form with bubble radius w as length scale: $\hat{s} = s/w$, $\hat{\varkappa} = \varkappa w$ and $\hat{\mathscr{E}} = \mathscr{E}/(EI/2w)$. We get an expression for

the non-dimensional form of the energy as:

$$\hat{\mathscr{E}} = \int_0^{\varphi} [(\hat{\varkappa}_g^2 + \hat{\varkappa}_n^2) + \Omega_g(\hat{\boldsymbol{\mathcal{S}}}(s) - \hat{\boldsymbol{\mathcal{S}}}_o) \cdot \hat{\boldsymbol{z}}] \, \mathrm{d}\hat{s}. \tag{4.3}$$

For a sphere we know that the normal curvature is a constant, $\varkappa_n = (1/w)$ everywhere and using this we can rewrite the energy expression as:

$$\hat{\mathscr{E}} = \int_0^{\varphi} [\hat{\varkappa}_g^2 + \Omega_g(\hat{\boldsymbol{\mathcal{S}}}(s) - \hat{\boldsymbol{\mathcal{S}}}_o) \cdot \hat{\boldsymbol{z}}] \, \mathrm{d}\hat{s} + \varphi. \tag{4.4}$$

4.4 Filament with free ends

When the ends of the filament are free, it is free to live anywhere on the sphere and it chooses a shape that minimises the energy described above. We start by looking at the shape of the filament when the effects of gravity are negligible and then move on to account for the effects of gravity.

4.4.1 Limit of zero gravity, $\Omega_g \to 0$

In the asymptotic limit of negligible gravity effects, *i.e.*, when $\Omega_g^{-1} \to \infty$, filament morphology is determined only by the bending energy and the contribution from potential energy becomes negligible. The solution amounts to minimising bending energy alone, given by:

$$\hat{\mathscr{E}} = \int_0^{\varphi} \hat{\varkappa}_g^2 \, \mathrm{d}\hat{s} + \varphi. \tag{4.5}$$

The constant φ remains fixed for a given filament length, l and bubble radius, w. ϕ is a positive quantity and we can easily see that $\hat{\varkappa}_g = 0$ is the state that minimises this energy. Moreover $\hat{\varkappa}_g = 0$ is the definition of a curve being a geodesic, and thus in the weak gravity limit the filament follows trajectories which are geodesics. This is a great circle, which is the geodesic on a sphere, for $\varphi \leq 2\pi$. Beyond this length of filament, i.e., $\varphi > 2\pi$ we expect the solution to deviate from a geodesic as filament would self-intersect if we increase the filament length. We can now define that the critical length for coiling using the coiling parameter as the critical filament length at which self-intersection occurs and filament starts coiling beyond this critical value. We use the variable φ_c to define the threshold for coiling, which for $\Omega_g^{-1} \to \infty$ we

see is $\varphi_c = 2\pi$. We do not take into account any capillary interaction energy of the filament with itself.

4.4.2 Finite gravito-bendability effects

One approach to understand the morphology of a filament when the gravity starts playing a role is to solve the Kirchoff equations for filaments represented in the Darboux frame. We however observe in experiments that the filament takes the shape of a longitude for a given length to bubble radius beyond which it starts coiling at a given polar angle, approximated by latitude, which is not a geodesic. Motivated by these experiments (detailed later), we model the filament shape based on two configurations: a longitude (which is a geodesic), a latitude, and calculate the critical coiling parameter, φ for transition from one to the other as a function of Ω_g.

Latitude

The parameterisation of filament shape lying along any latitude with polar angle ξ is given by:

$$u^{(2)} = \xi, u^{(1)} = \hat{s}/\lambda, \hat{\boldsymbol{\mathcal{S}}} = (\cos\xi\ \cos(\hat{s}/\lambda), \cos\xi\ \sin(\hat{s}/\lambda), \sin\xi). \tag{4.6}$$

Conservation of length, which is nothing but the inextensibility constraint, is enforced by setting $\lambda = \pm\cos\xi$. The potential energy of this configuration can be calculated as:

$$\hat{\mathcal{E}}_g^p = \int_0^{\varphi} \Omega_g(\mathbf{x} - \mathbf{x}_o) \cdot \hat{\boldsymbol{z}}\, \mathrm{d}\hat{s} \tag{4.7}$$

$$= \Omega_g \int_0^{\varphi} (\sin\xi + z_o)\mathrm{d}\hat{s} = \Omega_g(\sin\xi + z_o)\varphi \tag{4.8}$$

We can write the geodesic curvature of any latitude using the Christoffel symbol for a spherical metric as:

$$\hat{\varkappa}_g = \sqrt{g}\frac{\Gamma^2_{11}}{\cos^3\xi}, \tag{4.9}$$

$$\Gamma^2_{11} = -\frac{g_{22}}{2}\frac{\partial g_{11}}{\partial u^{(2)}} = \sin(2\xi), \tag{4.10}$$

$$\sqrt{g} = \cos\xi, \tag{4.11}$$

$$\hat{\varkappa}_g = \tan\xi. \tag{4.12}$$

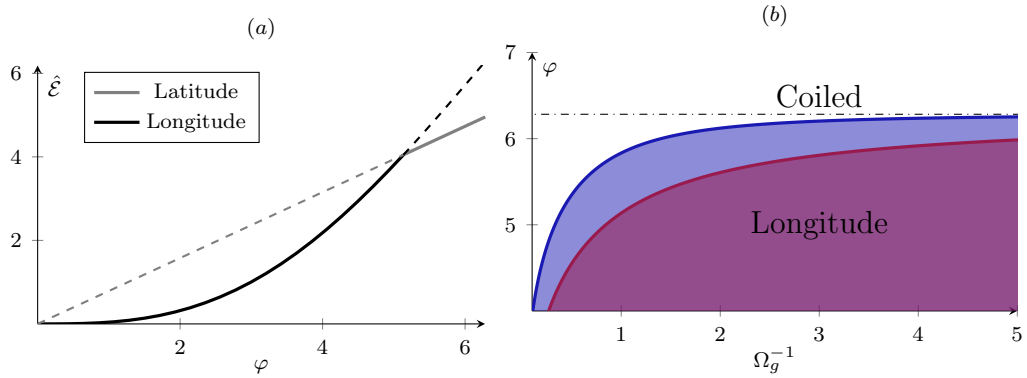

Figure 4.2: (a)Total energy of a filament as a function of its non-dimensional length, φ when it lies on a longitude and a latitude for $\Omega_g = 1$. Filaments choose the minimum of these and we see the mode switching at $\varphi_c = 5.13$. (b)Phase boundary defined based on intersection of energy $\hat{\mathscr{E}}_l, \hat{\mathscr{E}}_g$. The filament switches modes beyond φ_c indicated here as green solid line, based on minimum of either energies.

We see that apart from Γ^2_{11} all other components vanish for a spherical metric and $\sqrt{g}$ here is the square root of determinant of metric tensor. The complete energy of the latitude configuration becomes

$$\begin{aligned}\hat{\mathscr{E}}_g[\varphi;\Omega_g] &= \Omega_g\varphi(\sin\xi + z_o) + \int_0^{\varphi} \hat{\varkappa}_g^2 \,\mathrm{d}\hat{s} + \varphi,\\ &= \varphi(\Omega_g(\sin\xi + z_o) + 1 + \tan^2(\xi)), \qquad (4.13)\\ \frac{\delta\hat{\mathscr{E}}_g}{\delta\xi} &= \Omega_g\cos\xi + 2\tan\xi\sec^2\xi = 0. \qquad (4.14)\end{aligned}$$

Thus we have an φ-independent but Ω_g-dependent solution that minimises the energy for any latitude given by the solution to the following non-linear equation:

$$\implies \Omega_g\cos^4\xi = -2\sin\xi. \qquad (4.15)$$

Longitude

Along a longitude the potential energy of any filament configuration depends on where the starting point of the filament $\hat{s} = 0$ lies. We can denote an arbitrary longitude by the parameterisation: $u^{(2)} = \hat{s} - \vartheta, u^{(1)} = 0$. This gives rise to the potential energy of the configuration as: $\hat{\mathscr{E}}_l^p = \Omega_g[\cos\vartheta - \cos(\vartheta - \varphi) + z_o\varphi]$. Since all longitudes are geodesics, $\varkappa_g = 0$ along these

curves, leading to the total energy as:

$$\hat{\mathscr{E}}_l[\varphi;\Omega_g] = \Omega_g[\cos\vartheta - \cos(\vartheta-\varphi)] + \varphi(1+\Omega_g z_o), \tag{4.16}$$

We can minimise the energy by calculating variation with ϑ to give:

$$\frac{\delta\hat{\mathscr{E}}_l}{\delta\vartheta} = \Omega_g[-\sin\vartheta - \sin(\vartheta-\varphi)] = 0. \tag{4.17}$$

The ground state is thus given by:

$$\implies \vartheta_{\min} = \frac{[(2n+1)\pi+\varphi]}{2}. \tag{4.18}$$

The solution that indicates that the filament takes longitudes placed symmetrically around the south pole of the sphere.

4.4.3 Mode switching and coiling

As we have described earlier, the filament has two possible modes before coiling occurs. One where it occupies a longitude or any of the latitude. However in order to see which of these is selected, one has to look at the energy of these configurations. The filament shape is determined by whichever of latitude or longitude energy is minimum for a given coiling parameter and elasto-gravity bendability. In order to calculate the minimum energy, we look at eq. 4.13, 4.16 and as an example plot it for $\Omega_g = 1$ as a function of non-dimensional filament length or the coiling parameter φ in fig. 4.2(a). The minimum energy stays along the longitude trajectory as the energy of the solid black line is lower than the dashed gray line upto a critical value of $\varphi \leq 5.13$. Beyond this critical value of coiling parameter the solution branch shifts to that of a latitude, indicated by solid gray line, as the energy of the longitude exceed that of the latitude of the same length.

The purple solid curve in fig. 4.2(a) is where the filament moves from longitude to latitude, calculated as a function of φ for different values of Ω_g. The critical coiling parameter is reached, as we have defined earlier, only when the filament wraps a given latitude completely and comes in self-contact. This is indicated by the blue curve in fig. 4.2(b), which is calculated by using the relation $\varphi_c = 2\pi\cos(\xi_c)$, where ξ_c is the polar angle of the latitude configuration. It is interesting to find that the filament does not change its latitude location

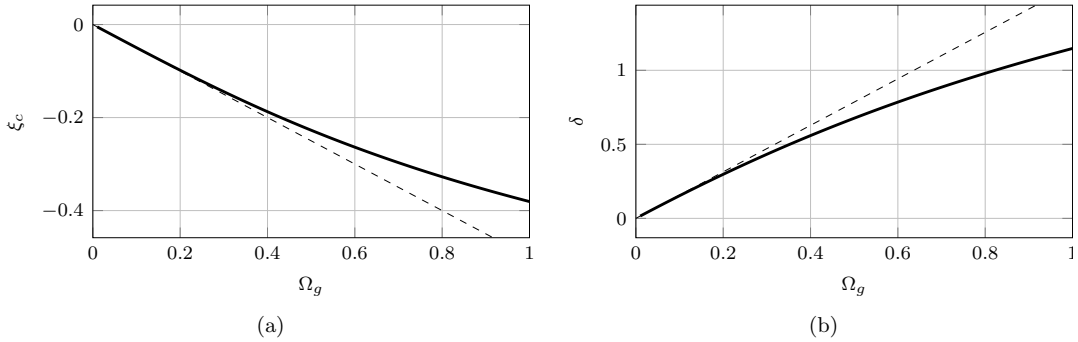

Figure 4.3: (a) Critical polar angle, ξ_c, (b) deviation of critical length from 2π, δ as a function of Ω_g which follow the asymptotic scaling derived above plotted here as dashed line..

after undergoing bifurcation from a longitudinal configuration (as ξ_c is independent of φ, seen in eq. 4.15). Further we see that as gravity becomes stronger or increase in Ω_g we see that the polar angle to which filament migrates moves towards south pole. This comes from a compromise between bending energy and potential energy, where filament chooses to bend more to reduce the potential energy with increase in Ω_g.

4.4.4 Asymptotic behaviour

We see from fig. 4.2(b) that the critical φ at which bifurcation from a longitude configuration to a latitude approaches $\varphi \to 2\pi$ as $\Omega_g \to 0$. This latitude is described by the polar angle and as $\varphi \to 2\pi$, the polar angle $\xi_c \to 0$. Thus we have two small parameters ξ_c and Ω_g and we evaluate their relationship by expanding the solution close to $\varphi \to 2\pi$ as $\Omega_g \to 0$. From the minimised solution we know that the latitude's polar angle satisfies:

$$\Omega_g \cos^4 \xi_c = -2 \sin \xi_c.$$

Expanding the above expression, we get the leading order behaviour:

$$\xi_c \sim -\frac{\Omega_g}{2}.$$

In order to find the relationship between the critical φ at which bifurcation happens in this asymptotic limit of $\Omega_g \to 0$, we expand the full energy expression for a latitude in eq. 4.13 as:

$$\hat{\mathscr{E}}_g = \varphi(\Omega_g(\sin\xi_c + z_o) + 1 + \tan^2(\xi_c)), \tag{4.19}$$

$$= \varphi(1 + \xi_c^2 + \Omega_g\xi_c) + \mathcal{O}(\xi_c^3), \tag{4.20}$$

$$\approx \varphi\left(1 - \frac{\Omega_g^2}{4}\right). \tag{4.21}$$

A similar expansion for the energy of a longitude can be performed to get

$$\hat{\mathscr{E}}_l = \varphi - 2\Omega_g \sin\frac{\varphi}{2}. \tag{4.22}$$

Since we are interested in the region close to $\varphi \to 2\pi$, we have the small parameter, $\delta = (2\pi - \varphi)$. The longitude energy can be written in terms of δ as:

$$\hat{\mathscr{E}}_l \approx 2\pi - \delta - \Omega_g\delta + \mathcal{O}(\delta^3) \tag{4.23}$$

The critical φ at which bifurcation happens is when $\hat{\mathscr{E}}_g = \hat{\mathscr{E}}_l$, and this can be evaluated by:

$$\frac{\Omega_g^2\delta}{4} - \frac{\pi\Omega_g^2}{2} = -\Omega_g\delta, \tag{4.24}$$

$$\delta \approx \frac{2\pi\Omega_g}{\Omega_g + 4} = \frac{\pi\Omega_g}{2} + \mathcal{O}(\Omega_g^2). \tag{4.25}$$

We plot in fig. 4.3(a, b) the asymptotic expressions derived above for ξ_c and δ in dashed lines and compare it with the full solution.

4.5 Effect of end-pinning

So far we have dealt with the case of filament ends being free, which lets the filament choose either of the geodesic or latitude configuration. In this subsection we deal with one end of the filament fixed, as in our experiments. Before we delve into the calculation, which is strongly motivated by what we observe in experiments, we describe the experimental results for the scenario with one end of filament hinged. As has been described, we explore the phase-space φ vs Ω_g^{-1} by changing length of filament L, R_b as well as thickness t of the filament. In our experiments, for a fixed length of filament hinged at north pole, we reduce the bubble radius

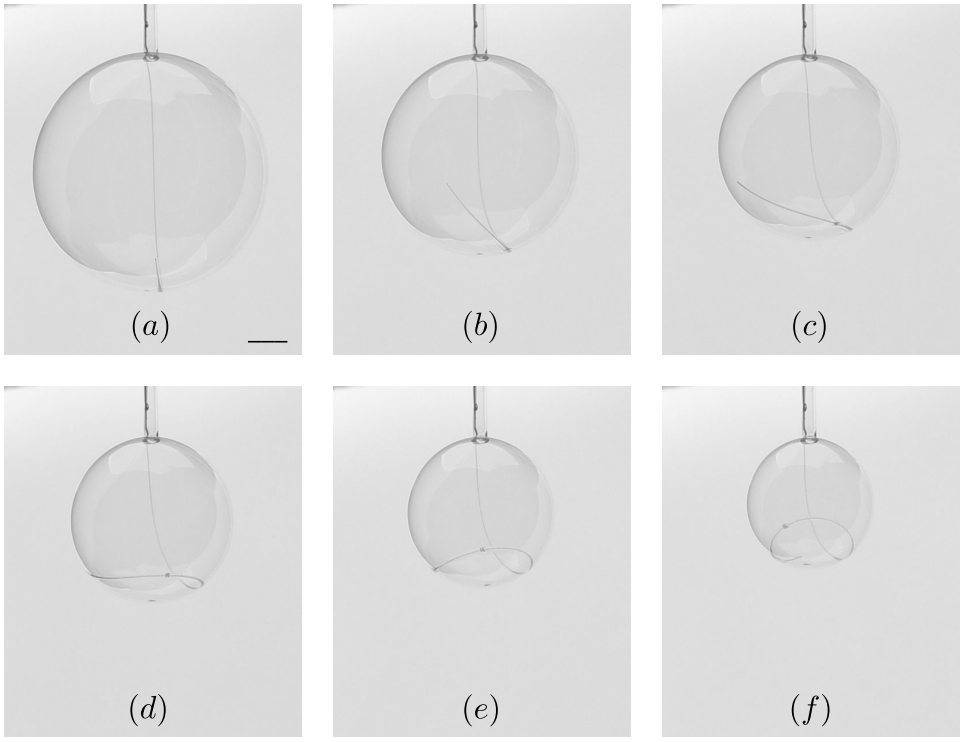

Figure 4.4: Sequence of images from experiments where we decrease the bubble size from $(a - f)$ for a fixed filament length. We see that the filament stays in the longitude shape and deviates form a longitude shape to a different shape at (b). As we further decrease the bubble size, the filament comes into self-contact in (f), which is the beginning of coiling. Scale bar is $3\mathrm{mm}$.

R_b and thus in the phase-space we travel along trajectories $1/R_b$ vs $1/R_b^3$. In fig. 4.5(a) we show this trajectory taken for each experiment using dashed line. Different trajectories correspond to different lengths of filaments. Along one trajectory, the purple dots correspond to filament configuration along a geodesic and blue dots correspond to deviation from it. We will describe the deviation in detail later in this section. We show the shape of the filament on the bubble for one such trajectory in fig. 4.4, where see in fig. 4.4 $(a-c)$ live along the longitude, shown as pink dots in fig. 4.5(a) and at (d) we see a deviation form this geodesic shape, which is the beginning of blue dots in fig. 4.5(a). We perform experiments with 11 different filament lengths and two different filament thicknesses $t = 70\mu\text{m}, 100\mu\text{m}$. As has been mentioned already, changing bending stiffness ($B \sim t^4$) and thus changing bubble size and filament thickness helps span different values of Ω_g.

The transition from pink dots to blue dots in fig. 4.5(a) is similar to the transition from a longitude state to a latitude state in the free ends case. We plot in fig. 4.5(a) the same curve in solid green on top of data points to see the match between prediction with free ends and experiments with fixed ends. We clearly see that there is mismatch in prediction of the transition φ value in both small and large Ω_g^{-1} case. This emphasises the role of boundary condition in predicting the bifurcation point. We develop a simplified geometric model with one end fixed to understand the mechanism of bifurcation observed in experiments.

4.5.1 Geometric model

The fixed end case differs from the previous calculation in that there is work done against gravity to hold it in place. In this section using our experience so far in writing energies for the longitude and latitude, we make the Maxwell construction of "phase-coexistence". We see in fig. 4.4(d) the the configuration just after bifurcation can be approximated by a combination of a part latitude and a part longitude. A fraction α of the non-dimensional length φ lies along a longitude and remaining fraction $(1-\alpha)\varphi$ lives along a latitude. We write the energy of such a state as:

$$\hat{\mathscr{E}} = \hat{\mathscr{E}}_l[\alpha\varphi] + \hat{\mathscr{E}}_g[(1-\alpha)\varphi], \tag{4.26}$$

$$\begin{aligned} &= \alpha\varphi(1+\Omega_g z_o) + \Omega_g\big\{\cos\vartheta - \cos(\vartheta-\alpha\varphi)\big\} \\ &\quad + (1-\alpha)\varphi\big\{(1+\Omega_g z_o) + \Omega_g(\sin\xi + z_o) + 1 + \tan^2(\xi)\big\}. \end{aligned} \tag{4.27}$$

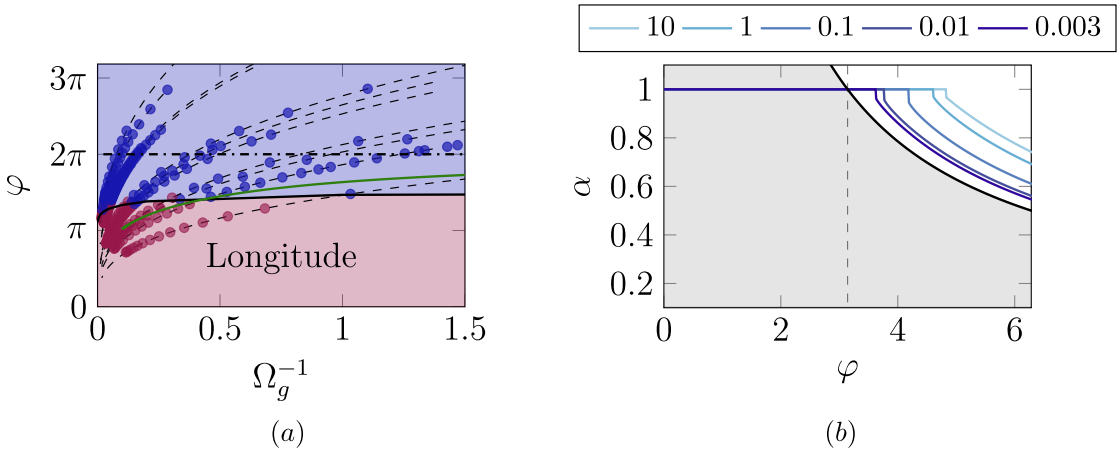

Figure 4.5: (a) Critical length φ_g for transition from a longitudinal state to a super-posed longitude-latitude state as a function of Ω_g^{-1} where circles correspond to data from experiments and the solid lines from calculation detailed in the text. (b) Bifurcation curve capturing the transition from a longitude state to a hybrid state. The vertical axis is the fraction of filament along longitude in the hybrid phase, α as a function of φ for five different Ω_g^{-1} values shown by different colours. $\alpha = 1$ corresponds to the filament being along a longitude state and deviation from 1 indicates the transition to a hybrid state. Thick black line corresponds to $\alpha\varphi = \pi$ showing that $\alpha \sim \varphi^{-1}$ for φ greater than the critical transition value.

Moreover we have the geometric constraint from conservation of length: $\alpha\varphi = (\pi/2 - \xi)$ and since the filament is hinged to the north pole, this implies $\vartheta = -\pi/2$. The resultant energy can be written after simplification as:

$$\hat{\mathscr{E}} = \alpha\varphi + \Omega_g \sin(\alpha\varphi) + (1-\alpha)\varphi\{\csc^2(\alpha\varphi) + \Omega_g \cos(\alpha\varphi)\} \tag{4.28}$$

The energy $\hat{\mathscr{E}}$ is however divergent when $\Omega_g^{-1} \to +\infty, \alpha\varphi \to \pi$, this is because the curvature along the latitude diverges as the square of curvature of the latitude portion whereas the fraction of length along latitude $(1-\alpha) \to 0$ only linearly. In order to avoid this divergence, we need a regularisation length scale coming from the sub-leading order physics. The regularisation in experiments come from the smaller length scales which have been neglected in the energy minimised here, such as l_{EC}. In order to emulate the physics from this length scales, we multiply the singular contribution by a function $\Lambda(\beta)$ that suppresses the

singularity. The energy then becomes:

$$\hat{\mathscr{E}} = \alpha\varphi + \Omega_g \sin(\alpha\varphi) + \Omega_g\varphi(1-\alpha)\cos(\alpha\varphi) + \epsilon \\ + (1-\alpha)\varphi\big\{(1-\Lambda(\alpha\varphi)-\Lambda(\alpha\varphi-\pi)-\Lambda(\alpha\varphi-2\pi))\csc^2(\alpha\varphi)\big\}, \tag{4.29}$$

$$\text{where } \Lambda(\beta) = \exp\left(-\frac{\beta^2}{\eta(\Omega)}\right).$$

Here $\eta(\Omega)$ is the cut-off non-dimensional length-scale associated with the capillary bendability, as this is the length scale that prevents the divergence in the experiments. When the radius of curvature along a latitude approaches the length-scale associated with capillary bendability, this energy expression is no more valid. We have added these regularising terms at three locations $\alpha\varphi = 0, \pi, 2\pi$ as all these locations lead to divergences in the energy. We also add an additional energy of constant magnitude ϵ, which is the energy contribution from the transition zone between the longitude and latitude that has not been accounted for exactly. In the next subsection we find how this transition zone energy scales with the non-dimensional numbers in the system.

The equilibrium configuration is given by extremising the one parameter energy expression in eq. 4.5.1, achieved by setting $\delta\hat{\mathscr{E}}/\delta\alpha = 0$. We also have the condition that $\alpha \in [0, 1]$. The transition we see in fig. 4.4 from a longitude to a "hybrid state" can be seen in the bifurcation diagram represented by the value of α as a function of φ for a fixed value of Ω_g. We plot this bifurcation diagram for different values of Ω_g in fig. 4.5(b). Firstly, considering a fixed value of Ω_g we see that the $\alpha = 1$ for different values of φ and there is a critical coiling parameter at which we see it deviate from this value. This point is nothing but the deviation from a longitude and as we keep increase the coiling parameter or the length for a fixed bubble size, we see this value decrease further, as $\alpha \sim \varphi^{-1}$ beyond bifurcation. This we see by plotting $\alpha\varphi = \pi$ as the solid black line in fig. 4.5(b). From the solid black curve in fig. 4.5(b) as well as the black curve in fig. 4.5(a), we see that the filament bifurcates from longitude state only after crossing the south pole. Which is why all the α values are above $\alpha = \varphi/\pi$. An important aspect of this bifurcation diagram is that the filament undergoes a first-order transition where there is a jump in the value of α at the critical coiling parameter at transition. This critical point for transition is calculated for different values of Ω_g^{-1} and plotted in fig. 4.5(a) as solid black line. We see that the fixed calculation approximated by our simple geometrical theory captures the transition accurately, both at small values of Ω_g^{-1} as well as $\Omega_g^{-1} \sim \mathcal{O}(1)$.

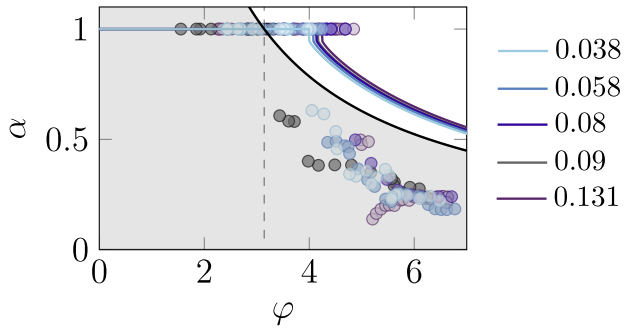

Figure 4.6: Comparison of different bifurcation curves measured in experiments and theory. Color of data points from experiments correspond to a fixed value of Ω_g^{-1} and the solid lines from theory for the same value of Ω_g^{-1}. Thick black line corresponds to $\alpha\varphi = \pi$ and the gray region shows that the length of filament along longitude is less than ϕ i.e., the longitude section does not cross the south pole in experiments while the theory predicts that it does cross south pole. Value of Ω_g^{-1} for each colour is shown on the right.

4.5.2 Comparing magnitude of α in experiments and theory

So far we have seen that our model captures accurately the criterion for transition from a longitudinal state to a hydrid state. The α value calculated from the theory now needs to be measured experimentally, however in all the data shown so far in fig. 4.5(a), the trajectory along φ vs Ω_g^{-1} clearly varies along both the axis, along $1/w$ vs $1/w^3$, as already mentioned. If we want to compare with the theoretical predictions of α, we need to keep Ω_g^{-1} fixed in a given experiment. This we do by holding the bubble size fixed and increasing the filament length on the surface. We do this for five different values of Ω_g^{-1} between $0.04 - 0.1$ and plot it in fig. 4.6(a). Firstly we see that the magnitude of α from experiments is lower than the magnitude found in the theory. Secondly we see that all the experimental values of α are below the $\alpha\varphi = \pi$ line while the theory predictions are above this line. Further in the calculation, though we see that the transition is happening for $\varphi > \pi$ $i.e.$ the filament crosses the south pole for all values of Ω_g^{-1} before undergoing transition, immediately after transition we see that the portion which is part of longitude is less than $\alpha\varphi < \pi$. This is not captured by the theory. In the theory, after the point where the filament deviates from the longitude part, the length of the filament along the longitude remains fixed and any further increase is added to the latitude. The reason for this has to do with the missing length-scale at the transition zone, as mentioned already. Account for this missing length scale would reduce the length of filament on the longitude and thus bringing the magnitude of α lower. We now estimate the energy contribution from this portion, which is as yet not accounted for in the theory, apart

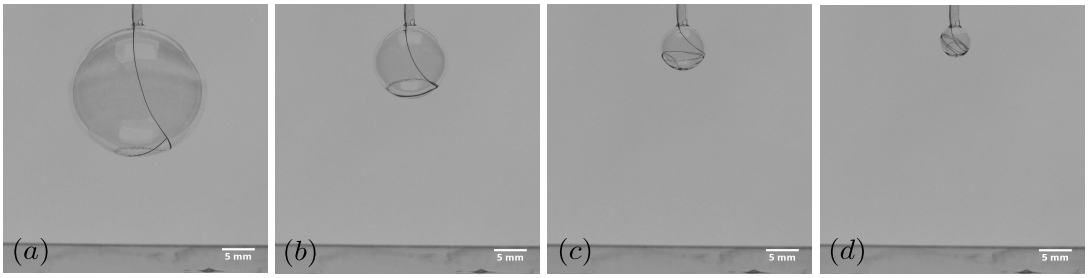

Figure 4.7: $(a - d)$ Sequence of images post-self contact, in the coiling phase, where we see the filament packing the surface of the bubble. Scale bar is $5\mathrm{mm}$.

from the constant ϵ.

4.5.3 Bending energy in transition zone

Estimating the contribution from the transition zone is useful since the contribution to the total energy of the filament comes from bending and potential energy along the filament latitude and longitude parts as well as the energy of the transition zone and see if accounting this energy would correctly capture the value of α. We can write the scaling of individual components of the energy $i.e.$ due to bending to be $\mathscr{E}_l \sim Bl/w^2$, gravitation to be $\mathscr{E}_g \sim \varrho g d^2 l^2$ and bending in the transition zone to be $\mathscr{E}_t \sim Bl_{\mathrm{eg}}(1/w^2 + 1/l_{\mathrm{eg}}^2)$. The same scaling can be written in non-dimensional terms in by scaling these energies with B/w as the energy scale to get:

$$\hat{\mathscr{E}}_l \sim \varphi,\ \hat{\mathscr{E}}_g \sim \Omega_g \varphi^2,\ \hat{\mathscr{E}}_t \sim (\Omega_g^{1/3} + \Omega_g^{-1/3}).$$

Though it might seem at first glance that the transition zone energy $\hat{\mathscr{E}}_t$ has singular contribution since it diverges in both limits of $\Omega_g^{-1} \to 0, \infty$, this is however not the case as the transition zone exists only when $\Omega_g, \Omega_g^{-1} \sim \mathcal{O}(1)$. It is also evident from the scaling above that the critical length for transition $\varphi \sim \Omega_g^{-1}$, which we have observed already in the perturbation expansion in the previous section with free ends. Though we have found out the scaling of $\hat{\mathscr{E}}_t$ with respect to Ω_g, this needs to be included in the calculation to see if the updated prediction captures the right α.

4.6 Coiling phase

We have studied the criterion for bifurcation from a longitudinal state to a hybrid state in the previous sections. And as we keep increasing the length of the filament, the filament comes into self-contact, which we define as the point of coiling. The theory developed so far fails after the filament comes in self-contact and we enter a different regime which we call the coiling phase where the filament start packing the surface of the bubble. The packing fraction is a purely geometric quantity given just by the length and thickness of the filament and bubble size. However the details of packing are different based on the magnitude of Ω_g^{-1} of the filament-bubble system. The mechanism of coiling in this phase remains to be explored both in theory and experiments. We however show the shape of coils we observe in fig. 4.7. Our theoretical model will consist now of a part of a filament along the longitude and the rest of the filament in a coiled state, approximated by a thick filament whose thickness is determined by the volume of filament in the non-geodesic part. The minimisation procedure, just as in the previous section, would involve identifying the polar angle where the filament finally rests.

4.7 Confinement vs Bendability

In chapter 1, we discussed the paradigm of confinement vs bendability and how it provides a framework to look at shape instabilities in elastic structures. We can place the coiling instability we have presented in this chapter again in this framework. Confinement in the coiling phase-diagram is represented by nothing but the coiling parameter. When the filament with a fixed filament length is confined to the bubble, the confinement of the filament increases with decrease in bubble size. The other axis we have in the coiling phase-diagram is nothing but the elasto-gravity bendability. As we traverse across the confinement axis, for a fixed bendability the filament undergoes instability as the paradigm predicts. In chapter 3 we saw that the confinement came about due to applied boundary tension and droplet surface tension whereas in the coiling case it comes about only due to substrate and filament geometry. Though confinement seems at first sight to manifest itself as a parameter in the wrapping phase-diagram and the coiling phase-diagram, it happens to be the obvious external control variable. By obvious control variable we mean that, for a fixed material of droplet or size of bubble which in turn fixes the bendability, the obvious external parameter to explore the phase-space is the tension or the filament length. Thus in all the instabilities studied so far we

see that confinement vs bendability provides a comfortable framework that provides an unifying picture, though the details of the mechanism of instabilities between different phases can be different.

4.8 Conclusion

In this chapter we showed that the substrate geometry can play a vital role in triggering instabilities in elastic filaments. Our experiments consisted of a spherical bubble with an elastic filament confined to the bubble's surface and with one end of the filament hinged on the north pole of the bubble. For a fixed bubble size, a short filament takes the shape of a geodesic, which is a longitude on a sphere. As we increase the length of the filament on the surface of the bubble, the filament makes a transition from a longitude to a shape approximated by a part longitude and a part latitude. We develop a simple geometric model that captures the critical length of transition from the longitude state to the hybrid state. The theoretical predictions of the fraction of filament along the longitude in the hybrid state over-predicts the observed values from experiments and this we reason is due to a missing energy cost in the theory, which arises from the curvature in the zone of transition from longitude to latitude. We place the coiling phase-diagram in the framework of confinement vs bendability that provides a universal method to understand pattern formation in elastic structures, leaving aside the details of instability mechanisms between different phases.

We have considered here the substrate to be a spherical bubble which has constant positive gaussian curvature everywhere. A future direction that we are currently pursuing is to consider a surface with constant negative curvature everywhere. We consider a catenoid shaped soap film between two circular rings held with axis parallel to gravity. Catenoid is a minimal surface with a symmetry axis of revolution. We would like to see if the geodesic has any role to play like the sphere scenario and further if there exists a coiling instability.

"This is what I mean when I say I would like to swim against the stream of time: I would like to erase the consequences of certain events and restore an initial condition. But every moment of my life brings with it an accumulation of new facts, and each of these new facts bring with it consequences; so the more I seek to return to the zero moment from which I set out, the further I move away from it...."

–Italo Calvino, If on a Winter's Night a Traveler

5 Dynamics of spherical particles in flow

This chapter is a verbatim reproduction of our article to be published in the Journal of Fluid Mechanics titled "*Accurate solution method for the Maxey-Riley equation, and the effects of Basset history*".

5.1 Introduction

Particles in fluid flows are ubiquitous [134], examples include plankton in the ocean [6, 59], colloidal spheres in Stokes flow, droplets in clouds [46, 57, 115], suspended particulate matter in the atmosphere and various industrial flows. The simplest way to study these flows is to assume a one-way interaction, where the particle dynamics is dictated by the flow, but does not disturb the flow, nor is it influenced by other particles. This is a good assumption when particles are far smaller than all relevant flow length scales, and when the suspension of particles is dilute, as is the case in several of the examples given above. In this setting, the particle obeys the Maxey-Riley (MR) [94] equation, which is a force balance in Lagrangian

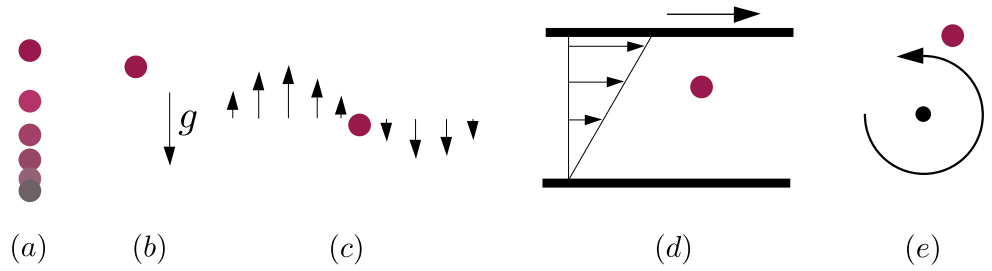

Figure 5.1: Situations for which analytical solutions including the Basset force are provided by the present approach. (a) A relaxing particle, (b) particle settling under gravity, (c) particle in a oscillating field, (d) particle in a shear flow, (e) particle in a single point vortex.

coordinates, given by

$$\dot{\boldsymbol{y}} = \boldsymbol{v}(t), \tag{5.1}$$

$$R\dot{\boldsymbol{v}} = \frac{\mathrm{D}\boldsymbol{u}}{\mathrm{D}t} - \frac{1}{S}(\boldsymbol{v}-\boldsymbol{u}) - \sqrt{\frac{3}{\pi S}}\left\{\frac{1}{\sqrt{t}}(\boldsymbol{v}(0)-\boldsymbol{u}(0)) + \int_0^t \frac{(\dot{\boldsymbol{v}}(s)-\dot{\boldsymbol{u}}(s))}{\sqrt{t-s}}\mathrm{d}s\right\}, \tag{5.2}$$

$$\beta \equiv \frac{\varrho_p}{\varrho_f},\ S \equiv \frac{1}{3}\frac{a^2/\nu}{T},\ R \equiv \frac{(1+2\beta)}{3}, \tag{5.3}$$

where $\boldsymbol{y}, \boldsymbol{v}$ are the vector position and velocity respectively of the particle, and $\boldsymbol{u}$ represents the (possibly spatially and temporally dependent) fluid velocity. We note here that when spatial variation in the fluid is not accounted for in (5.2), the equation is known as the Basset-Boussinesq-Oseen equation [29, 105]. As our focus is towards general fluid flows we stick to the nomenclature of Maxey-Riley equations. Dots represent Lagrangian derivatives in time t and $\mathrm{D}/\mathrm{D}t$ represents the material derivative with respect to the fluid velocity. Furthermore ϱ_p, ϱ_f are the particle and fluid density respectively, R the effective density ratio including added-mass effects, and S the Stokes number, defined here as the ratio of particle relaxation time-scale $(a^2/3\nu)$ to flow time-scale (T). The last term on the right hand side of (5.2) is known as the Basset history force or Basset history integral [12]. It is an integral force along the trajectory of the particle, from the initial time until time t, resulting from the differences in acceleration of particle and surrounding fluid, and will be of primary interest in this paper. An important contribution to the force balance was brought out by [47] who showed the existence of a singular contribution from a non-zero relative velocity at the initial time-instant. Thus far in the literature, the implications of this singular term are largely unexplored. We will discuss its significance in later sections.

Most studies concerning particle dynamics in the low Stokes number limit include contributions from the Stokes drag, the second term on the right-hand side in equation (5.2), but the Basset history integral is often neglected. The coefficient of this term is $\mathcal{O}(S^{1/2})$ relative to the Stokes drag, so it is nominally negligible at small Stokes number, but the factor it multiplies could cause the effect to become important in physical flows. A major hurdle in evaluating the Basset history integral is the continually increasing memory cost associated in computing this term. The inclusion of the Basset history integral renders the MR equations to not represent a dynamical system, i.e., the future evolution of the particle motion depends not only on the current position and velocity, but also on the entire solution up to that time. Standard analytical techniques such as performing a Laplace transform are in general not useful in solving this system the full nonlinear equation. Moreover, even for the linear case, inverting the Laplace transform of a general function $G(t)$ with a kernel of the form $\sim 1/\sqrt{t}$ multiplied to it does not lead to an explicit function of t. Thus researchers have resorted to quadrature schemes [135, 32] or approximations to the history kernel [74, 44, 105]. Since these techniques approximate the history-kernel and are not aimed at obtaining the true asymptotic behaviour, they neglect the aforementioned (most bothersome) singular contributions at $t = 0$, which is a valid assumption when particles and fluid have the same initial velocity, which we emphasize, may not hold in many physical situations. By construction, the approximate schemes mentioned are polynomial order accurate.

In this paper we present (i) analytical solutions, for the first time to our knowledge, of the complete Maxey-Riley equation, including the Basset history term, for particle dynamics in several canonical situations. The only solution we are aware of from earlier work is limited to a relaxing particle [47, 80] where they use a Laplace transform approach. We show that our approach provides a simpler and a more general solution. (ii) demonstrate a numerical approach, by means of an example, of particle dynamics near a point vortex, to solve the complete equations for any general flow to spectral accuracy, again for the first time to our knowledge. Our preference for spectral accuracy in the current work stems from our primary goal of investigating the relevance and impact of the Basset history integral on the dynamics of particles. Hence we seek to eliminate any possible source of error from lower-order schemes.

We do this by reformulating the equations of motion of the particle with the non-local history-dependence into a *local* problem for an extended dynamical system. The main principle employed in deriving the extended dynamical system is a domain extension [136]. In other words, we represent the entirety of the MR equation as a boundary condition to the

one-dimensional diffusion equation. The extended dynamical system couples three quantities that march in time: the position of the particle, the velocity of the particle and the field satisfying the diffusion equation (which effectively encodes the history term). The reformulation enables us to write solutions explicitly for spatially uniform fluid flows. We derive explicit expressions for (i) a particle relaxing in a stationary fluid. In this case, the equations simplify to a constant coefficient linear problem which can be explicitly solved using Laplace transform as well. However, even in this case, the solution by that approach is not an explicit function of time, but given as a convolution integral [47]; (ii) a particle settling under gravity, (iii) a particle in an oscillating background and (iv) a particle in planar Couette flow. For short times, we find the particle velocity relaxes faster when the Basset history integral is accounted for than when it is not. Moreover, on accounting for the effect of the history integral, a cross-over time exists beyond which the particle relaxes with a power-law decay, whereas the decay would be exponential without. In the flows we study, we find that though the transient behaviour of particles in flows is different, the infinite time behaviour remains unchanged, consistent with the analysis of [80].

The solution formula that we obtain is of a form where Watson's lemma [98] may be applied and hence the large-time behaviour is readily computable. Our reformulation of the MR equation has the additional benefit of being local. This allows us to construct a novel numerical scheme that obviates the issue of rising memory storage. Since the effect of the Basset history integral is accounted for in terms of a dynamical variable, our method may also be employed in large simulations with restarts. In large numerical computations of turbulence, for example in cloud flows, the number of particles considered could be of the order of billions. Our method offers a way of including the Basset history integral into such simulations without an unmanageable increase in storage requirements.

Close to a point vortex, upon neglecting the Basset history, the dynamics of particles has been shown to obey a boundary-layer structure [114, 40], where particles initially located within a critical radius r_c are able to form caustics and evacuate the vicinity of the vortex rapidly, whereas particles initially outside this radius do not form caustics, and so their dynamics may be represented by a velocity field. We define caustics as space-time points where two particles can exist simultaneously with different velocities. We demonstrate our numerical method by studying how the Basset history integral affects caustic formation. We show that the history integral shrinks the critical caustic radius, r_c for all Stokes numbers, but the scaling $r_c \sim \sqrt{S}$ is unchanged. Lastly, though all the boundary-bulk extension ideas are

applied here to MR equations that describe dynamics of a spherical particle, we show that an exact map can be applied to particles with other geometries such as spheroids and disks in a flow where an analogous Basset history integral exists. We discuss the implications of our findings to turbulent scenarios, where the effect of the Basset history integral on particle clustering, is still not clearly understood.

While our present study is devoted to the Maxey-Riley equations, we note that convective inertia effects become important beyond the diffusive time scale [90, 91, 95], however small the Reynolds number. So the asymptotic behaviour we calculate below using the MR equation will only be valid up to this time scale, beyond which we must use the entire Navier-Stokes equation to get the correct behaviour. For example, in a particle relaxing to rest in quiescent flow, as calculated in the pioneering work of [90], the relaxation behavour changes from a $1/\sqrt{t}$ decay, as predicted by the MR equation with Basset history, to a faster decay of $1/t^2$ at long times. In the present work, we assume a time-scale separation between the history effects arising out of unsteady inertial effects and the time-scale due to convective inertial corrections. As a consequence our long time asymptotic results are valid at time scales shorter than the convective scale ν/u_c^2, where u_c is a characteristic convective velocity. Two situations where there is at least two orders of magnitude of separation between the Stokes and convective time scales, and Basset history could be vital to understanding the relevant dynamics, are droplet growth in cloud flows, and sedimentation of marine snow. It is significant to note that that the technique developed here can be extended to account for the convective inertia as well, using a history kernel introduced by [90], which will be addressed in future work.

Before we dive into the details of the calculation, we describe our procedure to handle the Basset history term. It is known that the history integral is nothing but a half-derivative in time of the particle velocity relative to fluid motion and it is no surprise that the origins of this half-derivative has to do with the unsteady Stokes equation with particle momentum being diffused by viscosity. On the other hand, it is also known that the half-derivative is the Dirichlet-to-Neumann map for the diffusion equation on the half-line. Let us unpack the previous statement. Suppose $\boldsymbol{g}_0(t)$ is the Dirichlet condition for a function $\boldsymbol{q}(x,t)$ that satisfies the diffusion equation for $x > 0$ (with zero initial conditions). Then the half-derivative of $\boldsymbol{g}_0(t)$ is equal to the Neumann condition $\boldsymbol{q}_x(0,t)$. This fact allows us to relate the MR equation, which is an ordinary integro-differential equation, to a boundary condition to a diffusion equation. The boundary condition, which is the MR equation itself, is a time evolving

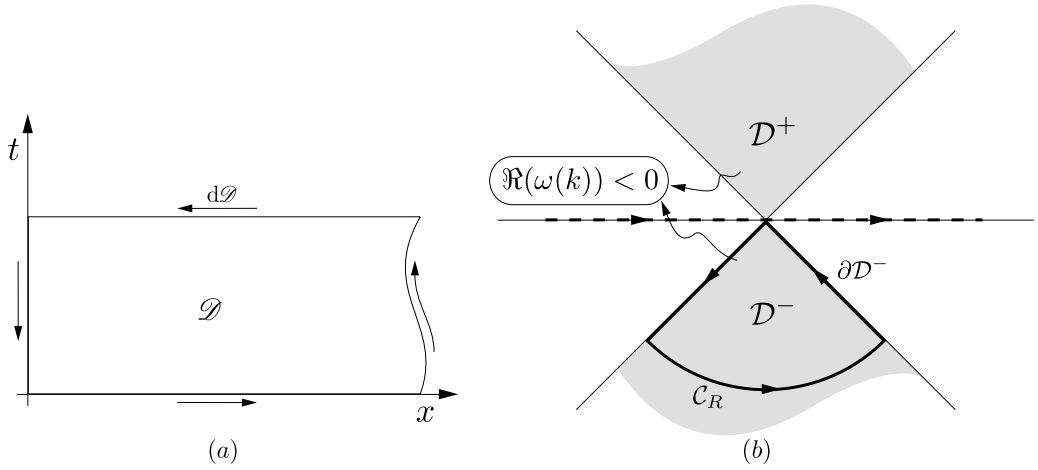

Figure 5.2: (a) Region $\mathscr{D}$ defined by $x \in [0, \infty), t \in [0, T]$ in which the diffusion equation evolves and $\mathrm{d}\mathscr{D}$ is its boundary. (b) Domain $\mathcal{D}^{\pm}$ where the integrating factor $\mathrm{e}^{\omega(k)t}$ decays. The boundary of this region in $\mathbb{C}^-$ is defined by contour $\partial\mathcal{D}^-$ and $\mathcal{C}_R$ whose various contributions help establish the relation between the Dirichlet and Neumann boundary conditions for the diffusion equation.

Robin-type boundary condition and using the Unified Transform Method, as described below, we are immediately able to solve for the particle evolution for arbitrary time-dependent flows.

5.2 Diffusion equation on half-line

Before we discuss the MR equation itself, we first describe a few results pertaining to the 1-D diffusion equation that are essential to our reformulation of the problem. The Unified Transform Method, alternatively known as the Fokas transform method, is employed in deriving the results in this section. These results are not new. Our intent is to introduce notation as well as the techniques that will be relevant in the following sections. Further details regarding the Unified Transform Method can be found in Fokas [50]. For a brief introduction to the method see Deconinck et al. [38].

Consider the 1-D diffusion equation on a half-line of '*pseudo*'-space x with a Dirichlet boundary condition given by $\boldsymbol{g}_o(t)$ at $x = 0$ and let $\boldsymbol{q}(x, t)$ be the variable that gets diffused. Note that x is a fictitious space, not to be confused with the physical space represented by y, so we call x a pseudo-space. It is used only to establish the relationship between the Basset history integral and the Neumann boundary condition for the diffusion equation. This

problem can be formulated in a time-interval $(0, T]$ as

$$\begin{aligned} \boldsymbol{q}_t &= \boldsymbol{q}_{xx}, & x > 0, t \in (0, T], \\ \boldsymbol{q}(x, 0) \equiv \boldsymbol{q}_o(x) &= 0, & x > 0, \\ \boldsymbol{q}(0, t) &= \boldsymbol{g}_o(t), & t \in [0, T]. \end{aligned} \tag{5.4}$$

Subscripts here denote partial derivatives and the evolution of the variable $\boldsymbol{q}(x, t)$ takes place in the $x - t$ plane in the domain $\mathscr{D}$ shown schematically in figure 5.2(a). As is typical for problems posed on a semi-infinite domain, we assume the field $\boldsymbol{q}(x, t)$ vanishes as $x \to \infty$ uniformly for all t. Though this problem may be solved using classical techniques, we employ the Unified Transform Method for reasons that will become evident in subsequent sections.

We begin by rewriting the diffusion equation in its divergence form using the '*local relation*' [38, 50, 39]

$$(\mathrm{e}^{-ikx+\omega(k)t}\boldsymbol{q})_t - (\mathrm{e}^{-ikx+\omega(k)t}(\boldsymbol{q}_x + ik\boldsymbol{q}))_x = 0, \; k \in \mathbb{C}, \tag{5.5}$$

which is valid in any small portion of $\mathscr{D}$ where $\omega(k) = k^2$. The local relation is simply the diffusion equation multiplied by $\mathrm{e}^{-ikx+\omega(k)t}$, as one can see by applying the product rule of differentiation to (5.5).

5.2.1 The global relation and some notation

Next we integrate equation (5.5), over the entirety of $\mathscr{D}$ and employ the divergence theorem to obtain a '*global relation*',

$$\iint_{\mathscr{D}} [(\mathrm{e}^{-ikx+\omega(k)t}\boldsymbol{q})_t - (\mathrm{e}^{-ikx+\omega(k)t}(\boldsymbol{q}_x + ik\boldsymbol{q}))_x] \mathrm{d}x \, \mathrm{d}t = 0, \tag{5.6}$$

$$\Rightarrow \int_{\mathrm{d}\mathscr{D}} [\mathrm{e}^{-ikx+\omega(k)t}\boldsymbol{q} \, \mathrm{d}x + \mathrm{e}^{-ikx+\omega(k)t}(\boldsymbol{q}_x + ik\boldsymbol{q}) \, \mathrm{d}t] = 0, \tag{5.7}$$

$$\Rightarrow \int_0^\infty \mathrm{e}^{-ikx}\boldsymbol{q}_o(x)\mathrm{d}x - \int_0^\infty \mathrm{e}^{-ikx+\omega(k)T}\boldsymbol{q}(x, T)\mathrm{d}x - \int_0^T \mathrm{e}^{\omega(k)t}(\boldsymbol{q}_x(0, t) + ik\boldsymbol{g}_o(t))\mathrm{d}t = 0. \tag{5.8}$$

The terms at the boundary of $\mathscr{D}$ at infinity vanish since $\boldsymbol{q}(x,t) \to 0$ as $x \to \infty$. Let us define the Fourier transform in pseudo-space as

$$\hat{\boldsymbol{q}}_o(k) = \int_0^\infty \mathrm{e}^{-ikx} \boldsymbol{q}_o(x)\, \mathrm{d}x, \tag{5.9}$$

$$\hat{\boldsymbol{q}}(k,T) = \int_0^\infty \mathrm{e}^{-ikx} \boldsymbol{q}(x,T)\, \mathrm{d}x, \tag{5.10}$$

and the time-transform of the boundary terms as

$$\tilde{\boldsymbol{g}}_o(\omega,T) = \int_0^T \mathrm{e}^{\omega(k)t} \boldsymbol{g}_o(t)\, \mathrm{d}t, \tag{5.11}$$

$$\tilde{\boldsymbol{g}}_1(\omega,T) = \int_0^T \mathrm{e}^{\omega(k)t} \boldsymbol{q}_x(0,t)\, \mathrm{d}t. \tag{5.12}$$

Further we define $\mathcal{D}^+$ as

$$\mathcal{D}^+ = \{k \in \mathbb{C} \,:\, \Re(\omega(k)) < 0\,, \Im(k) > 0\},$$

and $\mathcal{D}^-$ as

$$\mathcal{D}^+ = \{k \in \mathbb{C} \,:\, \Re(\omega(k)) < 0\,, \Im(k) < 0\},$$

as shown in figure 5.2(b). Note $\mathrm{e}^{\omega(k)t}$ is analytic, bounded and decaying for large k in these domains, a property we shall use repeatedly. Finally we arrive at the global relation given by

$$\hat{\boldsymbol{q}}_o(k) - \mathrm{e}^{\omega(k)T} \hat{\boldsymbol{q}}(k,T) - \tilde{\boldsymbol{g}}_1 - ik\tilde{\boldsymbol{g}}_o = 0, \qquad k \in \mathbb{C}^-. \tag{5.13}$$

Since the initial condition is zero everywhere on the real line, we have

$$\mathrm{e}^{\omega(k)T} \hat{\boldsymbol{q}}(k,T) + \tilde{\boldsymbol{g}}_1 + ik\tilde{\boldsymbol{g}}_o = 0, \qquad k \in \mathbb{C}^-. \tag{5.14}$$

5.2.2 Dirichlet to Neumann map

Equation (5.4) describes the Dirichlet boundary value problem for the diffusion equation. We now compute the associated Neumann condition, i.e., we ask what Neumann boundary condition would give the same solution as this Dirichlet condition in the entire domain. To do so we multiply equation (5.14) by $ik\mathrm{e}^{-\omega(k)t}$ for $0 < t < T$ and integrate over the contour

$\partial\mathcal{D}^-$, the boundary of $\mathcal{D}^-$ shown in figure 5.2(b).

$$\int_{\partial\mathcal{D}^-}\left[ik\int_0^T \mathrm{e}^{\omega(s-t)}\boldsymbol{q}_x(0,s)\,\mathrm{d}s - k^2\int_0^T \mathrm{e}^{\omega(s-t)}\boldsymbol{q}(0,s)\,\mathrm{d}s + ik\mathrm{e}^{\omega(k)(T-t)}\boldsymbol{q}(k,T)\right]\mathrm{d}k = 0. \tag{5.15}$$

After the manipulations detailed in Appendix 7.4.1, we obtain

$$-\pi\boldsymbol{q}_x(0,t) - \sqrt{\frac{\pi}{t}}\boldsymbol{q}(0,0) - \int_{-\infty}^{\infty}\int_0^t \mathrm{e}^{-k^2(t-s)}\dot{\boldsymbol{q}}(0,s)\,\mathrm{d}s\,\mathrm{d}k = 0. \tag{5.16}$$

Setting $k^2(t-s) = m^2$, where m is real and evaluating the resulting Gaussian integral, we obtain the Dirichlet-Neumann map as

$$\boldsymbol{q}_x(0,t) = -\sqrt{\frac{1}{\pi t}}\boldsymbol{q}(0,0) - \frac{1}{\sqrt{\pi}}\int_0^t \frac{\dot{\boldsymbol{q}}(0,s)}{\sqrt{t-s}}\,\mathrm{d}s. \tag{5.17}$$

The integral term above is the definition of the Riemann-Liouville half-derivative. This expression relating the Neumann condition for the diffusion equation and the Riemann-Liouville half-derivative forms the basis of our reformulation of the MR equations. More general connections between boundary-value problems to partial differential equations and fractional derivatives are explored in Vasan et al. [136]. For the sake of completeness, we provide the details of the Neumann to Dirichlet map derivation in appendix. 7.4.4.

5.3 Recasting the MR equation

We may now use equation (5.17) to rewrite the Maxey-Riley equation (5.2) in its entirety in a reference frame moving with the particle as

$$\dot{\boldsymbol{y}} = \boldsymbol{q}(0,t) + \boldsymbol{u}, \tag{5.18}$$

$$\boldsymbol{q}_t(0,t) + \alpha\boldsymbol{q}(0,t) - \gamma\boldsymbol{q}_x(0,t) = \boldsymbol{f}(\boldsymbol{q}(0,t),\boldsymbol{y},t), \tag{5.19}$$

$$\alpha = \frac{1}{RS},\ \gamma = \frac{1}{R}\sqrt{\frac{3}{S}},\ \boldsymbol{f}(\boldsymbol{q}(0,t),\boldsymbol{y}(t),t) = \left(\frac{1}{R}-1\right)\frac{\mathrm{D}\boldsymbol{u}}{\mathrm{D}t} - \boldsymbol{q}(0,t)\cdot\nabla\boldsymbol{u}, \tag{5.20}$$

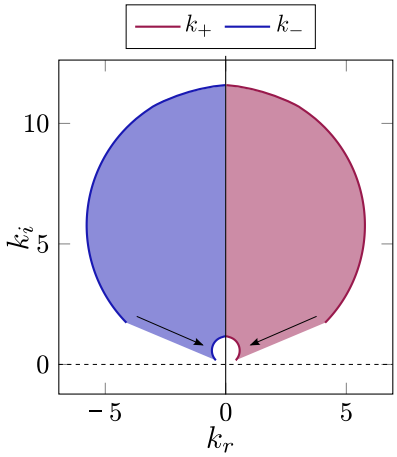

Figure 5.3: Region in $k \in \mathbb{C}^+$ where the poles $k_\pm$ from equation (5.32) are located for Stokes number S in the range $0.01-1$ and density ratios corresponding to R in the range $1/3-5$. As the Stokes number increases the poles approach the real-line shown using arrows and similarly as we increase density ratio. Note that without Basset history the poles would merely lie symmetrically on the k_r line.

where $\boldsymbol{q}(0,t) = \boldsymbol{v}(t) - \boldsymbol{u}(\boldsymbol{y}(t),t)$ is the relative velocity of the particle. In this choice of reference frame, with the history term on the left-hand side in (5.19), we are left with a forcing function $\boldsymbol{f}$ which is local in time, whereas in the original form (5.2) forcing appeared in a non-local manner. As $\boldsymbol{q}(0,t)$ and $\boldsymbol{q}_x(0,t)$ represent the Dirichlet and Neumann condition of a field satisfying the diffusion equation, we are naturally led to consider the following boundary-value problem

$$\boldsymbol{q}_t = \boldsymbol{q}_{xx}, \qquad x > 0, t \in (0,T], \tag{5.21}$$

$$\boldsymbol{q}(x,0) = 0, \qquad x > 0, \tag{5.22}$$

$$\boldsymbol{q}_t(0,t) + \alpha \boldsymbol{q}(0,t) - \gamma \boldsymbol{q}_x(0,t) = \boldsymbol{f}(\boldsymbol{q}(0,t), \boldsymbol{y}, t), \qquad t \in [0,T], \tag{5.23}$$

$$\dot{\boldsymbol{y}}(t) = \boldsymbol{q}(0,t) + \boldsymbol{u}(\boldsymbol{y}(t)), \qquad t \in [0,T], \tag{5.24}$$

$$\lim_{t \to 0} \boldsymbol{q}(0,t) = \boldsymbol{v}_o, \tag{5.25}$$

$$\boldsymbol{y}(0) = \boldsymbol{y}_o. \tag{5.26}$$

The MR equation (5.2) thus manifests itself as a non-linear modified Robin boundary condition, on the time axis of figure 5.2(a), to the diffusion equation. The general time-translational properties of MR equations and their interesting relation to the initial condition $\boldsymbol{q}(x,0)$ of

the heat equation in appendix. 7.4.5. This we will see forms the basis for our numerical scheme discussed in subsection. 5.5.2. We do not yet know $\boldsymbol{q}(0,t)$ on this axis, i.e., the particle velocity in the relative frame of reference, for which we derive an expression in the next sub-section. From here on we work with this form of the MR equation and the global relation (5.14) for the diffusion equation. Higher order corrections in particle size, the Faxén correction, etc. can also be accommodated in the forcing expression, $\boldsymbol{f}(\boldsymbol{q}(0,t),\boldsymbol{y},t)$. Here $\boldsymbol{u}$ is a known velocity field. In the general case, one would couple the MR equation with a fluid model (such as the Navier-Stokes equation) to simultaneously resolve particle locations and fluid velocities. An example of this kind, in the form of particles around a point vortex, is studied in a later section.

5.3.1 Solution for time-dependent forcing

The form of the MR equation (5.19-5.20), suggests the forcing function is both space and time-dependent. However it is instructive and useful to first study a case when the forcing is a function of time alone, i.e., $\boldsymbol{f}(t)$. The ideas presented here will later be extended to more complicated scenarios in later sections.

Using the definitions (5.11-5.12), we take the time-transform of the boundary condition (5.23) and after integrating by parts we get

$$(\mathrm{e}^{\omega(k)T}\boldsymbol{q}(0,T)-\boldsymbol{v}_o)+(\alpha-k^2)\tilde{\boldsymbol{g}}_o-\gamma\tilde{\boldsymbol{g}}_1=\tilde{\boldsymbol{f}}. \tag{5.27}$$

Here $\tilde{\boldsymbol{f}}$ is the time-transform of the function $\boldsymbol{f}$. Using the global relation (5.14) we eliminate $\tilde{\boldsymbol{g}}_1$ from the above expression and multiply the resulting equality by $ik\mathrm{e}^{-\omega(k)t}$ for $0<t<T$ and finally integrate over $\partial\mathcal{D}^-$. This leads to

$$\int_{\partial\mathcal{D}^-} ik\tilde{\boldsymbol{g}}_o(\omega,T)\mathrm{e}^{-\omega(k)t}\,\mathrm{d}k=\int_{\partial\mathcal{D}^-} ik\mathrm{e}^{-\omega(k)t}\left[\frac{\tilde{\boldsymbol{f}}-\mathrm{e}^{\omega T}\boldsymbol{q}(0,T)+\boldsymbol{v}_o-\gamma\mathrm{e}^{\omega T}\hat{\boldsymbol{q}}(k,T)}{(\alpha-k^2+ik\gamma)}\right]\mathrm{d}k, \tag{5.28}$$

$$\begin{aligned}\int_{\partial\mathcal{D}^-} ik\mathrm{e}^{-k^2t}\int_0^T \mathrm{e}^{k^2s}\boldsymbol{q}(0,s)\,\mathrm{d}s\,\mathrm{d}k=&\int_{\partial\mathcal{D}^-}\frac{ik\mathrm{e}^{-k^2t}\big(\tilde{\boldsymbol{f}}(k,T)+\boldsymbol{v}_o\big)}{(\alpha-k^2+ik\gamma)}\,\mathrm{d}k\\&-\int_{\partial\mathcal{D}^-} ik\frac{\mathrm{e}^{k^2(T-t)}\big(\boldsymbol{q}(0,T)+\gamma\hat{\boldsymbol{q}}(k,T)\big)}{(\alpha-k^2+ik\gamma)}\,\mathrm{d}k,\end{aligned} \tag{5.29}$$

where (in the second line) we have used the definition of $\tilde{\boldsymbol{g}}_0$ and the fact that $\omega(k)=k^2$. We

substitute $k^2 = il$ in the left-hand-side term above, which describes the boundary $\partial\mathcal{D}^-$, see figure 5.2(b), to arrive at

$$-\frac{1}{2}\int_{-\infty}^{\infty} \mathrm{e}^{-il(t-s)} \int_0^T \boldsymbol{q}(0,s)\,\mathrm{d}l\,\mathrm{d}s = \int_{\partial\mathcal{D}^-} \frac{ik\mathrm{e}^{-k^2t}\big(\tilde{\boldsymbol{f}}(k,T)+\boldsymbol{v}_o\big)}{(\alpha-k^2+ik\gamma)}\,\mathrm{d}k - \int_{\partial\mathcal{D}^-} ik\frac{\mathrm{e}^{k^2(T-t)}\big(\boldsymbol{q}(0,T)+\gamma\hat{\boldsymbol{q}}(k,T)\big)}{(\alpha-k^2+ik\gamma)}\,\mathrm{d}k, \tag{5.30}$$

$$\begin{aligned}-\pi\boldsymbol{q}(0,t) = &\int_{\partial\mathcal{D}^-}\int_0^t \frac{ik\mathrm{e}^{-k^2(t-s)}\boldsymbol{f}(s)}{(\alpha-k^2+ik\gamma)}\,\mathrm{d}k\,\mathrm{d}s + \int_{\partial\mathcal{D}^-}\frac{\boldsymbol{v}_o ik\mathrm{e}^{-k^2t}}{(\alpha-k^2+ik\gamma)}\,\mathrm{d}k\\ &+\int_{\partial\mathcal{D}^-}\int_t^T \frac{ik\mathrm{e}^{k^2(s-t)}\boldsymbol{f}(s)}{(\alpha-k^2+ik\gamma)}\,\mathrm{d}k\,\mathrm{d}s\\ &-\int_{\partial\mathcal{D}^-} ik\frac{\mathrm{e}^{k^2(T-t)}\big(\boldsymbol{q}(0,T)+\gamma\hat{\boldsymbol{q}}(k,T)\big)}{(\alpha-k^2+ik\gamma)}\,\mathrm{d}k,\end{aligned} \tag{5.31}$$

where we have used the standard Fourier inversion formula on the left-hand side. There are two poles due to the quadratic in the denominator of above equation which are located at

$$k_\pm = \frac{1}{2}(i\gamma \pm \sqrt{4\alpha-\gamma^2}). \tag{5.32}$$

Since both γ and α are positive parameters, the poles $k_\pm$ always lie in $\mathbb{C}^+$ and reach the real line for $\gamma = 0$, i.e., when Basset history is absent (see figure 5.3). An appeal to Jordan's lemma [1, page 222] shows that the third and fourth term (those involving function evaluations at T) in equation (5.31) do not contribute, since k^2 is negative in $\mathcal{D}^-$ and $(t-s) > 0$. It is not surprising that these two terms do not contribute as this only ensures causality: the dynamics of the particle for all times $t < T$ cannot depend on a quantity from future time T. Using the fact that e^{-k^2t} is decaying in the region outside $\mathcal{D}^-$, we can write the final solution expression as:

$$-\pi\boldsymbol{q}(0,t) = \int_{\partial\mathcal{D}^-}\int_0^t \frac{ik\mathrm{e}^{-k^2(t-s)}\boldsymbol{f}(s)}{(\alpha-k^2+ik\gamma)}\,\mathrm{d}s\,\mathrm{d}k - \int_{-\infty}^{\infty}\frac{\boldsymbol{v}_o ik\mathrm{e}^{-k^2t}}{(\alpha-k^2+ik\gamma)}\,\mathrm{d}k. \tag{5.33}$$

Note that the particle velocity is now given by the above expression directly (and explicitly) in terms of the initial condition $\boldsymbol{v}_o(=\boldsymbol{v}(0)-\boldsymbol{u}(0))$ and the forcing $\boldsymbol{f}(t)$ in the relative frame of reference. The quantity $\boldsymbol{q}(0,t)$ represents the Dirichlet boundary condition for the modified

Robin boundary value problem for the diffusion equation. Once the relative velocity $\boldsymbol{q}(0,t)$ is available, one may readily compute particle trajectories $\boldsymbol{y}(t)$ from (5.24).

Without the Unified Transform Method, one may not have suspected such a boundary value problem is indeed solvable. Of course, one could in principle have employed the Laplace transform to obtain the solution though a couple of issues arise then. If one were to use Laplace transform, the inverse would involve branch-cuts in the general case, which are difficult to evaluate, and as mentioned above, explicit solutions are most often not possible. However the Unified Transform Method provides the appropriate re-parameterisation to avoid these complications, and to further provide an explicit expression in t for the solution, given by equation (5.33). As we shall see in the following sections, especially when considering the nonlinear problem $\boldsymbol{f}(\boldsymbol{q}(0,t),\boldsymbol{y},t)$, the true benefit of adopting the new formulation is the local nature of the extended system which is precisely due to the connection between the MR equations and the diffusion equation.

5.4 Explicit solution for particular flows

In several fluid scenarios, there is a considerable separation between diffusive and convective time-scales. Two such examples are highlighted below. In such scenarios, the Basset history force has a non-negligible effect on the resultant particle dynamics. Consequently, we present several example flows which permit explicit treatment of the Basset history term and its impact on the particle motion.

- Clouds: In clouds the diffusion time-scale, τ for a droplet of size $a \sim 10\mu$m is $\mathcal{O}$(ms) while the energy dissipation rate of $\varepsilon \sim 10\text{m}^2/\text{s}^3$ leads to a Kolmogorov eddy of size $\eta_k \sim 0.1$mm. Calculating the convective velocity scale u_k using the relation $u_k\eta_k \sim \nu$ where ν is the kinematic viscosity, we get $u_k \sim 1$cm/s. From this we get the convective inertial time scale $\tau_{in} \sim \nu/u_k^2 = \mathcal{O}(0.1\text{s})$. We have a factor of $\mathcal{O}(100)$ showing that there is a long time region even at the length scale of a Kolmogrov eddy at which Basset history is expected to play a role.

- Planktons: Planktons in the ocean come in various sizes and different density ratios. The effect of turbulence on clustering [59] is poorly understood and we believe Basset history, given its non-trivial dynamics, might play a role in its settling. A plankton of size $a \sim 100\mu$m has a terminal velocity of $U_t \sim 0.1$mm/s when $\Delta\rho/\rho \sim 0.1$ (where $\Delta\rho$ is the difference between particle density and fluid density and ρ being density of water). The diffusive time scale $a^2/\nu \sim 1$s while the $\tau_{in} = \nu/U_t^2 \sim \mathcal{O}$(hrs). This

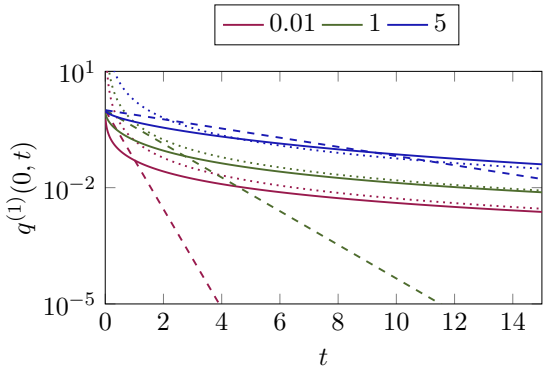

Figure 5.4: Particle velocity with (solid lines), and without (dashed lines) Basset history, along with the asymptotic solution (dotted lines) from equation (5.36). The curves from bottom to top correspond to three different density ratios respectively: light particles, with $\beta(=\varrho_p/\varrho_f) = 0.01$, neutrally buoyant particles with $\beta = 1$, and heavy particles with $\beta = 5$ at a fixed Stokes number of $S = 1$. The decay rate of particle velocity goes as $t^{-3/2}$ for long times when Basset history is accounted for, in contrast to the exponential decay when it is neglected.

clearly shows that such a huge time scale separation makes studying Basset history effects worthwhile. Also we suspect that the clustering of plankton could happen in short time, dynamics dominated by diffusive effects.

Given this motivation, we start looking at simple scenarios where fluid velocity is only time dependent and space independent as we build onto complex flows.

5.4.1 Example 1: A relaxing particle

In the absence of a background flow (namely when $\boldsymbol{f} = 0$), expression (5.33) for the relative velocity $\boldsymbol{q}(0,t)$, may be analysed using Watson's lemma. Since the real-line in k happens to be the path of steepest descent, Laplace's method provides the asymptotic behaviour for functions of the form

$$\mathscr{K}(\zeta) := \int_a^b \mathrm{e}^{g(\zeta)t}\psi(\zeta)\,\mathrm{d}\zeta \text{ as } t \to \infty,\ t > 0, \tag{5.34}$$

in terms of the local maximum value of function $g(\zeta)$ when $\zeta \in [a, b]$. This leads to the well-known asymptotic result for integrals of the above form

$$\mathscr{K}(\zeta) := \int_{-\infty}^{\infty} \mathrm{e}^{-\zeta^2 t}\psi(\zeta)\,\mathrm{d}\zeta \;\approx\; \sqrt{\frac{\pi}{t}}\sum_{n=0}^{\infty}\frac{\psi_n(0)}{2^{2n}n!}\,t^{-n},\ \text{as } t\to\infty. \tag{5.35}$$

On setting $\boldsymbol{f} = 0$ we see that the dominant contribution of the integral in (5.33) comes from $k = 0$. To leading order we have

$$\boldsymbol{q}(0,t) \approx \frac{\boldsymbol{v}_o}{\sqrt{\pi}t^{3/2}}\frac{\gamma}{2\alpha^2} + \mathcal{O}(t^{-5/2}), \qquad t \gg 0. \tag{5.36}$$

[47, 80] approached this problem by using Laplace transform. Their complete solution was provided in terms of convolutions and not directly as we obtain in equation (5.33). For large times however, [80] present the same equation as (5.36). Their solution for a relaxing particle is the only earlier closed form solution that we know of, which accounts for the initial conditions correctly. We contrast the complete solution (5.33) with the one obtained upon neglecting the Basset history integral in the original MR equation. This is equivalent to neglecting the Neumann term $\boldsymbol{q}_x(0,t)$ in equation (5.27) and repeating the calculation of $\boldsymbol{q}(0,t)$. Alternatively we just set $\gamma = 0$ in (5.33) to obtain

$$\pi\boldsymbol{q}(0,t) = \int_{-\infty}^{\infty}\frac{\boldsymbol{v}_o ik\mathrm{e}^{-k^2 t}}{(k^2-\alpha)}\,\mathrm{d}k. \tag{5.37}$$

The non-zero contribution to the integrand comes only from the poles as the integrand is odd leading to

$$\boldsymbol{q}(0,t) = \boldsymbol{v}_o\mathrm{e}^{-\alpha t}, \tag{5.38}$$

and is precisely the expression one gets by solving the Maxey-Riley equation directly without the history term (and $\boldsymbol{f} = 0$).

In figure 5.4 we plot the velocity obtained both by including the history integral and excluding it for three cases: neutrally buoyant ($\beta = 1$), light ($\beta = 0.01$) and heavy particle ($\beta = 5$). Two important features are evident. First, the solution with Basset history settles not exponentially but as a power-law (in this case a very slow $t^{-3/2}$). Secondly, there exists a cross-over time prior to which, a particle evolving under the influence of the Basset history in-

tegral and Stokes drag, relaxes faster than the particle evolving only under Stokes drag. However, after the cross-over time the particle that evolves only under Stokes drag relaxes faster. This contradicts the popular notion that Basset history acts as an effective drag. Thus far, for this example, we have considered the effect of varying density ratios on the particle relaxation time. Note, varying the Stokes number does not lead to substantially different velocity profiles since the Stokes number may be scaled out of the solution by replacing $k \to \tilde{k}/\sqrt{S}$ and $t \to \tilde{t}S$. Particle velocities for Stokes number $S \neq 1$ may be obtained from those depicted in figure 5.4 by suitably scaling time.

5.4.2 Example 2: Sedimenting particles

The dynamics of particles settling under gravity is relevant in industrial applications, for aerosol particles and droplets in the Earth's atmosphere, and for carbon sequestration by marine snow in the oceans. In this section a two-dimensional flow is considered, with a superscript $(\cdot)^{(2)}$ indicating the vertical component of the relevant vector, while $(\cdot)^{(1)}$ indicates the horizontal component. When the particle is acted upon by a body force such as gravity, the vertical component of forcing function $\boldsymbol{f}$, $f^{(2)}(t)$, is a constant of magnitude σ. This allows us to evaluate the time-transform explicitly as

$$\tilde{f}^{(2)}(\omega, T) = \int_0^T \sigma \mathrm{e}^{\omega s}\, \mathrm{d}s = \frac{\sigma(\mathrm{e}^{\omega T} - 1)}{\omega}.$$

The settling velocity of the particle is

$$\pi q^{(2)}(0,t) = \int_{-\infty}^{\infty} \frac{ik\mathrm{e}^{-k^2 t} v_o^{(2)}}{(\alpha - k^2 + ik\gamma)}\, \mathrm{d}k + \int_{-\infty}^{\infty} \frac{\sigma\gamma(1 - \mathrm{e}^{-k^2 t})}{((\alpha - k^2)^2 + k^2\gamma^2)}\, \mathrm{d}k. \tag{5.39}$$

A solution for this problem is provided in [29]. However, their solution necessitates a zero initial-velocity condition for the particle. Moreover their solution is in terms of sums of error functions, and so the asymptotic form for large time is difficult to glean directly. We evaluate the full solution (5.39), without the zero initial-velocity requirement, for the same particle density ratios as in the previous example (but fixed Stokes number $S = 0.01$), corresponding to neutrally buoyant, light and heavy particles: $\beta = 1, 0.01$ and 5, respectively, see figure 5.5(a, b). We also obtain the leading order asymptotic behaviour for the particle

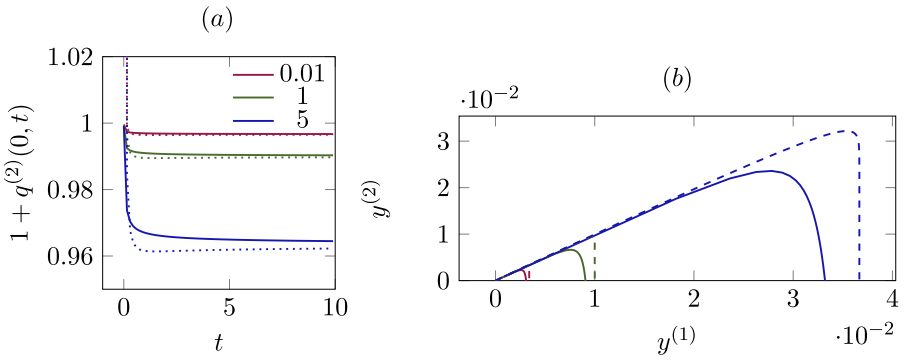

Figure 5.5: (a) Particle velocity relative to fluid, $q^{(2)}(0,t)$ along $y^{(2)}$-direction and (b) particle trajectory as a function of time for three density ratios, $\beta = 0.01, 1, 5$ corresponding to light, neutrally buoyant and heavy particle when acted upon by gravity for $S = 0.01, \sigma = -1$ in equation (5.39). The asymptotic expression for velocity in (5.41) is plotted as dotted line in (a) and the dashed line in (b) is the trajectory of particle without accounting for Basset history. Time taken by particles to reach $y^{(2)} = 0$ when accounted for Basset history for these density ratios is $t = 1.1, 1.15, 1.2$ and without Basset history it takes $t = 1, 1.01, 1.04$.

velocity

$$q^{(2)}(0,t) \approx c(\alpha,\gamma) + \frac{\sigma\gamma}{\alpha^2(\pi t)^{1/2}} + \mathcal{O}(t^{-3/2}), \qquad t \gg 0, \tag{5.40}$$

$$c(\alpha,\gamma) = \int_{-\infty}^{\infty} \frac{\sigma\gamma}{((\alpha - k^2)^2 + k^2\gamma^2)}\,\mathrm{d}k = \frac{\pi\sigma}{\alpha}, \tag{5.41}$$

where $c(\alpha,\gamma)$ is the velocity of the sedimenting particle at long times.

Note that the terminal velocity $c(\alpha,\gamma)$ is in fact the same quantity as that obtained for a particle in the absence of the Basset history force and more importantly, this terminal velocity is independent of γ. The expression $\sigma\pi/\alpha$ is the constant velocity obtained from a balance of gravitational forces and steady drag in our notation. The evaluation of the integral expression for $c(\alpha,\gamma)$ is via an appeal to the residue theorem, albeit for three different cases: $\gamma^2/\alpha < 4$, $\gamma^2/\alpha = 4$ and $\gamma^2/\alpha > 4$. In all three cases, the integral has the same value.

We observe that a sedimenting particle attains its terminal velocity at a rate of $t^{-1/2}$, which is far slower than the exponential trend as predicted without Basset history. It is worth noting that a sedimenting particle's relaxation is even slower than the $t^{-3/2}$ trend observed for the force-free relaxation (5.36). Another interesting feature of this dynamics, which would be missed on neglecting the Basset history integral, is that the long time trajectory of the particle is given by $y^{(2)} \sim -1/(y^{(1)} - \xi)$ (ξ being the final horizontal coordinate). This behaviour is

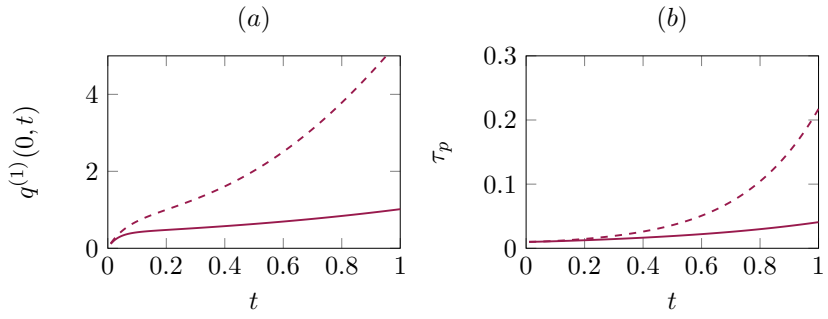

Figure 5.6: (a) Velocity as a function of time, of a particle growing in size as it sediments through a uniform distribution of smaller particles and coalesces with those it collides with. (b) Size of this particle, a as a function of time in terms of its relaxation time scale $\tau_p(\sim a^2)$ with initial $\tau_p = 0.01s, v_o^{(2)} = 0.01, \nu = 10^{-5}m^2/s$ and $\beta = 10$ in an environment with solid fraction $\varphi = 0.002$. Solid lines correspond to dynamics accounting for history effects while dashed to particles relaxation with Stokes drag alone.

anomalous in the sense that it is neither projectile nor ballistic.

The previous remarks suggest that Basset history could play a significant role in complex flows. For example, sedimentation rates of individual particles will determine how frequently particles collide with one another and coalesce as they sink. This question is of importance to estimating carbon sequestration by plankton in the ocean, raindrop growth, and for pulverised coal in thermal power plants. To this end, we make here a simple estimate for how a particle grows in size as it sediments through a sea of smaller particles.

It is simpler in this case to work with the dimensional equation, obtained by replacing $\sigma \to (\beta - 1)g/R, S \to \tau_p$, where g is gravity and $\tau_p = a^2/\nu$ is the particle time scale, so (5.39) reads as

$$\pi q^{(2)}(0,t) = \int_{-\infty}^{\infty} \frac{ik\mathrm{e}^{-k^2 t} v_o^{(2)}}{(\frac{1}{R\tau_p} - k^2 + \frac{ik}{R\sqrt{\tau_p}})}\,\mathrm{d}k - \int_{-\infty}^{\infty} \frac{\frac{(\beta-1)g}{R^2\sqrt{\tau_p}}(1 - \mathrm{e}^{k^2 t})}{((\frac{1}{R\tau_p} - k^2)^2 + \frac{k^2}{R^2\tau_p})}\,\mathrm{d}k. \tag{5.42}$$

Now k has the dimensions of $t^{-1/2}$ and $v_o^{(2)}, q^{(2)}(0,t)$ are dimensional velocities. We follow one large particle of growing radius a as it sediments through a quiescent fluid with a uniform distribution of identical small particles of radius $(a_s < a)$ occupying a solid fraction φ. The larger particle falls faster than the smaller ones, and in a short time Δt, it collides with all small particles whose centres lie within a cylinder of radius $(a + a_s)$ and height $q^{(2)}(0,t)\Delta t$. Assuming that all small particles it collides with will coalesce with the bigger particle and that

$a \gg a_s$, its volume increases by $\varphi\pi a^2 q^{(2)}(0,t)\Delta t$. Thus we get an evolution for the particle time-scale as

$$\tau_p^{(n)} = \left(\tau_p^{3/2} + \frac{3}{4}\varphi\tau_p \frac{q^{(2)}(0,t)\Delta t}{\sqrt{\nu}}\right)^{2/3}, \tag{5.43}$$

which modifies α, γ in equation (5.33). After each time interval Δt we reinitialise the system with a new initial condition $v_o^{(2)}$ being the velocity from the previous time instant and a new relaxation time $\tau_p^{(n)}$. For a droplet of $\nu \sim 10^{-5} m^2/s,\ a \sim 0.3mm, \beta = 10$ we get $\tau_p \sim 10^{-2}s$. In figure 5.6(a) we plot the dynamics of such a particle and in figure 5.6(b) the particle size is represented in terms of its time scale τ_p as a function of time for two scenarios: (i) accounting for history effects (solid lines) and (ii) only Stokes drag (dashed lines). We see that by neglecting the history force we will grossly overestimate particle size at a given time.

We have considered only vertical trajectories in this example. However in gravitational setting in turbulent particulate flows the anomalous trajectory could introduce non-trivial changes in the dynamics, which will be a topic for future study.

5.4.3 Example 3: Particle in an oscillatory background

We now consider the behaviour of a single particle with a background flow that oscillates with a single frequency. The forcing function is $f^{(2)}(s) = \sin(\lambda s)$ and the first term in equation (5.33) can be rewritten as

$$\mathscr{I} = \int_{-\infty}^{\infty}\int_0^t \frac{ik\mathrm{e}^{-k^2 m} f^{(2)}(t-m)}{(\alpha - k^2 + ik\gamma)}\,\mathrm{d}m\,\mathrm{d}k, \text{ with } m = (t-s), \tag{5.44}$$

$$= \int_{-\infty}^{\infty} \frac{i\lambda k}{(\alpha - k^2 + ik\gamma)}\left[\frac{\lambda\mathrm{e}^{-k^2 t} - \lambda\cos(\lambda t) + k^2\sin(\lambda t)}{(\lambda^2 + k^4)}\right]\mathrm{d}k. \tag{5.45}$$

The solution for the scenario with Stokes drag (but no Basset history integral) is

$$q^{(2)}(0,t) = q^{(2)}(0,0)\mathrm{e}^{-\alpha t} + \frac{\lambda\mathrm{e}^{-\alpha t}}{(\alpha^2+\lambda^2)} + \frac{\alpha\sin(\lambda t) - \lambda\cos(\lambda t)}{(\alpha^2+\lambda^2)}. \tag{5.46}$$

We evaluate this velocity expression as a function of time in figure 5.7(a) and find that with Basset history, particles oscillate with smaller amplitudes at early time, and that they attain their final periodic state faster than when Basset history is neglected. This behaviour, governed by the short-time dynamics, is qualitatively different from that of the cases we studied in earlier sections, where Basset history significantly slowed down the attainment of termi-

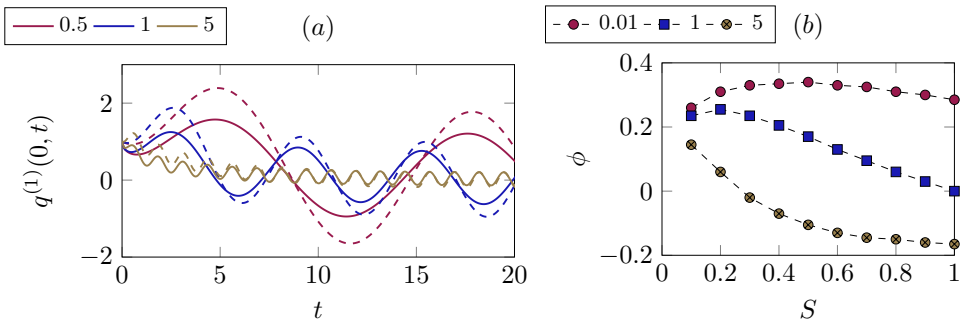

Figure 5.7: (a) Particle velocity relative to oscillating background flow when $\beta = 5, S = 1$ for three different oscillating frequencies, $\lambda = 0.5, 1, 5$. The dashed lines correspond to the solution with Stokes drag alone, and the solid line accounts for Basset history as well, from equation (5.45). (b) Phase difference, ϕ between solutions including and excluding history effects as a function of Stokes number, S, for a fixed $\lambda = 1$ and three density ratios, $\beta = 0.01, 1, 5$.

nal velocity. In particular, the Basset history integral is not simply an additional drag. We see that expressions (5.45) and (5.46) asymptote to similar expressions, albeit with a phase difference. We can quantify the phase difference ϕ that persists at long times between a particle with history effects and with only Stokes drag at long times. This is shown in figure 5.7(b) for Stokes number in the range $S = 0.1 - 1$ and for three different density ratios, $\beta = 0.01, 1, 5$. We should however remind ourselves that though we have chosen $\lambda \sim \mathcal{O}(1)$ where particle relaxation time scale and forcing are similar, the solution expression is general and applies to all scenarios with frequencies capped by the diffusive time scale.

5.5 Spatially dependent flows

Thus far we considered the MR equation with spatially uniform fluid flows. When the fluid flow varies in space, the MR equation is generically nonlinear and one does not obtain a closed-form expression for the particle velocity $\boldsymbol{q}(0,t)$. Most fluid flows are indeed spatially dependent. The role of the Basset history integral in determining the dynamics of inertial particles in such fluid flows has been investigated by others [102, 60, 34, 35, 33]. These studies focused on the contribution of the Basset history to particle collision rates, preferential concentration and residence time of heavy/light particles. All of the aforementioned studies employed the numerical scheme developed in [32] which approximates the singular kernel of the Basset history integral. In this section, we show how our reformulation of the MR equation may be readily adapted to the case of spatially dependent fluid flows. We emphasize that

no approximations are made in handling the singular kernel. Furthermore, the memory costs are constant in time.

We begin the discussion in subsection 5.5.1 by considering the dynamics of a particle in planar Couette flow. Since the fluid velocity is linear in the spatial variable, this spatially dependent problem is in fact exactly solvable. Moreover the exact solution found here may be used to simulate the dynamics of particles in more complicated, but slowly varying, flow fields by using the the leading order term in a gradient expansion of the fluid velocity.

Our next example, in subsection. 5.5.2, is that of a particle in the neighbourhood of a point vortex. Here we probe the effect of the history-integral on caustics formation and also the large-time behaviour of the particle. This requires some modification of our original method to handle nonlinear forcing functions, which we describe in detail below. The extension of the numerical method, presented in this section, to cases where the fluid velocity is not specified explicitly is straightforward, though not the topic of the present manuscript. It is thus our contention that the numerical method we develop here is directly applicable for including the history integral in any general flow.

5.5.1 Example 4: Migration in plane Couette flow

The Couette flow velocity profile is given by $u^{(1)} = \lambda y^{(2)}$. As before, the superscripts $(\cdot)^{(1)}$ and $(\cdot)^{(2)}$ represent the horizontal and vertical components respectively. The particle velocity evolution in such a background flow is given by

$$\partial_t \begin{bmatrix} q^{(1)}(0,t) \\ q^{(2)}(0,t) \end{bmatrix} = -\underbrace{\begin{bmatrix} \alpha & \lambda \\ 0 & \alpha \end{bmatrix}}_{\mathbb{M}} \begin{bmatrix} q^{(1)}(0,t) \\ q^{(2)}(0,t) \end{bmatrix} + \gamma \underbrace{\begin{bmatrix} 1 & 0 \\ 0 & 1 \end{bmatrix}}_{\mathbb{I}} \begin{bmatrix} q_x^{(1)}(0,t) \\ q_x^{(2)}(0,t) \end{bmatrix}. \tag{5.47}$$

Since the boundary condition is linear with constant coefficients, we may follow a similar procedure as earlier. We now have two diffusion equations coupled at an interface where the interfacial boundary condition in each is given by the MR equation (5.23). Note however, that the diffusion equations themselves (i.e. in the bulk) are decoupled from each other. As a result, the global relation for this system of diffusion equations is just the vector version of (5.14)

$$\mathrm{e}^{\omega(k)T}\hat{\boldsymbol{q}}(k,T) + \boldsymbol{g}_1(k,T) + ik\boldsymbol{g}_o(k,T) = 0, \qquad k \in \mathbb{C}^-. \tag{5.48}$$

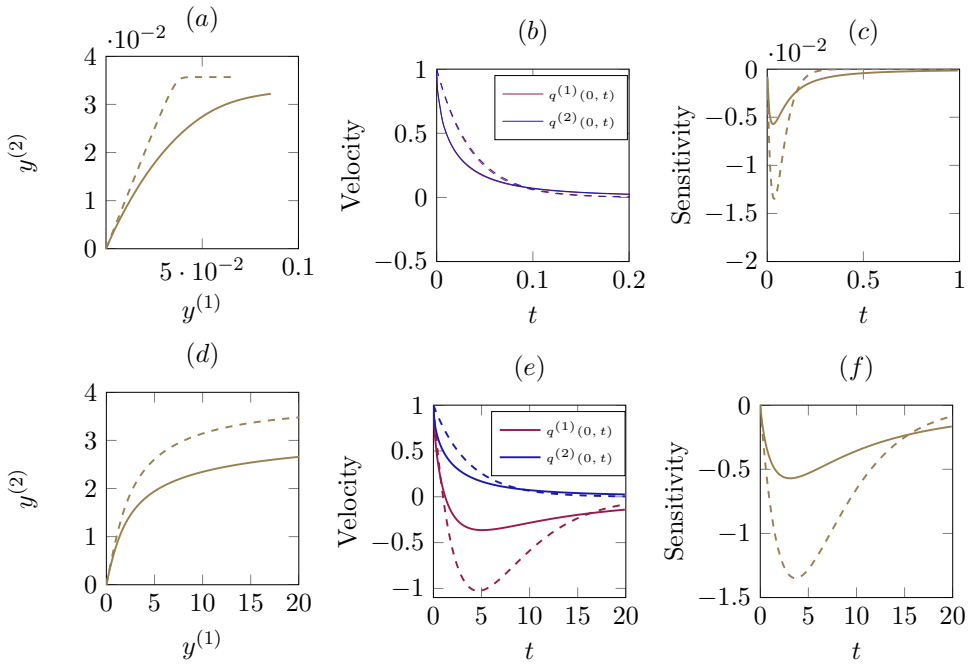

Figure 5.8: Particle dynamics in Couette flow. Solid lines are the solutions in equation (5.52), while dashed lines indicate dynamics upon neglecting Basset history in equation (5.53). Top row corresponds to solution for $S = 0.01$ and bottom for $S = 1$ for a fixed density ratio of $\beta = 5$. (a, d) Horizontal component $q^{(1)}(0, t)$ and vertical component $q^{(2)}(0, t)$ respectively of particle velocity relative to fluid velocity with initial velocity of particle relative to fluid $\boldsymbol{q}(0, 0) = 1$. (b, e) Particle trajectory as a function of time. (c, f) Off-diagonal component of sensitivity matrix in equation (5.55) which is due to shear in the flow.

The boundary condition becomes

$$\Big(\boldsymbol{q}(0,T)\mathrm{e}^{\omega T} - \boldsymbol{q}(0,0)\Big) - k^2\boldsymbol{g}_o(k,T) = -\mathbb{M}(\alpha,\gamma,\lambda)\boldsymbol{g}_o(k,T) + \gamma\boldsymbol{g}_1(k,T). \tag{5.49}$$

Eliminating $\boldsymbol{g}_1(k,T)$ just as earlier from the above equation, we get for $\boldsymbol{g}_o(k,T)$

$$\big((k^2 - ik\gamma)\mathbb{I} - \mathbb{M}(\alpha,\gamma,\lambda)\big)\boldsymbol{g}_o(k,T) = \Big\{\boldsymbol{q}(0,T)\mathrm{e}^{\omega T} - \boldsymbol{q}(0,0) + \gamma\hat{\boldsymbol{q}}(k,T)\mathrm{e}^{\omega T}\Big\} \tag{5.50}$$

$$\text{where } \big((k^2 - ik\gamma)\mathbb{I} - \mathbb{M}(\alpha,\gamma,\lambda)\big)^{-1} = \begin{bmatrix} (k^2-\alpha-ik\gamma)^{-1} & \lambda(k^2-\alpha-ik\gamma)^{-2} \\ 0 & (k^2-\alpha-ik\gamma)^{-1} \end{bmatrix}. \tag{5.51}$$

Multiplying the above equation by $ik\mathrm{e}^{-k^2t}$ and integrating over $\partial\mathcal{D}^-$ we obtain the solution

$$\pi\boldsymbol{q}(0,t) = -\int_{-\infty}^{\infty} ik\mathrm{e}^{-k^2t} \begin{bmatrix} (k^2-\alpha-ik\gamma)^{-1} & \lambda(k^2-\alpha-ik\gamma)^{-2} \\ 0 & (k^2-\alpha-ik\gamma)^{-1} \end{bmatrix} \boldsymbol{q}(0,0)\,\mathrm{d}k. \tag{5.52}$$

On the other hand, the solution to the MR equation without the Basset history integral simplifies to

$$\boldsymbol{q}(0,t) = \mathrm{e}^{-\alpha t} \begin{bmatrix} 1 & -\lambda t \\ 0 & 1 \end{bmatrix} \boldsymbol{q}(0,0). \tag{5.53}$$

The results are provided in figure 5.8. Sub-figures (a) and (d), respectively for Stokes number $S = 0.01$ and 1, show particle trajectories with and without Basset history. The $y^{(2)}$ coordinate has saturated to the values shown. Clearly the migratory behaviour is different, and neglecting Basset history predicts the final locations of the particles incorrectly. Furthermore, the relaxation time is longer with Basset history, i.e. the velocity decay is slower, as seen in figure 5.8(b,e). Note that the relative velocity is plotted here, so each particle at long time attains the local velocity of the Couette flow ($= \lambda y^{(2)}$). The solution expressions (5.52-5.53) readily lead to the following expressions for the sensitivity of the solution to a particle's initial

velocity

$$\left(\frac{\delta \boldsymbol{q}(0,t)}{\delta \boldsymbol{q}(0,0)}\right)_{\text{His}} = -\frac{1}{\pi}\int_{-\infty}^{\infty} ik\mathrm{e}^{-k^2 t}\begin{bmatrix}(k^2-\alpha-ik\gamma)^{-1} & \lambda(k^2-\alpha-ik\gamma)^{-2}\\ 0 & (k^2-\alpha-ik\gamma)^{-1}\end{bmatrix}\mathrm{d}k, \quad (5.54)$$

$$\left(\frac{\delta \boldsymbol{q}(0,t)}{\delta \boldsymbol{q}(0,0)}\right)_{\text{Sto}} = \mathrm{e}^{-\alpha t}\begin{bmatrix}1 & -\lambda t\\ 0 & 1\end{bmatrix}. \quad (5.55)$$

The eigenvalues of this sensitivity matrix provide the Lyapunov exponents and both eigenvalues are equal to 1 for the scenarios with and without Basset history. However the eigenvectors corresponding to these matrices are different and in figure 5.8 (c, f) we plot the evolution of the off-diagonal component for two different $S = 0.01, 1$.

5.5.2 Solution for non-linear spatial flows

So far, we have been able to explicitly compute the particle velocity, from $\tilde{\boldsymbol{g}}_0(\omega, T)$, see equation (5.31). However when the spatial dependence of the fluid is flow is nonlinear, i.e., when $\boldsymbol{f}$ depends on $\boldsymbol{y}$, equation (5.31) is not an explicit expression for the particle velocity. Consequently we resort to a numerical scheme to evolve the dynamics of the particle, which we present in this section. Our numerical method has the following advantages:

- The method completely eliminates the need to store the entire trajectory of the particle to evaluate the Basset history term.
- Our method achieves spectral accuracy by employing Chebyshev polynomials to evaluate the integrals involved.
- The method involves a fixed memory cost (of $\mathcal{O}(N)$, N being number of Chebyshev modes) independent of time, making long time simulations no more expensive than short time. This is useful to compute statistics in turbulent simulations.
- The effect of history can be recorded (with fixed memory size), enabling simulations to be restarted. Such a restart is impossible in other techniques owing to exponentially large memory costs in evaluating the integral. While preparing the manuscript we became aware of the work of [105] who approximate the history kernel by a summation of exponentials and achieve the desired accuracy. However we would like to highlight that our technique does not make any approximation to the kernel and we show later that all information due to history can be stored in a variable whose computation is of fixed memory throughout particle evolution. Moreover the form of the solution in

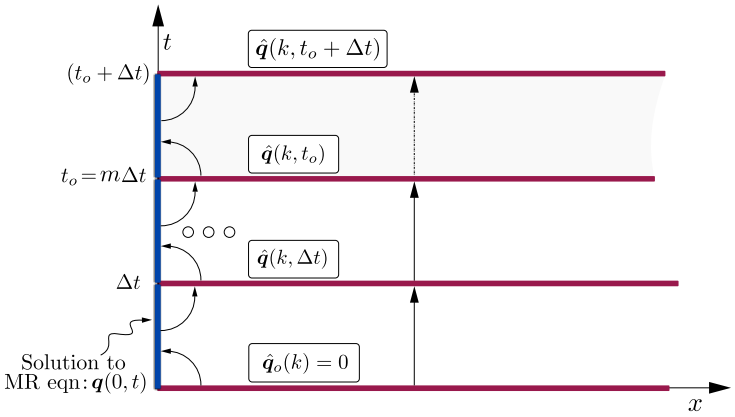

Figure 5.9: Schematic showing numerical scheme where we evaluate $\hat{\boldsymbol{q}}(k,t)$ at intervals t_o, $(t_o + \Delta t)$ from the solution at $t \in [t_o - \Delta t, t_o]$, $[t_o, t_o + \Delta t]$ and so on in order to eliminate the need to store $\boldsymbol{q}(0,t)$ from $t \in [0, t_o + \Delta t]$.

equation (5.33) is specially useful for studying asymptotic behaviour (ref. [136]), unlike other techniques.

In the following subsection we derive the equations we ultimately solve for the particle trajectory and in the subsequent subsection we provide the details of the numerical implementation.

Evolution equation for Basset history-integral

We begin by dividing the $x - t$ plane into domains of size $[0, \infty) \times [t_o - \Delta t, t_o]$, where $t_o = m\Delta t$ for some integer m, as shown in figure 5.9. Our procedure involves two steps, repeated for each such domain:

1. Using the initial condition $\boldsymbol{q}(x, t_o - \Delta t)$ in each domain (bottom wall of that domain in the figure), we compute the boundary condition $\boldsymbol{q}(0,t), t \in (t_o - \Delta t, t_o]$ (left wall of that domain). This is done by solving the Maxey-Riley equation, in the form given by equation (5.57) below. This equation is the extension of (5.33) to the case of arbitrary initial conditions. Moreover the forcing $\boldsymbol{f}$ is now a function of $\boldsymbol{q}(0,t)$ and/or $\boldsymbol{y}(t)$. So we start with a guess for $\boldsymbol{q}(0,t)$ and $\boldsymbol{y}(t)$, and iterate using a nonlinear solver. We thus have the Dirichlet condition on the left wall of figure 5.9, over $[t_o - \Delta t, t_o]$.

2. Using the computed boundary condition $\boldsymbol{q}(0,t)$ from the previous step and the known initial condition $\boldsymbol{q}(x, t_o - \Delta t)$, we directly compute $\boldsymbol{q}(x, t_o)$, the top wall of that domain, by using equation (5.58) which will be derived below. This step is equivalent

to solving the diffusion equation with a Dirichlet boundary condition and the solution of this boundary-value problem leads to the initial condition for the next domain, $t \in (t_o, t_o + \Delta t]$. Through an efficient use of the global relation, we do not require the explicit solution expression $\boldsymbol{q}(x, t_o)$, but only the Fourier transform $\hat{\boldsymbol{q}}(k, t_o)$ which simplifies the calculations considerably.

We recognise that our system size (namely, the number of dependent variables) is higher for a nonlinear case, and this is the price we need to pay to eliminate the rising memory costs coming from the nonlocal time integral term.

In the first domain alone $[0, \infty) \times [0, \Delta t]$, equation (5.33) may be used to obtain the particle velocity. We recognise that $\boldsymbol{f}$ now depends on $\boldsymbol{y}$ and $\boldsymbol{q}(0, t)$. Along with (5.24), where we set $T = \Delta t$, we now have two equations for two unknowns $\boldsymbol{y}$ and $\boldsymbol{q}(0, t)$ over the time interval $[0, \Delta t]$. In a standard numerical method, one would approximate the first integral of (5.33) using a quadrature rule. We however, adopt an alternative route (partly to ensure accuracy) by representing the unknowns $\boldsymbol{q}(0, t)$ and $\boldsymbol{y}(t)$ in terms of Chebyshev polynomials over the interval $[0, \Delta t]$. All integrals are readily evaluated to a high degree of accuracy. With the Chebyshev polynomial representation, equations (5.33) and (5.24) are solved using a nonlinear solver, here Newton's method, for the coefficients of the Chebyshev polynomials. Once we have $\boldsymbol{q}(0, t)$ (in terms of Chebyshev polynomials), we solve the diffusion equation with this *Dirichlet condition* to obtain the solution $\boldsymbol{q}(x, \Delta t)$. The evaluation of such new initial conditions at every $(t_o = m\Delta t)$ is possible precisely because of the relationship between Basset history integral and Neumann-condition to diffusion equation.

In all later domains, the initial condition $\boldsymbol{q}(x, t_o)$ is no longer zero. Indeed $\boldsymbol{q}(x, t_o)$ is the solution of the diffusion equation at this time. The global relation of the diffusion equation in the time interval $t \in (t_o, t_o + \Delta t]$ can be written as

$$\mathrm{e}^{k^2(t_o+\Delta t)}\hat{\boldsymbol{q}}(k, (t_o + \Delta t)) = \mathrm{e}^{k^2 t_o}\hat{\boldsymbol{q}}(k, t_o) - ik\tilde{\boldsymbol{g}}_o(k^2, t_o, t_o + \Delta t) - \tilde{\boldsymbol{g}}_1(k^2, t_o, t_o + \Delta t),\ k \in \mathbb{C}^-. \tag{5.56}$$

For the boundary terms represented by $\tilde{\boldsymbol{g}}_i(k^2, t_1, t_2)$, we have introduced the additional arguments t_1, t_2, which are the limits of the integral defining the time transform. This notation is also used in the forcing, as $\tilde{\boldsymbol{f}}(k^2, t_1, t_2)$. Following a procedure similar to that employed to

derive equation (5.31), we obtain the following expression for $\boldsymbol{q}(0,t)$

$$-\frac{\pi}{2}\boldsymbol{q}(0,t) = \underbrace{\int_0^\infty k\mathrm{e}^{-k^2(t-t_o)}\Im\{\mathscr{H}(k,t_o)\}\,\mathrm{d}k}_{\mathcal{H}(t)} + \underbrace{\int_0^\infty \Im\left\{\frac{k\mathrm{e}^{-k^2t}\tilde{\boldsymbol{f}}(k^2,t_o,t)}{(\alpha-k^2+ik\gamma)}\right\}\mathrm{d}k}_{\mathcal{F}(t)}, \quad t\in(t_o,t_o+\Delta t], \tag{5.57}$$

The term $\mathscr{H}(k,t_o)$ in the integrand of the first integral in the expression above, is the modified initial condition given by

$$\mathscr{H}(k,t_o) = \left\{\frac{\boldsymbol{q}(0,t_o)+\gamma\hat{\boldsymbol{q}}(k,t_o)}{(\alpha-k^2+ik\gamma)}\right\}.$$

This term encodes all the information about the history of the particle from $t\in(0,t_o]$. Equation (5.57) is thus the extension of equation (5.33) for a general initial condition to the diffusion equation. The renormalised initial condition $\mathscr{H}(k,t)$ itself evolves in time and this evolution is once again obtained from the global relation, see appendix 7.4.2 for details. We state the relevant equation here.

$$\mathscr{H}(k,t_o) = \mathrm{e}^{-k^2\Delta t}\mathscr{H}(k,t_o-\Delta t) - \underbrace{\mathrm{e}^{-k^2t_o}\int_{t_o-\Delta t}^{t_o}\mathrm{e}^{k^2s}\boldsymbol{q}(0,s)\,\mathrm{d}s}_{\mathscr{I}_1} - \underbrace{\mathrm{e}^{-k^2t_o}\frac{\tilde{\boldsymbol{f}}(k^2,t_o-\Delta t,t_o)}{(\alpha-k^2+ik\gamma)}}_{\mathscr{I}_2}. \tag{5.58}$$

Note all terms on right-hand side of (5.58), including the forcing term, are known since they depend on the previous time interval $[t_o-\Delta t,t_o]$. Equation (5.58) may also be written as a dynamical system for individual modes of history as

$$\dot{\mathscr{H}}(k,t)+k^2\mathscr{H}(k,t) = \boldsymbol{q}(0,t)+\frac{\boldsymbol{f}(t,\boldsymbol{y}(t),\boldsymbol{q}(0,t))}{(\alpha-k^2+ik\gamma)},\ t\in[t_o-\Delta t,t_o]. \tag{5.59}$$

Equations (5.57) and (5.58) represent the solution to the full MR equations for a particle in a time-dependent inhomogeneous flow field. Note the individual modes k of $\mathscr{H}(k,t)$ in equation (5.58) evolve independently. However the expression for the velocity in equation (5.57) depends on all of them, and indeed depends on the integral of the history.

We are now enabled to march repeatedly till any t_o from any $(t_o - \Delta t)$ using the set of initial conditions $\hat{\boldsymbol{q}}(k, t_o - \Delta t)$, solving equation (5.57) for $\boldsymbol{y}(t)$ and $\boldsymbol{q}(0, t)$ in the interval $(t_o - \Delta t)$ to t_o, and using these Dirichlet boundary conditions in equation (5.58) to get $\hat{\boldsymbol{q}}(k, t_o)$. Once again, we emphasize that the above procedure eliminates the need to store the entire particle velocity from the initial time instant. The effect of the Basset history integral is encoded in $\mathscr{H}(k, t)$.

5.5.3 Numerical technique

We now detail a numerical scheme to solve equations (5.57-5.58). The continuous variables t and k are restricted to a set of discrete values over their respective intervals, $t \in (t_o - \Delta t, t_o]$ and $k \in [0, \infty)$, leading to discrete times t_j and discrete wavenumbers k_l where $j = 1, \ldots, L; l = 0, \ldots, N$. In the case of t we employ Chebyshev nodes under an affine transform whereas for k we employ a mapped Chebyshev node appropriate for rational Chebyshev approximations. We then expand $\boldsymbol{q}(0, t)$ and $\mathscr{H}(k, t_o)$ in a Chebyshev polynomial basis $T_n(t)$ (rational Chebyshev polynomials for $\mathscr{H}$). We adopt a collocation approach to solve the resulting nonlinear equation.

The discrete version of equation (5.57) can be written as a nonlinear equation for the coefficients as

$$\mathscr{T}(t_j) \equiv \frac{\pi}{2}\boldsymbol{q}(0, t_j) + \mathcal{H}(t_j) + \mathcal{F}(t_j) = 0, \; t_j = t_o + \frac{\Delta t}{2}\left(1 + \cos\left(\frac{j\pi}{L}\right)\right), \tag{5.60}$$

where $j = 1, \ldots, L$. Details on how to compute each term in the above equation are presented in the Appendix 7.4.3. The contribution from $\mathscr{H}(k, t_o)$ is captured in $\mathcal{H}(t_j)$, whereas the contribution from the nonlinear forcing due to the fluid velocity field is present in $\mathcal{F}(t_j)$. An equation for the position, $\boldsymbol{y}$ can be obtained from the discretised version (5.24). A standard Newton root finder is employed to solve for $\boldsymbol{q}(0, t)$ and $\boldsymbol{y}(t)$ in the time interval $(n\Delta t, (n+1)\Delta t]$ for each $n = 0, 1, \ldots$ with an appropriate initial guess, typically $\boldsymbol{q}(0, t_j) = -2/\pi\mathcal{H}(t_j)$. Equation (5.58) on the other hand is a straightforward integral evaluation using known values of $\boldsymbol{q}(0, t_j)$ and $\mathscr{H}(k_j, t_o - \Delta t)$ from the previous time step. We show in the appendix that expanding $\boldsymbol{q}(0, t)$ and $\mathscr{H}(k, t_o - \Delta t)$ in Chebyshev basis allows us to pre-compute several terms which speeds up evaluation of expressions in (5.58).

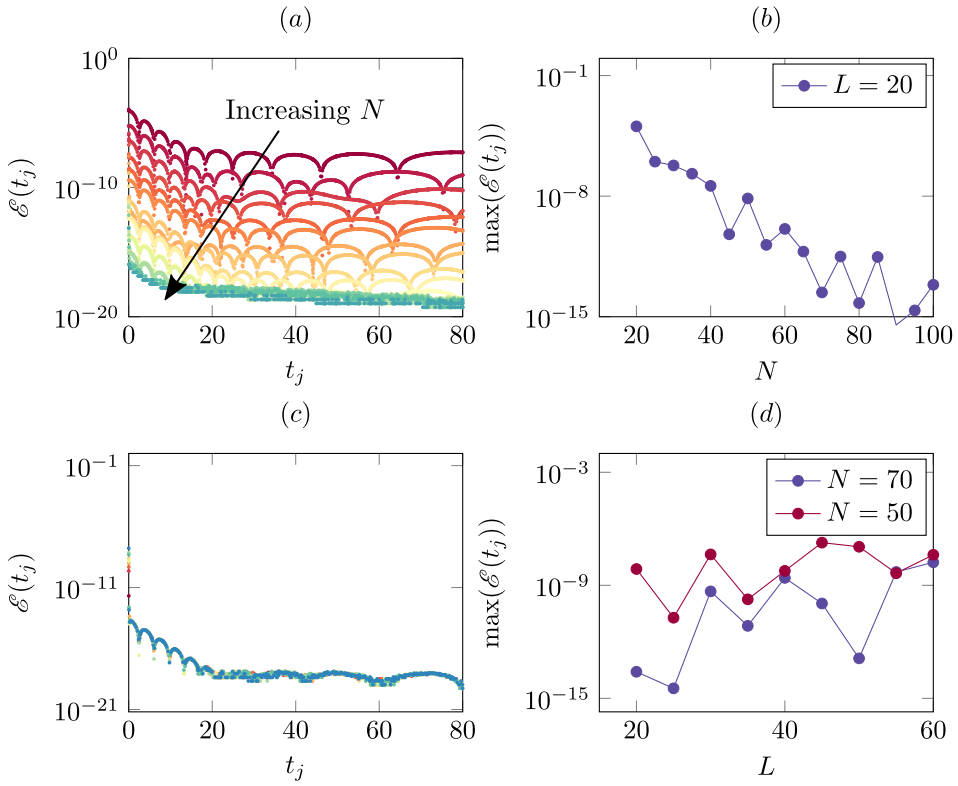

Figure 5.10: Error estimates for the solution to a relaxing particle using the numerical scheme developed in section (5.5.3). Error as a function of time for (a) different values of N at fixed $L = 20$ and (c) different values of L at fixed $N = 50, 70$. $(b), (d)$ Maximum of the error as we increase the number of Chebyshev modes in k and t.

5.5.4 Convergence properties and memory requirement of the numerical scheme

To study convergence of our numerical scheme, we compare the exact velocity of a relaxing particle (for which we have an analytic expression) to the numerical solution obtained from the scheme described above. We first check the numerical method's accuracy as a function of the number of Chebyshev nodes N in wave number $\tilde{k}$, where $\tilde{k}: \ k \in [0, \infty] \rightarrow [-1, 1]$. We also check the accuracy for number of Chebyshev nodes L in $t \in [t_o, t_o + \Delta t]$ within a time interval of length Δt. The error in the calculated solution is given by

$$\mathscr{E}(t_j) = |q^{(1)}(0, t_j) - q_e^{(1)}(0, t_j)|$$

where $q_e^{(1)}(0, t_j)$ is the exact solution evaluated at discrete t_j and $q^{(1)}(0, t_j)$ is the solution evaluated using the present numerical technique. In figure 5.10(a) we plot the error as a function of time for all the number of $\tilde{k}$ chosen and we see its magnitude decrease with increase in N. In figure 5.10(b) we plot the maximum value of $\mathscr{E}(t_j)$. We clearly see that error is small and decreases exponentially with increase in N for fixed $L = 20$. We can reach a desired accuracy by choosing the appropriate number of Chebyshev nodes N. Moving now to the convergence of solution with increase in nodes L in Δt we see there is a general increase in error in figure 5.10(d) for both fixed $N = 50$ and 70. Such a behaviour is expected and not an anomaly. Firstly observe that the maximum error is attained, for all different values of L, N, at the first grid-point i.e. t_1 in $t_j \in (0, \Delta t]$. This is because of the $t^{-1/2}$ singularity at $t = 0$. As we increase the number of Chebyshev nodes in the interval of length Δt, the first Chebyshev grid-point moves closer to this singularity. We can easily account for this behaviour by increasing the number of modes in space N. We show this by increasing the spatial Chebyshev modes from $N = 50$ to 70 in figure 5.10(d) which results in a drop in the maximum error.

We emphasize the advantage a Chebyshev basis provides in terms of computational efficiency. In order to compute the Chebyshev coefficients via the Discrete Chebyshev Transform (`DCT`), we only require $\mathcal{O}(N \log N)$ operations where N is the number of Chebyshev modes. This is done by leveraging Fast-Fourier Transform (`FFT`) package to evaluate the `DCT`s involved in the process of computing Chebyshev coefficients.

The memory requirement for our technique comes from storing the variables $\boldsymbol{q}(0, t_j)$ and $\mathscr{H}(k_j, t_o)$. Considering L modes in t_j, N modes in $\tilde{k}_j$ demands only storage of $\mathcal{O}(N +$

L) values for all times. Whereas the other techniques require a linearly increasing memory cost of $\mathcal{O}(t/\Delta t)$. For $N = 30, L = 20$ one requires to store only 50 values which remain fixed throughout the simulation. In this estimate we of course do not account for the pre-computed matrices which turn out to be three $N \times N$ matrices (see Appendix 7.4.3) resulting in another 2700 values for $N = 30$ but this initial cost remains constant and helps in shorter computation time.

5.5.5 Example 5: Single point vortex and caustics

The stationary flow-field corresponding to a single vortex is

$$\boldsymbol{u} = \frac{\Gamma}{2\pi}\hat{e}_z \times \frac{\boldsymbol{y}(t)}{|\boldsymbol{y}|^2}. \tag{5.61}$$

Though this flow field does not have a time varying component, it still has contributions from both $(\boldsymbol{u} \cdot \nabla)\boldsymbol{u}$ and $(\boldsymbol{q}(0,t) \cdot \nabla)\boldsymbol{u}$. This makes the system of evolution equations for particle position, $\boldsymbol{y}(t)$ and velocity, $\boldsymbol{q}(0,t)$ coupled and non-linear. The solution is given by

$$\boldsymbol{y}(t) = \boldsymbol{y}(0) + \int_o^t \boldsymbol{q}(0,s)\,\mathrm{d}s + \int_o^t \frac{\Gamma}{2\pi}\hat{e}_z \times \frac{\boldsymbol{y}(s)}{|\boldsymbol{y}|^2}\,\mathrm{d}s, \tag{5.62}$$

for the velocity evolution

$$\boldsymbol{q}_t(0,t) + \alpha\boldsymbol{q}(0,t) - \gamma\boldsymbol{q}_x(0,t) = \left(\frac{1}{R} - 1\right)(\boldsymbol{u} \cdot \nabla)\boldsymbol{u} - (\boldsymbol{q}(0,t) \cdot \nabla)\boldsymbol{u}. \tag{5.63}$$

Using the numerical technique described in the previous section, we solve for position and velocity for a Stokes number of $S = 0.01$, density ratio $\beta = 20$ and plot the radial and angular velocity in figure 5.11(a,b). Different lines in the figure correspond to different initial position separated by a distance of 0.15 though all particles start with a initial velocity of $(0.05, 0.05)$. Once the particles get centrifuged far away from the vortex, the trajectory follows $y^{(r)}(t) \sim t^{1/4}$, where $y(r)$ is the radial distance from the point vortex. Thus the radial velocity, $q^{(r)}(0,t) \sim t^{-3/4}$ as in figure 5.11(c). This long-time behaviour is the same as that obtained by [114] without Basset history. The history integral affects the transient behaviour and the approach to the long-time limit.

We discussed in the introduction about caustics near a vortex. As shown by [114] analyti-

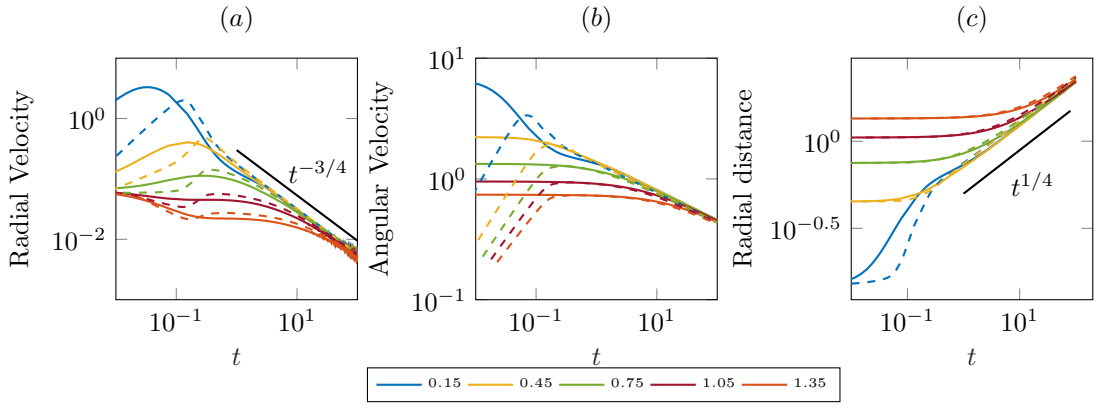

Figure 5.11: (a) Radial velocity, (b) angular velocity and (c) radial distance travelled by particles starting at 5 different locations separated by a non-dimensional distance of 0.15 at $S = 0.01, \beta = 10$ and with initial velocity of $\boldsymbol{v}_o = (0.05, 0.05), \Gamma = 2\pi$, the solid black lines correspond to power-law of $t^{-3/4}, t^{1/4}$. Solid lines represent simulation including the Basset history integral, Stokes drag and added mass effects while the dashed lines are for Stokes drag with added mass.

cally, and in two-dimensional simulations of turbulence, particles inside a critical radius, r_c are evacuated rapidly, resulting in a region of high particle concentration in the neighbourhood of r_c. In order to identify this critical radius including the effects of Basset history, we track the radial separation Δr between two particles that are initially placed close to each other. This is shown in figure 5.12(a) for various initial radial distance r_i from the vortex of the inner particle (the one closer to the vortex). When Δr crosses zero, caustics have occurred. We find that caustics occurs for $r_i \leq 0.44$, i.e., $r_c = 0.44$. for this Stokes number $S = 0.02$. Also, the trajectories of particles that exhibit caustics take different paths compared to ones that do not, in the phase-plane defined by Δv_r vs Δr where Δv_r is the difference in radial velocities for two closely placed particles (see [114]). This is shown in figure 5.12(b) where a negative value of Δv_r implies that the inner particle travels faster than its neighbour. When Δr goes negative it has overtaken its neighbour. Thus trajectories that cross the $y-$axis of the phase-plane form caustics.

In figure 5.12(c) we plot the critical radius, r_c (found by the location where $\min(\Delta r(t))$=0) as a function of the Stokes number S. Simulations with history integral and added mass effects included are shown as solid lines and with just Stokes drag as dotted lines. The history integral and added mass together reduce the region over which caustics are formed, and may cause a reduction in the number densities of particles predicted without the history term.

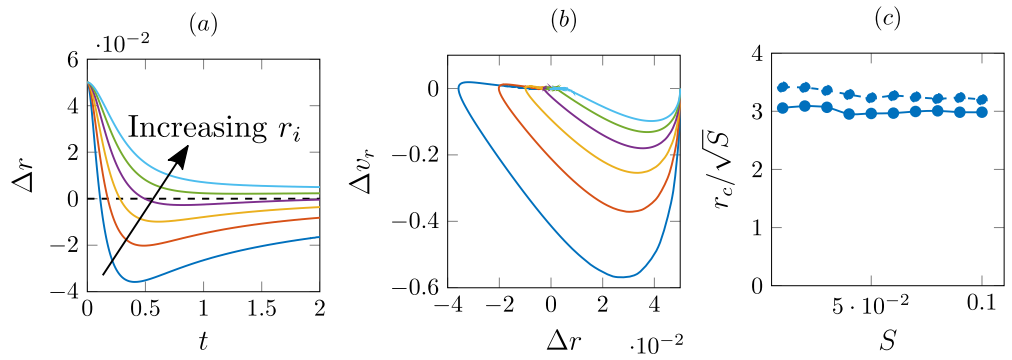

Figure 5.12: (a) Evolution of the difference in radial distance between particles Δr for different initial particle locations r_i separated by a distance 0.05 for Stokes number, $S = 0.02$. The critical particle location at which $\min(\Delta r)$ crosses t-axis is the location of end of caustic formation. (b) The phase-portrait defined by Δv_r the difference in radial velocity vs Δr also shows the transition from caustic formation to no caustic formation with increase in r_i. (c) Critical radius r_c for caustic formation as a function of Stokes number S with history-integral, added mass (solid line) and with Stokes drag alone (dashed line).

The implications for particle dynamics in turbulent fluids flows are beyond the realm of present article and will be explored in our upcoming study.

5.6 Discussion

5.6.1 Interpretation of the Dirichlet-Neumann map

The map that we establish between the Basset history integral and the Neumann condition of the 1-D diffusion equation arises on mathematical grounds, but can also be interpreted physically as follows. The diffusion equation that the variable $\boldsymbol{q}(x,t)$ obeys can be seen as diffusion of momentum from the particle boundary and the Neumann condition $\boldsymbol{q}_x(0,t)$ on the other hand would mean the flux of momentum transferred from the particle boundary in the form of shear stress to the bulk of fluid. The trail left by the particle motion is a consequence of this momentum flux that emanates from the particle boundary which has been shown to arise from the map between Dirichlet-Neumann conditions to diffusion equation. This relation to the diffusion or heat equation further emphasizes the fact that our analysis accounts for the momentum diffusion valid before any convective inertial effects impact the 'wake' generated by the particle.

Geometry	$\mathscr{C}_A$	$\mathscr{C}_a$
Sphere	1	1
Prolate spheroids ($\varkappa > 1$)	$\frac{2[\varkappa \ln(\varkappa + \sqrt{\varkappa^2 - 1}) - \sqrt{\varkappa^2 - 1}]}{\varkappa^2 \sqrt{\varkappa^2 - 1} - \varkappa \ln(\varkappa + \sqrt{\varkappa^2 - 1})}$	$\frac{4(\varkappa^2-1)}{3[(2\varkappa^2-1)\ln\left(\varkappa+\sqrt{1-\varkappa^2}\right)/\sqrt{\varkappa^2-1}-\varkappa]}$
Oblate spheroids ($\varkappa < 1$)	$\frac{2[\varkappa \cos^{-1}\varkappa - \sqrt{1-\varkappa^2}]}{\varkappa^2\sqrt{1-\varkappa^2} - \varkappa\cos^{-1}\varkappa}$	$\frac{4(1-\varkappa^2)}{3[(1-2\varkappa^2)\cos^{-1}\left(\varkappa/\sqrt{1-\varkappa^2}\right)+\varkappa]}$
Disk	$\left(\frac{4}{\pi}\right)$	$\left(\frac{8}{3\pi}\right)$

Table 5.1: Comparison of drag-coefficients [29] of different particle shapes where $\varkappa$ is the aspect ratio of spheroid, $\mathscr{C}_A$ is the additional coefficient for added mass term, $\mathscr{C}_a$ is the additional coefficient for stokes drag, $\mathscr{C}_H = \mathscr{C}_a^2$ is in front of Basset history integral.

5.6.2 Different geometries

In the present manuscript, we have focussed on our reformulation of the Maxey-Riley equation for spherical particles. The technique used employed here is, however, general and extends immediately to other particle shapes. The only additional requirement for spheroids and disks travelling parallel to their axis of symmetry is the redefinition of the three non-dimensional quantities

$$\hat{\beta} = \beta/\mathscr{C}_A, \quad \hat{\alpha} = \mathscr{C}_a\alpha, \text{and} \quad \hat{\gamma} = \mathscr{C}_H\gamma,$$

which respectively appear in equation (5.2) as coefficients to the added mass term, the Stokes drag term and the Basset history integral. In table 5.1 we show how these quantities vary from that of a sphere as the aspect ratio $\varkappa$ is varied. The solution for all time-dependent spatially homogeneous flows can now be easily written for all these geometries as

$$-\pi\boldsymbol{q}(0,t) = \int_{\partial\mathcal{D}^-} \frac{ik\mathrm{e}^{-k^2t}\tilde{\boldsymbol{f}}(k)}{(\hat{\alpha} - k^2 + ik\hat{\gamma})}\,\mathrm{d}k - \int_{-\infty}^{\infty} \frac{\boldsymbol{v}_o ik\mathrm{e}^{-k^2t}}{(\hat{\alpha} - k^2 + ik\hat{\gamma})}\,\mathrm{d}k. \tag{5.64}$$

The numerical method developed for spatially non-linear time dependent flow fields is usable without any change.

5.6.3 Implications to physical scenarios

In this paper we explored a range of scenarios, from that of a particle relaxing to zero velocity from a given initial velocity to a particle in a non-linear flow such as the point-vortex. Real

flow situations are often describable by a combination of these simple flow situations. Our results on the droplet growth highlight that for raindrop formation rates, the Basset history integral is important. Our exact solutions for oscillating flow can directly be used to study particle dynamics in synthetic turbulence, defined by a superposition of sinusoidal forcing of different frequencies (see e.g. [105]). As has been shown in [114] the behaviour of the particle in the presence of a point vortex is directly applicable to 2-D turbulence. The fact that the critical radius for caustic formation shrinks will have implications for droplet clustering.

5.7 Conclusion

The Maxey-Riley equation has been used extensively by researchers, but most often by neglecting the history integral, primarily due to the difficulty in handling this term. The nonlocality in this term has been the barrier in terms of numerical progress as memory requirements keep increasing with time. This is a major hurdle especially when a large number of particles need to be simulated in high Reynolds number turbulence. Another barrier was that restarting a simulation with history integrals was practically impossible, owing to exponentially large storage requirements. Both these issues have been addressed in this paper by reformulating the Maxey-Riley equation as a boundary condition of the 1-D diffusion equation. Several analytical solutions to the complete Maxey-Riley equation, which can form the basis for gradient expansions in more complicated background flows, have been obtained. Our analysis suggests that the Basset history may not be categorised as an additional drag on a particle. Its effect on particle velocity is seen to cause a more rapid stretched-exponential decay at short times and a power-law at long times. Basset history, we show, has effects on particles settling under gravity, droplet growth rate and migration in a simple shear, in all of which neglecting this term would result in a qualitatively different (and incorrect) prediction. Our numerical scheme is the first spectrally accurate method to our knowledge for the complete Maxey-Riley equation. Its implementation is straightforward, since Chebyshev coefficients can be computed efficiently using the `FFTW` package. Several open questions, e.g. regarding statistical properties of particles in homogeneous isotropic turbulence can be studied by this approach, and the effect of Basset history in turbulence understood. The larger question of understanding the MR equation from a dynamical systems perspective is as yet unanswered, as is the question of whether attractors are modified by the history integral.

6

Conclusion and future directions

In this thesis we have considered the role of elasticity and hydrodynamics interaction in determining the behaviour of filaments and spherical particles. We have explored using table top experiments the behaviour of filaments, also supplementing the observations in experiments with a theory that captures the observations accurately. In order to understand the dynamics of tiny rigid spherical particles in a fluid flow we have developed a novel numerical technique that captures the history effects of the particle accurately.

The experiments we have performed have provided the following insights into the mechanics of elastic filaments:

- Large deformation of an elastic filament across its length results in tension inside the filament and this tension modifies the relaxation rate of elastic filaments.
- Large localised deformation of an elastic filament by contact forces such as capillary force can affect large scale features such as contact angle.
- Substrate geometry over which an elastic filament resides plays a vital role in the morphological instabilities of the filament.

We know that a fluid of constant density interacts with other fluid or a solid structure through capillary forces at the fluid interface and viscous forces in the bulk of the fluid. Apart from providing broad insights mentioned above, our experiments and theoretical models

provides a novel way by which fluid forces, both capillary and viscous, can interact with elastic filaments to result in pattern formation in the fluid-elastic system.

In the case of dynamics of particles in fluid flow, our numerical technique opens up a plethora of possible scenarios where the effect of Basset history can be immediately understood. To our knowledge, ours is the only technique which allows for restarting of simulation with the right initial condition for the particles. Beyond the implications with respect to spherical particles, the method mends itself to anisotropic particles such as spheroids. Furthermore, this is the first instance where Unified Transform Method has been used to create a numerical scheme, opening up possibilities to extend our methodology in other fields where this technique is used.

Using the studies conducted here, these are some of the future directions that can be pursued with our results as starting point:

- Filaments in microorganisms are active, with stresses inside the filament arising out of chemical gradients. This stress can easily be accounted in our model and this opens up questions such as motility of microorganisms and their efficiency which is currently a topic of serious research. Beyond single filament dynamics, understanding the collective motion of active filaments with hydrodynamic interaction is a nascent topic in terms of both experiments and theory.

- In chapter 3, we performed experiments to explore only the partial-wetting phase and several features of the partial-wrapping and complete-wetting phase are as yet unexplored. Our quasi-2D experimental setup yields itself to exploring these phases easily.

- Leveraging the wrapping technique for parceling 2D droplet using filaments, shown in chapter 3, we can create an array of 2D droplets. Using this collection of 2D droplets protected by an elastic boundary, we can study difficult questions such as response of collection of 2D soft discs (approximated by the wrapped droplet) to shear and other external forces.

- In order to understand the role of substrate geometry in triggering instabilities, we have only seen the tip of the iceberg. Our results only pertain to the specific case of an elastic filament confined to a sphere. Does a filament behave differently on a hyperbolic surface i.e. surface with negative Gaussian curvature. Moreover, the bigger question of shapes of elastic filaments on an arbitrary 2D surface is as yet unexplored.

- Particle dynamics in fluid flows accounting for Basset history force is shown in our work to be important in several cases. However in order to simulate their dynamics when there are a large number of them, such as in clouds, our numerical method can be difficult to implement. In such a scenario we have proposed in chapter 5 that using

leading order terms in gradient expansion, we can locally approximate flows using linear profiles and evaluate particle dynamics in a simpler way. This remains to be done and can be done immediately using our technique.

- Sedimenting rain droplet from cloud grows in size mainly through collision and the role of history force on this accumulation rate is as yet unknown, both in experiments and through simulation.

Apart from the questions proposed here, which rely on the results presented in this thesis, our experimental tools are useful beyond these questions. Our procedure for preparing thin filaments, measuring tension inside filaments using soft-beams, the fluorescence technique used to visualise thin filaments, and filament tracking technique are useful in a wide variety of contexts.

7 Appendix

All the codes used to extract shape of filament, shape of droplet and bubble are available on GitHub.

7.1 Relaxing elastic filament

7.1.1 Extracting filament shape

The procedure we follow to track the filament in the relaxing filament experiments involves a series of processes. They are:

- Extracting image sequence from experiments that capture the dynamics of the filament. Then trimming the image to the region of interest where the filament is situated. Such a trimmed image is shown in fig. 7.1(a).
- The trimmed image is then passed through thresholding to capture its boundaries and then a pruning procedure. This procedure is intended to capture the centerline of the filament. We get an image like the one shown in fig. 7.1(b).
- After capturing the discrete pixels along the filament centerline, we have to arrange these pixel coordinates in the right order, so that we can then calculate the arc-length form of the filament centerline. In order to do this, we borrow the technique developed to create formulas for any curve on Wolfram Blog. This technique chooses a

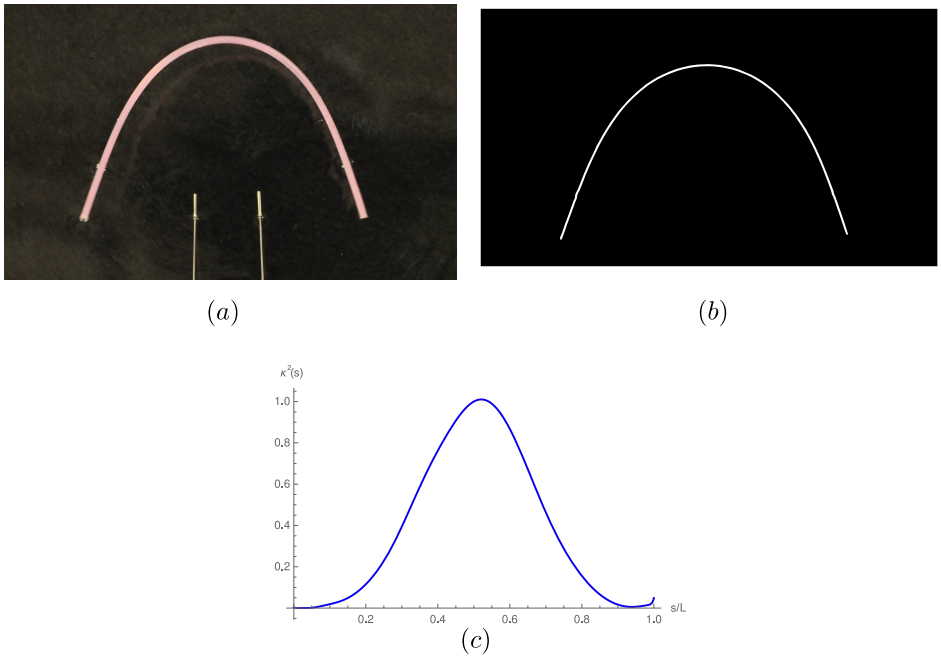

Figure 7.1: (a) Experimental image of the filament (in pink), (b) extracted shape of the filament centerline, (c) calculated square of curvature along the filament arc-length using B-Spline fit to the shape in (b) after arranging the pixel coordinates in right order.

random pixel in the image and then looks around in the neighbourhood for points and arranges them in an array such that nearest ones are next in the array while farther ones appear later in the array.

- After arranging the points in the right order, we then fit B-Spline curve to these points.
- Using the fit B-Spline, we calculate the curvature along the filament. We plot in fig. 7.1(c) the square of curvature computed from the image shown fig. 7.1(a).

7.1.2 Expression for $L(t)$

The evolution of vectors at the boundary of the filament can be written as:

$$\bar{\mu}\partial_t \boldsymbol{r}|_0 = -\boldsymbol{r}_{ssss}|_0 + [\boldsymbol{r}_s \partial_s T(s)]|_0 \tag{7.1}$$

$$\bar{\mu}\partial_t \boldsymbol{r}|_L = -\boldsymbol{r}_{ssss}|_L + [\boldsymbol{r}_s \partial_s T(s)]|_L \tag{7.2}$$

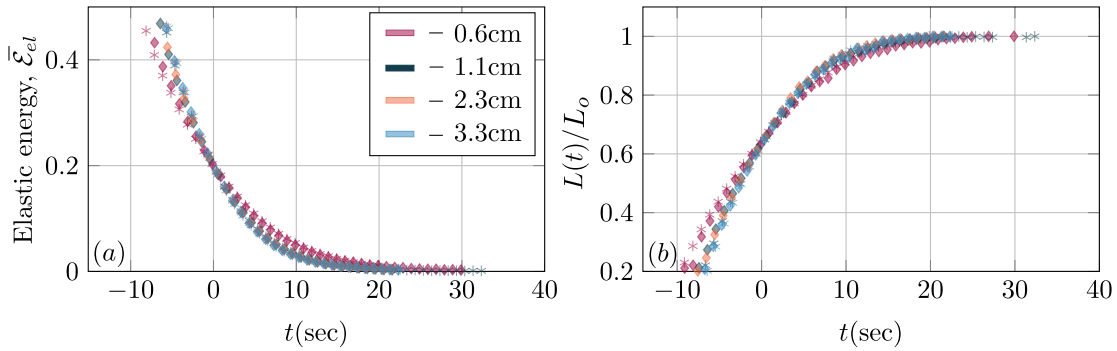

Figure 7.2: (a) Energy, (b) end-to-end distance for different heights of glycerol. We do not see any significant effect except at the shallowest height of $0.6cm$.

For symmetric initial conditions that we use in experiments, we can write:

$$\boldsymbol{r}_{ssss}|_0 = \boldsymbol{r}_{ssss}|_L$$
$$\partial_s T(s)|_0 = -\partial_s T(s)|_L$$

Now using these the vector connecting the ends evolves as,

$$\bar{\mu}\partial_t(\boldsymbol{r}|_0 - \boldsymbol{r}|_L) = \partial_s T(s,t)|_0[\boldsymbol{r}_s|_0 + \boldsymbol{r}_s|_L] \tag{7.3}$$
$$\bar{\mu}\partial_t \bar{L}(t)\boldsymbol{e_x} = 2\partial_s T(s,t)|_0 \cos(\theta(t))\boldsymbol{e_x} \tag{7.4}$$

where $\theta(t)$ is the angle between the tangent vector at $s = 0$ and the horizontal. This shows that the end-to-end distance depends only on the gradient of tension at the boundary and bending is eliminated from the equation.

7.1.3 Independence of height of glycerol

One might be concerned that the relaxation dynamics would be affected by the depth of the glycerol in the container. In our experiments, the filament is placed at the glycerol-air interface. We report here the minimum height of glycerol required in the beaker for the filament relaxation dynamics to be not affected by the volume of glycerol in the container. Fig. 7.2 shows the relaxation for four different height: $h = 0.6cm, 1.1cm, 2.3cm, 3.3cm$. We see that for height greater than $0.6cm$, the dynamics remain the same. Thus in all our experiments, a height greater than $3.3cm$ is used.

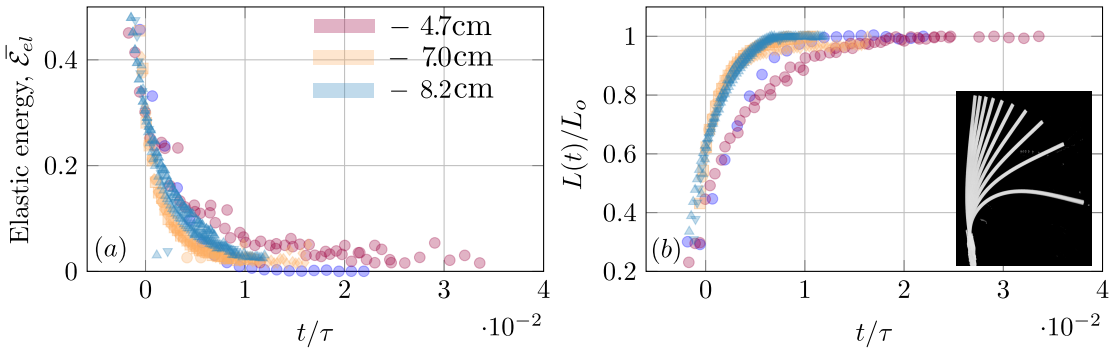

Figure 7.3: $\bar{\mathcal{E}}_{el}$ and $L(t)/L_o$ vs t/τ for a filament with one end clamped and the other end deformed. $L(t)$ is obtained by mirroring the image about the normal at the hinged end. The effective length calculated by combining the mirrored image and the normal relaxation is represented by L_o. Blue circles correspond to relaxation of the symmetric initial configuration described earlier.

7.1.4 Effect of hydrodynamic interaction

The model used to simulate the filament neglects the hydrodynamic interaction between different points along the filament as mentioned in the main text. But these interactions are present in the experiments and thus to see if the relaxation is radically modified by these interactions, we perform the following experiment. We clamp one end of the filament and deform the other end and let it relax from this configuration. The relaxation is mirrored about the normal at the fixed end and the effective length of this combined filament is L_o. Now $L(t)$ is calculated for this combined picture that consists both the mirrored part and the actual relaxation. Fig. 7.3 shows $\bar{\mathcal{E}}_{el}$ vs t/τ and $L(t)/L_o$ vs t/τ for three different lengths and we see that the collapse is spread. The blue rounds are that of the symmetric relaxation from earlier experiments. Though this does not conclusively quantify the effect of hydrodynamic interaction, we see that τ is not exorbitantly modified.

7.1.5 Effect of contact angle

The Bond number for the stiffer VPS measured is 5.6×10^{-3} and that of softer VPS is 3.0×10^{-2} and thus effects of density can be neglected. We have measured the wetting properties of glycerol over VPS and validate our approximation that the motion of the filament is 2D. We see that,

The effective diameter of filament under contact with glycerol for two diameters - $1.04mm$,

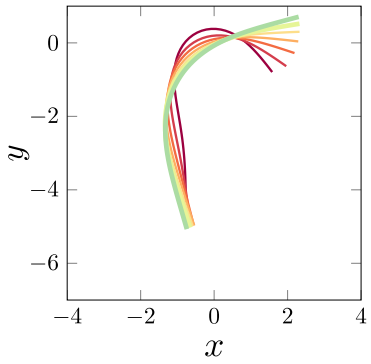

(a) (b)

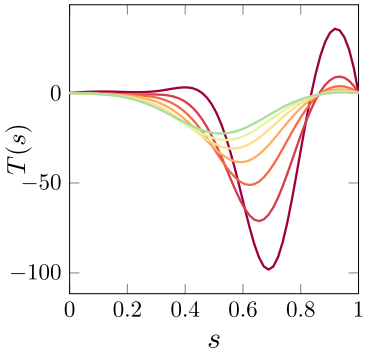

(c) (d)

Figure 7.4: (a, c) Two arbitrary asymmetric initial conditions relaxing to symmetric states with (b, d) showing similar behaviour from numerics. (d) We see that the tension, $T(s)$ moves towards regions of zero bending force and becomes symmetric. Even after symmetrising, the tension is still of finite amplitude, indicating that the system is still non-linear.

Contact angle of stiffer VPS	102.4^o
Contact angle of softer VPS	94.6^o
Density of softer VPS	$1.02g/cc$
Density of stiffer VPS	$1.18g/cc$
Density of glycerol	$1.216g/cc$

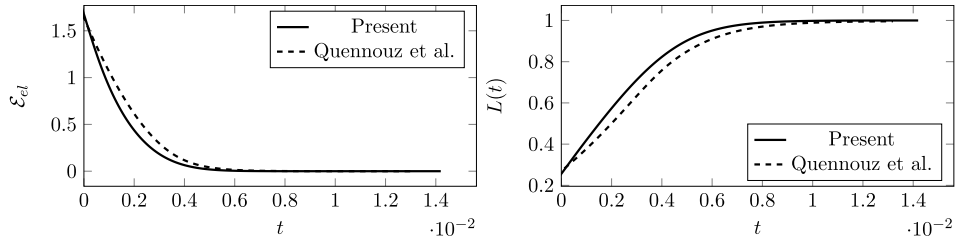

Figure 7.5: Results comparing the method used in Quennouz et al. [112] assuming anisotropic drag for the filament with that of the present technique without anisotropic drag.

$0.57mm$ used in our experiments is now (see fig.2 of main article): $d = 1.0367mm, 0.5682mm$ for stiffer VPS and $1.0159mm$, $0.5568mm$ for softer VPS. This shows that the contact area of the filament is approximately half that of the surface area of the filament (neglecting surface defects). It is also worth noting that the dependence of the drag force per unit length on the cylinder has only a logarithmic dependence on the cylinder diameter, making the effect weak. This we believe is the reason behind minimal contribution of contact angle effects on the factor of 4.2 in the article. Fischer et. al.[49] point out this drag dependence on the interface Boussinesq number (see their fig. 2). For a length-to-diameter ratio of $\sim$ 100, as in our experiments, they observe a strong dependence on the interfacial Boussinesq number. A discussion regarding this has been added to the experimental methods section.

7.1.6 Anisotropic drag

We implemented the drag in Quennouz et al. [112] and we plot below in fig. 7.5 a comparison of implementations of the anisotropic and isotropic drag. As expected, we see relatively small effects of the anisotropy due to movement primarily along the normal direction of the filament. We have proceeded with the isotropic implementation, as the drag coefficients are then independent of the aspect ratio L/d. This allows us to collapse the primary variations in the experimental data, without worrying about the smaller effects of the anisotropy.

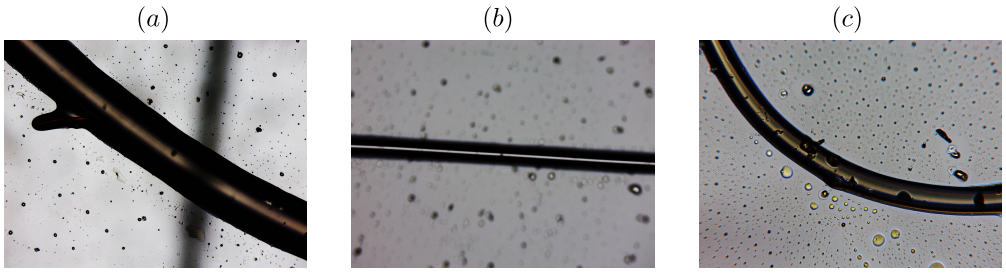

Figure 7.6: Filaments made out of PDMS imaged under a microscope. These filaments have a diameter of $(a)30\mu$m, $(b)80\mu$m and $(c)190\mu$m.

7.2 Wrapping experiments

7.2.1 Making thin PDMS filaments

Here describe briefly the procedure we follow to make thin elastic filaments.

- In order to make PDMS filaments we need Sylgard 184 Silicone Elastomer Kit and Accelerator.
- We take the polymer base, accelerator and cross-linker in the ratio 1:2:10. And mix it in a petri dish.
- We centrifuge the mixture to remove bubbles.
- Once the mixture starts to settle, we wait for a time window between 35-45 minutes at room temperature before we make filaments.
- Within this time window we find that the mixture is neither a solid nor a liquid but in a state of transition between the two phases. Now we take a droplet of this mixture in a capillary tube and pull this droplet using tweezers.
- The pulling process results in a long thread which can then be hanged.
- Once the filament sets to a solid, which takes place within 2 hours after mixing the ingredients, we can use them in our experiments.

After making these filaments we inspect them under a microscope to check for the uniformity of the filament diameter. In fig. 7.6 we show some of the filaments made using this procedure.

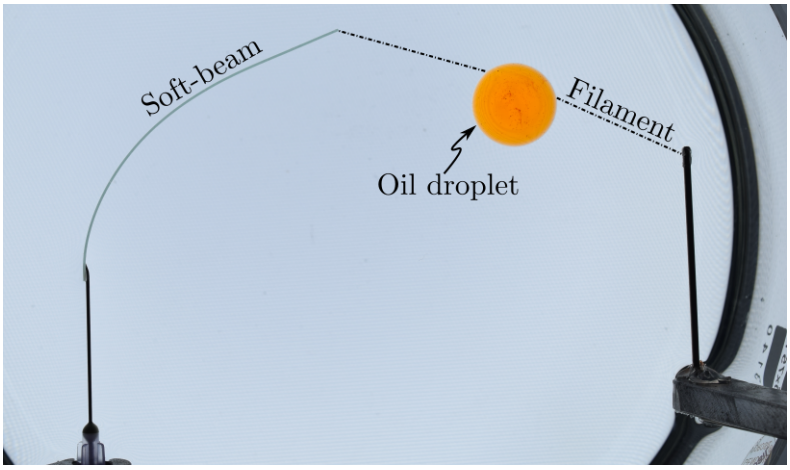

Figure 7.7: Image of the experimental setup with floating droplet in orange (due to Sudan Red dye). One end of the filament is attached to the soft-beam whose end displacement is used to measure tension. The other end of the filament is attached to a rigid rod which is attached to a translational stage. Soft-beam diameter if 0.5mm for scale.

7.2.2 2-D EXPERIMENTAL SETUP

The experimental setup for the contact angle and wrapping experiments involve a droplet floating at air-water interface. In fig. 7.7 we show the setup with all the components. The soft beam in turquoise colour, attached to one end of the filament, is made out of VPS and is connected to the end of a needle. These filaments are fabricated using the same procedure described in chapter 2, using capillary tubes. The other end of the filament is attached to a rigid rod. This rigid rod is then attached to a micrometer translational stage whose displacement controls the tension in the filament. We attach the filament to the soft-beam as well as the rigid rod using Fevikwik cyanoacrylate.

7.2.3 FLUORESCENCE EXPERIMENTS

In the fluorescence experiments discussed in chapter 3 we use Nile Red dye mixed in Ethanol to coat the filament and then let ethanol evaporate. The dyed filament is floated at the interface of the water bath. Using cylindrical lens we convert the circular cross-section of the laser beam into a sheet. We then shine this sheet of laser close to the interface and capture the shape of filament after filtering using a red filter.

We have shown in chapter 3 the shape captured using fluorescence on in high bendability

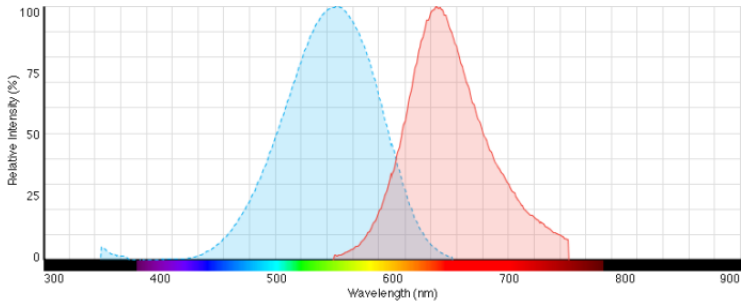

Figure 7.8: Fluorescence spectra of Nile Red. We shine laser in the green part of the spectrum and the emissions happen in the red part. (Image credit: Thermo Fisher)

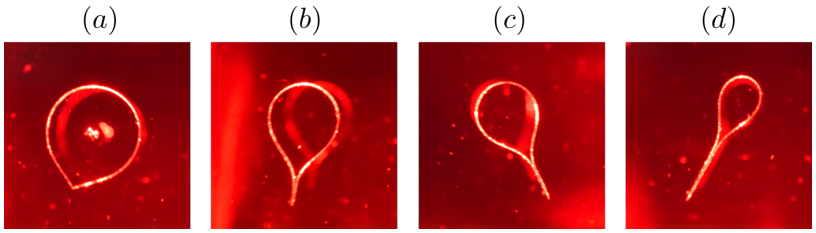

Figure 7.9: Shapes of filament captured using fluorescence post self-contact. $(a-d)$ shows the shapes as we keep decreasing the volume of oil droplet.

and one in low bendability before the filament is wrapped. Here in fig. 7.9 we show the image of filament shapes post wrapping where the filament is in self-contact.

7.2.4 Measuring contact angle

In order to extract the contact angle from the experimental images, we use the following technique.

- Colour the droplet alone such that it is visible in a uniform light.
- Threshold the droplet image to get the boundary of the droplet.
- Calculate the curvature along the boundary of the droplet to identify shart corners. These sharp corners represent the droplet-filament contact lines. An example of the experimental image superposed with extracted droplet boundary and contact line is shown in fig. 7.9(a).
- After finding these contact lines, we need the slope information to extract the contact angles. In order to identify the right point to estimate the slope, we estimate the angle as a function of the points along the droplet next to the contact line. In fig. 7.9(b) we

plot the angles estimated as a function of the index of point from contact line, on both sides (left contact line, right contact line) of the droplet.

- We choose the slope using the point where $(\vartheta + \phi)$ plateaus in fig. 7.9(c).

7.2.5 Pinning effects of droplet contact line with filament

In order to understand the pinning effects of droplet contact line with the elastic filament, we experiments to see if there is any hysteresis in the ϑ, ϕ vs R_b, R_d plane. We start the experiments by decreasing the boundary tension of the filament and after sufficiently small tension value, we increasing it. In fig. 7.9(c) we plot estimated values of ϑ, ϕ as a function of R_d, R_b. We see that the fluctuation in the values of contact angles is small and thus we neglect the effects of contact line pinning.

7.3 Coiling experiments

7.3.1 Experimental set up and details

The experimental setup used in the coiling experiments consists of a capillary tube at whose end hangs the bubble, a filament holder, mirror to get the bottom view of bubble, uniform light source, and a camera. This setup is shown in fig. 7.11, mounted on a stainless steel breadboard. The bubble is blown out of a syringe connected to a micropump.

The soap solution used to make these bubbles are made out of DAWN soap solution with a high concentration of glycerol to reduce drainage in the bubble. The volume ratio of soap solution to glycerol in our bubbles is 1:3. In our experiments we reduce the bubble size for a fixed filament size, and we find that bubble solution with this concentration is stable up to 15 minutes. Another aspect in our experiments is that we do not want the surface energy of the filament affecting the filament shape thus we coat the filament with soap solution before feeding onto the bubble surface.

In order to make the filament visible under uniform light, we coat the filament with Sudan Red using the same procedure described earlier for PDMS filaments. However for silicone filaments used in coiling experiments we found that if the filament is coated with Sudan Red + Ethanol while the filament rests on a micro-slide, the filament gained natural curvature after Ethanol evaporates. In order to avoid this natural curvature, we created a bath of Sudan Red

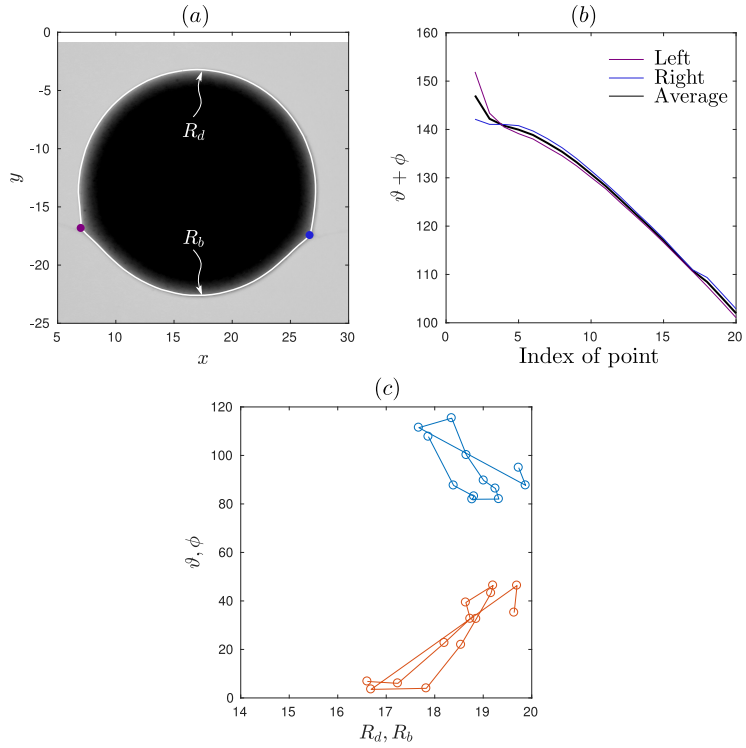

Figure 7.10: (a) Extracted shape of droplet from experiment super-imposed over the experimental image. Dots are the corners representing the contact line of droplet. R_b, R_d are the radius of curvature of the buckled zone and droplet. (b) Calculated value of $(\vartheta + \phi)$ as a function of the index of point from the contact line used to estimage ϑ, ϕ. (c) Estimated value of θ, ϕ as a function of R_d, R_b (in mm) from experiments for repeated cycles of increase and decrease of tension in the filament.

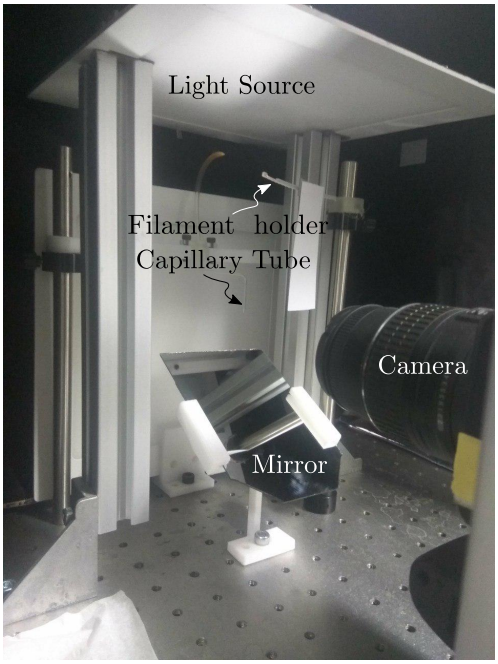

Figure 7.11: Photo of the experimental setup used in the coiling experiments in chapter 4. The bubble is held at the end of the capillary tube. The filament holder is used to feed the filament onto the bubble surface. We use mirror to observe the bottom view of the bubble to get the shape of the coils. The setup is lit from the top of the bubble and behind the bubble.

+ Ethanol and floated the filament at the interface of this bath. After removing the filament from this bath, we dry the filament by hanging with one end fixed. This procedure we find resulted in straight filaments but now with a layer of Sudan Red, making the filament visible when imaged.

7.4 History effects on particle dynamics

7.4.1 Dirichlet to Neumann map

For the convenience of the reader, we present here the details of the Dirichlet to Neumann map for the diffusion equation. This calculation may also be found in [50]. We begin with the global relation for the 1-D diffusion equation, equation (5.14), and derive an expression for $\boldsymbol{q}_x(0,t)$ in terms of $\boldsymbol{q}(0,t)$. To do so we multiply (5.14) by $ik\mathrm{e}^{-\omega(k)t}$, for $0 < t < T$, and integrate over the contour $\partial\mathcal{D}^-$ as depicted in figure 5.2(b). We denote by $\mathcal{D}^-$ ($\mathcal{D}^+$) the regions of the complex$-k$ plane where $\Re(\omega(k) = k^2) < 0$ and $\Im(k) < 0$ (respectively, $\Im(k) > 0$). Note for $k \in \mathcal{D}^{\pm}$, $\mathrm{e}^{\omega(k)t}$ is bounded and decaying for $t > 0$ as $k \to \infty$. We now have

$$\int_{\partial\mathcal{D}^-} [ik\mathrm{e}^{\omega(k)(T-t)}\hat{\boldsymbol{q}}(k,T) + ik\mathrm{e}^{-\omega(k)t}(\tilde{\boldsymbol{g}}_1 + ik\tilde{\boldsymbol{g}}_o)]\,\mathrm{d}k = 0. \tag{7.5}$$

The first term in the integral affords no contribution. This follows by noting that the integral of this term along $\mathcal{C}_R$, see figure 5.2(b), vanishes as $R \to \infty$ for $(T-t) > 0$. Moreover since there are no poles in $\mathcal{D}^-$, the integral of the first term along the contour $\partial\mathcal{D}^-$ is also zero. Next we employ the definition of $\tilde{\boldsymbol{g}}_0$ and $\tilde{\boldsymbol{g}}_1$ to obtain

$$\int_{\partial\mathcal{D}^-} \left[ik \int_o^T \mathrm{e}^{\omega(k)(s-t)}\boldsymbol{q}_x(0,s)\,\mathrm{d}s - k^2 \int_o^T \mathrm{e}^{\omega(k)(s-t)}\boldsymbol{q}(0,s)\,\mathrm{d}s \right] \mathrm{d}k = 0. \tag{7.6}$$

The integrand of the contour integral in the above expression consists of the sum of two terms. For the first term we substitute $k^2 = il,\ l \in \mathbb{R}$ to obtain

$$-\frac{1}{2}\int_0^T \int_{-\infty}^{\infty} \mathrm{e}^{-il(t-s)}\boldsymbol{q}_x(0,s)\,\mathrm{d}l\,\mathrm{d}s - \int_{\partial\mathcal{D}^-} k^2 \left(\int_0^T \mathrm{e}^{k^2(s-t)}\boldsymbol{q}(0,s)\,\mathrm{d}s \right) \mathrm{d}k = 0. \tag{7.7}$$

The Fourier inversion theorem then allows us to replace the first term with the Neumann condition $\boldsymbol{q}_x(0,t)$. The second term on the left-hand side may be simplified as follows. First

we integrate by parts once and then deform the integral from $\partial\mathcal{D}^-$ to the real line

$$-\pi \boldsymbol{q}_x(0,t) - \int_{\partial\mathcal{D}^-} k^2 \left[\left(\frac{\mathrm{e}^{k^2(T-t)}\boldsymbol{q}(0,T) - \mathrm{e}^{-k^2 t}\boldsymbol{q}(0,0)}{k^2} \right) - \int_0^T \mathrm{e}^{k^2(s-t)}\dot{\boldsymbol{q}}(0,s)\,\mathrm{d}s \right] \mathrm{d}k = 0, \tag{7.8}$$

$$\begin{aligned} \Rightarrow -\pi \boldsymbol{q}_x(0,t) &- \int_{-\infty}^{\infty} \mathrm{e}^{-k^2 t}\boldsymbol{q}(0,0)\,\mathrm{d}k \\ &- \int_{\partial\mathcal{D}^-} \left[\mathrm{e}^{k^2(T-t)}\boldsymbol{q}(0,T) - \left(\int_0^t + \int_t^T \right) \mathrm{e}^{k^2(s-t)}\dot{\boldsymbol{q}}(0,s)\,\mathrm{d}s \right] \mathrm{d}k = 0, \end{aligned} \tag{7.9}$$

$$\Rightarrow -\pi \boldsymbol{q}_x(0,t) - \sqrt{\frac{\pi}{t}}\boldsymbol{q}(0,0) - \int_{-\infty}^{\infty}\int_0^t \mathrm{e}^{k^2(s-t)}\dot{\boldsymbol{q}}(0,s)\,\mathrm{d}s\,\mathrm{d}k = 0. \tag{7.10}$$

The last term of (7.9) consists of an integral over $s \in (t,T]$. This term vanishes since for $(s-t) > 0$, $\mathrm{e}^{k^2(s-t)}$ is analytic, bounded and decays at infinity for $k \in \mathcal{D}^-$. An appeal to Jordan's lemma assures us that the contribution from this term is zero. A similar argument implies the term with $\boldsymbol{q}(0,T)$ also vanishes. Switching the order of integrations for the integral term in (7.10) leads to the final expression for the Dirichlet to Neumann map

$$\boldsymbol{q}_x(0,t) = -\sqrt{\frac{1}{\pi t}}\boldsymbol{q}(0,0) - \frac{1}{\sqrt{\pi}}\int_0^t \frac{\dot{\boldsymbol{q}}(0,s)}{\sqrt{t-s}}\,\mathrm{d}s. \tag{7.11}$$

7.4.2 History evolution

Multiplying the boundary condition (5.23) by $\mathrm{e}^{k^2 t}$ and integrating over $t \in [t_o, t_o + \Delta t]$ leads to

$$\begin{aligned} \mathrm{e}^{k^2(t_o+\Delta T)}\boldsymbol{q}(0,t_o+\Delta t) - \mathrm{e}^{k^2 t_o}\boldsymbol{q}(0,t_o) + (\alpha - k^2)\tilde{\boldsymbol{g}}_o(k^2,t_o,t_o+\Delta t) \\ - \gamma\tilde{\boldsymbol{g}}_1(k^2,t_o,t_o+\Delta t) = \tilde{\boldsymbol{f}}(k^2,t_o,t_o+\Delta t). \end{aligned} \tag{7.12}$$

We may now eliminate $\tilde{\boldsymbol{g}}_1(k^2,t_o,t_o+\Delta t)$ in (5.56) using the above expression. Multiplying the resulting expression by $k\mathrm{e}^{-k^2 t}/(\alpha - k^2 + ik\gamma)$ and integrating over $\partial\mathcal{D}^-$ results in the

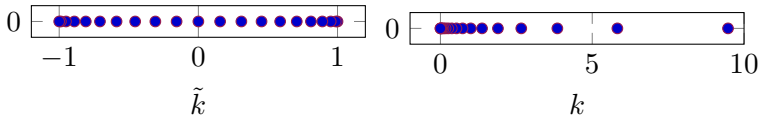

Figure 7.12: Map of variable $k \to \tilde{k}$, where $\tilde{k}_l$ are Gauss-Lobatto grid-points, the discrete version of $\tilde{k}$, which is used to evaluate integral in equation (7.15).

following relation for the Dirichlet condition $\boldsymbol{q}(0,t)$

$$i\pi \boldsymbol{q}(0,t) = \boldsymbol{q}(0,t_o) \int_{\partial\mathcal{D}^-} \frac{k\mathrm{e}^{-k^2(t-t_o)}}{(\alpha - k^2 + ik\gamma)}\,\mathrm{d}k + \int_{\partial\mathcal{D}^-} \frac{k\mathrm{e}^{-k^2 t}\tilde{\boldsymbol{f}}(k^2,t_o,t_o+\Delta t)}{(\alpha - k^2 + ik\gamma)}\,\mathrm{d}k + \int_{\partial\mathcal{D}^-} \frac{k\mathrm{e}^{-k^2(t-t_o)}\hat{\boldsymbol{q}}(k,t_o)}{(\alpha - k^2 + ik\gamma)}\,\mathrm{d}k, \quad t_o \le t \le t_o + \Delta t. \tag{7.13}$$

To obtain the above expression we appeal to Jordan's lemma several times in order to eliminate integrals that vanish. Equation (7.13) may be deformed back to the real line to obtain equation (5.57).

Equation (7.13) expresses $\boldsymbol{q}(0,t)$ in terms of an initial condition $\boldsymbol{q}(0,t_o)$, itself (via $\tilde{\boldsymbol{f}}$) and $\hat{\boldsymbol{q}}(k,t_o)$. We now derive an expression to relate $\hat{\boldsymbol{q}}(k,t_o)$ and $\hat{\boldsymbol{q}}(k,t_o+\Delta t)$ in order to obtain a rule to update the $\hat{\boldsymbol{q}}$. Once again, eliminating $\tilde{\boldsymbol{g}}_1$ from the global relation (5.56) and (7.12) we obtain after a bit of algebra

$$\mathrm{e}^{k^2(t_o+\Delta t)}\mathscr{H}(k,t_o+\Delta t) + \tilde{\boldsymbol{g}}_o(k^2,t_o,t_o+\Delta t) = \mathrm{e}^{k^2 t_o}\mathscr{H}(k,t_o) + \frac{\tilde{\boldsymbol{f}}(k^2,t_o,t_o+\Delta t)}{(\alpha - k^2 + ik\gamma)}, \tag{7.14}$$

where

$$\mathscr{H}(k,t_o) = \left\{ \frac{\boldsymbol{q}(0,t_o) + \gamma\hat{\boldsymbol{q}}(k,t_o)}{(\alpha - k^2 + ik\gamma)} \right\},$$

which at the initial time instant is $\mathscr{H}(k,0) = \boldsymbol{q}(0,0)/(\alpha - k^2 + ik\gamma)$. A similar relation exists between $\mathscr{H}(k,t_o-\Delta t)$ and $\mathscr{H}(k,t_o)$ (obtained by considering (7.12) and (5.56) for the time interval $[t_o - \Delta t, t_o]$) which is precisely (5.58).

7.4.3 Evaluating individual terms in equation (5.57)

In order to reach equation (5.60), there are four steps in the process of building $\mathcal{H}(t_j)$ and $\mathcal{F}(t_j)$. We start with the first step which is to evaluate indefinite integrals. In order to evaluate

integrals of the following type numerically

$$\mathscr{P}(t) := \int_{-\infty}^{\infty} \mathscr{B}(k) \mathrm{e}^{-k^2 t}\, \mathrm{d}k = \int_{0}^{\infty} \Im\{\mathscr{B}(k)\} \mathrm{e}^{-k^2 t}\, \mathrm{d}k. \tag{7.15}$$

Integrals of this form are prevalent in both equation (5.57-5.58) for smooth functions $\mathscr{B}(k)$ which are well behaved in the entire interval $k \in (-\infty, \infty)$. We first map the variable $k \to \tilde{k}$ using the transformation: $k = (1+\tilde{k})/(1-\tilde{k})$, $\tilde{k} \in [-1, 1)$. Using this map, we can expand the function $\Im\{\mathscr{B}(k)\}$ using Chebyshev basis as: $\sum_{n=0}^{N} c_n T_n(\tilde{k})$. Using Fast Fourier Transform (FFT) packages, we compute c_n and evaluate the integration $\mathscr{P}(t)$. Thus evaluating this integral just requires one forward Chebyshev Transform (CT). We show in figure 7.12 the map between Gauss-Lobatto grid points $\tilde{k}_l \in [-1, 1)$ and $k_l \in [0, \infty)$. Using this method we can evaluate the entire expression $\mathcal{H}(t_j)$.

We move to the second step in evaluating the equation (5.57) which is the term $\mathcal{F}(t_j)$. For a given guess $\boldsymbol{q}(0, t_j)$, which we take as $-2/\pi \mathcal{H}(t_j)$, we can evaluate $\boldsymbol{f}(\boldsymbol{q}(0, t_j), t_j)$. The next step is then to compute from this given $\boldsymbol{q}(0, t_j)$ the integral $\mathcal{F}(t)$:

$$\mathcal{F}(t) = \int_{0}^{\infty} \Im\left\{ \frac{k \mathrm{e}^{-k^2 t} \tilde{\boldsymbol{f}}(k^2, t_o, t)}{(\alpha - k^2 + ik\gamma)} \right\} \mathrm{d}k, \quad t \in [t_o, t_o + \Delta t], \tag{7.16}$$

$$= \int_{t_o}^{t} \boldsymbol{f}(\boldsymbol{q}(0, s)) \int_{0}^{\infty} \Im\left\{ \frac{k \mathrm{e}^{-k^2 (t-s)}}{(\alpha - k^2 + ik\gamma)} \right\} \mathrm{d}k\, \mathrm{d}s. \tag{7.17}$$

Substituting $(t - s) = m$, we get:

$$\mathcal{F}(t) = \int_{0}^{t-t_o} \boldsymbol{f}(\boldsymbol{q}(0, t-m)) \underbrace{\int_{0}^{\infty} \Im\left\{ \frac{k \mathrm{e}^{-k^2 (t-s)}}{(\alpha - k^2 + ik\gamma)} \right\} \mathrm{d}k}_{\mathscr{L}(m)}\, \mathrm{d}m. \tag{7.18}$$

We can now expand $\boldsymbol{f}(\boldsymbol{q}(0, t-m)) = \sum_{n=0}^{N} c_n T_n((t-m) - (t_o + \Delta t/2)/(\Delta t/2))$ with c_n being function of $\boldsymbol{q}(0, t_j)$. We choose $t - t_o = \tilde{t}$, which eliminates the t_o dependence from

the expansion and this lets us write

$$\mathcal{F}(t_j) = \sum_{l=0}^{N} c_n \int_0^{\tilde{t}_j} T_n\left(\frac{(\tilde{t}_j - m) - \Delta t/2}{\Delta t/2}\right)\mathscr{L}(m)\,\mathrm{d}m,\ \tilde{t}_j \in [0, \Delta t], \tag{7.19}$$

$$= \sum_{l=0}^{N} c_n \mathbb{M}_{nj}. \tag{7.20}$$

We can precompute $\mathbb{M}_{nj}$, which is a $N \times N$ matrix, and evaluating $\mathcal{F}(t_j)$ again requires only one CT. The next term in equation (5.58) needs a small trick to simplify and is given by

$$\mathscr{I}_1 = \int_{t_o - \Delta t}^{t_o} \mathrm{e}^{-k^2(t_o - s)}\boldsymbol{q}(0, s)\,\mathrm{d}s, \tag{7.21}$$

$$= \Delta t \int_0^1 \mathrm{e}^{-k^2\tau}\boldsymbol{q}(0, t_o - \Delta t\tau)\,\mathrm{d}\tau,\ \text{where } s = t_o - \Delta t\tau, \tag{7.22}$$

$$= \frac{\Delta t}{k^2}\int_0^{k^2} \mathrm{e}^{-\lambda}\boldsymbol{q}(0, t_o - \Delta t\frac{\lambda}{k^2})\,\mathrm{d}\lambda,\ \text{with } \tau = \frac{\lambda}{k^2}. \tag{7.23}$$

We immediately see from this expression that for large k, the integral goes to: $\boldsymbol{q}(0, t_o)\Delta t/k^2 + \mathcal{O}(1/k^2)$ implying that this part can be separately evaluated by Taylor expansion around t_o. This gives rise to

$$\mathscr{I}_1 = \begin{cases} \int_{t_o - \Delta t}^{t_o} \boldsymbol{q}(0, s)\,\mathrm{d}s, & \text{if } k = 0 \\ \\ \frac{\Delta t}{k^2}\left[\boldsymbol{q}(0, t_o)(1 - \mathrm{e}^{-k^2}) + \int_0^{k^2} \mathrm{e}^{-\lambda}\left(\boldsymbol{q}(0, t_o - \Delta t\frac{\lambda}{k^2}) - \boldsymbol{q}(0, t_o)\right)\mathrm{d}\lambda\right], & \text{if } k \neq 0 \end{cases} \tag{7.24}$$

The second term in the above equation is evaluated by expanding $\boldsymbol{q}(0, t)$ using values at $t = t_j$ when $t_o \leq t_j \leq (t_o + \Delta t)$ as $\sum_{n=0}^{N} a_n T_n(\tilde{t})$ where $\tilde{t} = (2t - (2t_o + \Delta t))/\Delta t$ is the map from $t \to \tilde{t}$. Given this polynomial approximation, we can write the integral as a precomputed matrix $\mathbb{D}_{nm}$ times the CT vector of $\boldsymbol{q}(0, t_j)$, a_n. The subsequent integral $\mathscr{I}_2$ follows the same argument and we can use the exact same matrix $\mathbb{D}_{nm}$ to compute it. Thus to compute $\mathscr{T}(t_j)$, all that we need is precomputed matrices $\mathbb{D}_{nm}$ and $\mathbb{M}_{nj}$ beyond which it is computing two CTs for each time, $t_o \leq t_j \leq (t_o + \Delta t)$.

7.4.4 Neumann-Dirichlet map for heat equation

When the global relation of the heat equation is multiplied by $\mathrm{e}^{-\omega(k)t}$ we get:

$$\int_{\partial\mathcal{D}^-} [\mathrm{e}^{\omega(k)(T-t)}\hat{q}(k,T) + \mathrm{e}^{-\omega(k)t}(\tilde{g}_1 + ik\tilde{g}_o)]\,\mathrm{d}k = 0. \tag{7.25}$$

The first term in the integral has no contribution because $(T-t) > 0$ by definition and as the contribution from $\mathcal{C}_R$ (see fig. 5.2) is zero as $R \to \infty$ since $\mathrm{e}^{\omega(k)s}$ is decaying for large k and $s > 0$. Combining this with the fact that there are no poles in $\mathcal{D}^-$ ensures that the integral along contour $\partial\mathcal{D}^-$ is zero. After we expand the other two terms we get:

$$\int_{\partial\mathcal{D}^-} \left[\int_0^t \mathrm{e}^{-\omega(t-s)} q_x(0,s)\,\mathrm{d}s + \int_t^T \mathrm{e}^{\omega(s-t)} q_x(0,s)\,\mathrm{d}s + ik \int_0^T \mathrm{e}^{\omega(s-t)} q(0,s)\,\mathrm{d}s \right] \mathrm{d}k = 0. \tag{7.26}$$

The second term in the above expression give no contribution since $(s-t) > 0$ and $\partial\mathcal{D}^-$ is the region of decaying $\mathrm{e}^{\omega(k)t}$, essentially due to Jordan's lemma. The first one can now be mapped to the real line as there are no poles in $\mathbb{C}^-$. Due to the direction of definition of the contour, we get an additional negative sign:

$$-\int_0^t \left(\int_{-\infty}^{\infty} \mathrm{e}^{-k^2(t-s)} q_x(0,s)\,\mathrm{d}k \right) \mathrm{d}s + \int_{\partial\mathcal{D}^-} \left(ik \int_0^T \mathrm{e}^{k^2(s-t)} q(0,s)\,\mathrm{d}s \right) \mathrm{d}k = 0. \tag{7.27}$$

The next step is to substitute $k\sqrt{t-s} = m$ in the first term so that it becomes a Gaussian integral and the second term can be simplified since we know $\partial\mathcal{D}^-$ is where $k_r = \pm k_i$, which implies the boundary $\partial\mathcal{D}^{\pm}$ is given by $k^2 = il$ and this leads to $ik\mathrm{d}k = -\mathrm{d}l/2$. Substituting this we get:

$$-\int_0^t \left(\int_{-\infty}^{\infty} \mathrm{e}^{-m^2} \frac{q_x(0,s)}{\sqrt{t-s}}\,\mathrm{d}m \right) \mathrm{d}s - \frac{1}{2}\int_0^T \left(\int_{-\infty}^{\infty} \mathrm{e}^{-il(t-s)} q(0,s)\,\mathrm{d}l \right) \mathrm{d}s = 0 \tag{7.28}$$

(7.29)

We thus have the final map from Neumann to Dirichlet boundary condition as:

$$q(0,t) = -\frac{1}{\sqrt{\pi}} \int_0^t \frac{q_x(0,s)}{\sqrt{t-s}}\,\mathrm{d}s. \tag{7.30}$$

In section app. 7.4.1 we saw the derivation of Dirichlet to Neumann map, and in 1-D this result reads:

$$q_x(0,t) = -\sqrt{\frac{1}{\pi t}}q(0,0) - \frac{1}{\sqrt{\pi}}\int_0^t \frac{\dot{q}(0,s)}{\sqrt{t-s}}\,\mathrm{d}s. \tag{7.31}$$

However when the initial condition $q_o(x)$ is not zero, we have:

$$q_x(0,t) = -\sqrt{\frac{1}{\pi t}}q(0,0) - \frac{1}{\sqrt{\pi}}\int_0^t \frac{\dot{q}(0,s)}{\sqrt{t-s}}\,\mathrm{d}s - \int_{\partial\mathcal{D}^-} ik\mathrm{e}^{-k^2t}\hat{q}_o(k)\,\mathrm{d}k. \tag{7.32}$$

Now for a system starting from time $t = 0$ traversing upto $(t_o + \tau)$, the above expression becomes:

$$-\pi q_x(0,t_o+\tau) = \sqrt{\frac{\pi}{(t_o+\tau)}}q(0,0) + \sqrt{\pi}\int_0^{t_o+\tau} \frac{\dot{q}(0,s)}{\sqrt{t_o+\tau-s}}\,\mathrm{d}s. \tag{7.33}$$

We expect the same solution for a system starting at t_o and traversing a duration of τ but with a different initial condition for the heat equation. We can then write:

$$-\pi q_x(0,t_o+\tau) = \sqrt{\frac{\pi}{\tau}}q(0,t_o) + \sqrt{\pi}\int_0^{\tau} \frac{\dot{q}(0,t_o+s)}{\sqrt{\tau-s}}\,\mathrm{d}s + \int_{\partial\mathcal{D}^-} ik\mathrm{e}^{-k^2\tau}\hat{q}(k,t_o)\,\mathrm{d}k. \tag{7.34}$$

From heat equation we know the global relation precisely as:

$$\hat{q}_o(k) - \mathrm{e}^{\omega(k)T}\hat{q}(k,T) - \tilde{g}_1 - ik\tilde{g}_o = 0\;\forall\, k \in \mathbb{C}^-. \tag{7.35}$$

We can evaluate this expression for $T = t_o$ and we thus get:

$$\hat{q}(k,t_o) = -(\tilde{g}_1 + ik\tilde{g}_o)\mathrm{e}^{-\omega(k)t_o}\;\forall\, k \in \mathbb{C}^-. \tag{7.36}$$

We thus have the following integral for the map starting from t_o:

$$-\pi q_x(0,t_o+\tau) = \sqrt{\frac{\pi}{\tau}}q(0,t_o) + \sqrt{\pi}\int_0^{\tau} \frac{\dot{q}(0,t_o+s)}{\sqrt{\tau-s}}\,\mathrm{d}s - \int_{\partial\mathcal{D}^-} ik\mathrm{e}^{-k^2(t_o+\tau)}(\tilde{g}_1 + ik\tilde{g}_o)\,\mathrm{d}k. \tag{7.37}$$

The first term can be evaluated as:

$$\mathscr{I}_1 = -\int_{\partial\mathcal{D}_-}\int_0^{t_o} ik\mathrm{e}^{-k^2(t_o+\tau-s)}q_x(0,s)\,\mathrm{d}s\,\mathrm{d}k, \text{ here } (t_o+\tau-s)>0\,\forall\, s\in(0,t_o), \tag{7.38}$$

$$= -\int_{\partial\mathcal{D}_-}\int_0^{t_o} ik\mathrm{e}^{-k^2(t_o+\tau-s)}q_x(0,s)\,\mathrm{d}s\,\mathrm{d}k. \text{ Substituting } k^2=il, \tag{7.39}$$

$$= -f12\int_{\partial\mathcal{D}_-}\int_0^{t_o} ik\mathrm{e}^{-il(t_o+\tau-s)}q_x(0,s)\,\mathrm{d}s\,\mathrm{d}l, \tag{7.40}$$

$$= -\pi\int_0^{t_o} q_x(0,s)\delta(t_o+\tau-s)\,\mathrm{d}s = 0. \tag{7.41}$$

The second term now simplifies to become:

$$\mathscr{I}_2 = -\int_{\partial\mathcal{D}_-}\int_0^{t_o} k^2\mathrm{e}^{-k^2(t_o+\tau-s)}q(0,s)\,\mathrm{d}s\,\mathrm{d}k, \tag{7.42}$$

$$= -\int_{\partial\mathcal{D}_-} k^2\left\{\frac{\mathrm{e}^{-k^2\tau}q(0,t_o)-\mathrm{e}^{-k^2(t_o+\tau)}q(0,0)}{k^2}-\int_0^{t_o}\frac{\mathrm{e}^{-k^2(t_o+\tau-s)}}{k^2}\dot{q}(0,s)\right\}\mathrm{d}s, \tag{7.43}$$

These three integrals can be immediately evaluated using Gaussian integral form after which we get:

$$\mathscr{I}_2 = -\sqrt{\frac{\pi}{\tau}}q(0,t_o)+\sqrt{\frac{\pi}{t_o+\tau}}q(0,0)+\sqrt{\pi}\int_0^{t_o}\frac{\dot{q}(0,s)}{\sqrt{t_o+\tau-s}}\,\mathrm{d}s. \tag{7.44}$$

Substituting this back to eq.7.34 we get:

$$-\pi q_x(0,t) = \sqrt{\frac{\pi}{t_o+\tau}}q(0,0)+\sqrt{\pi}\int_0^{\tau}\frac{\dot{q}(0,t_o+s)}{\sqrt{\tau-s}}\,\mathrm{d}s+\sqrt{\pi}\int_0^{t_o}\frac{\dot{q}(0,s)}{\sqrt{t_o+\tau-s}}\,\mathrm{d}s \tag{7.45}$$

which is precisely the terms in eq. 7.33 which thus shows that when the system starts from zero or t_o and navigates till $(t_o+\tau)$, the effective Neumann condition remains the same while the initial condition for the scenario starting at t_o changes. We will use this result in the following section.

7.4.5 Time translational properties of Maxey-Riley equation

Autonomous system of ordinary differential equations have the property of time translational invariance. If the ordinary equation:

$$\dot{w}(t) = f(w(t)), \qquad w(0) = w_o \tag{7.46}$$

has a solution $w(t)$, then $p(t) = w(t-t_o)$ is also a solution. We can easily see it by substituting this in the equation with $s = t - t_o$:

$$\dot{p}(t) = \frac{\mathrm{d}}{\mathrm{d}t} w(t - t_o) = \frac{\mathrm{d}}{\mathrm{d}s} w(s) = f(w(s)) = f(p(t)). \tag{7.47}$$

However this is not the case for the Maxey-Riley equation specifically due to the presence of the history integral. We now take the 1-dimensional version of Maxey-Riley just for the sake of illustration however adding indices make it 2/3-dimensional immediately. We can write the MR equation for relative velocity of a particle with the background velocity acting as forcing as:

$$\dot{w}(t) = -\alpha w(t) - \gamma \left\{ \frac{w(0)}{\sqrt{\pi t}} + \frac{1}{\sqrt{\pi}} \int_0^t \frac{\dot{w}(s)}{\sqrt{t-s}} \mathrm{d}s \right\} + f(w(t), u(t)). \tag{7.48}$$

Now we translate in time by mapping $t \mapsto t_o + \tau$ under which we get:

$$\frac{\mathrm{d}w}{\mathrm{d}t}(t_o + \tau) = -\alpha w(t_o + \tau) - \gamma \left\{ \frac{w(0)}{\sqrt{\pi(t_o + \tau)}} + \frac{1}{\sqrt{\pi}} \int_0^{t_o+\tau} \frac{\dot{w}(s)}{\sqrt{t_o + \tau - s}} \mathrm{d}s \right\} \tag{7.49}$$

$$+ f(w(t_o + \tau), u(t_o + \tau)). \tag{7.50}$$

Now we replace $w(t_o + \tau)$ by $p(\tau)$ and we get:

$$\frac{\mathrm{d}p(\tau)}{\mathrm{d}t} = -\alpha p(\tau) - \gamma \left\{ \frac{w(0)}{\sqrt{\pi(t_o + \tau)}} + \frac{1}{\sqrt{\pi}} \int_0^{t_o+\tau} \frac{\dot{w}(s)}{\sqrt{t_o + \tau - s}} \mathrm{d}s \right\} + f(p(\tau), u(\tau)). \tag{7.51}$$

We now add and subtract terms to make it look like eq. 7.50:

$$\frac{\mathrm{d}p(\tau)}{\mathrm{d}t} = -\alpha p(\tau) - \gamma\left\{\frac{p(0)}{\sqrt{\pi\tau}} + \frac{w(0)}{\sqrt{\pi(t_o+\tau)}} - \frac{p(0)}{\sqrt{\pi\tau}} + \frac{1}{\sqrt{\pi}}\int_0^{t_o}\frac{\dot{w}(s)}{\sqrt{t_o+\tau-s}}\mathrm{d}s \right. \tag{7.52}$$

$$\left. + \frac{1}{\sqrt{\pi}}\int_{t_o}^{t_o+\tau}\frac{\dot{w}(s)}{\sqrt{t_o+\tau-s}}\mathrm{d}s\right\} + f(p(\tau),u(\tau)). \tag{7.53}$$

We now make the substitution $s' = s - t_o$ to get:

$$\frac{\mathrm{d}p(\tau)}{\mathrm{d}t} = -\alpha p(\tau) - \gamma\left\{\frac{p(0)}{\sqrt{\pi\tau}} + \frac{1}{\sqrt{\pi}}\int_0^{\tau}\frac{\dot{p}(s')}{\sqrt{\tau-s'}}\mathrm{d}s'\right\} \tag{7.54}$$

$$\underbrace{-\gamma\left\{-\frac{p(0)}{\sqrt{\pi\tau}} + \frac{w(0)}{\sqrt{\pi(t_o+\tau)}} + \frac{1}{\sqrt{\pi}}\int_0^{t_o}\frac{\dot{w}(s)}{\sqrt{t_o+\tau-s}}\mathrm{d}s\right\}}_{\mathscr{I}_2} + f(p(\tau),u(\tau)). \tag{7.55}$$

We can immediately see that the second part of this equation exactly resembles eq. 7.44 whose contribution comes from starting the solution from t_o with new initial condition $\hat{q}(k,t_o)$. From this expression it is clear that the propagation of MR equation with the history integral does not obey the properties of autonomous ordinary differential equation but on mapping this to the boundary of heat equation, we convert this into a simple partial differential equation. Further the difference in solution arising out of translating the solution by t_o *i.e.*, the additional terms in eq. 7.55 come from restarting MR with new initial condition $\hat{q}(k,t_o)$.

7.4.6 Generalised Dirichlet to Neumann map

In this section we look at slightly different partial differential equation, in order to show that the technique we develop is general and can be extended to linear PDEs with constant coefficients of higher order.

$$q_t + q_{xxx} = 0, \qquad x > 0, t \in (0,T], \tag{7.56}$$

$$q(x,0) = q_o(x), \qquad x > 0, \tag{7.57}$$

$$q(0,t) = g_o(t), \qquad t \in (0,T]. \tag{7.58}$$

It is easy to see that the dispersion relation for this system is: $\omega(k) = -ik^3$. We can evaluate the region in which $\Re(\omega(k)) < 0$, and is given by:

$$\mathcal{D} = \left\{ k : \arg k \in \left(\frac{\pi}{3}, \frac{2\pi}{3}\right) \cup \left(\pi, \frac{4\pi}{3}\right) \cup \left(\frac{5\pi}{3}, 2\pi\right) \right\}. \tag{7.59}$$

These three domains are represented by $\mathcal{D}^+, \mathcal{D}_1^-, \mathcal{D}_2^-$ show in fig.X. Writing again the above system in conservative form, we find the global relation to be:

$$\hat{q}_o(k) - [k^2 \tilde{g}_o(\omega, T) - ik\tilde{g}_1(\omega, T) - \tilde{g}_2(\omega, T)] = \mathrm{e}^{\omega T} \hat{q}(k, T). \tag{7.60}$$

Now the discrete symmetries of the dispersion relation are $\nu_1(k) = \mathrm{e}^{\frac{2\pi i}{3}}$ and $\nu_2(k) = \mathrm{e}^{\frac{4\pi i}{3}}$. When $k \in \mathcal{D}^+$, we find that $\nu_1(k), \nu_2(k)$ lie in $\mathcal{D}_1^-, \mathcal{D}_2^-$. We can write the global relation, for $k \in \mathcal{D}^+$ with $\Omega = \mathrm{e}^{\frac{2\pi i}{3}}$ as:

$$\hat{q}_o(\Omega k) - [\Omega^2 k^2 \tilde{g}_o(\omega, T) - i\Omega k\tilde{g}_1(\omega, T) - \tilde{g}_2(\omega, T)] = \mathrm{e}^{\omega T} \hat{q}(\Omega k, T), \tag{7.61}$$

$$\hat{q}_o(\Omega^2 k) - [\Omega k^2 \tilde{g}_o(\omega, T) - i\Omega^2 k\tilde{g}_1(\omega, T) - \tilde{g}_2(\omega, T)] = \mathrm{e}^{\omega T} \hat{q}(\Omega^2 k, T). \tag{7.62}$$

Using eq. 7.60, 7.61 we can write $\tilde{g}_1$ in terms of $\tilde{g}_o$ as:

$$ik\tilde{g}_1(\omega, T) = -\Omega^2 k^2 \tilde{g}_o(\omega, T) - \frac{1}{(\Omega - 1)} \left[\hat{q}_o(\Omega k) - \hat{q}_o(k) \right] \tag{7.63}$$

$$- \frac{\mathrm{e}^{\omega T}}{(\Omega - 1)} \left[\hat{q}(k, T) - \hat{q}(\Omega k, T) \right]. \tag{7.64}$$

We now use the handy trick we have used extensively above, *i.e.*, multiply above expression by $k\mathrm{e}^{ik^3 t}$ and integrate over the domain $\partial\mathcal{D}^+$. After a bit of algebra, quite similar to the earlier calculation, we end up with:

$$q_x(0, t) = \frac{3\Omega^2 \varrho_1(t)}{2\pi} q(0, 0) + \frac{3\Omega^2 \varrho_2}{2\pi} \int_0^t \frac{\dot{q}(0, s)}{(t - s)^{\frac{1}{3}}} \, \mathrm{d}s, \tag{7.65}$$

$$\varrho_1(t) = \int_{\partial\mathcal{D}^+} \mathrm{e}^{ik^3 t} \, \mathrm{d}k, \; \varrho_2 = \int_{\partial\mathcal{D}^+} \mathrm{e}^{ik^3} \, \mathrm{d}k. \tag{7.66}$$

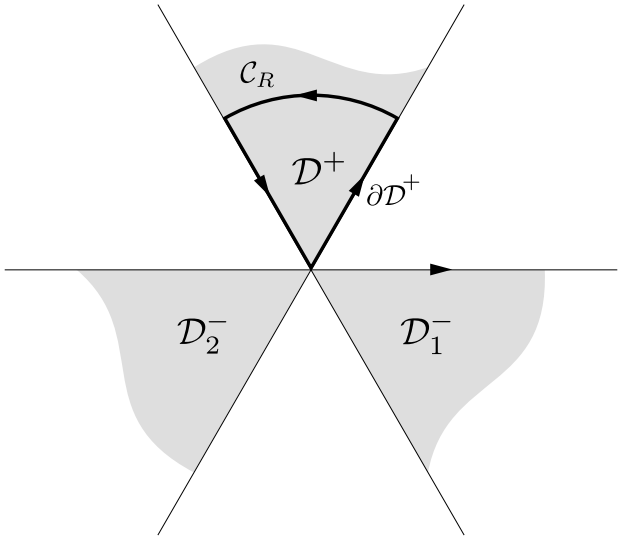

Figure 7.13: Regions $\mathcal{D}^+, \mathcal{D}^-_{1,2}$ in the complex k-plane where the dispersion relation $\omega(k) = -ik^3$ is well defined $i.e., \Re(\omega(k)) < 0$ and the integral path $\partial\mathcal{D}^+$ used to find the generalised Dirichlet to Neumann map.

7.4.7 Converting IDE to a boundary condition to PDE

Let us consider now the IDE of the form:

$$\dot{v}(t) + \alpha v(t) - \gamma\left\{\frac{3\Omega^2\varrho_1(t)}{2\pi}v(0) + \frac{3\Omega^2\varrho_2}{2\pi}\int_0^t \frac{\dot{v}(s)}{(t-s)^{\frac{1}{3}}}\,\mathrm{d}s\right\} = f(t). \tag{7.67}$$

From the equivalence established for the Maxey-Riley equation, we can clearly see that this equation again can be written as a boundary condition to a PDE:

$$q_t + q_{xxx} = 0, \qquad x > 0, t \in (0, T], \tag{7.68}$$

$$q(x, 0) = q_o(x), \qquad x > 0, \tag{7.69}$$

$$q_t(0, t) + \alpha q(0, t) - \gamma q_x(0, t) = f(t). \tag{7.70}$$

The time-transform of the boundary condition becomes:

$$\mathrm{e}^{\omega T} q(0, T) - q(0, 0) + (\alpha + ik^3) - \gamma\tilde{g}_1 = \tilde{f}. \tag{7.71}$$

We can solve for $\tilde{g}_o(\omega, T)$ to give:

$$\tilde{g}_o(\omega, T) = \frac{q(0,0) + \tilde{f}(\omega, T)}{(ik^3 + (\Omega+1)ik\gamma + \alpha)} - \frac{\mathrm{e}^{\omega T} q(0,T)}{(ik^3 + (\Omega+1)ik\gamma + \alpha)} \tag{7.72}$$

$$- \frac{i\gamma}{(ik^3 + (\Omega+1)ik\gamma + \alpha)} \left[\frac{\hat{q}_o(k) - \hat{q}_o(\Omega k)}{k(\Omega - 1)} \right] \tag{7.73}$$

$$+ \frac{i\gamma \mathrm{e}^{\omega T}}{(ik^3 + (\Omega+1)ik\gamma + \alpha)} \left[\frac{\hat{q}(k,T) - \hat{q}(\Omega k, T)}{k(\Omega - 1)} \right]. \tag{7.74}$$

On multiplying this above expression by $k^2 \mathrm{e}^{ik^3 t}$ for $t < T$ and integrating over $\partial\mathcal{D}^+$, we find the solution to be:

$$-\frac{2\pi}{3} q(0,t) = \int_{\partial\mathcal{D}^+} \frac{k^2 \mathrm{e}^{ik^3 t} \{ q(0,0) + \tilde{f}(\omega, t) \}}{(ik^3 + (\Omega+1)ik\gamma + \alpha)} \, \mathrm{d}k \tag{7.75}$$

$$- \int_{\partial\mathcal{D}^+} \frac{i\gamma k \mathrm{e}^{ik^3 t}}{(ik^3 + (\Omega+1)ik\gamma + \alpha)} \left[\frac{\hat{q}_o(k) - \hat{q}_o(\Omega k)}{(\Omega - 1)} \right] \mathrm{d}k. \tag{7.76}$$

References

[1] Mark J Ablowitz and Athanassios S Fokas. *Complex variables: introduction and applications*. Cambridge University Press, 2003.

[2] José Alvarado, Jean Comtet, Emmanuel de Langre, and AE Hosoi. Nonlinear flow response of soft hair beds. *Nature Physics*, 13(10):1014, 2017.

[3] Bruno Andreotti and Jacco H Snoeijer. Soft wetting and the shuttleworth effect, at the crossroads between thermodynamics and mechanics. *Europhysics Letters*, 113(6):66001, 2016.

[4] Arnaud Antkowiak, Basile Audoly, Christophe Josserand, Sébastien Neukirch, and Marco Rivetti. Instant fabrication and selection of folded structures using drop impact. *Proceedings of the National Academy of Sciences*, 108(26):10400–10404, 2011.

[5] Arnaud Antkowiak, Basile Audoly, Christophe Josserand, Sébastien Neukirch, and Marco Rivetti. Instant fabrication and selection of folded structures using drop impact. *Proceedings of the National Academy of Sciences*, 108(26):10400–10404, 2011.

[6] M Niazi Ardekani, G Sardina, L Brandt, L Karp-Boss, RN Bearon, and EA Variano. Sedimentation of elongated non-motile prolate spheroids in homogenous isotropic turbulence. *arXiv preprint arXiv:1611.10284*, 2016.

[7] R Arquier, S Karkar, A Lazarus, O Thomas, C Vergez, and B Cochelin. Manlab: an interactive path-following and bifurcation analysis software, 2010.

[8] Guillermo Arreaga, Riccardo Capovilla, Chryssomalis Chryssomalakos, and Jemal Guven. Area-constrained planar elastica. *Physical Review E*, 65(3):031801, 2002.

[9] Basile Audoly. Lecture notes on thin structures.

[10] Basile Audoly and Sébastien Neukirch. Fragmentation of rods by cascading cracks: why spaghetti does not break in half. *Physical review letters*, 95(9):095505, 2005.

[11] Basile Audoly and Yves Pomeau. *Elasticity and geometry: from hair curls to the non-linear response of shells*. Oxford University Press, 2010.

[12] Alfred Barnard Basset. *A treatise on hydrodynamics: with numerous examples*, volume 2. Deighton, Bell and Company, 1888.

[13] Jérémie Bec, Holger Homann, and Samriddhi Sankar Ray. Gravity-driven enhancement of heavy particle clustering in turbulent flow. *Physical review letters*, 112(18):184501, 2014.

[14] Michael Benzaquen, Thomas Salez, and Elie Raphaël. Intermediate asymptotics of the capillary-driven thin-film equation. *Eur. Phys. J. E*, 36(8):1–7, 2013.

[15] Michael Benzaquen, Paul Fowler, Laetitia Jubin, Thomas Salez, Kari Dalnoki-Veress, and Elie Raphaël. Approach to universal self-similar attractor for the levelling of thin liquid films. *Soft matter*, 10(43):8608–8614, 2014.

[16] Miklós Bergou, Max Wardetzky, Stephen Robinson, Basile Audoly, and Eitan Grinspun. Discrete elastic rods. *ACM transactions on graphics (TOG)*, 27(3):63, 2008.

[17] José Bico, Benoît Roman, Loic Moulin, and Arezki Boudaoud. Adhesion: elastocapillary coalescence in wet hair. *Nature*, 432(7018):690, 2004.

[18] José Bico, Étienne Reyssat, and Benoît Roman. Elastocapillarity: When surface tension deforms elastic solids. *Annual Review of Fluid Mechanics*, (0), 2018.

[19] ND Brubaker and J Lega. Capillary-induced deformations of a thin elastic sheet. *Philosophical Transactions of the Royal Society A: Mathematical, Physical and Engineering Sciences*, 374 (2066):20150169, 2016.

[20] P-T Brun, Basile Audoly, Alain Goriely, and Dominic Vella. The surprising dynamics of a chain on a pulley: lift off and snapping. *Proc. R. Soc. A*, 472(2190):20160187, 2016.

[21] P-T Brun, Chikara Inamura, Daniel Lizardo, Giorgia Franchin, Michael Stern, Peter Houk, and Neri Oxman. The molten glass sewing machine. *Phil. Trans. R. Soc. A*, 375(2093):20160156, 2017.

[22] Pierre-Thomas Brun, Neil Ribe, and Basile Audoly. An introduction to the mechanics of the lasso. *Proceedings of the Royal Society A: Mathematical, Physical and Engineering Science*, 470 (2171):20140512, 2014.

[23] John WM Bush and David L Hu. Walking on water: biolocomotion at the interface. *Annual Review of Fluid Mechanics*, 38:339–369, 2006.

[24] AC Callan-Jones, P-T Brun, and B Audoly. Self-similar curling of a naturally curved elastica. *Physical review letters*, 108(17):174302, 2012.

[25] ME Cates. Complex fluids: the physics of emulsions. *Soft Interfaces: Lecture Notes of the Les Houches Summer School: Volume 98, July 2012*, 98:317, 2017.

[26] E. Cerda and L. Mahadevan. *Geometry and Physics of Wrinkling*, volume 90. February 2003. doi: 10.1103/PhysRevLett.90.074302.

[27] Dinesh Chandra and Shu Yang. Capillary-force-induced clustering of micropillar arrays: is it caused by isolated capillary bridges or by the lateral capillary meniscus interaction force? *Langmuir*, 25(18):10430–10434, 2009.

[28] Nicolas Clauvelin, Basile Audoly, and Sebastian Neukirch. Elasticity and electrostatics of plectonemic dna. *Biophysical journal*, 96(9):3716–3723, 2009.

[29] Roland Clift, John R Grace, and Martin E Weber. *Bubbles, drops, and particles*. Courier Corporation, 2005.

[30] John Cotton and Wally Grant. Computational models of hair cell bundle mechanics: I. single stereocilium. *Hearing research*, 197(1):96–104, 2004.

[31] John O Dabiri. Jellyfish-inspired propulsion. *Integrative and Comparative Biology*, 51(S1):E29–E29, 2011.

[32] Anton Daitche. Advection of inertial particles in the presence of the history force: Higher order numerical schemes. *Journal of Computational Physics*, 254:93–106, 2013.

[33] Anton Daitche. On the role of the history force for inertial particles in turbulence. *Journal of Fluid Mechanics*, 782:567–593, 2015.

[34] Anton Daitche and Tamás Tél. Memory effects are relevant for chaotic advection of inertial particles. *Physical review letters*, 107(24):244501, 2011.

[35] Anton Daitche and Tamás Tél. Memory effects in chaotic advection of inertial particles. *New Journal of Physics*, 16(7):073008, 2014.

[36] Benny Davidovitch, Robert D Schroll, Dominic Vella, Mokhtar Adda-Bedia, and Enrique A Cerda. Prototypical model for tensional wrinkling in thin sheets. *Proceedings of the National Academy of Sciences*, 108:18227–18232, 2011. doi: 10.1073/pnas.1108553108.

[37] Emmanuel De Langre. Effects of wind on plants. *Annu. Rev. Fluid Mech.*, 40:141–168, 2008.

[38] Bernard Deconinck, Thomas Trogdon, and Vishal Vasan. The method of fokas for solving linear partial differential equations. *SIAM Review*, 56(1):159–186, 2014.

[39] Bernard Deconinck, Qi Guo, Eli Shlizerman, and Vishal Vasan. Fokas's unified transform method for linear systems. *Quarterly of Applied Mathematics*, 2017.

[40] P Deepu, S Ravichandran, and Rama Govindarajan. Caustics-induced coalescence of small droplets near a vortex. *Physical Review Fluids*, 2(2):024305, 2017.

[41] Eusebius J Doedel, Thomas F Fairgrieve, Björn Sandstede, Alan R Champneys, Yuri A Kuznetsov, and Xianjun Wang. Auto-07p: Continuation and bifurcation software for ordinary differential equations. 2007.

[42] C Duprat, S Protiere, AY Beebe, and HA Stone. Wetting of flexible fibre arrays. *Nature*, 482 (7386):510, 2012.

[43] Hervé Elettro, Sébastien Neukirch, Fritz Vollrath, and Arnaud Antkowiak. In-drop capillary spooling of spider capture thread inspires hybrid fibers with mixed solid–liquid mechanical properties. *Proceedings of the National Academy of Sciences*, 113(22):6143–6147, 2016.

[44] Husam A Elghannay and Danesh K Tafti. Development and validation of a reduced order history force model. *International Journal of Multiphase Flow*, 85:284–297, 2016.

[45] Arthur A Evans, Saverio E Spagnolie, Denis Bartolo, and Eric Lauga. Elastocapillary self-folding: buckling, wrinkling, and collapse of floating filaments. *Soft Matter*, 9(5):1711–1720, 2013.

[46] G Falkovich, A Fouxon, and MG Stepanov. Acceleration of rain initiation by cloud turbulence. *Nature*, 419(6903):151, 2002.

[47] Mohammad Farazmand and George Haller. The maxey–riley equation: Existence, uniqueness and regularity of solutions. *Nonlinear Analysis: Real World Applications*, 22:98–106, 2015.

[48] Benjamin Pietro Filardo. Pliant mechanisms for extracting power from moving fluid, April 13 2010. US Patent 7,696,634.

[49] TM Fischer, P Dhar, and P Heinig. The viscous drag of spheres and filaments moving in membranes or monolayers. *Journal of Fluid Mechanics*, 558:451–475, 2006.

[50] A. S. Fokas. *A unified approach to boundary value problems*. CBMS-NSF regional conference series in applied mathematics, Society for Industrial and Applied Mathematics (SIAM), Philadelphia, PA, 2008.

[51] Yoël Forterre, Jan M Skotheim, Jacques Dumais, and Lakshminarayanan Mahadevan. How the venus flytrap snaps. *Nature*, 433(7024):421, 2005.

[52] Mattia Gazzola, Médéric Argentina, and Lakshminarayanan Mahadevan. Scaling macroscopic aquatic locomotion. *Nature Physics*, 10(10):758, 2014.

[53] James M Gere and Stephen Prokofevich Timoshenko. *Theory of elastic stability*. Dover Publications, 2009.

[54] Luca Giomi and Lakshminarayanan Mahadevan. Minimal surfaces bounded by elastic lines. *Proc. R. Soc. A*, 468(2143):1851–1864, 2012.

[55] Raymond E Goldstein and Stephen A Langer. Nonlinear dynamics of stiff polymers. *Physical review letters*, 75(6):1094, 1995.

[56] Alain Goriely. Twisted elastic rings and the rediscoveries of michell's instability. *Journal of Elasticity*, 84(3):281–299, 2006.

[57] Rama Govindarajan and S. Ravichandran. Cloud microatlas. *Resonance*, 22(3):269–277, Mar 2017. ISSN 0973-712X.

[58] Jeffrey S Guasto, Roberto Rusconi, and Roman Stocker. Fluid mechanics of planktonic microorganisms. *Annual Review of Fluid Mechanics*, 44:373–400, 2012.

[59] Ksenia Guseva, Anton Daitche, Ulrike Feudel, and Tamás Tél. History effects in the sedimentation of light aerosols in turbulence: The case of marine snow. *Physical Review Fluids*, 1(7): 074203, 2016.

[60] Ksenia Guseva, Anton Daitche, and Tamás Tél. A snapshot attractor view of the advection of inertial particles in the presence of history force. *The European Physical Journal Special Topics*, 226(9):2069–2078, 2017.

[61] Gerhard J Herndl and Thomas Reinthaler. Microbial control of the dark end of the biological pump. *Nature geoscience*, 6(9):718, 2013.

[62] Evan Hohlfeld and Lakshminarayanan Mahadevan. Unfolding the sulcus. *Physical review letters*, 106(10):105702, 2011.

[63] Douglas P Holmes, P-T Brun, Anupam Pandey, and Suzie Protière. Rising beyond elastocapillarity. *Soft matter*, 12(22):4886–4890, 2016.

[64] Jiangshui Huang, Megan Juszkiewicz, Wim H De Jeu, Enrique Cerda, Todd Emrick, Narayanan Menon, and Thomas P Russell. Capillary wrinkling of floating thin polymer films. *Science*, 317(5838):650–653, 2007.

[65] Jiangshui Huang, Benny Davidovitch, Christian D Santangelo, Thomas P Russell, and Narayanan Menon. Smooth cascade of wrinkles at the edge of a floating elastic film. *Physical review letters*, 105(3):038302, 2010.

[66] Jeremy S Hyams and Gary G Borisy. Isolated flagellar apparatus of chlamydomonas: characterization of forward swimming and alteration of waveform and reversal of motion by calcium ions in vitro. *Journal of cell science*, 33(1):235–253, 1978.

[67] Mohammad K Jawed, Fang Da, Jungseock Joo, Eitan Grinspun, and Pedro M Reis. Coiling of elastic rods on rigid substrates. *Proceedings of the National Academy of Sciences*, 111(41): 14663–14668, 2014.

[68] Mohammad K Jawed, NK Khouri, F Da, E Grinspun, and Pedro M Reis. Propulsion and instability of a flexible helical rod rotating in a viscous fluid. *Physical review letters*, 115(16): 168101, 2015.

[69] Elizabeth R Jerison, Ye Xu, Larry A Wilen, and Eric R Dufresne. Deformation of an elastic substrate by a three-phase contact line. *Physical review letters*, 106(18):186103, 2011.

[70] Stefan Karpitschka, Anupam Pandey, Luuk A Lubbers, Joost H Weijs, Lorenzo Botto, Siddhartha Das, Bruno Andreotti, and Jacco H Snoeijer. Liquid drops attract or repel by the inverted cheerios effect. *Proceedings of the National Academy of Sciences*, 113(27):7403–7407, 2016.

[71] Eleni Katifori. The transport network of a leaf. *Comptes Rendus Physique*, 19(4):244–252, 2018.

[72] Joseph B Keller. Ponytail motion. *SIAM Journal on Applied Mathematics*, 70(7):2667–2672, 2010.

[73] Hunter King, Robert D Schroll, Benny Davidovitch, and Narayanan Menon. Elastic sheet on a liquid drop reveals wrinkling and crumpling as distinct symmetry-breaking instabilities. *Proceedings of the National Academy of Sciences*, 109(25):9716–9720, 2012.

[74] Joy Klinkenberg, HC de Lange, and Luca Brandt. Linear stability of particle laden flows: the influence of added mass, fluid acceleration and basset history force. *Meccanica*, 49(4):811–827, 2014.

[75] Andrei S Kozlov, Johannes Baumgart, Thomas Risler, Corstiaen PC Versteegh, and AJ Hudspeth. Forces between clustered stereocilia minimize friction in the ear on a subnanometre scale. *Nature*, 474(7351):376–379, 2011.

[76] Deepak Kumar, Joseph D Paulsen, Thomas P Russell, and Narayanan Menon. Wrapping with a splash: High-speed encapsulation with ultrathin sheets. *Science*, 359(6377):775–778, 2018.

[77] Deepak Kumar, Joseph D Paulsen, Thomas P Russell, and Narayanan Menon. Wrapping with a splash: High-speed encapsulation with ultrathin sheets. *Science*, 359(6377):775–778, 2018.

[78] Horace Lamb. *Hydrodynamics*. Cambridge university press, 1993.

[79] Lev Davidovich Landau and EM Lifshitz. *Course of Theoretical Physics Vol 7: Theory of Elasticity*. Pergamon Press, 1959.

[80] Gabriel Provencher Langlois, Mohammad Farazmand, and George Haller. Asymptotic dynamics of inertial particles with memory. *Journal of nonlinear science*, 25(6):1225–1255, 2015.

[81] George V Lauder. Fish locomotion: recent advances and new directions. *Annual review of marine science*, 7:521–545, 2015.

[82] Eric Lauga. Bacterial hydrodynamics. *Annual Review of Fluid Mechanics*, 48:105–130, 2016.

[83] Eric Lauga and Thomas R Powers. The hydrodynamics of swimming microorganisms. *Reports on Progress in Physics*, 72(9):096601, 2009.

[84] Anna Lee, P-T Brun, J Marthelot, G Balestra, F Gallaire, and Pedro M Reis. Fabrication of slender elastic shells by the coating of curved surfaces. *Nature communications*, 7:11155, 2016.

[85] Raph Levien. The elastica: a mathematical history. *University of California, Berkeley, Technical Report No. UCB/EECS-2008-103*, 2008.

[86] Lei Li, Harishankar Manikantan, David Saintillan, and Saverio E Spagnolie. The sedimentation of flexible filaments. *Journal of Fluid Mechanics*, 735:705–736, 2013.

[87] Haiyi Liang and L Mahadevan. Growth, geometry, and mechanics of a blooming lily. *Proceedings of the National Academy of Sciences*, 108(14):5516–5521, 2011.

[88] James Lighthill. Flagellar hydrodynamics. *SIAM Review*, 18(2):161–230, 1976.

[89] Anke Lindner and Michael J Shelley. Elastic fibers in flows. *Fluid–Structure Interactions at Low Reynolds Numbers (ed. C. Duprat & HA Stone), Royal Society of Chemistry*, 2014.

[90] Phillip M Lovalenti and John F Brady. The hydrodynamic force on a rigid particle undergoing arbitrary time-dependent motion at small reynolds number. *Journal of Fluid Mechanics*, 256: 561–605, 1993.

[91] Phillip M Lovalenti and John F Brady. The force on a sphere in a uniform flow with small-amplitude oscillations at finite reynolds number. *Journal of Fluid Mechanics*, 256:607–614, 1993.

[92] L Mahadevan and Joseph Bishop Keller. The shape of a möbius band. *Proc. R. Soc. Lond. A*, 440(1908):149–162, 1993.

[93] Joel Marthelot and PT Brun. Rayleigh-taylor mediated microstructures. *Bulletin of the American Physical Society*, 2018.

[94] Martin R Maxey and James J Riley. Equation of motion for a small rigid sphere in a nonuniform flow. *The Physics of Fluids*, 26(4):883–889, 1983.

[95] Renwei Mei and Ronald J Adrian. Flow past a sphere with an oscillation in the free-stream velocity and unsteady drag at finite reynolds number. *Journal of Fluid Mechanics*, 237:323–341, 1992.

[96] Oliver Miler, Ismail Albayrak, Vladimir Nikora, and Matthew O□Hare. Biomechanical properties of aquatic plants and their effects on plant–flow interactions in streams and rivers. *Aquatic sciences*, 74(1):31–44, 2012.

[97] JT Miller, Arnaud Lazarus, Basile Audoly, and Pedro M Reis. Shapes of a suspended curly hair. *Physical review letters*, 112(6):068103, 2014.

[98] Peter David Miller. *Applied asymptotic analysis*, volume 75. American Mathematical Soc., 2006.

[99] Vijay Narayan, Sriram Ramaswamy, and Narayanan Menon. Long-lived giant number fluctuations in a swarming granular nematic. *Science*, 317(5834):105–108, 2007.

[100] Janna C Nawroth, Hyungsuk Lee, Adam W Feinberg, Crystal M Ripplinger, Megan L McCain, Anna Grosberg, John O Dabiri, and Kevin Kit Parker. A tissue-engineered jellyfish with biomimetic propulsion. *Nature biotechnology*, 30(8):792, 2012.

[101] Sebastien Neukirch, Arnaud Antkowiak, and Jean-Jacques Marigo. The bending of an elastic beam by a liquid drop: A variational approach. *Proceedings of the Royal Society A: Mathematical, Physical and Engineering Sciences*, 469(2157):20130066, 2013.

[102] Stefano Olivieri, Francesco Picano, Gaetano Sardina, Daniele Iudicone, and Luca Brandt. The effect of the basset history force on particle clustering in homogeneous and isotropic turbulence. *Physics of fluids*, 26(4):041704, 2014.

[103] Anupam Pandey, Derek E Moulton, Dominic Vella, and Douglas P Holmes. Dynamics of snapping beams and jumping poppers. *EPL (Europhysics Letters)*, 105(2):24001, 2014.

[104] Anupam Pandey, Stefan Karpitschka, Luuk A Lubbers, Joost H Weijs, Lorenzo Botto, Siddhartha Das, Bruno Andreotti, and Jacco H Snoeijer. Dynamical theory of the inverted cheerios effect. *Soft matter*, 13(35):6000–6010, 2017.

[105] M Parmar, S Annamalai, S Balachandar, and A Prosperetti. Differential formulation of the viscous history force on a particle for efficient and accurate computation. *Journal of Fluid Mechanics*, 844:970–993, 2018.

[106] Joseph D Paulsen, Vincent Démery, Christian D Santangelo, Thomas P Russell, Benny Davidovitch, and Narayanan Menon. Optimal wrapping of liquid droplets with ultrathin sheets. *Nature materials*, 14(12):1206, 2015.

[107] Joseph D Paulsen, Vincent Démery, Christian D Santangelo, Thomas P Russell, Benny Davidovitch, and Narayanan Menon. Optimal wrapping of liquid droplets with ultrathin sheets. *Nature materials*, 14(12):1206, 2015.

[108] Joseph D Paulsen, Vincent Démery, K Buğra Toga, Zhanlong Qiu, Thomas P Russell, Benny Davidovitch, and Narayanan Menon. Geometry-driven folding of a floating annular sheet. *Physical review letters*, 118(4):048004, 2017.

[109] Miguel Pineirua, José Bico, and Benoit Roman. Capillary origami controlled by an electric field. *Soft Matter*, 6(18):4491–4496, 2010.

[110] Edward M Purcell. Life at low reynolds number. *Am. J. Phys*, 45(1):3–11, 1977.

[111] Charlotte Py, Paul Reverdy, Lionel Doppler, José Bico, Benoit Roman, and Charles N Baroud. Capillary origami: spontaneous wrapping of a droplet with an elastic sheet. *Physical review letters*, 98(15):156103, 2007.

[112] N Quennouz, M Shelley, O du Roure, and A Lindner. Transport and buckling dynamics of an elastic fibre in a viscous cellular flow. *Journal of Fluid Mechanics*, 769:387–402, 2015.

[113] Ahmad Rafsanjani, Yuerou Zhang, Bangyuan Liu, Shmuel M Rubinstein, and Katia Bertoldi. Kirigami skins make a simple soft actuator crawl. *Science Robotics*, 3(15):eaar7555, 2018.

[114] S Ravichandran and Rama Govindarajan. Caustics and clustering in the vicinity of a vortex. *Physics of Fluids*, 27(3):033305, 2015.

[115] S Ravichandran and Rama Govindarajan. Vortex-dipole collapse induced by droplet inertia and phase change. *Journal of Fluid Mechanics*, 832:745–776, 2017.

[116] Pedro M Reis, Sunghwan Jung, Jeffrey M Aristoff, and Roman Stocker. How cats lap: water uptake by felis catus. *Science*, 330(6008):1231–1234, 2010.

[117] Leif Ristroph, Attila J Bergou, John Guckenheimer, Z Jane Wang, and Itai Cohen. Paddling mode of forward flight in insects. *Physical review letters*, 106(17):178103, 2011.

[118] Marco Rivetti and Sébastien Neukirch. Instabilities in a drop-strip system: a simplified model. *Proceedings of the Royal Society A: Mathematical, Physical and Engineering Sciences*, 468(2141): 1304–1324, 2012.

[119] Marco Rivetti and Sébastien Neukirch. The mode branching route to localization of the finite-length floating elastica. *Journal of the Mechanics and Physics of Solids*, 69:143–155, 2014.

[120] Benoit Roman and José Bico. Elasto-capillarity: deforming an elastic structure with a liquid droplet. *Journal of Physics: Condensed Matter*, 22(49):493101, 2010.

[121] Daniela Rus and Michael T Tolley. Design, fabrication and control of soft robots. *Nature*, 521 (7553):467, 2015.

[122] RD Schroll, M Adda-Bedia, E Cerda, J Huang, N Menon, TP Russell, KB Toga, D Vella, and B Davidovitch. Capillary deformations of bendable films. *Physical review letters*, 111(1):014301, 2013.

[123] Eran Sharon, Benoît Roman, Michael Marder, Gyu-Seung Shin, and Harry L Swinney. Mechanics: Buckling cascades in free sheets. *Nature*, 419(6907):579, 2002.

[124] Raymond A Shaw. Particle-turbulence interactions in atmospheric clouds. *Annual Review of Fluid Mechanics*, 35(1):183–227, 2003.

[125] Amy E Shyer, Tuomas Tallinen, Nandan L Nerurkar, Zhiyan Wei, Eun Seok Gil, David L Kaplan, Clifford J Tabin, and L Mahadevan. Villification: how the gut gets its villi. *Science*, 342 (6155):212–218, 2013.

[126] R Aditi Simha and Sriram Ramaswamy. Hydrodynamic fluctuations and instabilities in ordered suspensions of self-propelled particles. *Physical review letters*, 89(5):058101, 2002.

[127] Robert W Style, Rostislav Boltyanskiy, Yonglu Che, JS Wettlaufer, Larry A Wilen, and Eric R Dufresne. Universal deformation of soft substrates near a contact line and the direct measurement of solid surface stresses. *Physical review letters*, 110(6):066103, 2013.

[128] William Thielicke and Eize J Stamhuis. Pivlab–towards user-friendly, affordable and accurate digital particle image velocimetry in matlab. *Journal of Open Research Software*, 2(1):e30, 2014.

[129] Darcy Wentworth Thompson et al. On growth and form. *On growth and form.*, 1942.

[130] Stephen Timoshenko. *Strength of materials*. New York, 1930.

[131] K Bugra Toga, Jiangshui Huang, Kevin Cunningham, Thomas P Russell, and Narayanan Menon. A drop on a floating sheet: boundary conditions, topography and formation of wrinkles. *Soft Matter*, 9(34):8289–8296, 2013.

[132] John Toner, Yuhai Tu, and Sriram Ramaswamy. Hydrodynamics and phases of flocks. *Annals of Physics*, 318(1):170–244, 2005.

[133] A.-K. Tornberg and M. J. Shelley. Simulating the dynamics and interactions of flexible fibers in Stokes flows. *Journal of Computational Physics*, 196:8–40, May 2004.

[134] Federico Toschi and Eberhard Bodenschatz. Lagrangian properties of particles in turbulence. *Annual review of fluid mechanics*, 41:375–404, 2009.

[135] MAT Van Hinsberg, JHM ten Thije Boonkkamp, and Hans JH Clercx. An efficient, second order method for the approximation of the basset history force. *Journal of Computational Physics*, 230(4):1465–1478, 2011.

[136] Vishal Vasan, S Ganga Prasath, and Rama Govindarajan. Wellposedness of fractional differential equations with applications to the maxey-riley equation. *In preparation*, 2018.

[137] Dominic Vella, Arezki Boudaoud, and Mokhtar Adda-Bedia. Statics and inertial dynamics of a ruck in a rug. *Physical review letters*, 103(17):174301, 2009.

[138] Romain Vermorel, Nicolas Vandenberghe, and Emmanuel Villermaux. Rubber band recoil. *Proceedings of the Royal Society A: Mathematical, Physical and Engineering Sciences*, 463 (2079):641–658, 2006.

[139] Roman Vetter, Falk K Wittel, and Hans J Herrmann. Morphogenesis of filaments growing in flexible confinements. *Nature communications*, 5:4437, 2014.

[140] Chris H Wiggins and Raymond E Goldstein. Flexive and propulsive dynamics of elastica at low reynolds number. *Physical Review Letters*, 80(17):3879, 1998.

[141] Jing Yang, Charles W Wolgemuth, and Greg Huber. Kinematics of the swimming of spiroplasma. *Physical review letters*, 102(21):218102, 2009.

[142] T. S. Yu, E. Lauga, and A. E. Hosoi. Experimental investigations of elastic tail propulsion at low Reynolds number. *Physics of Fluids*, 18(9):091701, September 2006.